Numerical Modelling of Processes Governing Selective Laser Sintering

Numerische Modellierung der maßgeblichen Prozesse beim selektiven Lasersintern

Zur Erlangung des akademischen Grades Doktor-Ingenieur (Dr.-Ing.)
genehmigte Dissertation von M.Tech. Ram Dayal aus Jodhpur (Indien)
Februar 2014 – Darmstadt – D 17

TECHNISCHE
UNIVERSITÄT
DARMSTADT

FACHBEREICH
MASCHINENBAU

TTD
Technische Thermodynamik

Numerical Modelling of Processes Governing Selective Laser Sintering
Numerische Modellierung der maßgeblichen Prozesse beim selektiven Lasersintern

Vom Fachbereich Maschinenbau an der Technischen Universität Darmstadt
zur Erlangung des akademischen Grades eines Doktor-Ingenieurs (Dr.-Ing.)
genehmigte Dissertation von M.Tech. Ram Dayal aus Jodhpur (Indien)

1. Gutachten: PD Dr.-Ing. habil. Tatiana Gambaryan-Roisman
2. Gutachten: Prof. Dr.-Ing. Eberhard Abele
3. Gutachten: Prof. Dr.-Ing. Peter Stephan

Tag der Einreichung 25.02.2014
Tag der mündlichen Prüfung 14.05.2014

Darmstadt 2014 – D17

This thesis is online available at:
Universitäts- und Landesbibliothek Darmstadt
tuprints (`http://tuprints.ulb.tu-darmstadt.de`)

Dedicated to
my parents

Eidesstaatliche Erklärung zur Dissertation

Hiermit versichere ich, die vorliegende Dissertation ohne Hilfe Dritter nur mit den angegebenen Quellen und Hilfsmitteln angefertigt zu haben. Alle Stellen, die aus Quellen entnommen wurden, sind als solche kenntlich gemacht. Diese Arbeit hat in gleicher oderähnlicher Form noch keiner Prüfungsbehörde vorgelegen.

Darmstadt, den 25. Februar 2014 Ram Dayal

Acknowledgements

This PhD thesis was prepared during my employment as a research associate at the Center of Smart Interfaces and Institute of Technical Thermodynamics of the Technische Universität Darmstadt. The study was funded partly CSI Seed fund and partly by the German Research Foundation DFG (Deutsche Forschungsgemeinschaft) through the project GA 736/6-1.

In the years that I worked at TU Darmstadt, I have been indebted to many individuals who have contributed directly or indirectly to the completion of this work. I would like to express my deepest gratitude to PD Dr.-Ing. habil. Tatiana Gambaryan-Roisman. She trusted me to work on this challenging and exciting research topic. Without her scientific guidance, support and encouragement, this thesis would not have been possible.

I thank Prof. Dr.-Ing. Eberhard Abele for his insightful comments and scientific inputs during the course of this work. I also thank Prof. Dr.-Ing. Peter Stephan, firstly, being very supporting Institute head, and secondly, for agreeing to examine my thesis.

Cordial thanks go to all my colleagues from the institute for creating an excellent research environment. My deepest thanks go to Nitin, Mete, Matthias, Selin for being a very good company during all these years. I would like to thank Axel and Philipp for helping prepare German version of the abstract. Many thanks my student Jitendra for helping to finish this task in time. I would like to acknowledge the collaboration of my colleagues from PTW, Mr. Hanns A. Stoffregen and Mr. Jakob Fischer who provided experimental support for this study.

I would like to thank our secretaries Mrs. Gaby Gunkel, Mrs. Heike Kagerbauer, and our former secretary Mrs. Monika Medina España for their help with administrative work.

The biggest motivating factor for me has been the love and support of my family. My father who always let me free to do the things I liked. My best support during this journey has been my wife, I would like to thank her with my deepest gratitude. Lastly, I would like to thank my kids, Gannu and Sana for making my life wonderful at home.

Darmstadt, February 25, 2014 Ram Dayal

Abstract

This study is focused on numerical investigation of heat transfer, melting, solidification and coalescence of metallic particles invoked by laser heating in application to selective laser sintering. The selective laser sintering is a promising additive manufacturing technology, applicable to a wide range of materials and products demanding a high degree of customization. Besides having potential advantages over conventional manufacturing, layer-by-layer synthesis poses challenges concerning mechanical properties, repeatability, limited choice of materials, slow production rate etc. This is due to the lack of understanding of the process variables and underlying physics.

The metal powder is subjected to local heating by constant or pulsed irradiation from a moving laser source. The powder is sintered due to liquid-liquid contact growth during partial melting of particles retaining an unmelted solid core. The interparticle contacts are developed by capillary flow of the melt driven by high curvature gradients in the vicinity of the contact. The densification is accompanied by mutual approaching of solid cores, growing size of liquid neck between the particles and finally by particle cooling and melt solidification. The process involves multiple modes of heat transfer, phase change, mass and momentum transport in powder bed and is therefore very complex.

Separate thermal models are developed to describe heat transfer at different length scales. The thermal model for radiation absorption and its transport in powder bed is based on non-continuum approach considering the discrete nature of medium. On the other hand, particle scale model describes evolution of the temperature field and phase change in a particle, while assuming surrounding granular powder as homogeneous medium. Model predictions are compared with experiments conducted on a commercial sintering system Eosint M270.

Finally a representative case of two particles in contact is considered for coupled thermal and hydrodynamic analysis. The governing equations for heat transfer and flow of liquid melt are solved using boundary element method. The coupled model accounts for heat transfer, phase change during laser heating cycle and resulting melt flow due to surface tension forces simultaneously. Detailed study of the effect of process parameters on particle temperature evolution, contact growth and densification rate is conducted and discussed.

Zusammenfassung

Diese Studie befasst sich mit der numerischen Untersuchung von Wärmetransport-, Schmelz-, Erstarrungs- und Koaleszensvorgängen von metallischen Partikeln mittels Erwärmung durch selektives Lasersintern. Selektives Lasersintern ist ein vielversprechendes Produktionsverfahren zur Herstellung von kundenspezifischen und individuellen Produkten, welches auf eine Vielzahl von Materialien angewendet werden kann. Neben den Vorteilen gegenüber herkömmlichen Produktionsverfahren, stellt die schichtweise Produktion besondere Anforderungen an mechanische Eigenschaften, Reproduzierbarkeit, Auswahl der Materialien, Geschwindigkeit des Produktionsprozesses usw.. Dies resultiert aus dem noch unzureichenden Verständnis der Prozessvariablen und der zugrunde liegenden Physik.

Das Metallpulver wird durch konstante oder pulsierende Strahlung einer sich bewegenden Laserquelle lokal erwärmt. Dabei wird das Pulver durch den Kontakt der geschmolzenen Partikeloberflächen bei zunächst noch festem Partikelkern gesintert. Der Kontakt zwischen den Partikeln wird aufgrund der Kapillarströmung des geschmolzenen Metalls hergestellt, angetrieben durch die große Oberflächenkrümmung im Kontaktbereich der Partikel. Die Verdichtung des Materials resultiert aus der gegenseitigen Annäherung der festen Partikelkerne, der Vergrößerung des flüssigen Bereichs zwischen den Kernen und schließlich aus dem Abkühlen beziehungsweise Erstarren des gesamten Materials. Dieser Prozess beinhaltet verschiedene Arten des Wärmetransports, Phasenübergänge, Massen- und Impulstransport und ist somit sehr komplex.

Es werden verschiedene thermische Modelle zur Beschreibung des Wärmetransports auf unterschiedlichen Längenskalen entwickelt. Das thermische Modell zur Beschreibung der Strahlungsabsorption sowie des Transports der Strahlung im Pulver basiert auf einem diskreten Ansatz zur Berücksichtigung der Nichthomogenität des Materials. Demgegenüber basiert das Partikel-Skalen-Modell zur Beschreibung der Temperatur und des Phasenübergangs im Partikel auf der Annahme, dass das umgebende Pulver als homogenes Medium betrachtet werden kann. Die Vorhersagen des Modells werden mit Experimenten am kommerziellen Sinterapparat Eosint M270 verglichen.

Schließlich wird der repräsentative Fall zweier sich berührender Partikel zur gekoppelten, thermischen und hydrodynamischen Analyse betrachtet. Die zur Beschreibung des

Wärme- und Stofftransports im flüssigen Metall benötigten Gleichungen werden mittels der Boundary-Element-Method gelöst. Das gekoppelte Modell berücksichtigt gleichzeitig Wärmetransport, Phasenübergang sowie Stofftransport des geschmolzenen Materials aufgrund von Oberflächenspannungen. Eine detaillierte Studie des Einflusses der Prozessparameter auf die Temperaturverteilung in den Partikeln, die Vergrößerung der Kontaktfläche zwischen den Partikeln und der Verdichtung der Partikel wird durchgeführt und ausgewertet.

Contents

List of Figures

List of Tables

Nomenclature

Roman Symbols

Symbol	Meaning	SI unit
$a_{o,P,E,W}$	coefficients of discretized equation	$[-]$
A	area	$[\mathrm{m}^2]$
C_{ij}	contact conductance between pair i,j	$[\mathrm{WK}^{-1}]$
c	radius of contact area	$[\mathrm{m}]$
c_p	specific heat capacity	$[\mathrm{Jkg}^{-1}\mathrm{K}^{-1}]$
D	diameter of the molten pool	$[\mathrm{m}]$
d	distance between the sphere centres	$[\mathrm{m}]$
E	internal energy of control volume	$[\mathrm{J}]$
E_α	rate of energy absorbed	$[\mathrm{W}]$
E_ρ	rate of energy reflected	$[\mathrm{W}]$
E_e	rate of energy emitted	$[\mathrm{W}]$
E_{inc}	rate of energy incident	$[\mathrm{W}]$
E_Y	effective Young's modulus	$[\mathrm{Nm}^{-2}]$
e_i	energy of each ray at source	$[\mathrm{J}]$
$\hat{e}$	unit vector	$[-]$
$\hat{e}_R$	unit vector in ray direction	$[-]$
f	frequency	$[\mathrm{Hz}]$
f_r	radial basis function	$[-]$
$\mathbf{f}$	surface traction	$[\mathrm{Nm}^{-2}]$
$f_{i,j}$	x and y components of surface traction	$[\mathrm{Nm}^{-2}]$
F_{ij}	view factor	$[-]$
F_{melt}	ratio of characteristic times (t_{melt}/t_{ht})	$[-]$
F_{sh}	shrinkage factor	$[-]$
F_{stokes}	ratio of characteristic times (t_{stokes}/t_{ht})	$[-]$
$\vec{\mathbf{F}}$	contact force	$[\mathrm{N}]$
$\vec{\mathbf{g}}$	acceleration due to gravity	$[\mathrm{m}^2\mathrm{s}^{-1}]$
G	Green's function	$[\mathrm{Hz}]$
h_{ref}	reference height of levelling plane	$[\mathrm{m}]$
H_f	enthalpy of fusion	$[\mathrm{Jkg}^{-1}]$
i	counter	$[-]$
I	radiation intensity	$[\mathrm{Wm}^{-2}]$
I_0	radiation intensity at the bed surface	$[\mathrm{Wm}^{-2}]$

Roman Symbols

Symbol	Meaning	SI unit
I^{ω}	mass moment of inertia	[kgm^2]
K	curvature	[m^{-1}]
l	arc length	[m]
L	length	[m]
L_p	length of molten pool	[m]
m	mass	[kg]
$\hat{n}$	unit normal vector	[−]
N	number of divisions, surfaces, rays	[−]
N_L	number of internal collocation node points	[−]
N_p	number of particles in interaction volume	[−]
N_X	number of particles intersected by reference levelling plane	[−]
$\bar{N}_X$	average number of particles intersected by reference levelling plane	[−]
O	ray origin	[−]
p	pressure	[Pa]
P_i	node point i	[−]
P_0	rated power	[W]
P_{avg}	average power	[W]
P_{peak}	peak power	[W]
q	heat flux	[Wm^{-2}]
q_0	heat flux at the powder bed surface	[Wm^{-2}]
q_{p0}	heat flux at the particle surface	[Wm^{-2}]
Q	dimensionless heat flux	[−]
$\dot{Q}$	heat transfer rate	[W]
Q_{src}	volumetric heat source	[Wm^{-3}]
r	radius	[m]
r_b	laser beam radius	[m]
r_c	particle core radius	[m]
$r_h t$	radius of heated powder region	[m]
r_n	neck radius	[m]
r_p	particle radius	[m]
$r_{x,y,z}$	length ratios	[−]
$\vec{r}$	position vector	[−]
R_e	effective radius of contact pair	[m]
R_{eqm}	characteristic length	[m]
R_K	radius of curvature	[m]
$\vec{R}$	ray	[−]

Roman Symbols

Symbol	Meaning	SI unit
S	length of domain boundary	$[-]$
S_0	length of domain boundary before coalescence	$[\mathrm{m}]$
S_{eqm}	length of domain boundary at equilibrium	$[\mathrm{m}]$
t_{exp}	time	$[\mathrm{s}]$
t_{ht}	characteristic time for heat conduction	$[\mathrm{s}]$
t_{melt}	characteristic time for melting	$[\mathrm{s}]$
t_p	pulse duration	$[\mathrm{s}]$
t_{stokes}	characteristic time	$[\mathrm{s}]$
t_*	dimensionless time (t/t_{ht})	$[-]$
t	time	$[\mathrm{s}]$
$\hat{t}$	unit tangent vector	$[-]$
T_C	core temperature	$[\mathrm{K}]$
T_S	surface temperature	$[\mathrm{K}]$
T	temperature	$[\mathrm{K}]$
T_{ijk}	stress field associated with stokes flow	$[\mathrm{m}^{-1}]$
u	temporary variable	$[-]$
$\vec{\mathbf{u}}$	velocity vector	$[\mathrm{ms}^{-1}]$
$\vec{\mathbf{v}}$	velocity vector	$[\mathrm{ms}^{-1}]$
v_n	normal velocity	$[\mathrm{ms}^{-1}]$
v_s	laser scan speed	$[\mathrm{ms}^{-1}]$
v_s^p	threshold velocity	$[\mathrm{ms}^{-1}]$
v_s^c	limiting scan velocity	$[\mathrm{ms}^{-1}]$
v_{res}	control volume	$[\mathrm{ms}^{-1}]$
V	control volume	$[\mathrm{m}^{-3}]$
V_{int}	interaction volume	$[\mathrm{m}^{-3}]$

Greek Symbols

α	absorptivity	$[-]$
α_e	effective absorptivity for granular medium	$[-]$
η	attenuation coefficient	$[\mathrm{m}^{-1}]$
η_e	effective attenuation coefficient for granular medium	$[\mathrm{m}^{-1}]$
β	angle	$[{}^{c}]$
β_m	coefficient	$[-]$
β_D	viscoelastic damping constant	$[\mathrm{Nsm}^{-1}]$
β_K	elastic spring constant	$[\mathrm{Nm}^{-1}]$
δ	overlap between the particles	$[\mathrm{m}]$
ϵ_e	effective emissivity	$[-]$
ϵ	emissivity	$[-]$
κ	thermal diffusivity	$[\mathrm{m}^2\mathrm{s}^{-1}]$
λ	thermal conductivity	$[\mathrm{Wm}^{-1}\mathrm{K}^{-1}]$
μ	dynamic viscosity	$[\mathrm{Pas}]$
ξ	inverse ellipse parameter	$[-]$
ω	angular velocity	$[{}^{c}\,\mathrm{s}^{-1}]$
Ω	solid angle	$[\mathrm{sr}]$
φ	angle	$[{}^{c}]$
ϕ	particle diameter	$[\mathrm{m}]$
ϕ_b	laser beam diameter	$[\mathrm{m}]$
ϕ_m	mean particle diameter	$[\mathrm{m}]$
Φ	diameter of molten pool	$[\mathrm{m}]$
ρ	density	$[\mathrm{kg\,m}^3]$
ρ_{pack}	packing density	$[-]$
σ	Stefan-Boltzmann constant	$[\mathrm{Wm}^{-2}\mathrm{K}^{-1}]$
γ	surface tension	$[\mathrm{Nm}^{-1}]$
τ	torque	$[\mathrm{Nm}]$
θ	angle	$[{}^{c}]$
θ_T	dimensionless temperature	$[-]$
ε	convergence criterion	$[-]$
ε_{ijk}	Levi-Civita symbol	$[-]$
Γ	domain boundary, interface	$[-]$
Υ	random number	$[-]$
Ψ	liquid fraction	$[-]$
$\mho$	internal domain	$[-]$

Subscripts

Symbol	Meaning
n	normal component
t	tangential component
max	maximum
min	minimum
in	incoming
out	outgoing
src	source
e	east face of control volume
E	node to east
w	west face of control volume
W	node to west
P	central node
mp	melting point

Superscripts

Symbol	Meaning
n	new
o	old
RBM	rigid body motion
D	disturbance component
∞	undisturbed component
J	jet
L	liquid
m	temperature measurement plane within the test specimen
N	nozzle
$real$	real or actual surface boundary condition
s	top surface of the test specimen, also referred to as the impingement surface
sat	saturated
sub	subcooled
sup	superheat
T	test specimen
V	vapor

Abbreviations

Symbol	Meaning
AM	Additive manufacturing
BEM	Boundary Element Method
CAD	Computer aided design
EBM	Electron beam melting
LM	Layered manufacturing
OPD	Optical penetration depth
SFF	Solid freeform fabrication
SLS	Selective laser sintering
SLM	Selective laser melting
3D	Three dimensional

1

Introduction

The ever increasing competition in the world market for manufactured products along with development of new frontiers demanding highly customized products in shortest possible time has lead to the development of new methods of manufacturing which have ability to challenge the position of conventional manufacturing.

1.1 Layered Manufacturing

Layered Manufacturing (LM), Additive Manufacturing (AM) or Solid Freeform Fabrication (SFF) is a class of manufacturing methods that has seen a rapid growth over the years since inception in late 80's. In contrast to conventional manufacturing processes (involving material removal to achieve final shape), the layered manufacturing is an additive process wherein the part is built by sequentially fusing thin layers of material one over another. Due to additive build-up principle it has an inherent advantage of producing parts of unlimited geometrical complexity offering possibilities for optimization even by geometrical means. The process makes use of sliced CAD data to generate successive layers from bottom to top resulting in the final product.

Layered manufacturing enables quick production of complex three-dimensional parts of designed macro and microstructure directly from CAD data, completely eliminating the intermediate tooling steps, therefore shortening production time and reducing associated costs. Another significant advantage associated with LM technique is the cost of production as well as production time does not increase with the degree of complexity.

The invention of layered manufacturing has brought a breakthrough in manufacturing technology because of immense benefits associated with it. However, development of layered manufacturing is strongly related to advancement in other technologies including CAD, 3D imaging, Laser technology, and materials. Since 1988, more than twenty different variants of layered manufacturing technology have been introduced and still counting. This technology still remains a very active area of research and development.

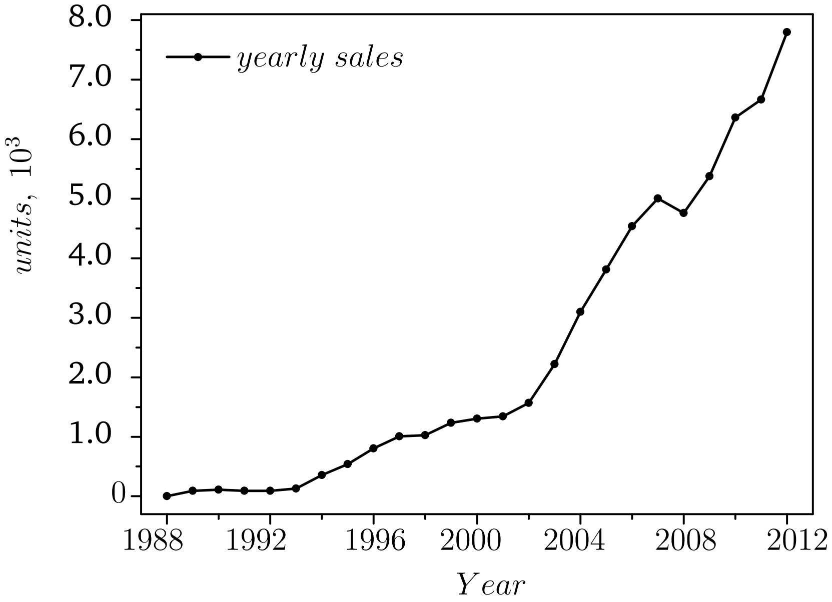

Figure 1.1 Yearly sale of additive manufacturing units worldwide [135]

The exponential growth of annual sales figures (see Fig. 1.1) for additive manufacturing units around the world confirms the growing acceptance of additive manufacturing as the new norm in industry. Besides promising outlook and potential advantages, additive manufacturing also has some drawbacks. Since inception the LM processes have significantly improved in speed, accuracy as well as in its ability to process range of materials, however they still lag behind conventional processes in terms of part reproducibility, limited part volume $(< 0{\cdot}5m^3)$ and no economics of scale [72], [83], [15]. Furthermore, "in layered manufacturing the process, its technological capability and used materials are absolutely dependent; there is no combinatorial freedom at all"[82]. The radar chart shown in Fig. 1.2 illustrates the present state of layered manufacturing techniques vis-à-vis conventional manufacturing. Future directions should be focussed to overcome the present limitations.

In recent years the use of additive manufacturing for direct production of part is continuously increasing, as shown in Fig. 1.3, even the market demand for additive manufacturing is dominated by applications in direct manufacturing of end use parts (see Fig. 1.4). However, most of the existing AM technologies are limited to making prototypes and models used during product development cycle [73] as they do not allow processing of common engineering materials to meet the functional requirements with respect to mechanical properties and thus lack

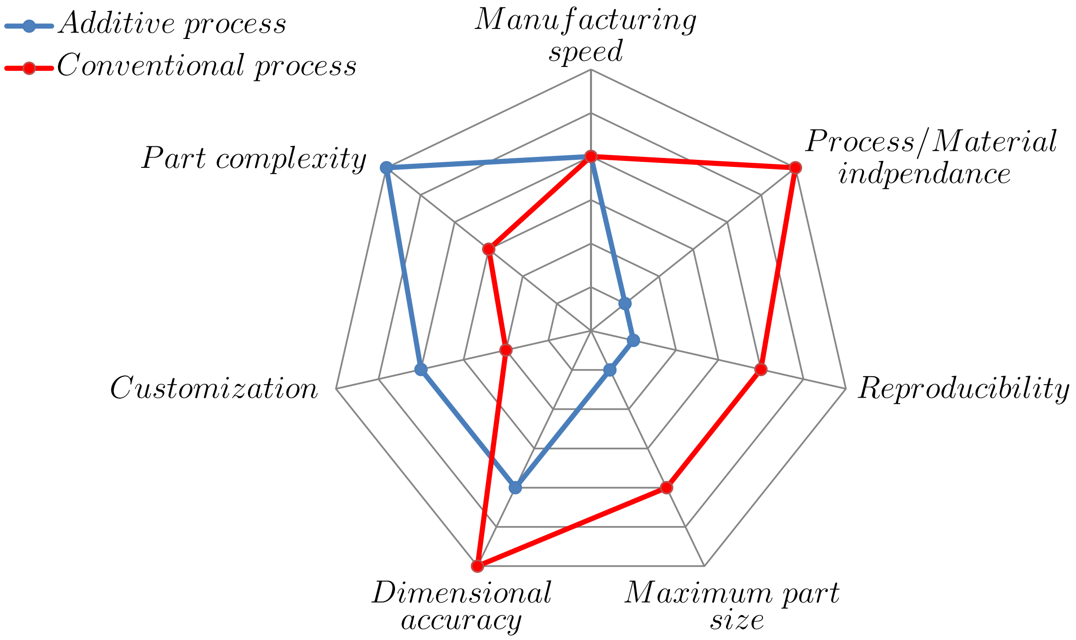

Figure 1.2 Performance mix of additive manufacturing with respect to conventional Manufacturing [1]

generic applications. The powder bed based fusion technologies are most versatile with regard to materials as well as applications ranging from aerospace, automotive, medical etc. Selective Laser Sintering (SLS) is one such powder bed based fusion technology that holds potential to qualify as emerging disruptive technology in manufacturing sector. In the prospect of qualifying the requirements of direct manufacturing sector SLS and its variants (Selective laser melting (SLM), Electron beam melting (EBM)) show great potential based on their ability to process

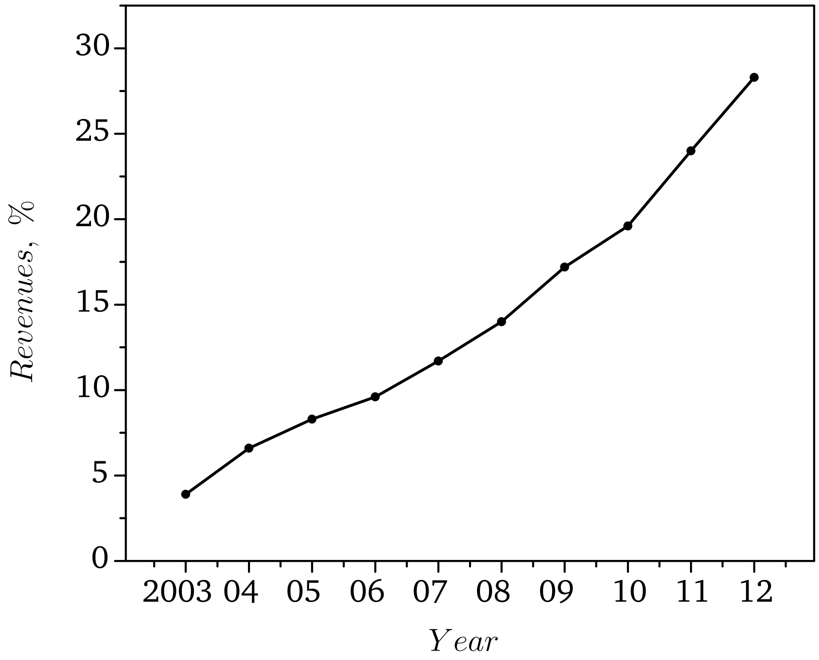

Figure 1.3 Growth of direct manufacturing revenues as percentage of total revenues from additive manufacturing worldwide [135]

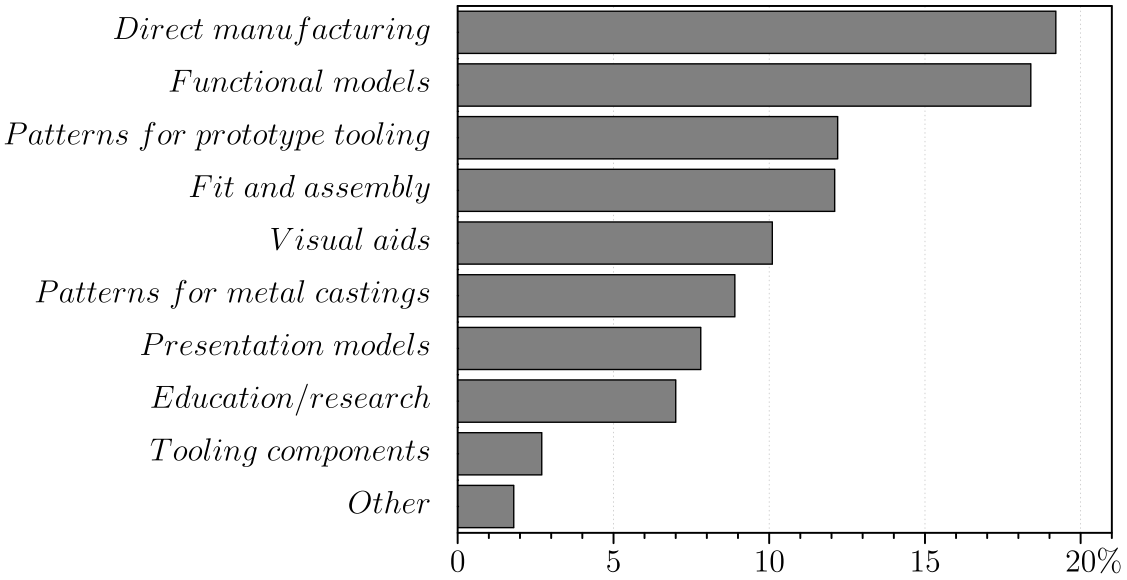

Figure 1.4 Applications of additive manufacturing with respect to end use [134]

common engineering materials as well as the resulting mechanical properties of manufactured parts. In the following section selective laser sintering technique is considered in detail.

1.2 Selective Laser Sintering: An overview

Selective Laser Sintering is a powder based layered manufacturing technology where scanning laser beam is used as a heat source to fuse the layers of powder particles. As a type of layered manufacturing it inherits all the advantages associated with it. Among all the layered manufacturing techniques SLS is one of the most versatile. In principle the SLS technology is applicable to any material available in powder form, since it is based on localized heating and resulting fusion of the powder particles. It is this property of laser sintering technology that makes it an ideal candidate for study and development of the process for new material systems, especially metals and alloys. In addition, SLS offers highest local discontinuity by varying material composition of a part in a controlled manner thus opening up further scope for part tailoring in terms of property and material gradient [61].

The main components of a SLS machine are shown in Fig.1.5. The Laser unit is responsible for generating radiation heat source that interacts with the powder particles and impart enough energy to cause melting and subsequent bonding between the particles. The purpose of optical unit is to scan the laser beam on the powder bed as per the CAD data. It consists of beam expanders and light weight scanning galvanometer mirrors to control the positioning of laser beam on the powder bed. The powder deposition system consists of a powder hopper and a re-coater to deposit a very thin layer of loose powder on the build platform before every laser exposure step.

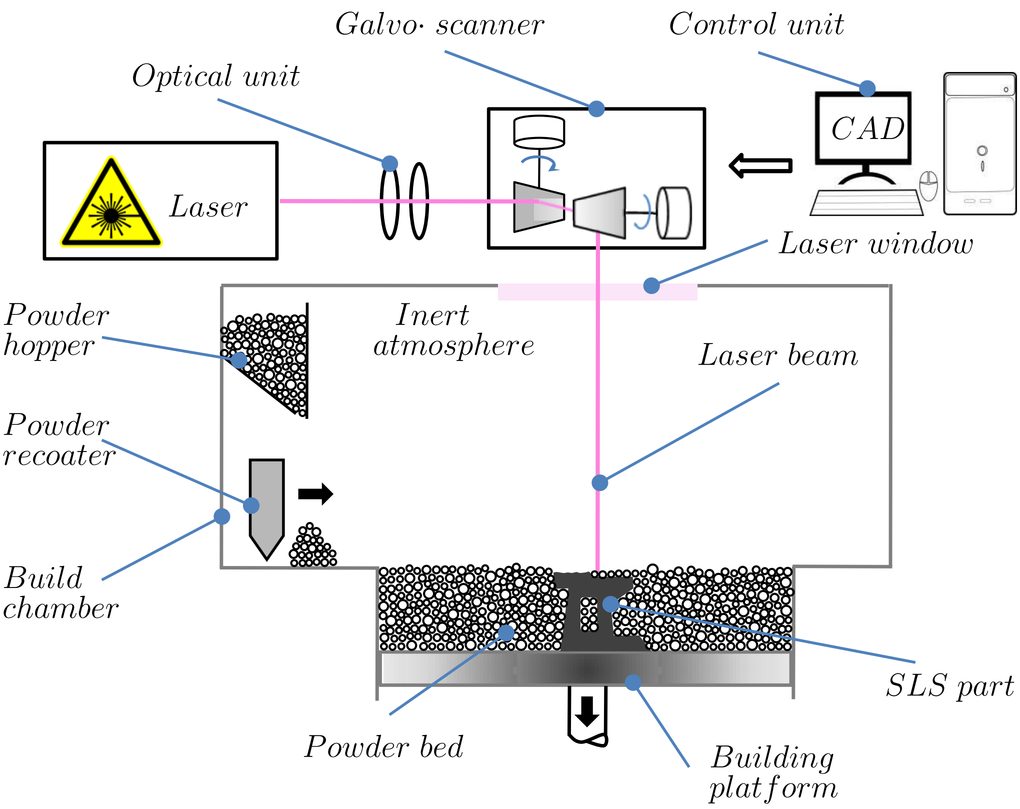

Figure 1.5 The components of a Selective laser sintering system

The complete SLS process from design to final product can be subdivided into two stages: preparation stage and fabrication stage. The preparation stage refers to generating input geometrical data of physical object and is independent from the fabrication stage. A schematic of the fabrication stage of laser sintering process cycle is shown in Fig. 1.6. The whole cycle consists of four basic steps repeated over till the product is fully formed. The steps are as follows:

1. Recoating: A very thin layer of heat-fusible powder is deposited on top of the building platform.
2. Exposure: Laser beam scans over a cross section that matches the corresponding layer in the CAD model, subsequently bonding the particles and fusing with the adjoining layers.
3. Lowering building platform: The building platform moves downward to accommodate next layer of loose powder.
4. Powder dispensing.

In the proceeding sections we will give a brief overview of materials and lasers used for selective laser sintering, a detailed review with respect to materials and lasers is available in research article by Kruth et al. [74].

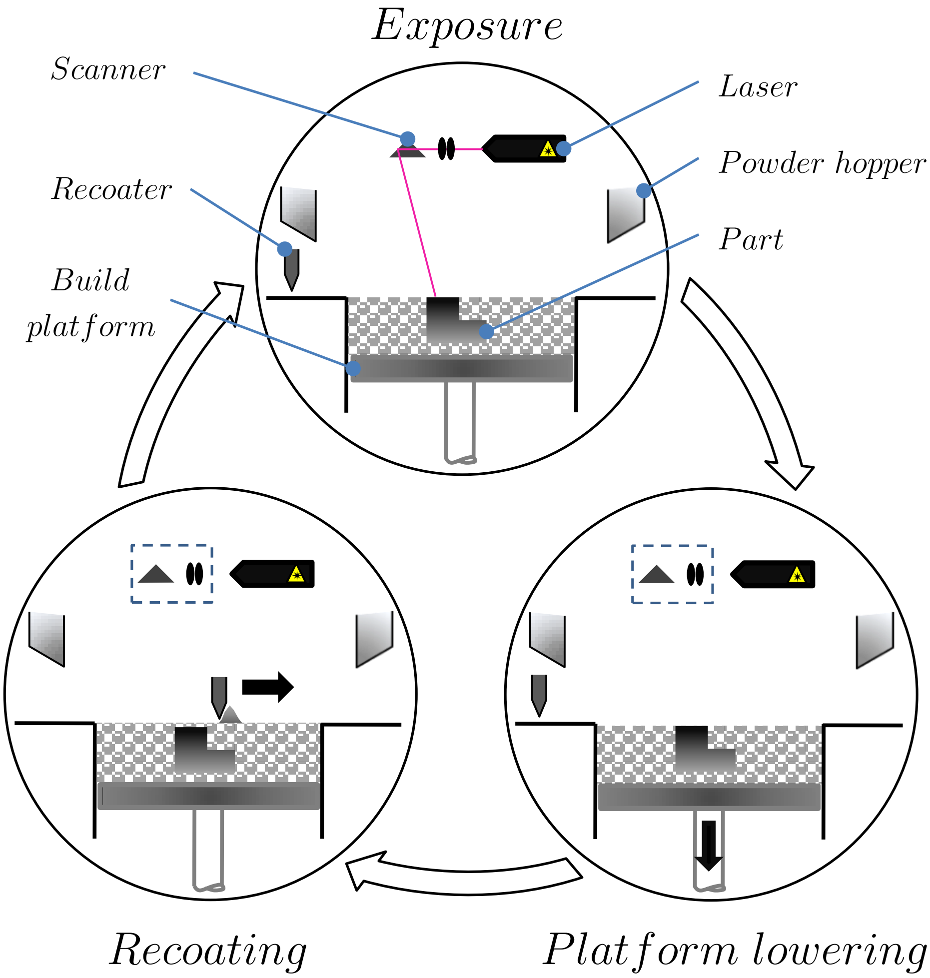

Figure 1.6 Steps during SLS process

1.2.1 Materials for SLS

Ideally SLS is suitable to process any material, that is available in powder form. The commonly used materials for SLS include polymers, metals, ceramics, and composites. The basic material property required for powder particles is their ability to fuse together when subjected to heating. Based on this criterion materials used in SLS process can be subdivided into two classes:

1. Different materials are used as a binder and as a structural material. Material systems under this class can be further subdivided into three groups according to the type of powder grains used.
   (a) Separate grains. Binder particles are usually much smaller than structural ones. These particles melt preferentially due to lower melting point and higher surface to volume ratio than the particles of structural material.
   (b) Composite grains. Composite powder grains contain both the binder and the structural material within each individual powder grain.

    (c) Coated grains. Another possibility is to coat the structural grain with the binder material. This has advantage of ensuring preferential absorption of laser radiation by binder alone due to optical properties of the coating.

2. There is no distinct binder and structural material in this material systems. Rather the distinction is due to laser induced phase change. This class of materials can be subdivided into two groups.

    (a) Single component powders. In this case the heat supplied to a powder particle is controlled in such a way that only the outer surface of the particle is molten while core remains unmelted. So the molten material acts as a binder between the non-molten particle cores.

    (b) Powder mixtures (tailored). These materials can be called "tailored", because their composition is tuned specifically for laser sintering process and they do not correspond to any conventional metals as used in other manufacturing processes.

Both tailored and conventional metals have been developed for SLS. In recent times the trend has been towards using conventional materials, in order to improve the acceptance of this new manufacturing method in established applications.

1.2.2 Lasers for SLS

The SLS process is significantly influenced by the interaction between the laser radiation and the metal powder. Most of the commercial sintering machines in the market use CO2 or Nd:YAG lasers in continuous mode. Recent studies with pulsed laser source [**?**] indicate that pulsed laser source is more suitable for SLS applications, where only partial melting is desired. On the other hand, in SLM all the powder has to be melted and therefore continuous mode is preferred.

The radiation absorptivity of metals increases with decreasing wavelength of the source. Therefore, using Nd:YAG offers better absorption characteristics than using CO2 lasers and allows achieving larger melting depth for the same power density [119]. Another advantage of using (Nd:YAG) solid state fiber laser is the ability to use optical fiber to guide the beam enabling very fine resolution and part quality. In recent years, with the great improvements in part accuracy and quality due to materials and process developments, the quality of the laser focus is becoming a limiting factor. Therefore, the newest generation of SLS machines are using fiber lasers and disc lasers which offer good beam quality and focusing capabilities. For example the EOSINT M 270 uses a 200 Watt ytterbium fiber laser, while the Trumaform LF 250 uses a disc laser.

1.2.3 Potentials and barriers

Driven by the need to fulfill the ever increasing market demand for customized products, the SLS technology is on the threshold of moving beyond prototyping to manufacturing of final parts (rapid manufacturing) from metals [75], [83], [19], [42]. The process is suitable for low volume production of materials difficult to process conventionally and for fabrication of complex parts of high aggregate value. It offers great potential for mass customization. SLS has found application in diverse fields including aerospace, automotive, biomedical, consumer, electrical and electronics industry. In most of the above applications it is desirable to have near full density of bulk material and therefore the sintered parts are further processed before they are put to use.

SLS can have applications in the fabrication of porous metal foams with high degree of control over the final microstructure and porosity. Development of functionally graded materials, integration of sensors, electronics [111] or other functional parts in the product can be realized during the fabrication stage itself.

Besides potential applications and advantages the key barriers to wider acceptance of SLS as an established manufacturing technology are:

- High component cost compared to conventional manufacturing methods. There are many factors that contribute to it (e.g slow production rates, expensive powder materials, no economics of scale etc.)
- The process lacks consistency and repeatability between the parts, largely due to lack of understanding of the process variables and underlying physics. There is limited data for detailed modelling and simulation of process. Lack of pre production simulation and planning leads to in process errors.
- Need for post production finishing to meet the product specification (e.g. surface finish, heat treatment, removal of support structure etc.)
- Limited material availability and strong process material dependence. There is need to develop material systems specially suited for laser sintering.

The strong interdependence of materials and processes in most of the additive manufacturing techniques has restricted their applications and growth potential. However, selective laser sintering holds the promise of being versatile in processing a variety of engineering materials (e.g. polymers, metals, ceramics etc.). The technology is still maturing and further research is needed for improving our understanding of processes governing interlayer bonding [10]. The present state of art relies heavily on empirical data obtained experimentally, even that too is very limited for metallic powders due the complexity of the physical mechanisms involved (e.g. absorption of laser radiation by metal powder, heat transfer inside the powder, melting, melt flow, solidification, shrinkage etc.).

Given the physical complexity of the problem, combined with multiple length scales, very short time frames and high laser intensities render experiments extremely difficult to set up, perform and evaluate. On the other hand numerical modelling offers almost endless scope for introducing system complexity and detailed multi-scale analysis.

2

State of Art

The roots of technology for laser sintering of metal powders dates back to patents of Ciraud and Housholder in 1970s [27], [57], who independently gave the concept of SLS and selective laser melting (SLM), but it was until late 1992 when Deckard, Beaman and colleagues at University of Texas [33] developed the first commercial machine based on the principle of SLS. In this chapter an overview of previous research in the field of selective laser sintering is presented. The whole chapter is divided into four sections. An overview of possible binding mechanisms for laser sintering of particles is given in first section. In the next section, heat transfer studies relevant to granular beds as well as single particle in the powder bed. Third section involves discussion about previous research in the field of coalescence of particles during laser sintering. In the final section previous experimental investigations are discussed.

2.1 Binding mechanisms

It is relatively new powder metallurgy process as opposed to conventional sintering. The novelties in the process arise due to localised heating using focussed heat source (laser beam), layer by layer build up technique and materials used. The ability to process a wide variety of engineering materials is one of the key features of SLS. The prevailing binding mechanisms for each of this variety of materials are given in Fig. 2.1. A detailed review of binding mechanisms for SLS of powder bed based fusion technology is performed by Kruth et al. [73]

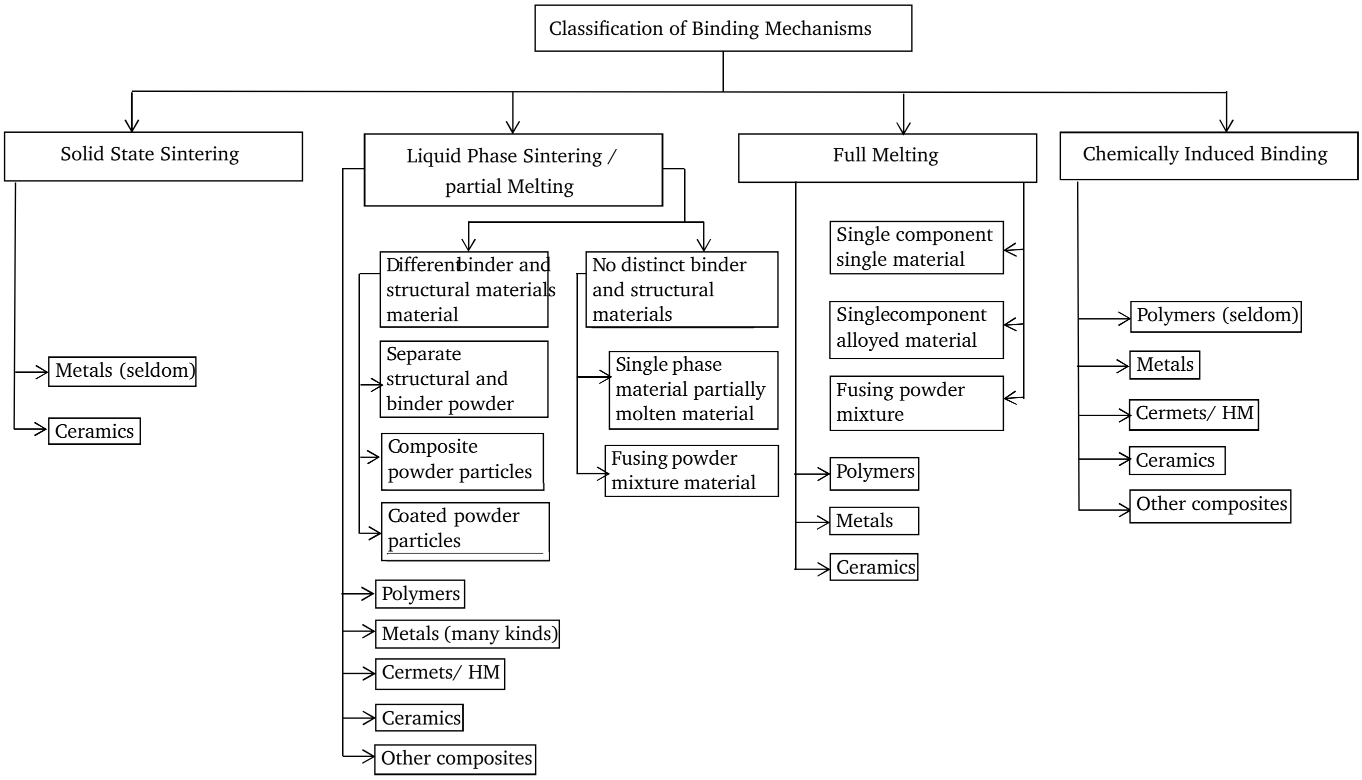

Figure 2.1 The possible binding mechanisms during laser sintering based on type of powder materials [73]

2.1.1 Solid state sintering

Solid state binding occurs at a temperature well below the melting point of the powder material and is primarily governed by diffusion of metal atoms between adjacent particles in solid state. However, the diffusion process is slow compared to the typical time scale of laser particle interaction (having magnitude of order few ms) during laser sintering. This is due very low diffusion coefficients ($10^{-9} - 10^{-15} m^2 s^{-1}$) [98] in solid state. This mechanism is not applicable for laser sintering except for post processing of laser sintered metallic or ceramic parts [83]. The dominant physical process associated with SLS are heat transfer and sintering of powder particles.

2.1.2 Liquid phase sintering/partial melting

Liquid phase sintering involves a coexisting liquid and particulate solid during some part of the thermal cycle. The presence of liquid provides both a capillary force and transport medium that promotes densification. Liquid phase sintering can be physically realized using a variety of combinations of powder materials, based on the distinction between binder and structural material as classified in section 1.2.1. Liquid phase sintering/partial melting is one of the most preferred binding mechanism for laser sintering and in the recent times, efforts are being put for using single component conventional materials, in order to improve the acceptance of this new manufacturing method in established applications.

2.1.3 Full melting

In full melting, powder particles are subjected to high power laser beam causing them to completely melt and join, thus enabling the production of fully dense objects (upto 99.9% dense) [75] Even other mechanical properties are comparable to those of the bulk material. The mechanism is equally suited for a variety of materials however, its application for metallic powders is more demanding at the same time challenging too, as it requires very strict control of process parameters to produce defect free parts. As very high temperature gradients and shrinkage during phase change leads to part internal stresses and distortion in the part [88] and other defects like balling and poor surface finish.

2.2 Heat transfer studies

2.2.1 Granular medium

Heat transfer in granular medium is crucial in wide range of applications such as powder metallurgy, thermal insulation, chemical reactors, and many other domains. Due to the nature of interactions between particle grains - strongly influencing the bulk behaviour - and multiple length scales involved, it is still an area of active research. This problem is directly relevant to modern powder bed fusion based additive manufacturing, where the process is initiated by localized heating of powder bed by a focused energy beam (e.g. SLS, SLM, EBM etc.).

According to literature all heat transfer studies in granular medium can be classified as continuum based or discrete particle based approach [67] . In continuum approach the granular bed is assumed as a homogeneous medium having effective properties, while these properties are modelled separately or obtained experimentally. On the other hand in discrete particle approach, the packed bed is explicitly modelled and discrete nature of system is taken into account while considering the involved phenomenon.

It is well established fact that the aggregate behaviour of a powder is considerably different from that of individual particles or that of the bulk material. Various studies are reported in literature to model the effective properties of a packed bed considering the applicable modes of heat transfer. Chen and Churchill [23] conducted experimental investigation of radiation heat transfer in packed bed and reported influence of bed parameters on effective properties. Yagi and Kunii [138] proposed model for effective thermal conductivity considering both radiation and conduction. A significant number of similar models are reported in literature [24, 39, 60, 81, 101].

As far as radiation heat transfer is concerned the theory of independent scattering/absorption of radiation [14, 20, 64] is applicable when the interaction between the radiation and a particle is not influenced by the presence of neighbouring particles. This is relevant for porous media with porosity greater then 0.95 [67]. However, most of the practical powder beds have porosity lower than the specified independent limit. Therefore radiative properties of the bed cannot be predicted from the properties of single particle. Singh and Kaviny [109] used Monte-Carlo method for radiative heat transfer through mono-dispersed powder bed. They proposed a discrete ordinate method based scaling approach so that independent radiative properties can be scaled to obtain effective properties in dependent regime. The scaling factor is expressed as a function of bed porosity alone and effect of emissivity is found to be small.

In the review of radiation heat transfer in packed bed done by Tien [114], the use of discontinuous approach based on Monte-Carlo and/or ray-tracing are found to be natural choice for predicting radiative heat transfer in granular systems. Chan and Tien [21] used discrete model to determine radiative properties of packed bed, they treated particulate medium as regularly packed system and investigated a representative unit cell using ray-tracing techniques. Kudo et al. [79] adopted Monte-Carlo technique for radiation heat transfer in representative unit cell. Yang et al. [139] investigated radiation in randomly packed bed using Monte-Carlo method.

Majority of research work on granular beds in past is devoted to determine effective properties of the medium [5, 23, 24, 81, 138] so that continuum approach is applicable. However, the work of Rao and Toor [100, 101] indicates that the validity of continuum approach depends on the relative size of particles in the medium and the heated boundary. When the both the length scales are comparable, the discrete nature of the medium must be taken into account. Basically the assumption of continuum treatment is violated with respect to local thermal equilibrium [67] under the conditions of extremely localized heating in the bed as found in case of SLS.

The interparticle conduction in the powder bed is strongly dependent on nature of contact between the particles as well as packing structure of the particulate medium [43], even the particle size distribution and properties of individual ingredients are important when investigating powder mixtures. A number of studies, relevant to conduction heat transfer in granular medium, have been reported [24, 110, 124, 146] with varying degree of relaxations regarding some or all of these parameters.

Based on the review of heat transfer studies non-continuum approach is adopted in the present work, in order to explicitly model individual particles in the powder bed. Interparticle conduction and radiation heat transfer modes are considered in the study while convection heat transfer is neglected [138] for stagnant bed.

2.2.2 SLS specific heat transfer studies

Over the last decade many studies particularly applicable to SLS have been reported in literature. Heat transfer studies to investigate sintering of binary mixture of metal powders were carried out by Pak and Plumb [93], Zhang et al. [141–143]. The numerical model considered the shrinkage of powder bed due to density change as well as liquid flow under the action of surface tension forces. In this work the powder was modeled as an effective medium and the effective properties were obtained empirically.

A thermal model to predict the behaviour of a representative particle in the powder bed during laser sintering was proposed by Fischer et al. [40, 41]. This model describes the instationary temperature distribution in the particle grain resulting from periodic laser pulses. The authors studied the influence of pulse frequency on temperature evolution in the particle. The minimum pulse energy required to fully melt the particle can be calculated and for lower values only partial melting is possible. However, the phase change in the powder particles is not modelled explicitly. The model predicts a nearly linear increase of average powder temperature with time.

Melting and resolidification of metal powder particle under the influence of nanosecond laser pulse was investigated by Konrad et al. [71]. They predicted step-like temperature rise in the particle with every pulse. Influence of pulse frequency, pulse duration, laser fluence and particle size on melting-solidification characteristics was studied. This model considers the interaction between laser beam and a powder particle alone in isolation from its surroundings and thus does not reflect the influence of heat transfer between the particle and surrounding medium on temperature evolution of a single particle.

Dedicated heat transfer studies in granular medium for application to laser sintering are rare, Gusarov et.al. [49] proposed a model for effective thermal conductivity of powder bed under conditions identical to laser sintering. Gusarov and Kruth [47] used continuous approach to model powder bed and used two flux method to solve radiation transfer equation. The method relies on experimental data or discrete models for effective properties of the bed. This model is further extended to include conduction heat transfer and diffusion equation is solved by finite difference [50].

Wang and Kruth [130] developed a ray-tracing model to simulate the energy absorption and penetration during the SLS of metal powders. Their model, which is based on geometrical optics, yields the evolution of the energy absorption in the powder and accordingly predicts the sintering zone dimension. However, this model did not account for conduction heat transfer between powder particles in contact, which is a significant fraction of total heat transfer for packed beds having very small powder particles [138].

Most recent studies concerning heat transfer modelling and stability of laser sintered tracks are reported by Gusarov et al. [48, 137]. They investigated heat transfer in a homogeneous bed while explaining stability of molten sintered tracks and the observed balling phenomena based on Plateau-Rayleigh criterion for capillary instability of a liquid cylinder. The mechanism of balling phenomena during SLS of metal powders is also investigated by Tolochko et al. [118, 120]. The balling phenomenon is attributed the non-uniform distribution of heat along the thickness of powder layer, that results in irregular shrinkage along the depth. A simple model based on differences in thermal expansion of layers to explain balling process is provided.

Studies devoted to modelling of heat transfer in materials subjected to moving heat source are also relevant to SLS. The temperature distribution in a homogeneous medium due to moving laser source can be modelled by using the heat source method developed by Carslaw and Jaeger

[18], provided the effective properties of the medium are known. Several researchers [29, 56, 96] have investigated the effect of a moving heat source on heating of a finite and semi-infinite medium. However, direct application of similar approach for granular medium is prone to errors [67, 100]

Numerous other heat transfer studies related to the influence of process parameters are reported in the literature [6, 25, 26, 34, 51, 70, 106, 133, 140], however, the list is not exhaustive.

2.3 Studies relevant to bonding of metallic powders

One of the earliest studies focussed on fundamentals of laser sintering process is done by Bourell et al. [11], they explained the bonding mechanisms for different powder particles as well as principles of machine operations. Further Bunnel et al. [16, 17] also described the mechanisms for obtaining high density parts from loose metal powder layers using scanning laser beam. They outlined liquid phase sintering as one of the principles playing important role during SLS of metallic powders.

Dedicated studies intended to understand the basic binding mechanisms governing SLS of metals are rare. Tolochko et al. [115–117] studied the joining of two spherical particles of nickel alloy under the action of laser irradiation as well as laser sintering of thin layers of powder. They concluded that particles under the influence of laser source experience only surface melting and join by formation of interparticle contacts by migration of molten layer to the area of contact. The processes of melting and migration occur simultaneously and are accompanied by mutual approach of the particles.

Klocke et al. [69] investigated the coalescence of two metal particles. Coalescence experiments were carried out with pure copper and stainless steel. They observed different coalescence behaviour of copper and stainless steel and concluded that if the pure metal particles are heated to temperatures above the melting point, they are completely melted due to high laser power and coalesce immediately whenever the particles are in contact, which results in an undesired balling effect. On the other hand, if the alloy particles are heated to temperatures between solidus and liquidus, viscous sintering during semisolid stage (which occurs during melting for most alloys) becomes the major mechanism of particles bonding.

The elementary process causing laser sintering is coalescence (bonding) of metal particles in contact. Unlike polymers, metals do not exhibit any softening phenomenon on heating below melting point. In addition the of surface diffusion does not qualify as binding mode because the diffusion process is very slow compared to the time scale of laser particle interaction during laser sintering [66]. Therefore, bonding between particles occur at the time of phase-change (in presence of liquid melt) during laser sintering of metal powders [69, 118]. Numerous studies related to sintering of completely viscous particles are reported in literature [59, 80, 102, 121], however, the coalescence of particles during phase change in presence of solid core - as it usually happens with laser sintering of metallic powders - is relatively untouched. Such a study is important to understand the laser sintering dynamics and importance of involved length and time scales.

Over the period during which SLS has evolved, efforts at modelling this process have been made [36, 91], but they are limited to sintering of polymers. Most of the numerical models for description of the temperature distribution in the powder bed and sintering have been based either the classic viscous sintering models of Frenkel and Mackenzie-Shuttleworth, or an empirical Arrhenius shrinkage model based on dilatometry data. Furthermore, most of the experiments in the field of SLS of metal powders are commercial machine specific and are aimed at establishing a new process [2, 37, 78, 105] or at carrying out feasibility studies for new material system [52, 53, 76, 90].

2.4 Aim and outline of the thesis

The analysis of the state of art gives a clear picture of the enormous potential of the SLS technology of metal powders, to meet the ever increasing demand for manufacturing of highly customized products with microstructure and mechanical properties equivalent to or even superior to the conventionally processed materials, in an economical way. Based on the type of powder material used, SLS of metals can be broadly classified as (a) SLS of single component powders and (b) SLS of multi-component powders. The binding of particles during SLS of multi-component powders is due to liquid phase sintering whereas single component metal powders sinter by partial melting of particles which requires a rather strict control of process parameters. Until now no comprehensive numerical model or predictive tool have been developed, which is able to comprehensively describe the sintering mechanism for either class of materials.

The main objective of this work is to develop numerical models for simulation of heat transfer and hydrodynamic during laser sintering of metal powders. The core of the numerical modelling would be the CFD simulation of heat transfer, phase change and hydrodynamics in a powder bed during the sintering process. The thermal model must account for heat transfer occurring at multiple length scales, i.e. thermal behaviour of the granular powder bed subjected to moving laser radiation source as well as the thermal and phase change characteristics resolved at the particle scale. This includes developing separate models to simulate heat transfer at different length scales. Further to investigate hydrodynamics during laser sintering a coupled boundary element model is developed to predict contact growth due to coalescence between melting particles in contact. The model development work and its computer implementation is carried out in-house using Fortran 90.

The validation of developed models by comparing the simulation results with benchmark analytical and numerical solutions available in literature as well as comparison with experiments performed at the Institute of Production Management, Technology and Machine Tools (PTW), also comes under the scope of present work. Finally, applying the developed models to gain an insight into the complex thermo-hydrodynamic phenomenon during laser sintering.

The outline of the thesis is as follows:

Chapter 1: The introductory chapter gives a brief overview of the additive manufacturing technology and its growth potential. Preliminary details of selective laser sintering process and the involved binding mechanisms is also provided.

Chapter 2: This chapter includes literature survey of existing research relevant to selective laser sintering.

Chapter 3: This chapter deals with the modelling and validation of thermal processes which dominate laser sintering.

Chapter 4: The modelling and validation of coupled heat transfer, phase change and sintering hydrodynamics at particle length scale.

Chapter 5: In this chapter the simulation results from the developed thermal and coalescence models are presented and discussed. The model predictions are also compared with experiments conducted on commercial sintering systems.

Chapter 6: The concluding remarks from this study are given and outlook for future studies is presented in this chapter.

3

Numerical modelling of heat transfer in powder bed

Laser sintering is a complex process initiated by localized heating of powder layer using laser beam. Among various phenomena that occur during the process (e.g. energy absorption, interparticle heat transfer, coalescence etc.) most of them are either purely thermal or thermally induced. The significance of thermal phenomena underlines the need to develop a thermal model to improve our understanding of laser sintering process.

3.1 Introduction

This chapter deals with the modelling of thermal processes which dominate laser sintering. The main objectives of thermal modelling are as follows:

1. Investigate the heat transfer to the loose powder bed caused by absorption of incident laser radiation and subsequent diffusion
2. Study phase change induced by laser-particle interaction
3. Predict radiative properties of candidate powder mixtures for sintering
4. Estimate the sintering zone

The complete thermal model has been developed in three stages. First stage includes modelling the geometry of the powder bed of given size distribution. After modelling of powder bed geometry, a ray-tracing approach is adopted to simulate radiation heat transfer and radiation absorption from laser source to powder. In addition, inter-particle radiation and conduction is also considered in this discrete thermal model, however, the minimum resolved scale in this model corresponds to the particle size. The final stage consists of numerical modelling to investigate interaction between a single representative particle and laser beam. This model resolves the particle scale thermal transients and phase change, thus providing for length scales the missing in the discrete thermal model.

3.2 Modelling powder bed geometry

Layer by layer deposition of powdered material is a key step in selective laser sintering, yielding a loosely packed irregular structure. This packing structure represents the state of powder before consolidation due to sintering. A number of experiments [9, 95, 103, 104] and numerical studies [8, 28, 85, 87, 89, 125] on random packing of particles are reported in literature. However, studies pertaining to the conditions existing during laser sintering are rare [144].

The purpose of this step is to simulate a randomly generated powder bed of poly-dispersed particles. Powder material may be single-component or multi-component mixture. Powder grains are not necessarily spherical in all cases. However, using this assumption simplifies the modelling significantly. Only the coordinates of centre and radius of a sphere are needed to define a sphere completely, whereas a non-spherical surface may need a number of parameters to define it. Moreover, it is difficult to estimate overlaps between non-spherical surfaces.

A review of various sphere packing algorithms reveal that existing models can be broadly classified into three types:

1. Ballistic or sequential addition algorithms [8, 125, 126]
2. Collective rearrangement algorithms [62, 86]
3. Dynamic algorithms [30, 145]

Ballistic and rearrangement algorithms are purely mathematical means to generate a model of disorderly packed structure. These algorithms, although simple, yet fail to take into account the mechanical interactions between the particles in their modelling approach. On the other hand in dynamic algorithms, the motion of individual particles is governed by Newtonian mechanics. These algorithms incorporate energy losses (due to friction, collision, deformation etc.) during packing process to obtain the final packing. For the present work we have chosen dynamic packing method to model the geometry of packed bed since it is derived based on mechanics of particle interactions during packing. In the following subsection the details of this method are provided.

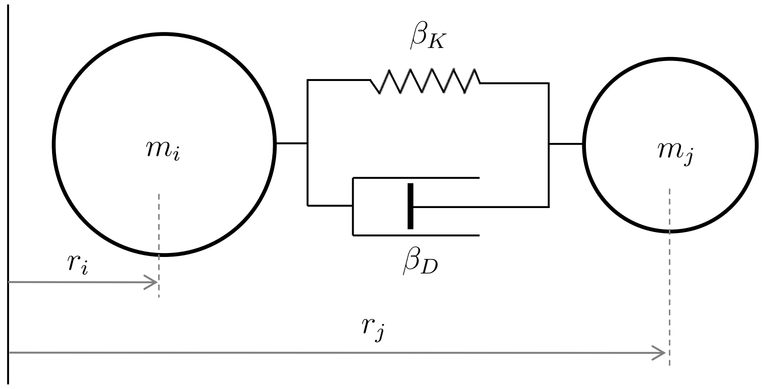

Figure 3.1 Spring-dashpot model

3.2.1 Model details

In the dynamic packing model the particles interact with each other or with walls only during the contact. A spring-dashpot configuration (Fig. 3.1) is used to model contact mechanics during interaction and thus determines the contact forces. This is a simplified means to model energy dissipation and elasticity during collision. Here the spring force represents an elastic force between colliding particles and the damping force between the particles is provided by a dashpot. The motion of particles in the system is described by classical Newtonian mechanics [65]. The equations of motion are therefore for linear motion

$$m_i \frac{d\vec{\mathbf{v}}_i}{dt} = -m_i \vec{\mathbf{g}} + \sum_{j=1}^{N_i} \vec{\mathbf{F}}_{ij} \; ,$$

and for angular motion

$$I_i^{\omega} \frac{d\vec{\omega}_i}{dt} = \sum_{j=1}^{N_i} \left| \vec{\mathbf{F}}_t \right| \times \vec{r} \, , \tag{3.1}$$

where $\vec{\mathbf{F}}_{ij} = \vec{\mathbf{F}}_n + \vec{\mathbf{F}}_t$, is the resultant contact force between the particles in contact, $\vec{\mathbf{F}}_n$, $\vec{\mathbf{F}}_t$ are normal and tangential components of contact force, respectively and N_i is number of particles in

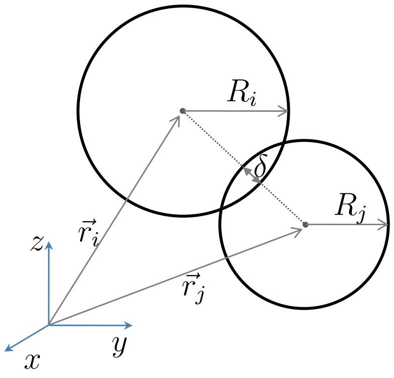

$$\delta = (R_i + R_j) - (\vec{r}_i - \vec{r}_j) \cdot \hat{e}_{ij}$$

$$\hat{e}_{ij} = \frac{(\vec{r}_i - \vec{r}_j)}{(\vec{r}_i - \vec{r}_j)}$$

$$\vec{v}_{ij} = \dot{\vec{r}}_i - \dot{\vec{r}}_j$$

$$\vec{v}_n = (\vec{v}_{ij} \cdot \hat{e}_{ij}) \hat{e}_{ij}$$

$$\vec{v}_t = (\vec{v}_{ij} - \vec{v}_n)$$

Figure 3.2 Scheme of contact force

contact pairs with i^{th} particle. The expression for normal and tangential components of contact force between a pair of touching particles i and j (Fig. 3.2) is given by

$$\vec{\mathbf{F}}_n = \sqrt{\delta R_e}(\beta_{Kn}\delta\hat{e}_{ij} - \frac{m_i m_j}{m_i + m_j}\beta_{Dn}\vec{\mathbf{v}}_n) \ , \tag{3.2}$$

$$\vec{\mathbf{F}}_t = \sqrt{\delta R_e}(-\beta_{Kt}\mathbf{s}_t - \frac{m_i m_j}{m_i + m_j}\beta_{Dt}\vec{\mathbf{v}}_t) \ , \tag{3.3}$$

where δ is the overlap between the particles, $R_e = R_i R_j/(R_i + R_j)$ is an effective radius, and $\hat{e}_{ij}$ is a unit vector along the line joining particle centres. $\vec{\mathbf{v}}_n$ and $\vec{\mathbf{v}}_t$ are normal and tangential components of relative velocity between the particles, and $\beta_{Kn,t}$ and $\beta_{Dn,t}$ are elastic and viscoelastic constants respectively. $\mathbf{s}_t$ is tangential displacement between the particles during the contact interval. Each of the two components of inter-particle contact force in equations (3.2) and (3.3) is composed of a conservative part and a dissipative part. The conservative part is characterized by the elastic constant, and the dissipative part is characterized by damping constant. The state of every individual particle at any instant is obtained by time integration of Newton's equations of motion (3.1) for each particle in the system. The complete detail of interaction laws and granular model can be found in [107].

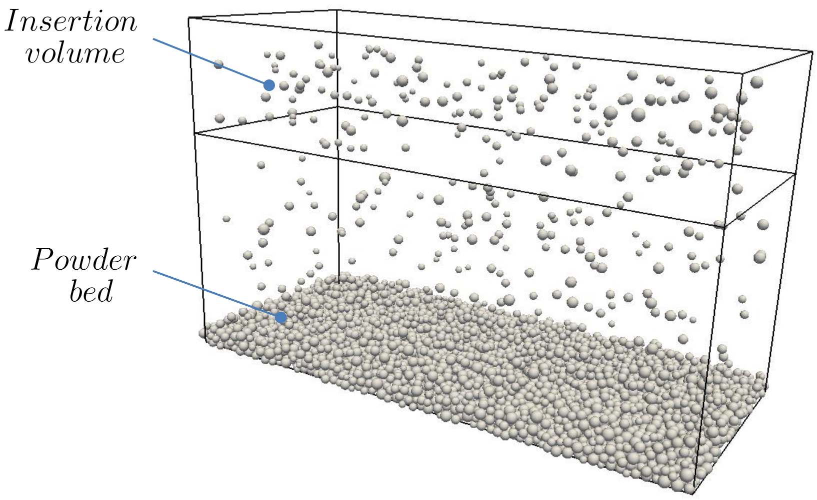

Figure 3.3 Schematic of insertion volume

The growth of the particle bed in the model starts by dropping the particles from a fixed height. This is achieved by inserting a group of particles of desired size distribution into a relatively small volume above the bed (Fig. 3.3) and allowing them to fall under the influence of gravity. The spatial distribution of particles in this insertion volume is random. When a group of inserted particles fall out of the insertion volume, another group of particles is inserted. This insertion continues at regular intervals until the desired fraction of total volume is filled with particles. However, the simulation stops only when all the particles settle down resulting in a randomly packed structure. The total kinetic energy of the particles is used as a measure of the dynamic state of the system. The particles lose their kinetic energy due to dissipation during each collision (inelastic). The particulate system is thus considered static when its kinetic energy becomes negligible, and the resulting packing structure is ready for further analysis.

The granular package in LAMMPS molecular dynamic simulator [97] has been used to generate the randomly packed bed of poly-dispersed spherical particles of a given size distribution. LAMMPS is a freely-available open-source code, distributed under the terms of the GNU Public License. The package uses dynamic algorithm to simulate the behaviour of particulate system with a variety of initial and/or boundary conditions. The current version of LAMMPS is written in C++, while earlier versions were written in Fortran.

The input parameters needed for generating randomly packed bed using granular package in LAMMPS are listed in Table 3.1. In absence of any specific data for coefficient of restitution and friction coefficient, simulations were performed to determine their influence on final packing structure. They are found to have insignificant influence on final packing structure. Therefore, the specified values are selected to obtain a packed bed in lesser simulation time. Besides the inputs given in the table, particle size distribution is also needed for obtaining poly-dispersed bed. This is done by scripting the desired frequency distribution of the particles in the input file.

Table 3.1 Input parameters for packing model

Input parameter	Value	Unit
Gravity	9.81	ms^{-2}
Young's modulus	Material specific	Nm^{-2}
Density	Material specific	kgm^{-3}
Poisson ratio	Material specific	-
Coefficient of restitution	0.8	-
Friction coefficient	0.5	-
Dropping velocity	0.0	ms^{-1}

3.2.2 Levelling

In order to obtain an evenly levelled surface on the packed bed (obtained from granular package), a criterion is devised to filter out the particles causing unevenness on the bed surface. Only the particles satisfying this criterion remain as part of levelled bed while others are excluded. The simplest way is to fix a reference height of a horizontal plane and then remove all the particles with their centres above the plane. As shown in Fig. 3.4, using this criterion leads to maximum unevenness of around one particle diameter for mono-dispersed bed and often does not yield optimum levelling, especially for shallow bed configuration, hence it is not recommended. Therefore, adopting an alternate approach to adjust the height of reference plane while selectively rejecting some of the particles such that the average distance between

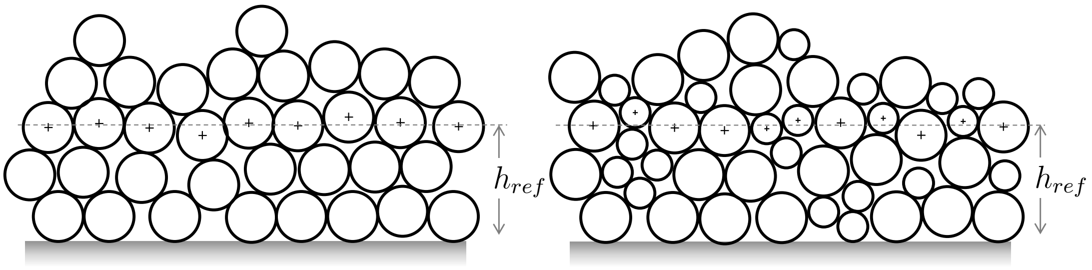

Before levelling

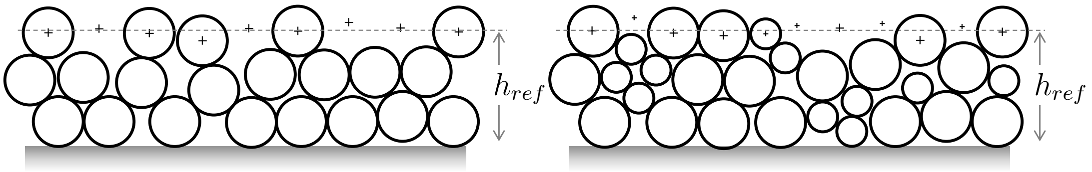

After levelling (method 1)

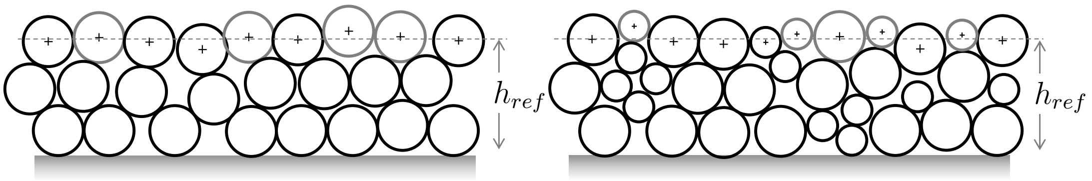

After levelling (method 2)

Figure 3.4 Comparison of levelling approach for mono-dispersed and poly-dispersed powder beds

the plane and the centre of the particles it is intersecting is minimum. The key steps of the developed levelling algorithm are detailed below.

1. Select a reference height for a horizontal plane.
2. Calculate the number of particles intersected by this plane as well as evaluate average distance of intersected particles from the reference plane.
3. Remove those intersected particles having their centre above the reference plane(starting from farthest to closest particle in that order) and continue as long as newer average distance of intersected particles after each rejection is lower than previously calculated value. It is important to recognize that successively removing the intersected particles above the reference plane may not always decrease average distance of intersected particles from that plane, because contribution to average distance due to these particles may be lower than the average value. Furthermore, particles cannot be removed beyond a specified limit particles satisfying the criterion given by ($N_X \geqslant 0{\cdot}9\bar{N}_X$).
4. If the average distance of intersected particles from the reference plane is less then selected tolerance, then levelling is achieved, otherwise go to next step .
5. Obtain new height of reference plane as $h^n_{ref} = h^o_{ref} + \Delta h$ and go to step 2.

For poly-dispersed powder bed few amendments are needed to avoid removal of particles which do not contribute to unevenness on the surface as indicated in Fig. 3.4. These amendments include: (a) making the reference plane height as a function of particle radius as

$$h_{ref}(i) = h_{ref} + r_{max} - r(i) \; ,$$

where r_{max} is the radius of the biggest particle in the poly-dispersed bed. Then using respective reference planes for each of the particles to calculate their contribution to the average distance. (b) A bigger sized particle can not be removed as long as smaller particles having centre lying above it exists in the bed, since this is not physical.

This levelling approach shields against large unevenness on the bed surface as it does not allow any rejection when the distance of particle is smaller then average distance and contribution to average distance is almost same due to intersected particles lying above and below the reference plane.

3.2.3 Packing parameters

On the basis of model of the bed geometry developed in the previous section, its characteristic bed parameters can be determined. The commonly used bed parameters to characterize a packed state are packing density (or porosity) and coordination number. Packing density represents the density of powder bed relative to that of bulk material. It is given by the fraction of volume occupied by powder particles in a given volume of bed. Coordination number specifies average number of particles in contact with a given particle and indicate connectivity of particles as well as transfer of forces in the packed structure. Besides these two mean parameters, other statistical functions like pair correlation function, size distribution, coordination number distribution etc. are also used to describe packed beds [85].

3.3 Laser irradiation and heat transfer in the powder bed

During selective laser sintering, laser beam acts as the source of energy in the powder bed as shown in Fig. 3.5. Heat transfer to powder particles from laser beam scanning over the powder bed (followed by melting, coalescence, solidification) is not only the primary phenomenon but it also influences the processes following thereafter. Knowing the spatial distribution of laser energy in the powder bed is essential for the prediction of sintered zone and for understanding sintering mechanisms.

A powder bed is a loosely packed structure of solid particles which are surrounded by interconnected voids. This open pore structure of powder enables the radiation to penetrate several particle diameters deep (due to multiple reflections) into the bed in contrast to dense material where the penetration depth is extremely small (order of few nano meters). In addition, the voids on the bed surface act as black surface, thus increasing absorptivity in powder form. So

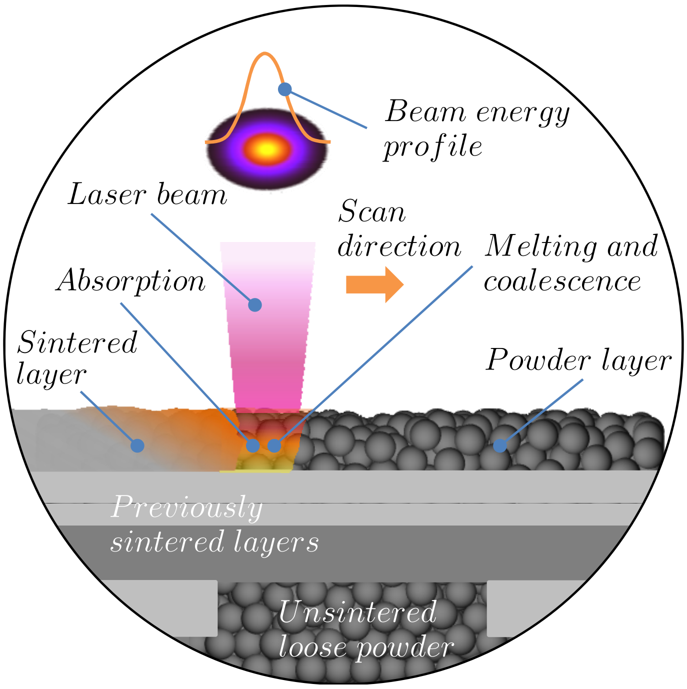

Figure 3.5 Schematic of laser sintering showing key phenomena occurring during the process

powders exhibit higher absorbance as well as increased radiation penetration compared to dense material. On the other hand, effective thermal conductivity of powder material is relatively low. The resulting combined effect is reduced heat losses during sintering.

Majority of work in the past has been devoted to determination of the effective thermo-physical properties of the granular medium, so that continuum approach is readily applicable. Despite the homogeneous models being developed by properly accounting the discreteness of the system, adequacy of the continuum approach also depends upon relative length scales of boundary conditions and on the size scale of particles [101] in the medium.

This section is devoted to development of a thermal model for laser energy absorption and its transport in poly-dispersed granular media, with specific significance during selective laser sintering of metal powders. The heat transfer in the powder bed is extremely localized (around the moving laser beam), and the assumption of continuum treatment is violated with respect to local thermal equilibrium [67]. The powder bed does not exhibit homogeneous behaviour under these conditions [101]. Furthermore, experimental data is often rare to model powder bed as a homogeneous medium. Therefore, non-continuum approach is adopted in this study, in order to explicitly model individual particles in the powder bed using dynamic packing algorithm [97]. However, heat transfer at the particle scale is modelled using lumped approach. It presents a suitable approach to solve the moving heat source problem in granular medium while directly considering the discrete nature of the medium.

The Ray-tracing approach is used to model laser radiation source (absorption and propagation) in the granular medium. Thermal radiation heat transfer is expected to play the dominant role during laser sintering, because heating due to laser source is extremely localized (order of laser beam size) along the specified scan paths. In addition, the duration of laser-particle interaction is sufficiently short (of order $1/10$ of millisecond) to be significantly influenced by interparticle conduction. As a result, very high temperatures (above melting point) are encountered by the particles in the zone of interaction, whereas mean temperature of the powder bed is hardly changed.

Laser sintering takes place in stagnant inert atmosphere (to ensure non-oxidizing atmosphere) under low pressure conditions [136] and for the case of metal powders, high thermal conductivity ratio between the particles and the gas ($k_s/k_g \approx 10^3$) enables to consider the conduction through contact between the particles alone while neglecting conduction through thin gas film near contact surfaces [24, 49]. Likewise, radiant heat transfer between neighbouring voids is also neglected since the major contribution is due to radiation between highly conducting solid surfaces [35] . Furthermore, convection heat transfer is neglected, since studies [138] indicate that for packed bed configurations the contribution due to free convective heat transfer mechanism is very small. Thus, as a first step towards developing a more comprehensive model the primary focus has been on modelling of laser radiation source in the powder bed and subsequent heat transport due to radiation exchange between solid particles and conduction through contact between the particles. The geometry of the powder bed does not change during the computations and coalescence of particles is not taken in to account. The inclusion of the effect of particles coalescence into the powder bed scale heat transfer model is extremely challenging, however, a coupled heat transfer and coalescence model for a representative two particle case is developed and discussed in the next chapter.

3.3.1 Ray-tracing for energy absorption in the powder bed

Ray-tracing is a simple optical method to describe light propagation and scattering through a complex medium. It has a variety of applications like image rendering in modern computer graphics [132], radiation heat transfer [5, 58] and view factor calculations [129]. It is a statistical method, which involves tracing a large number of individual rays travelling through a medium while recording all the associated events. The method is independent of coordinate

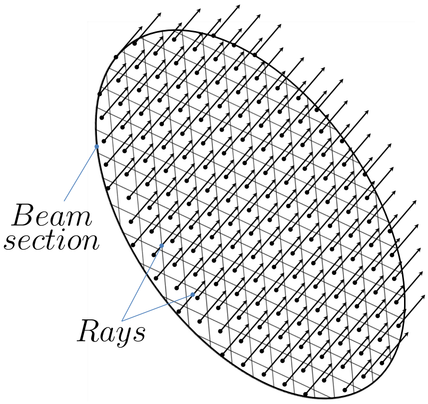

Figure 3.6 Laser beam partitioned into rays (each arrow represents an individual ray).

system and does not require any domain discretization. These features make it an ideal method for radiation heat transfer problems involving complex and irregular geometry. However, it is applicable only within the limits of geometrical optics without appreciable diffraction [114]. The main idea behind this approach is to partition the radiation beam (Fig. 3.6) into large number of energy bundles (rays) and follow the path of each individual ray as it travels through the computational domain (powder bed in this case). Each ray has some amount of energy associated with it (depending on the source strength) at the origin and it is tracked until it imparts all its energy to the interacting medium or it escapes out of the system.

The simulation starts by shooting a large number of rays from a plane circular area (laser beam cross-section) positioned above the powder bed. A ray at any instant is completely defined by its origin, direction cosines, and the amount of energy associated with it. The energy of each ray at the source is given by

$$e_i = \frac{P_o \Delta t}{N} f(x_i, y_i) \ , \tag{3.4}$$

where N is total number of rays used to represent the laser beam, P_o is power of beam, and $f(x_i, y_i)$ is the factor to account for spatial distribution of energy in the laser beam. For a Gaussian beam of radius r_b, the distribution factor is given as

$$f(x_i, y_i) = 2 \cdot \exp\left(-2\frac{(x_i - x_c)^2 + (y_i - y_c)^2}{r_b^2}\right) \ , \tag{3.5}$$

where (x_i, y_i) and (x_c, y_c) are coordinates of ray origin at the source and beam centre respectively.

Random numbers are used to generate uniformly distributed origin points. The idea is to make use of their statistical property of being uniformly distributed in the range $\varUpsilon \in [0, 1]$ to obtain ray origin points and thus avoid discretizing the shooting plane. The coordinates of ray origin on a plane circular surface is given by

$$\begin{aligned} x_i &= x_c + \sqrt{2u}\cos\theta \\ y_i &= y_c + \sqrt{2u}\sin\theta \end{aligned} \tag{3.6}$$

such that

$$\theta = 2\pi \Upsilon_\theta$$

and

$$u = \frac{r_b^2}{2}\Upsilon_u$$

where Υ_θ, Υ_u are random numbers. Each of the N rays is then tracked one by one for possible ray-particle intersection. Upon interaction the ray looses a fraction of its energy to the particle depending on its surface properties and remaining portion is reflected along with it. The absorption of laser energy by a particle leads to increase in of internal energy of the particle. The particles are assumed to be opaque so there is no transmission of energy through a particle. Radiative properties are assumed to be constant over an individual surface, however different surfaces may have different properties. A new set of direction cosines are obtained for the reflected ray (both diffuse and specular reflection can be accounted), and it is tracked again for possible intersection with other particles. Keeping the account of internal energy increase in each particle in the bed and that reflected out of the bed helps in determining the energy distribution in the bed and the radiative properties of the powder bed.

Following a ray path in the computational domain essentially consists of a set of ray-surface interaction routines to find the intersection between a ray and an object in three-dimensional space. For the present study a ray-sphere interaction algorithm is the heart of ray-tracing code, since the sphere is the primary geometric unit representing a particle. The main idea involved in determining intersection between a ray and a given sphere is explained here, while complete details of ray-sphere interaction algorithm adopted in this model are available in [45]. The conditions necessary for any ray to intersect a sphere are:

1. The ray should be pointing towards the sphere,
2. the shortest distance between the ray and the sphere centre should be less than sphere radius.

Defining a ray by its origin $\vec{O}$ and unit vector $\hat{e}_R$ along its direction, such that

$$\vec{R}(\psi) = \vec{O} + \psi\hat{e}_R \tag{3.7}$$

is the vector equation of ray and parameter ψ can take any real value giving different points on the ray. To find if a ray points towards the given sphere (see Fig. 3.7), the projection of vector $\vec{OC}$ on the ray as $\vec{OC}\cdot\hat{e}_R$ is evaluated. The ray points towards sphere if the dot product is positive. In that case the shortest distance L_{CD} between the ray and sphere center is computed as shown in Fig. 3.8. This distance is compared with sphere radius to determine if the ray is

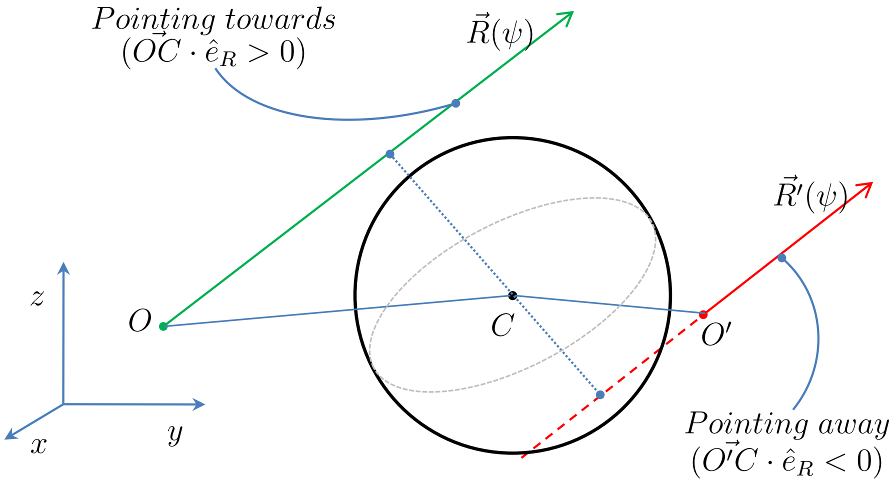

Figure 3.7 Representation to evaluate how a ray is directed with respect to a given sphere.

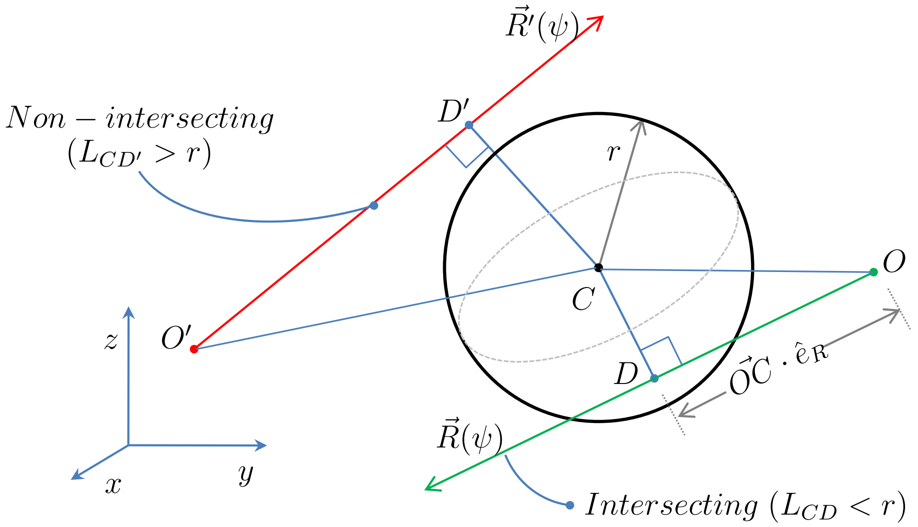

Figure 3.8 Shortest distance from a sphere center to the rays (pointing towards it) to detect the intersecting rays.

intercepted by sphere or not. The exact point of intersection is obtained geometrically from the Fig. 3.9.

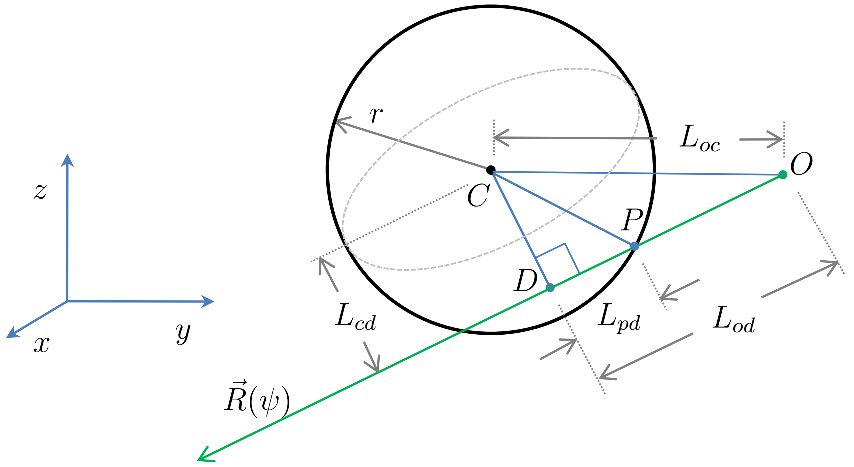

Figure 3.9 Evaluating ray-sphere intersection point (P) in three dimensional space.

3.3.2 View factor calculation

The strategy for inter-particle radiation involves adapting Ray-tracing for evaluating view factors and then solving for radiation exchange between the interacting surfaces using a novel algorithm. View factors in radiation exchange problems are purely geometrical quantities that indicate how surfaces view each other and consequently determining the radiation exchange between them. Besides few simple cases, deriving analytical formula for view factor calculation can be extremely challenging or impossible. Statistical Ray-tracing approach is a suitable alternative for cases involving complex surfaces.

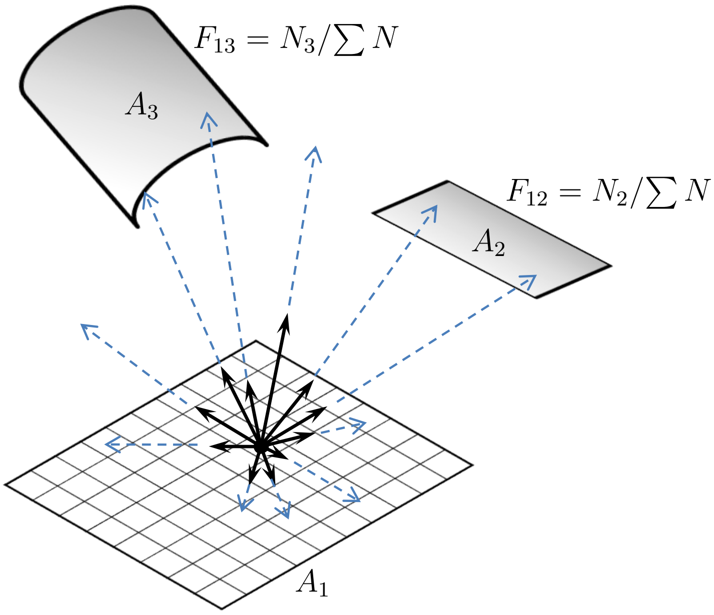

Figure 3.10 Schematic for evaluating view factor between interacting surfaces

Ray-tracing method to calculate view factor is explained here for a sample case shown in Fig. 3.10, where N_2 and N_3 are number of rays intercepted by the surfaces 2 and 3 respectively and ΣN is total number of rays leaving the surface 1. By definition the view factor is the fraction of total emitted radiation from one surface that is intercepted by another surface. If we represent the radiation leaving a surface by sufficiently large number of discrete rays and register the total number of such rays intercepted by other surfaces, then the ratio of intercepted rays to total rays fired can be used as view factor.

The method is very simple to apply and nearly independent of geometrical complexities. However, it is important that average behaviour of the rays is representative of actual radiation leaving the surface, by ensuring uniform ray density and following directional or spectral dependence (if any). This is achieved by dividing the emitting surface into a number of elemental areas, where each area acts as an origin for multiple rays which are fired in different directions at random while following the corresponding probability distribution of emitting radiation (e.g. ray direction for a diffuse surface is given by $\varphi = 2\pi\Upsilon_\varphi$ and $\theta = \sin^{-1}\sqrt{\Upsilon_\theta}$, where Υ_θ and Υ_φ are random numbers between 0 and 1) [64].

In order to obtain uniformly distributed points on a spherical surface, the following method is used. In spherical coordinate system a point in three-dimensional space is defined by (r, θ, φ) as shown in Fig. 3.11, where θ and φ are zenith and azimuth angles, respectively, such that $0 \leqslant \theta \leqslant \pi$ and $0 < \varphi \leqslant 2\pi$. For obtaining evenly distributed points on a sphere of radius r centred at origin, the standard practice of incremental addition by a fixed value (e.g. $\theta_i = \theta_{i-1} + \Delta\theta$ or $\varphi_i = \varphi_{i-1} + \Delta\varphi$, where $\Delta\theta = \frac{\pi}{N_\theta}$, $\Delta\varphi = \frac{2\pi}{N_\varphi}$) yields a non-uniform distribution of points with clustering near the poles(see Fig. 3.12(a)). Even the random selection of θ and φ values as per equations

$$\theta = \pi\Upsilon_\theta \ , \ \varphi = 2\pi\Upsilon_\varphi \ , \tag{3.8}$$

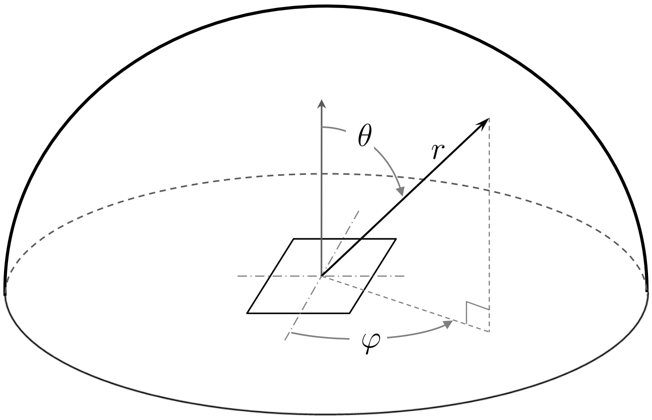

Figure 3.11 Spherical coordinate system

where Υ_θ and Υ_φ are random numbers between 0 and 1 results in an equally biased distribution (see Fig. 3.12(b)).

To avoid clustering, the whole surface area of sphere is divided in such a way that solid angle subtended by each elemental area is equal. The geometric centres of these areas will have a uniform distribution over the sphere. Mathematically solid angle is given by

$$d\Omega = \sin\theta d\theta d\varphi \cdot \tag{3.9}$$

When $d\theta$ and $d\varphi$ are assumed to be constant, variation of $d\Omega$ with θ leads to the clustering of points near the poles. To avoid this clustering, a new variable u is introduced so that

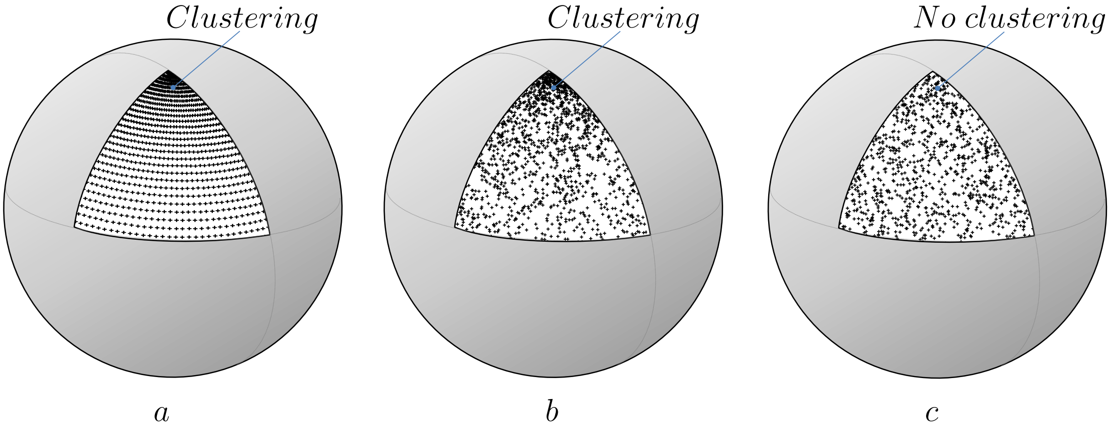

Figure 3.12 Distribution of ray origin points on spherical surface (a) uniform increment of θ and φ, (b) random selection of θ and φ, (c) uniform solid angle.

$$du = \sin\theta d\theta \tag{3.10}$$

that yields

$$u = \cos\theta \cdot \tag{3.11}$$

By substituting u in Eqn. (3.9) for solid angle, we obtain

$$d\Omega = du d\varphi \cdot \tag{3.12}$$

Now a random selection of u and φ from a given range ($u \in [-1, 1]$, $\varphi \in [0, 2\pi)$) satisfies the condition $d\Omega = du d\varphi \approx$ constant, since the randomly selected points are assumed to be sufficiently uniform over the total range [131]. Fig. 3.12(c) shows the generated distribution of points with no clustering observed.

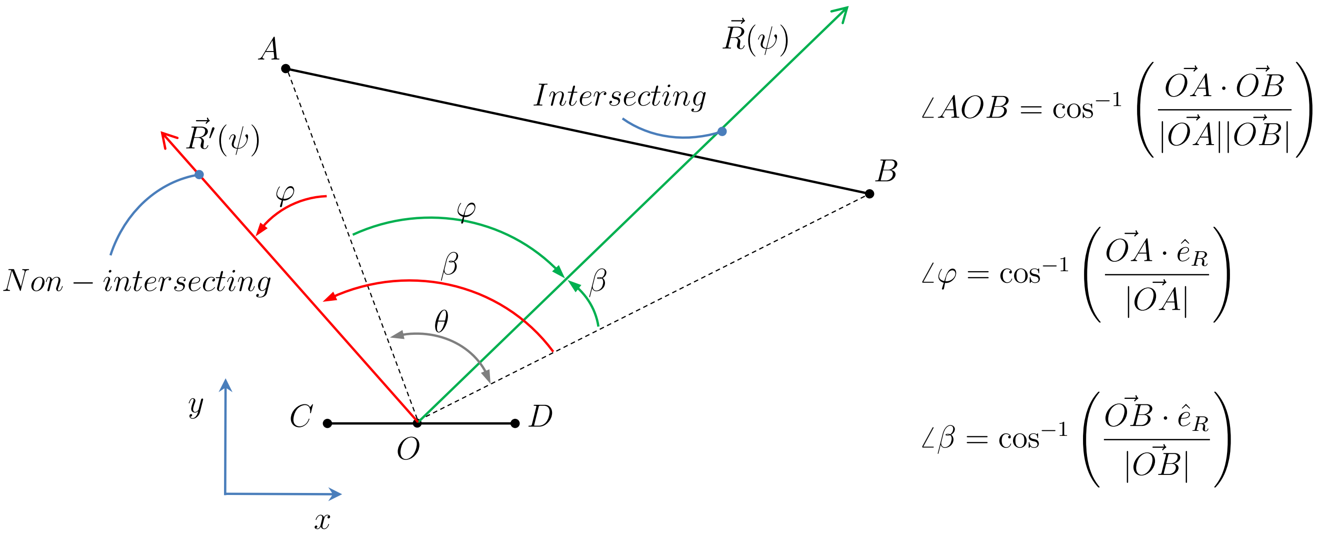

Figure 3.13 Ray-tracing to calculate view factor between two dimensional surfaces.

Ray-surface intersection is a key component of the view factor calculation using ray tracing. Just qualifying the rays as intersecting or non-intersecting with a given surface is sufficient to evaluate view factor, while determination of exact position of ray-surface intersection is redundant. Consider a sample case involving two straight lines as shown in Fig. 3.13. Segment AB is selected as interceptor and CD as shooting segment. Now an arbitrary ray $\vec{R}(\psi)$ from segment CD will intersect line AB if the angles which the ray make with OA and OB are both smaller then $\angle AOB$. Necessary conditions for intersection are given in form of logical truth Table 3.2.

Similarly for three-dimensional case, general condition for a ray intersecting with plane polygon ABCD (see Fig. 3.14) is obtained by ensuring that any point on the ray should be on the same side of the plane (containing ray origin and two vertices) as that of next vertex of polygon following a given order. Considering a set of three vertices A, B, C as shown in Fig. 3.14, a point on the ray $\vec{R}(\psi)$ is on the same side of plane AOB as that of vertex C if

$$\hat{e}_R \cdot \hat{n} = \hat{e}_{OC} \cdot \hat{n} \ , \tag{3.13}$$

where

$$\hat{n} = \frac{\vec{OA} \times \vec{OB}}{\left|\vec{OA} \times \vec{OB}\right|} ,$$

and $\hat{e}_{OC}$ and $\hat{e}_R$ are unit vectors in the direction of vectors $\vec{OC}$ and ray $\vec{R}(\psi)$, respectively. When the condition (3.13) is true for all the sets of ordered pairs of three vertices of interceptor polygon, the ray is termed intersecting. A ray-sphere intersection algorithm [45] has been already discussed in the previous section. Important steps of algorithm for view factor calculation are presented in the form of a flow chart in Fig. 3.15.

Table 3.2 Truth table

$\varphi \leq \theta$	$\beta \leq \theta$	Intersecting ($\varphi \leq \theta \wedge \beta \leq \theta$)
True	True	True
True	False	False
False	True	False
False	False	False

3.3.3 Radiation exchange

In spite of incorporation of the geometrical complexities into the view factor calculation (see section 3.3.2), modelling of radiation exchange between surfaces can be a complicated task, especially when a system consists of a large number of interacting surfaces. Since all the surfaces in the domain emit, absorb and reflect radiation simultaneously, any emitted radiation undergoes multiple reflections (while being partially absorbed) during the exchange process.

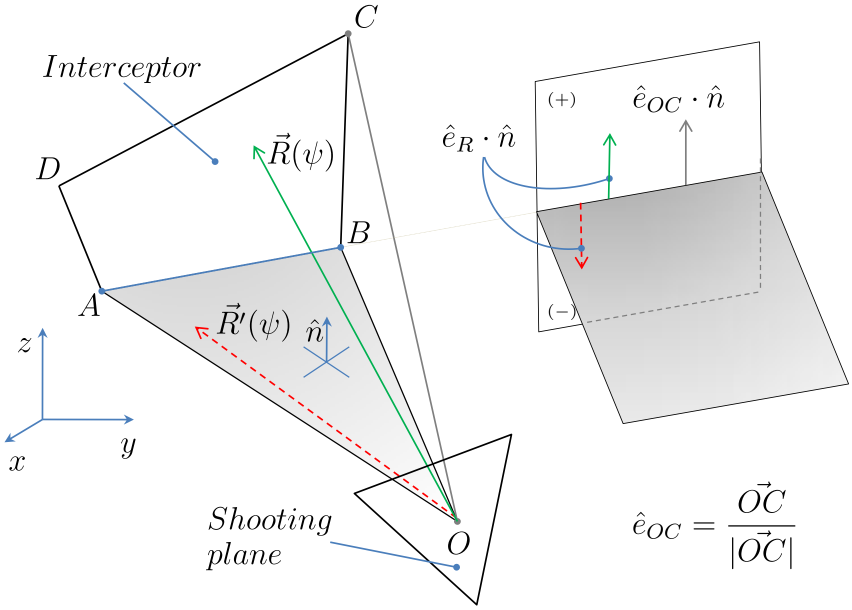

Figure 3.14 Ray-tracing to calculate view factor between three dimensional plane surfaces.

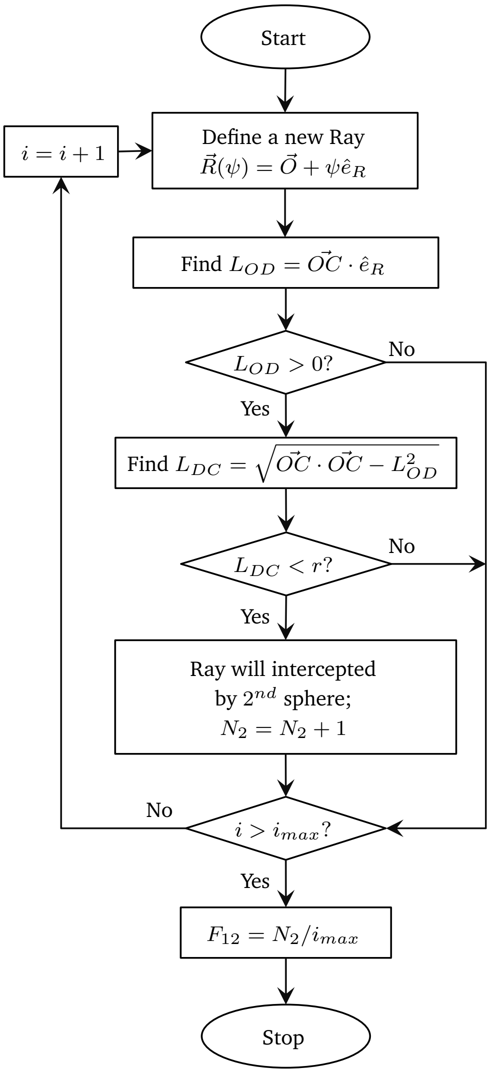

Figure 3.15 Flowchart for calculating view factor between spherical surfaces (refer to Fig. 3.7 and 3.8 for geometrical details included in the flowchart).

Based on underlying physics of radiation exchange, we have developed a simple multi-step iterative procedure to evaluate net radiation exchange by each surface. It is done by successively accounting for absorbed fraction of emitted, reflected and re-reflected energy from all the contributing surfaces. The method avoids formulation of algebraic equations and hence no matrix inversion is needed.

Given the initial state of a system of N surfaces (see Fig. 3.16), the energy emitted by each of the surfaces per unit time is given by

$$E_\epsilon(i) = \epsilon_i \sigma T_i^4 A_i \; , \tag{3.14}$$

using Stefan-Boltzmann law. Now the energy incident on an arbitrary surface j due to pure emission from all the surfaces in the system is given by

$$E_{inc}(j) = \sum_{i=1}^{N} F_{ij}\epsilon_i \sigma T_i^4 A_i \ , \tag{3.15}$$

and corresponding absorbed and reflected radiation by this surface are

$$E_{\alpha}(j) = \alpha_j E_{inc}(j) \ , \tag{3.16}$$

$$E_{\rho}(j) = (1-\alpha_j) E_{inc}(j) \cdot \tag{3.17}$$

Similarly absorbed and reflected fractions can be calculated for all the other surfaces. Direct evaluation of net energy exchange using equation:

$$Q_{net}(j) = E_{\alpha}(j) - E_{\epsilon}(j) \tag{3.18}$$

is not relevant at this stage (except for black surfaces for which all the energy incident is absorbed and nothing is reflected back), because the exchange of reflected radiation from the surfaces is still not accounted. Proper accounting of reflected radiation while satisfying the energy balance of the whole system is key point of the solution. This is done by continuously updating energy absorbed by each surface due to reflected radiation, till the cumulative sum of reflected energy from all the surfaces becomes negligible.

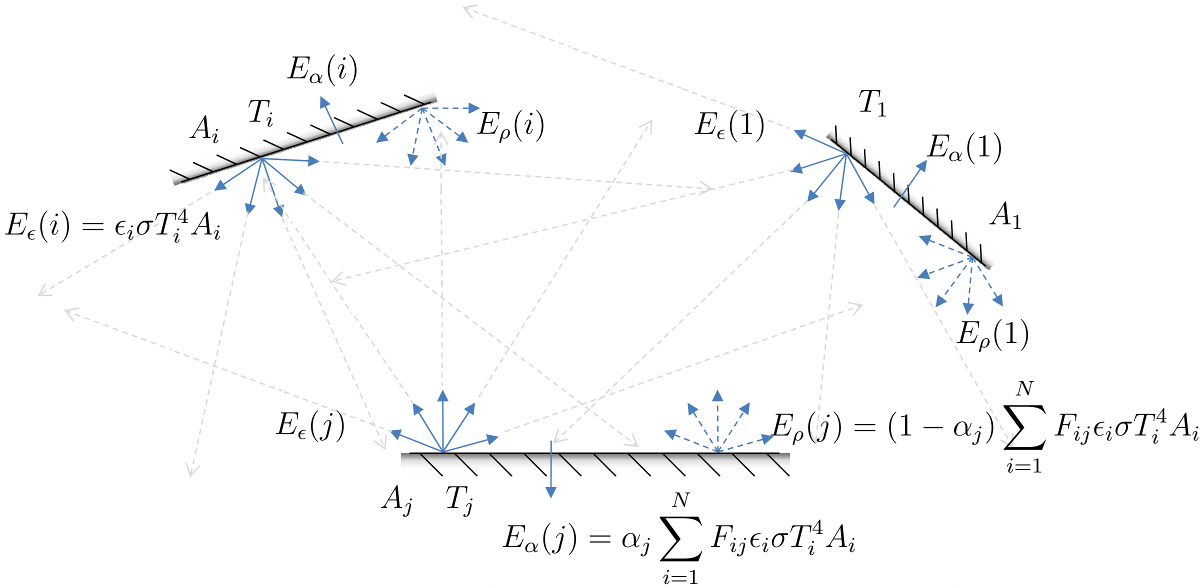

Figure 3.16 Schematic of radiation exchange between surfaces.

We assume that reflected energy propagates between the interacting surfaces in the same way as that of emitted energy. This is true for diffuse-grey surfaces, and real surfaces closely follow diffuse-grey behaviour. Therefore, new values of absorbed and reflected fractions for all the surfaces due to reflected part can be evaluated by simply repeating the same step for calculating absorbed and reflected fractions (Eqs. (3.16) and (3.17), respectively). However, for this step the reflected energy from the surface is used in place of emitted energy (as we are calculating energy exchange due to reflected part alone). Now, the energy absorbed by each surface is incremented with the latest value, and the computation process is repeated with the new reflected part till overall energy balance is fulfilled. The appropriate expression for incident radiation on the surface j due to reflection from all the surfaces at a given time step is given by

$$E_{inc}(j) = \sum_{i=1}^{N} F_{ij} E_\rho(i) \ , \tag{3.19}$$

and corresponding absorbed fraction is updated as given by equation

$$E_\alpha(j) = E_\alpha^o(j) + \alpha_j E_{inc}(j) \cdot \tag{3.20}$$

The expression of re-reflected fraction is unchanged and obtained using equation (3.17). It is evident that reflected energy from an arbitrary surface decreases progressively with every loop for updating absorbed energy by the surface. Summation of reflected fraction from all the surfaces at any stage during the calculation is a measure of energy imbalance. Hence it is ideal parameter to decide on convergence.

$$\frac{\sum_{i=1}^{N} E_\rho(i)}{\sum_{i=1}^{N} \epsilon_i \sigma T_i^4} \leqslant \varepsilon \cdot \tag{3.21}$$

The relative value of convergence parameter less than 10^{-4} ensures energy imbalance of $0{\cdot}01\%$ or lower. The outlined method is very simple to implement numerically. The flow chart for the algorithm is presented in Fig. 3.17. This completes modelling for laser energy absorption and its transport in the powder bed due to radiation. It is important to note here that spectral dependence of material emissivity is not considered in this analysis, however, incorporated in the model in subsequent studies.

3.3.4 Interparticle conduction

Heat conduction in the powder bed is strongly dependent on the nature of contact between the particles as well as packing structure of the particulate medium [43]. Even the particle size distribution and properties of individual ingredients are important when investigating powder mixtures. A number of studies, relevant to conduction heat transfer in granular medium, have been reported [24, 110, 124, 146] with varying degree of relaxations regarding some or all of these parameters.

The thermal particle dynamic approach developed by Vargas and McCarthy [124] has been adopted for heat transfer in granular medium. Like many other methods for conduction in

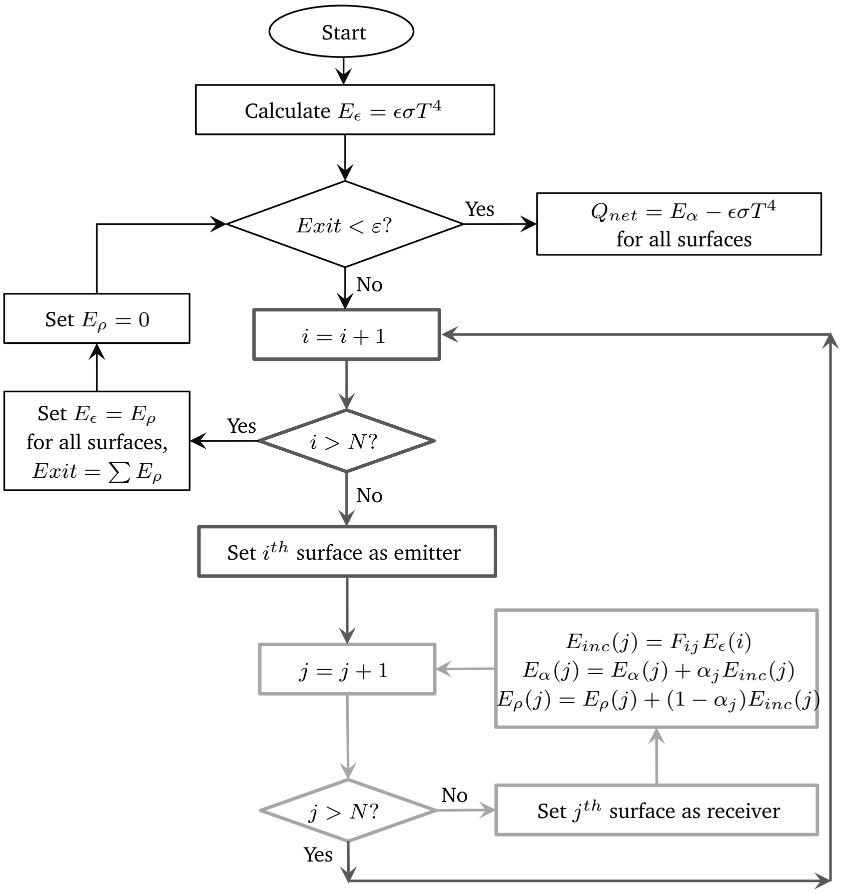

Figure 3.17 Flowchart for thermal radiation exchange between interacting surfaces.

discrete medium, the structural details like number of contacts, contact area and other heterogeneity in the powder bed are obtained from simulated packed bed. Therefore, it is crucial to model packed bed using dynamic packing algorithms making use of contact mechanics theories. The key assumptions of the thermal particle dynamic model are:

1. The contact thermal resistance between the particles is significantly large as compared to thermal resistance in the particles, such that $Bi \ll 1$, where $Bi = 2c/\pi r$ and c is contact radius between particles in contact. Thus, temperature within the particle can be assumed to remain uniform. The temperature gradients exists only near the contact points (Fig. 3.18).

2. Thermal disturbances in a particle do not propagate beyond its immediate neighbours during a time step, so that many simultaneous two body interactions can be scaled up to model multi-body system [30].

Mathematically $\Delta T_i/(T_j - T_i) \ll 1$ during a time step, which is considered as criterion for selecting the time step size, where T_i, T_j are temperatures of neighbouring particles. Under these conditions heat transfer between each pair of particles is almost independent of neighbouring

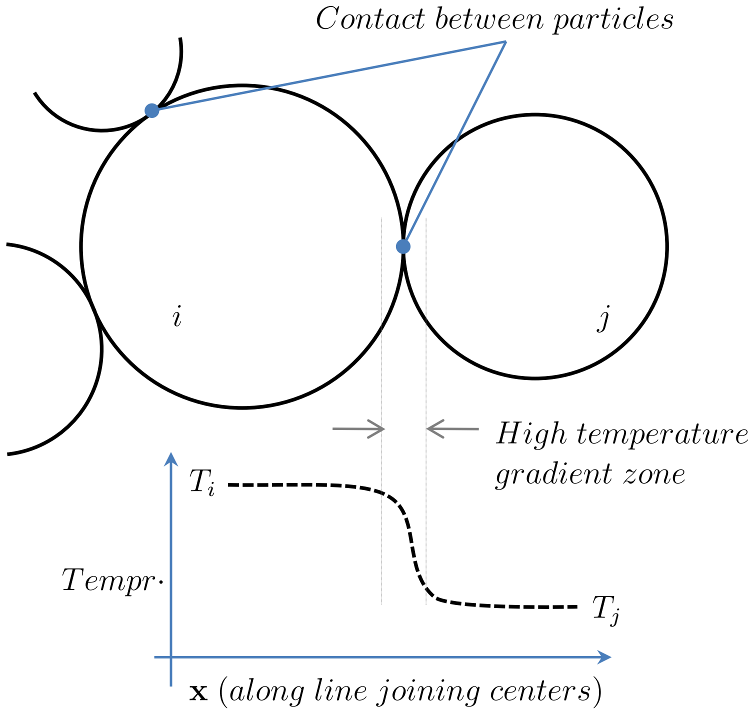

Figure 3.18 Schematic of assumed temperature distribution between particles in contact.

pairs, and net heat transferred to a particle due to conduction with its neighbouring particles is given by:

$$Q_i = \sum_{j=1}^{N} C_{ij}(T_j - T_i) \ , \tag{3.22}$$

where N is number of neighbouring particles in contact with particle i and C_{ij} is contact conductance between the pair ij. The contact conductance C_{ij} depends on the contact force between the particles. This is obtained using Hertz's theory as

$$C_{ij} = 2\lambda_e c = 2\lambda_e \left(\frac{3\vec{\mathbf{F}}_n R_e}{4E_Y} \right)^{\frac{1}{3}} \ , \tag{3.23}$$

where λ_e is effective thermal conductivity of the particles and c represents the radius of contact area. $\vec{\mathbf{F}}_n$ is the normal contact force between the particles, R_e is the effective radius of contact pair (see Section 3.2.1) and E_Y is effective Young's modulus.

The rate of temperature change of a particle i when interacting with another individual particle j is given in differential form as

$$\frac{dT_i}{dt} = \frac{C_{ij}(T_j - T_i)}{mC_p} \ , \tag{3.24}$$

where, m is the mass of particle and C_p is specific heat. Now considering each contact pair of a particle in isolation, the temperature rise for a particle i due to its contact with another particle j at the end of a time step is obtained from equation (3.24) by integrating as:

$$\int_t^{t+\Delta t} \frac{dT_i}{(T_j - T_i)} = \frac{C_{ij}}{mC_p} \int_t^{t+\Delta t} dt \ , \tag{3.25}$$

to obtain

$$T_i^{t+\Delta t} = T_j^t - \left(T_j^t - T_i^t\right) exp\left(-\frac{C_{ij}}{mC_p}\Delta t\right) \ , \tag{3.26}$$

by subtracting T_i^t from both sides,

$$\Delta T_{ij} = T_i^{t+\Delta t} - T_i^t = \left(T_j^t - T_i^t\right)\left(1 - exp\left(-\frac{C_{ij}}{mC_p}\Delta t\right)\right) \ , \tag{3.27}$$

and net rise in temperature due to all the neighbouring particles is obtained by adding up the individual contribution as

$$\Delta T_i = \sum_{j=1}^{N} \Delta T_{ij} \ . \tag{3.28}$$

3.3.5 Summary of solution method

The solution involves various individual steps executed one by one: evaluation of laser heat source in the powder bed, view factor calculation followed by radiation exchange and interparticle conduction. The important steps of solution scheme are listed below:

1. Read or define the computational domain consisting of interacting surfaces.
2. Specify the initial conditions.
3. Calculate view factors between all the interacting pairs. This calculation is done only once and the values are stored for later use.
4. Evaluate heat source in the powder bed using ray-tracing.
5. Solve for energy exchange between surfaces due to radiation and evaluate radiation heat flux at the surface.
6. Solve for contribution due to conduction heat transfer.
7. Determine the particle temperature.
8. Advance time ($t = t + \Delta t$) and goto step 4.

The computer implementation of developed models and solution algorithm are done using Fortran 90 for Windows/Linux platforms using Intel Fortran compiler.

3.3.6 Validation

All the components of overall solution method are validated by solving a series of test cases and comparing results with their corresponding known solutions.

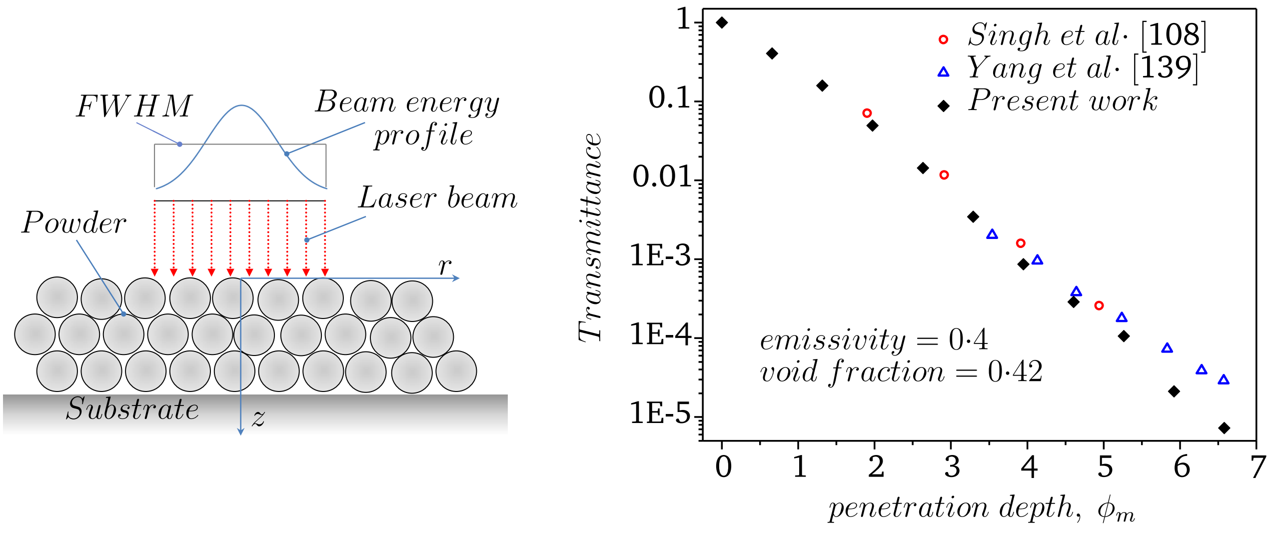

(a) (b)

Figure 3.19 Transmittance through a randomly packed bed of specularly reflecting opaque spherical mono-sized particles of diameter $4{\cdot}0\ mm$.

Ray-tracing for radiation absorption: The ray-tracing algorithm to model radiation heat source in the powder bed is validated by evaluating variation of radiation intensity along the bed depth. Figure 3.19(a) shows the schematic of powder bed irradiated by a laser beam. As can be seen in Fig. 3.19(b), the radiation intensity $I(z)$ decreases exponentially along the depth. The transmittance values, obtained under the identical set of input conditions as in existing literature [108, 139], are in good agreement with reported solutions. In present simulation, the transmittance value at a given depth is obtained by calculating all the downward radiation energy crossing through an imaginary plane at that depth. The normal to the plane is along the original beam direction.

Ray-tracing for view factor: Further, to establish the ability of the developed ray-tracing for evaluating radiation view factors, three test cases have been considered, for which analytical solutions are available [64]. For all the three cases view factors are calculated for wide range of ratios of geometrical parameters. The results are compared with corresponding analytical solutions. The first geometrical configuration represents two rectangular planes perpendicular to each other with one edge in common as shown in Fig. 3.20, while the second configuration

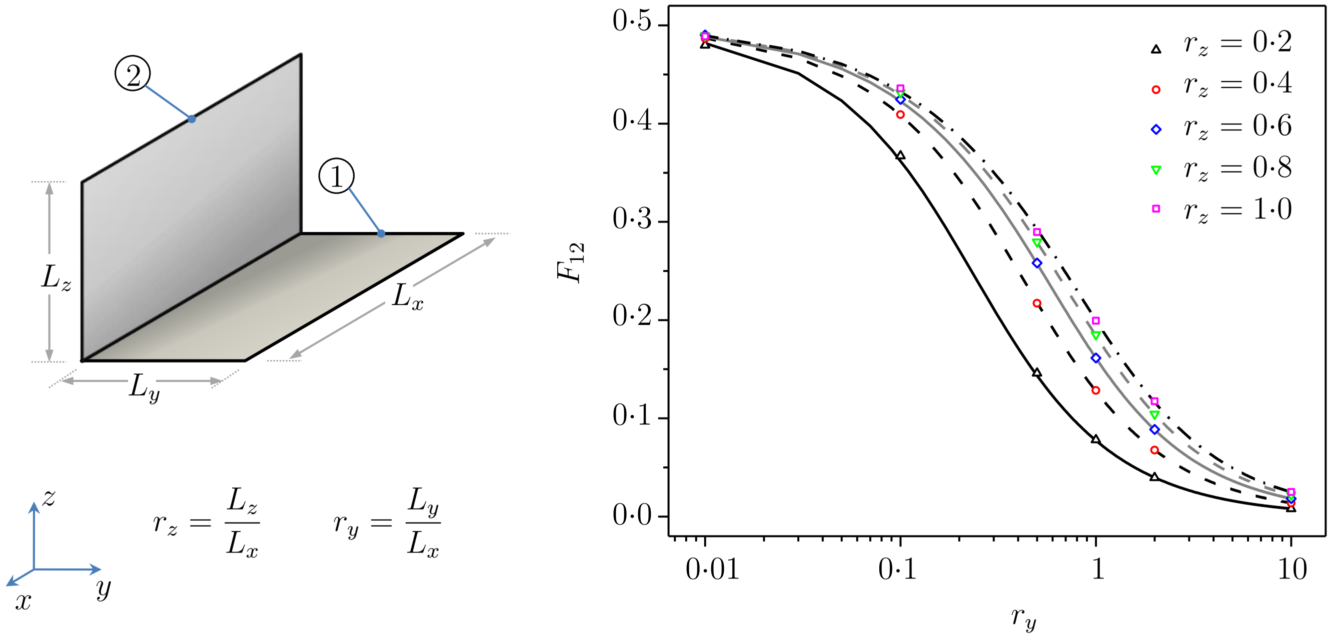

Figure 3.20 View factors calculated for two rectangular surfaces perpendicular to each other. The lines represent exact solution.

is that of two parallel rectangular planes (see Fig. 3.21). The obtained results are in excellent agreement with analytical solutions throughout the range of geometrical ratios considered.

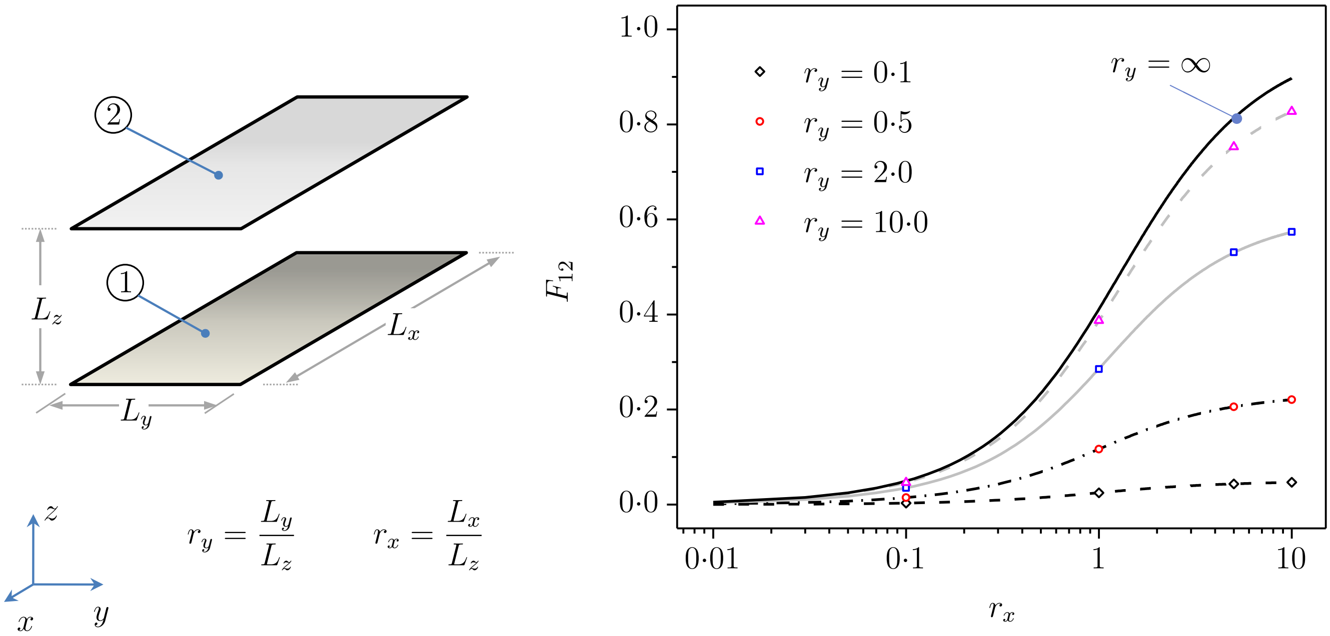

Figure 3.21 View factors calculated for two rectangular surfaces parallel to each other. The lines represent exact solution.

The third test case is selected for its direct application to sintering problem, where a spherical surface is the basic geometrical unit of powder bed. Thus, we have considered a case which involves two equal spherical surfaces separated by a distance d in space. The view factor between two surfaces is calculated for increasing distance between them. Figure 3.22 shows a good agreement with analytical solution.

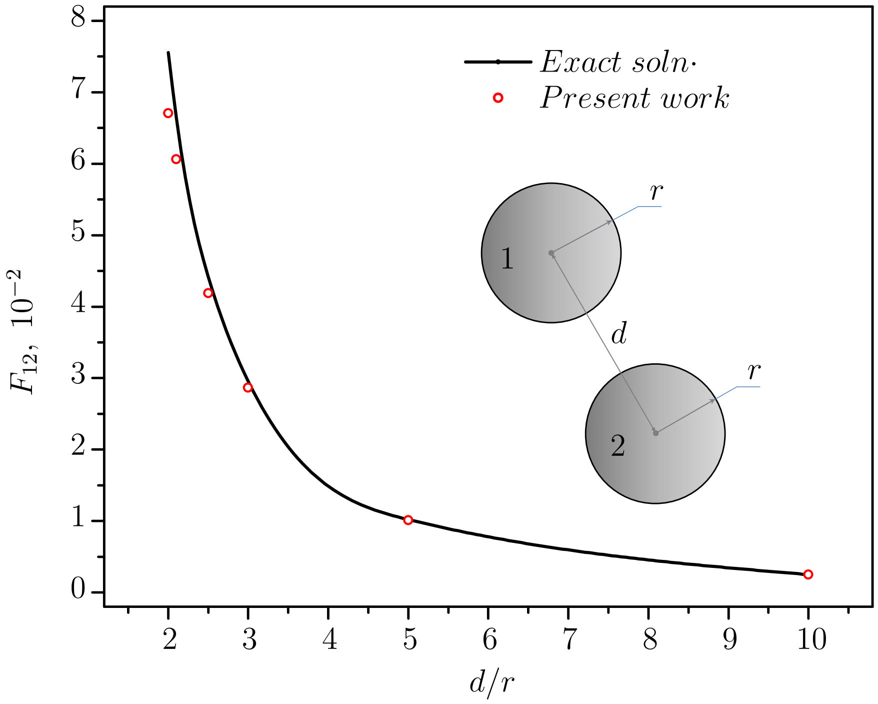

Figure 3.22 View factor between two spherical surfaces: the values calculated using ray-tracing compared with exact solution.

Thermal radiation exchange: The method developed to solve radiation heat exchange between interacting surfaces is validated by solving simple textbook problems and evaluating the accuracy of solution. For the first case radiation heat transfer between two infinitely long parallel planes is calculated. The schematic of involved surfaces and input parameters are shown in Fig. 3.23. The calculated heat flux values are given in Table 3.3. Similarly the method is

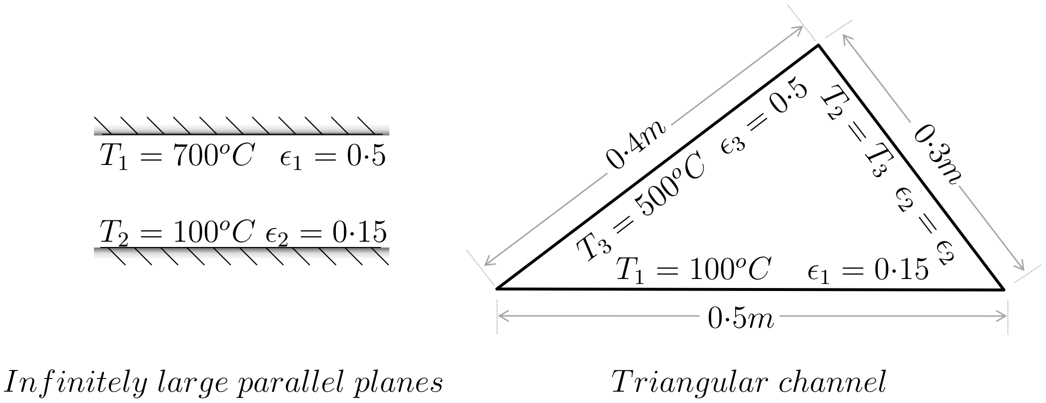

Figure 3.23 Test cases to validate radiation exchange between surfaces.

Table 3.3 Case 1, radiation exchange between infinately large parallel plates

Convergence criterion, ε	q_{12}, Wm^{-2} (simulated)	(net-radiation)	error, %
10^{-4}	6487.081	6485.535	0.02
10^{-5}	6485.653		0.002

applied to solve radiation heat transfer among three interacting surfaces (maintained at given temperatures) and corresponding results are listed in Table 3.4.

Table 3.4 Case 2, radiation exchange in a triangular channel

Convergence criterion	q_1, Wm^{-2} (simulated)	(net-radiation)	error, %
10^{-4}	1299.21	1293.9	0.410
10^{-5}	1299.30		0.417

Nevertheless, many important findings of this model have led to considerable simplification in the subsequent laser-particle interaction model in the next section.

3.4 Transient heat transfer in single particle during exposure

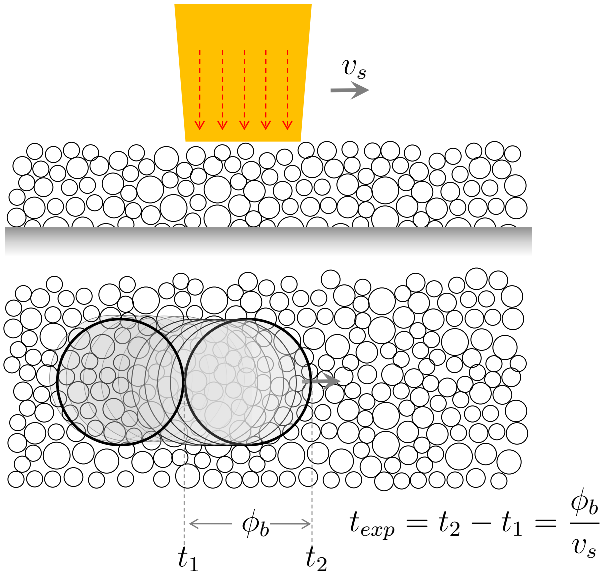

Figure 3.24 Schematic of laser particle exposure time in the powder bed.

In the previous section we compute the heat transported to individual particles in the powder bed due to the action of the laser source and predicted the overall distribution of energy in the powder bed. However, the details of thermal transients on a particle scale are still missing due to modelling assumptions. The model is unable to predict thermal gradients in the particle leading to partial melting. Understanding of phase change transients of a particle is extremely relevant for predicting densification since melting and solidification are primary consolidation mechanisms during laser sintering of metal powders. Furthermore, laser sintering being an extremely fast process since the duration of interaction between a particle and the scanning laser beam is few milliseconds long (Fig. 3.24). The actual phenomenon at any instant during the process, is localized to an area under the moving laser beam and thus transient thermal characteristics of individual particles are key to understanding laser sintering mechanism. Moreover, depending on the nature of laser source (e.g. pulsed laser or continuous wave), the thermal characteristics of a particle can be significantly different.

This section is dedicated to the development of a thermal model to study the characteristics of a representative particle subjected to laser heating. A schematic of computational domain for particle scale thermal evolution during SLS is shown in fig. 3.25. It consists of a particle at the centre surrounded by loose powder. Granular powder is modelled as a homogeneous medium having effective thermo-physical properties. The distinction between two sub-domains can be made by their respective properties. Only conduction heat transfer with phase-change is relevant in the computational domain because powder bed is modelled as continuum. Influence of convection and radiation within the powder bed can only be affected through effective transport properties of the powder bed. The primary aim of this model is to study the temperature evolution in a single particle to calculate the development of the molten shell on the heated particles, which is important for coalescence of particles. The state of surrounding particles is of less significance, however, their presence is needed to estimate their influence on the behaviour of the representative particle under consideration.

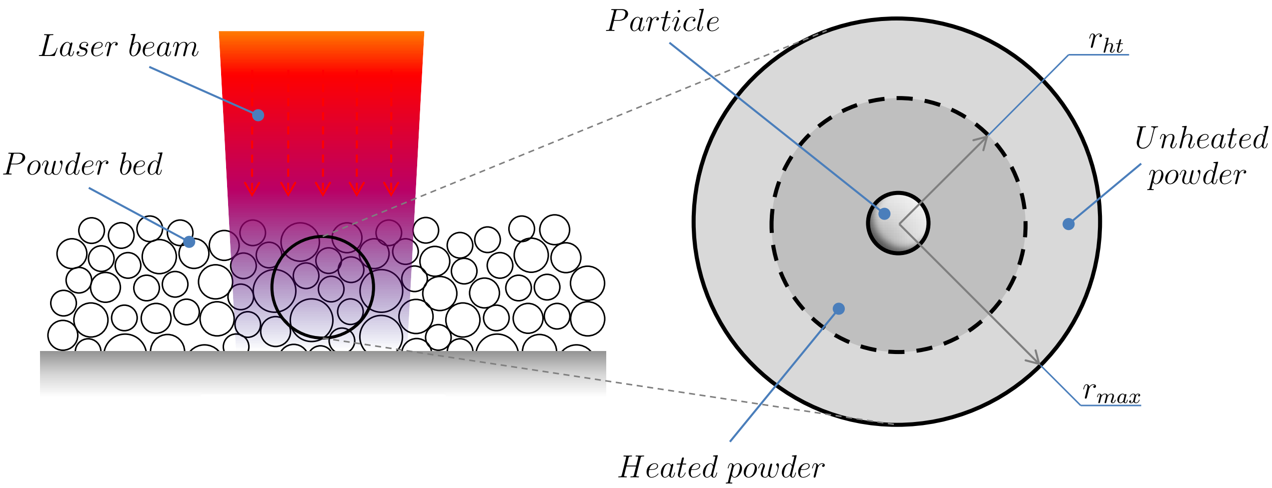

Figure 3.25 Schematic of the computational domain.

3.4.1 Governing equation and boundary conditions

The central representative particle in the computational domain is assumed to be homogeneously irradiated by laser radiation. Scattering of laser beam by powder particles and multiple reflections lead to almost homogeneous irradiation of particles at the depth of around a mean diameter from powder surface. This is also confirmed by our previous thermal model for heat transfer in the discrete granular medium.

This assumption simplifies the problem into one-dimensional heat transfer in spherical coordinates by exploiting the spherical symmetry. The corresponding governing equation has following form:

$$\frac{\partial(\rho C_p T)}{\partial t} = \frac{1}{r^2}\frac{\partial}{\partial r}\left(r^2\lambda\frac{\partial T}{\partial r}\right) + \dot{Q}_{src}, \tag{3.29}$$

where, $\dot{Q}_{src}$ denotes the heat source term. This includes the contribution due to volumetric heating by laser beam as well as the latent heat of melting and solidification during phase change as per the given equation

$$\dot{Q}_{src} = \dot{Q}_{src}^{laser} + \dot{Q}_{src}^{ph}\,, \tag{3.30}$$

the detailed derivations for each of the individual terms of source term are given in following sections.

Since the particle is assumed to be homogeneously irradiated, the symmetry boundary condition is used at the center of the particle:

$$\frac{\partial T}{\partial r}_{|r=0} = 0, t \geq 0\cdot \tag{3.31}$$

Since the size of the powder bed in a real process is much larger than the particle size, the present problem can be posed in an unbounded domain with the following initial and boundary conditions:

$$T(r,0) = T_0, \quad 0 \leq r \leq \infty, \tag{3.32}$$

$$T(r,t) = T_0, \quad r \to \infty, \tag{3.33}$$

where T_0 is the initial temperature of the powder bed. However, in order to solve the problem numerically, it is necessary to pose it in a finite computational domain $0 \leq r \leq r_{max}$. To determine a physically meaningful boundary condition at $r = r_{max}$, consider an auxiliary problem of an instationary heat conduction without heat sources and in the absence of phase change in a spherically-symmetric domain $r_{ht} \leq r \leq \infty$ subject to initial and boundary conditions (3.32, 3.33) and a boundary condition:

$$\lambda\frac{\partial T}{\partial r}_{|r=r_{ht}} = q_{ht}, t \geq 0\cdot \tag{3.34}$$

If the value of q_{ht} is chosen in such a way that the time-averaged heat generation rate in the region $0 \leq r \leq r_{ht}$ due to the laser source in an original problem is equal to the total heat flow rate at $r = r_{ht}$ in an auxiliary problem, then the temperature fields at $r >> r_{ht}$ for the original and auxiliary problems are very close. The temperature profile which satisfies Eq. (3.29) subject to initial condition (3.32) and boundary conditions (3.33, 3.34) is given by the following equation [18]:

$$T(r_{max}, t) = \frac{r_{ht}^2\, q_{ht}}{\lambda_e r_{max}} \left[\mathtt{erfc} \left(\frac{r_{max} - r_{ht}}{2\sqrt{\kappa_e t}} \right) - \mathtt{exp} \left(\frac{r_{max} - r_{ht}}{r_{ht}} + \frac{\kappa_e t}{r_{ht}^2} \right) \mathtt{erfc} \left(\frac{r_{max} - r_{ht}}{2\sqrt{\kappa_e t}} + \frac{\sqrt{\kappa_e t}}{r_{ht}} \right) \right] + T_{in}, \tag{3.35}$$

where r_{ht} defines the boundary of the heat generation area in the powder, determined by the laser beam diameter, r_{max} is an arbitrarily chosen radial position which defines the outer boundary of computational domain and κ_e is the effective thermal diffusivity of the metal powder. Equation (3.35) defines the last boundary condition for the problem describing heat transfer and phase change in a powder particle.

3.4.2 Discretization

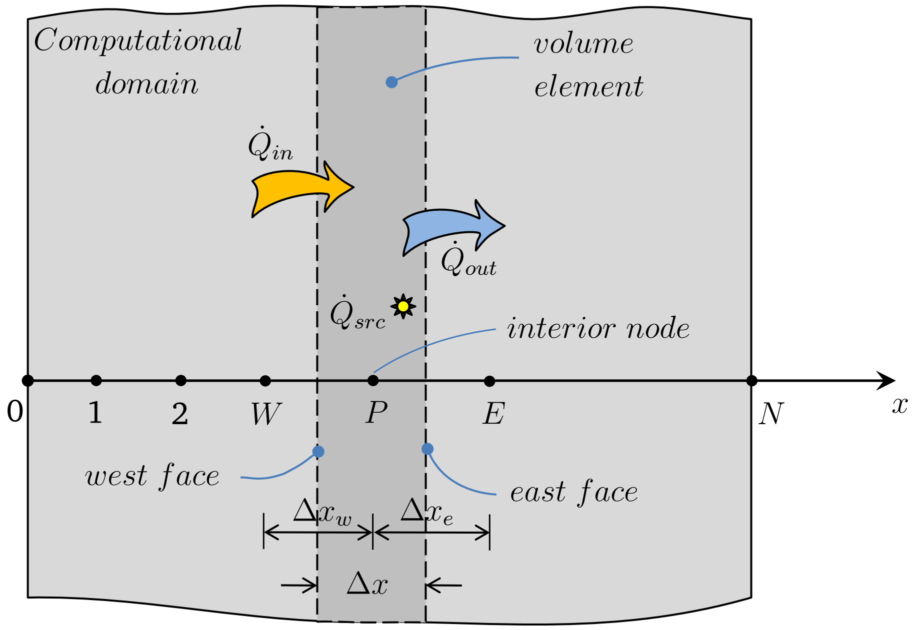

Figure 3.26 Domain discretization

We apply energy balance over a typical control volume shown in Fig. 3.26 to obtain discretized form of governing equation.

$$\dot{E} = \dot{Q}_{in} - \dot{Q}_{out} + \dot{Q}_{src} \tag{3.36}$$

where E is the internal energy of the control volume, $\dot{Q}_{in}$ and $\dot{Q}_{out}$ represent the conduction heat transfer on both the sides of the control volume, and $\dot{Q}_{src}$ denotes the heat source in the control volume. Using Fourier's law of heat conduction at east and west face of the control volume:

$$\dot{Q}_{in} = -k_w A_w \frac{dT}{dx}_{|w} ; \dot{Q}_{out} = -k_e A_e \frac{dT}{dx}_{|e} ; \tag{3.37}$$

in terms of nodal values

$$\dot{Q}_{in} = -k_w A_w \left(\frac{T_P - T_W}{\Delta x_w} \right) ; \dot{Q}_{out} = -k_e A_e \left(\frac{T_E - T_P}{\Delta x_e} \right) ; \dot{E} = \frac{\rho C_p \Delta V (T_P - T_P^o)}{\Delta t} \tag{3.38}$$

after substitution the energy balance for control volume P is given as

$$\frac{\rho C_p \Delta V (T_P - T_P^o)}{\Delta t} = k_e A_e \left(\frac{T_E - T_P}{\Delta x_e} \right) - k_w A_w \left(\frac{T_P - T_W}{\Delta x_w} \right) + \dot{Q}_{src} \Delta V \tag{3.39}$$

and final form of discretized governing equation is obtained after rearrangement.

$$a_P T_P = a_E T_E + a_W T_W + a_o T_P^o + source \tag{3.40}$$

for $P = 1, 2, 3 \cdots\cdots N$ where $E = P + 1$, $W = P - 1$ and a_P, a_E, a_W and a_o are coefficients of nodal variables that depend on control volume geometry as well as thermo-physical properties assigned to the control volume. The present form of discretized equation is obtained without reference to any specific coordinate system, thus the same formulation is applicable for all coordinate systems provided the area of the control volume faces are calculated exactly. A typical non-uniform grid used for simulation is shown in Fig. 3.27. Around 200 nodes are used for simulation with very fine spacing near the particle surface to accurately resolve thermal transients in the particle. The size of computational domain is 75 μm.

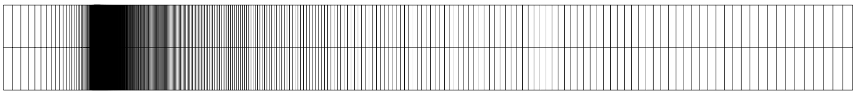

Figure 3.27 Typical grid used for simulation

3.4.3 Modelling phase change

In the present formulation we have included phase change by means of an additional source term. Therefore the expression for discretized equation remains unaffected except an additional source term that appears only for the control volume undergoing phase-change. The expression for this additional source due to phase-change is again obtained by considering energy balance in a control volume, that is subjected to phase-change. The properties of liquid and solid phase are assumed identical. The model can be easily adjusted to the case if this assumption is relaxed. We can write energy balance equation (3.36) for control volume P (see Fig. 3.26) as

$$\frac{\rho C_p \Delta V (T_P - T_P^o)}{\Delta t} = \dot{Q}_{in} - \dot{Q}_{out} + \dot{Q}_{src} \Delta V , \tag{3.41}$$

where $\dot{Q}_{src}$ is the total source term in the control volume. Consider a condition such that $T_P > T_{mp}$ and $T_P^o \leq T_{mp}$ i.e. during the time interval Δt the temperature of the control volume changed from $T_P^o \leq T_{mp}$ to $T_P > T_{mp}$, this means that the particular control volume underwent the phase change (melting). During the phase change the internal energy of the control volume increases while its temperature remains equal to T_{mp} and the energy balance for the control volume accepts the following form:

$$\frac{\rho C_p \Delta V (T_{mp} - T_P^o)}{\Delta t} + \frac{\rho H_f \Delta V \Delta \Psi}{\Delta t} = \dot{Q}_{in} - \dot{Q}_{out} + \dot{Q}_{src}^{laser} \Delta V \tag{3.42}$$

where $\Delta\Psi$ represents the fraction of the control volume undergone the phase change and $\dot{Q}_{src}^{laser}$ is source term due to laser heating alone. We can also rewrite equation (3.41) as

$$\frac{\rho C_p \Delta V (T_{mp} - T_P^o)}{\Delta t} + \frac{\rho C_p \Delta V (T_P - T_{mp})}{\Delta t} = \dot{Q}_{in} - \dot{Q}_{out} + (\dot{Q}_{src}^{laser} + \dot{Q}_{src}^{ph}) \Delta V \tag{3.43}$$

Using equation (3.42) and (3.43) the change in phase fraction in the control volume is approximated as

$$\Delta\Psi = \frac{C_p (T_P - T_{mp})}{H_f} \tag{3.44}$$

while expression for source term due to phase change is given by

$$\dot{Q}_{src}^{ph} = \frac{\rho H_f \Delta\Psi}{\Delta t} \tag{3.45}$$

All the control volumes have their phase identity defined by respective phase fraction. For example if Ψ stands for liquid fraction then the control volumes which are completely solid will have $\Psi = 0$ and similarly liquid cells will have their $\Psi = 1$ while for phase-change cell $0 < \Psi < 1$. Having identified a control volume undergoing phase change, corresponding source term is added to discretized conduction equation of that cell and complete set of algebraic equations are solved again till convergence.

3.4.4 Modelling the laser source term

Physically the laser heating is a volumetric heating phenomenon and in order to capture the thermal transients of a particle accurately during short time frame of laser particle interaction, it is required to model the radial variation of laser intensity in the particle. This section describes the derivation of volumetric heat source for powder and particle due laser heating. The non-uniformity of the spatial energy distribution in the beam has been neglected because the particle size is much smaller than the beam diameter. For a laser source of average power P_o, the incident radiation intensity at the powder bed is expressed as:

$$I_{inc} = \frac{P_o}{\pi r_b^2}, \tag{3.46}$$

A fraction of the incident laser intensity is reflected at the surface, and the remaining is absorbed by the powder layer. If α_e is effective absorptivity of the powder bed then the transmitted intensity at the powder bed surface is given as

$$I_o = \alpha_e I_{inc} \tag{3.47}$$

Following Beer-Lambert's law of radiation absorption [92], variation of heat flux along the bed depth is given by

$$I_o(z) = I_o \text{exp}^{-\eta_e z}, \tag{3.48}$$

where η_e is the effective absorption coefficient of the powder material and z is the distance from bed surface. At any instant during sintering only a certain volume of powder bed, that is directly under the laser beam is subjected to laser heating. It is known as interaction volume and it can be characterized by laser beam diameter and optical penetration depth of laser radiation into the powder bed. Based on the energy absorption model results for laser energy distribution in the powder bed 5.24(b), an approximate expression for interaction volume can be given as

$$V_{int} = 2{\cdot}0\phi_m \pi r_b^2 \ , \tag{3.49}$$

where ϕ_m is mean size of particles in the powder bed. The axial variation of heat generation rate due to absorbed laser energy in the laser-powder interaction volume is given by

$$\dot{Q}_{int}(z) = -\frac{dI_o(z)}{dz} = \eta_e I_o \text{exp}^{-\eta_e z} \ . \tag{3.50}$$

Further, to determine effective heat source for a representative particle in powder bed, energy generation rate in the interaction volume is obtained by integrating the eqn. 3.53 over the penetration depth of laser beam in the powder bed.

$$\dot{Q}_{int} = \int_0^{OPD} \dot{Q}_{int}(z) \pi r_b^2 dz = \alpha_e \left(1 - \frac{1}{e}\right) P_o \ , \tag{3.51}$$

where OPD is optical penetration depth of laser beam in the powder bed. This can be determined from our previous model for spatial energy distribution in the powder bed. Assuming uniform heat generation in the interaction volume due to laser beam, the obtained heat generation rate for an individual particle in the interaction volume is given by

$$\dot{Q}_p = \dot{Q}_{int} / N_p, \tag{3.52}$$

where N_p is number of particles in the interaction volume. The resulting volumetric heat generation rate, considering the radiation attenuation within the particle is given by

$$\dot{Q}_{src}^{laser} = \dot{Q}_p(r) = \eta \frac{\dot{Q}_p}{4\pi r_p^2} \text{exp}^{-\eta(r_p - r)} \ , \quad 0 < r \leq r_p, \tag{3.53}$$

where

$$\int_0^{r_p} \dot{Q}_p(r) 4\pi r_p^2 dr = \dot{Q}_p \ , \tag{3.54}$$

this is fulfilled if $\eta r_p \gg 1$. This valid due to the large absorption coefficient (order $10^8 m^{-1}$) for metals. Consequently, the volumetric heat source is negligible in the whole particle except for a very thin layer near the particle surface.

In the real industrial process, each particle is surrounded by other grains, which are also heated by the laser energy. To describe the laser-induced heating of the surrounding powder, equivalent volumetric heat generation (averaged over space and time) is modelled in the powder. Using energy deposition rate in the interaction volume (see equation 3.51), the source term in the powder is given by

$$\dot{Q}_{src}^{laser} = \frac{\dot{Q}_{int}}{V_{int}} \ , \quad r_p < r \leq r_{ht} \ . \tag{3.55}$$

3.4.5 Solution algorithm

The key steps involved in solving laser induced heat transfer and phase change in a representative particle during laser sintering are listed below:

1. Define initial conditions and boundary conditions.
2. Evaluate source term due to laser heating.
3. Solve single phase conduction equation for control volume temperature.
4. Identify the control volumes undergoing phase change.
5. Calculate appropriate source/sink term due to phase change using equation (3.45).
6. Update the source terms and repeat steps 3 to 5 till convergence.
7. Update temperature, phase fraction for all the control volumes and advance to next time step.

3.4.6 Validation

An estimate of average temperature rise in the particle between two consecutive laser pulses can be determined by energy balance in the particle, assuming no heat loss to surrounding powder. Total energy generated in a particle during the heating pulse is used to raise its internal energy and hence temperature rise during the pulse under such conditions is given by

$$\Delta T_{pulse} = \frac{\dot{Q}_p}{\rho_p V_p C_p f} \tag{3.56}$$

and the calculated temperature rise using Eqn. (3.56) compares almost exactly with the numerical solution. Figure 3.28 shows the temperature evolution in the particle and corresponding estimate by energy balance. This serves as a good measure to verify the laser source modelling. The developed solution algorithm for heat transfer with phase change is validated by solving

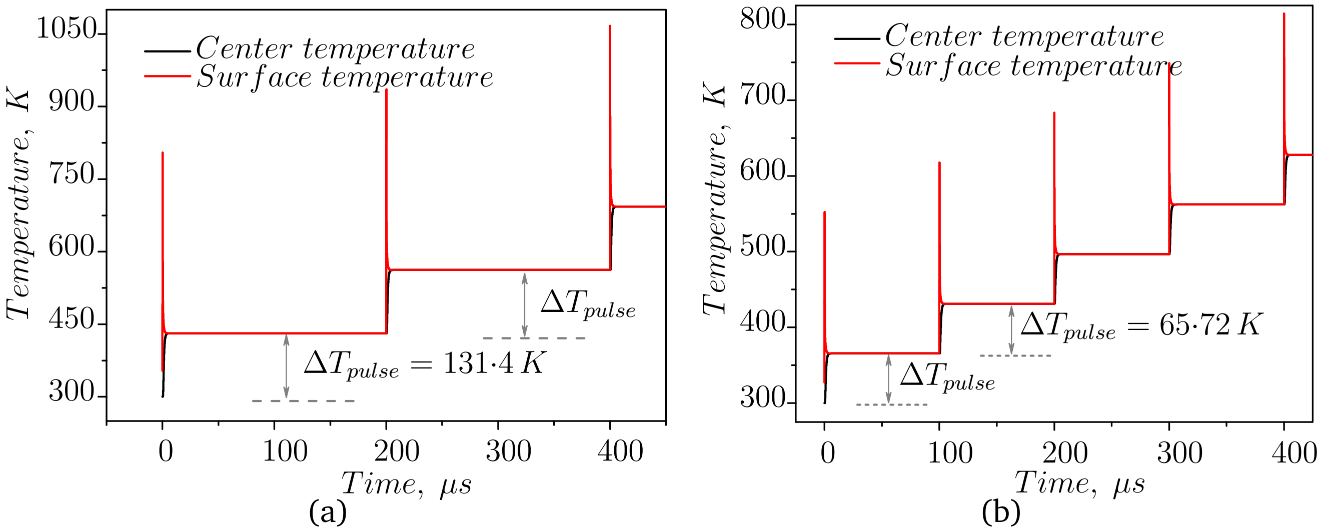

Figure 3.28 Average temperature rise per pulse in an isolated particle for two different laser pulse frequencies, (a) Pulse frequency = 5 KHz, (b) Pulse frequency = 10 KHz ($P_o = 1\,W$, $r_p =$ 11 μm) thermo-physical properties of the material is given in Table 5.8.

Stefan problem for which analytical solution is available in the book of Carslaw and Jaeger [18]. Figure 3.29 compares the predictions for temperature evolution at a fixed point and solid-liquid interface position for one-dimensional Stefan problem specified as per [127]. Both temperature and melting front are in good agreement with analytical solution.

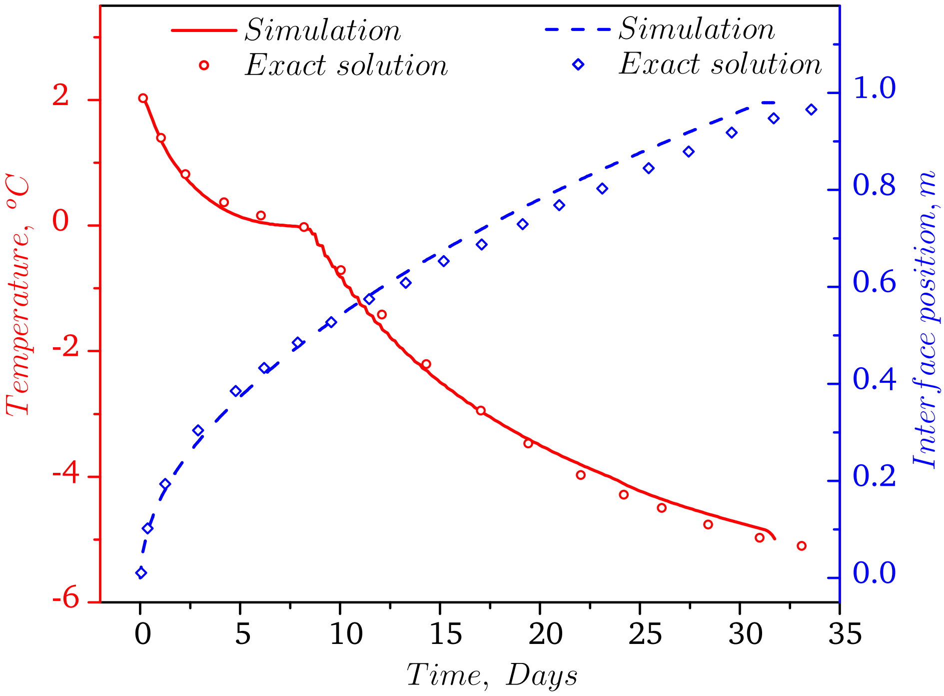

Figure 3.29 Comparison of temperature history at x = 0.5m from the cold end and interface position for one dimensional Stefan problem specified as per [127] ($\rho = 1\,kg\,m^{-3},\ \lambda = 2\,W\,m^{-1}\,K^{-1},\ C_p = 2{\cdot}5\,MJ\,kg^{-1}\,K^{-1},\ H_f = 100\,MJ\,kg^{-1},\ T_{in} = 2\ {}^oC,\ T_{x=0} = -10\ {}^oC,\ T_{mp} = 0\ {}^oC,\ L = 1\,m$).

4

Modelling the particles coalescence

After having modelled heat transport in a powder bed in previous chapter, next logical step towards the overall goal of modelling sintering process is to investigate thermally induced sintering hydrodynamics.

4.1 Introduction

This chapter is primarily devoted to model coalescence of partially or completely melted particles. Our approach to understanding the sintering of metallic powders is to begin with the study of a simple representative geometry of coalescing particles, and thus we choose the coalescence of two particles in contact, for being the simplest representation of mechanism of densification during laser sintering. The overall coalescence model is developed in two stages. First stage focusses on modelling of the hydrodynamic part of problem (isothermal coalescence), without considering any heat transfer and phase-change. However, in a real process the coalescence is accompanied by melting or solidification due to laser heating. Therefore, the second modelling stage involves extending isothermal coalescence model to include heat transfer and phase change.

The objectives of this chapter are the following:

1. Modelling the coalescence of viscous particles with solid cores
2. Modelling simultaneous heat transfer, phase-change and coalescence of particles

Thus enabling the investigation of key phenomena governing the selective laser sintering (melting of the particles and their coalescence) in a coupled manner to help us gain the understanding of laser sintering mechanisms. The modelling approach in this chapter is dictated by need to model densification mechanism for single component metallic powders, especially for producing complex open pore porous structures. Sintering by partial melting is most relevant binding mechanism [77] for such a case.

4.2 Modelling coalescence hydrodynamics

According to classification of binding mechanisms, laser sintering of multicomponent metal powders is categorised under liquid phase sintering, characterized by melting of low melting point particles providing both capillary force and transport medium to promote densification. On the other hand, the single component metallic powders are sintered due to liquid-liquid contact growth during partial melting of particles having melted surface and unmelted solid core. The interparticle contacts are formed by fusing molten surfaces due to attractive capillary forces. The contact growth is driven by high curvature gradients at the contact. Liquid melt acts as wetting as well as lubricating medium enhancing mobility and rearrangement of cores during densification. The densification is accompanied by mutually approaching solid cores and growing size of liquid neck between the particles. Upon cooling and solidification the particles stay permanently bonded via solidified necks joints between the particles.

According to experiments and theory proposed by previous researchers [69, 77, 115] as well as numerical modelling [32, 40, 71] for metallic particles, the melt flow driven by surface tension force is a dominant densification mechanism for metal particles. Only the liquid-liquid interaction between neighbours is considered. Solid cores are assumed as particles suspended in liquid medium.

4.2.1 Mathematical model

Consider two cylindrical particles with viscous shell and solid cores at their centres, having a finite contact as shown in Fig. 4.1. The free surface of the coalescing particles is denoted by Γ_o and solid-liquid interfaces by Γ_1 and Γ_2. The two particles of radius R_p are connected by a liquid neck of radius r_n. The initial shape of free surface Γ_o is chosen as an inverse ellipse having Cartesian coordinates given by

$$x(\theta) = R_{eqm}[(1-\xi^2)(1+\xi^2)^{-\frac{1}{2}}(1+2\xi\cos(2\theta)+\xi^2)^{-1}](1+\xi)\cos(\theta)\ , \tag{4.1}$$

$$y(\theta) = R_{eqm}[(1-\xi^2)(1+\xi^2)^{-\frac{1}{2}}(1+2\xi\cos(2\theta)+\xi^2)^{-1}](1-\xi)\sin(\theta)\cdot \tag{4.2}$$

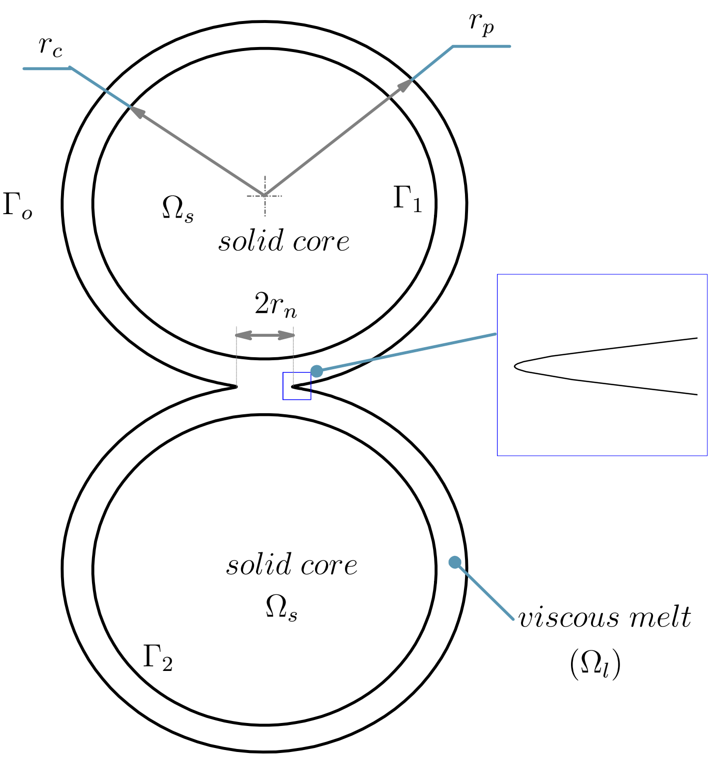

Figure 4.1 Schematic of computational domain for coalescence of particles

This shape corresponds to analytical solution for coalescence of two viscous cylinders [55]. The initial neck radius r_n is given by

$$r_n(0) = R_{eqm}(1-\xi)(1+\xi^2)^{-\frac{1}{2}}, \tag{4.3}$$

where R_{eqm} is the radius of a cylinder having the same volume as two cylinders of radius r_p. In case of completely viscous particles ($r_c = 0$), this corresponds to final equilibrium radius of coalesced particles. $0 \leq \theta < 2\pi$ and $\xi = 0{\cdot}87$. Coalescence of particles during sintering is modelled under the assumption of vanishing Reynolds. The flow is described by the continuity equation:

$$\nabla \cdot \mathbf{u} = 0, \tag{4.4}$$

and the Stokes equation:

$$-\nabla p + \mu(\nabla^2 \mathbf{u}) = 0, \tag{4.5}$$

where p is the pressure, μ is the fluid dynamic viscosity, and $\mathbf{u}$ is the fluid velocity vector. The influence of gravitational force is neglected, and the solid cores are assumed to be neutrally buoyant. In the case of inertialess particles the net hydrodynamic force and torque acting on a solid particle must be equal to zero [84]. These conditions be represented in terms of surface traction $\mathbf{f}$ at the solid-liquid interface at the n^{th} particle as

$$F_i^n = \int_{\Gamma_n} f_i(\mathbf{x})dl(\mathbf{x}) = 0,\ \tau_z^n = \varepsilon_{zjm}\int_{\Gamma_n} f_j(\mathbf{x})(\mathbf{x}-\mathbf{x}_c^n)_m dl(\mathbf{x}) = 0, \tag{4.6}$$

where $i = 1, 2$ denotes components in x and y direction, l is the arc length along the interface, $\mathbf{x}_c^n$ is the position vector of the centre of n^{th} particle, the subscript m denotes the m^{th} component of the vector. At the free surface Γ_o between viscous fluid and surrounding gas, surface traction is given by

$$\mathbf{f} = \gamma K \mathbf{n}, \tag{4.7}$$

where γ is surface tension at the free surface, $\mathbf{n}$ is unit normal vector to the boundary pointing into the fluid, and K is curvature of the free surface. At the solid-liquid interface the condition of continuity of velocity vector should be fulfilled. Governing equations are solved along with boundary conditions to simulate the hydrodynamic behavior of coalescing particles during sintering. The time evolution of particle boundaries is obtained from the velocity $\mathbf{u}$ using the kinematic boundary condition.

$$\frac{d\mathbf{x}}{dt} = \mathbf{u}(\mathbf{x}) \quad (\mathbf{x} \in \Gamma) \tag{4.8}$$

4.2.2 Boundary element formulation

There are two commonly employed numerical approaches to solve a boundary value problem. In the first approach the solutions are forced to satisfy the boundary condition exactly while minimizing the error in satisfying the governing differential equation. This corresponds to domain discretization methods like FEM, FVM, FDM etc. In second approach, the fundamental solution of the governing differential equation is used to approximate the solution inside the domain while minimizing the error in satisfying the boundary conditions. This approach corresponds to a Boundary Element Method (BEM). The BEM is based on transforming the differential equation into an integral equation over the domain boundary. The boundary integrals are obtained numerically using quadrature rules. The main advantage of this method is that the problem dimension is reduced by one order, since the discretization is needed only at the boundary. The other important feature of BEM is that the value of normal derivatives of the potential at the domain boundary are solved for, unlike other methods where normal derivatives are obtained indirectly from potential values in the domain. More details about the method and its applications can be found elsewhere [4, 7, 12, 13, 99]. Since we are particularly interested in the evolution of domain boundary during particle coalescence, BEM is ideally suited for it and facilitates local mesh refinement in advantageous way and more accurate for linear problems.

To derive boundary integral formulation for motion of solid cores and free surface evolution under the influence of curvature gradients, the velocity vector $\mathbf{u}$ is first resolved into two components as

$$\mathbf{u} = \mathbf{u}^{\infty} + \mathbf{u}^{D}, \tag{4.9}$$

where $\mathbf{u}^{\infty}$ is an undisturbed component which prevails in absence of any solid core, and $\mathbf{u}^{D}$ is a disturbance component due to the presence of solid core. Now the total velocity of the fluid at the solid core surface can be given as

$$\mathbf{u}^{\infty} + \mathbf{u}^{D} = \mathbf{u}^{RBM} = \mathbf{v} + \omega \times \mathbf{x}, \tag{4.10}$$

where $\mathbf{v}$ and ω are translational and rotational velocity of the solid core, superscript RBM stands for rigid body motion. Unlike the problems where the undisturbed component of the fluid flow $\mathbf{u}^{\infty}$ is known *a priori*, $\mathbf{u}^{\infty}$ needs to be determined by solving a separate subproblem for completely viscous particles (without considering any core) using boundary integral equation for two-dimensional stokes flow given by

$$cu_j(\mathbf{x_0}) = -\frac{1}{4\pi\mu}\int_{\Gamma_0} f_i(\mathbf{x})G_{ij}(\mathbf{x},\mathbf{x_0})dl(\mathbf{x}) + \frac{1}{4\pi}\int_{\Gamma_0} u_i(\mathbf{x})T_{ijk}(\mathbf{x},\mathbf{x_0})n_k(\mathbf{x})dl(\mathbf{x}), \tag{4.11}$$

for $j = 1, 2$, and Einstein's summation convention is used over repeated-indices; f_i denotes the i^{th} component of the boundary traction, G_{ij} is the free-space Green's function and T_{ijk} is associated stress field [99].

$$c = \begin{cases} 1 & \text{if } \mathbf{x_0} \text{ lies inside } \Gamma_0 \text{ ,} \\ \frac{1}{2} & \text{if } \mathbf{x_0} \text{ lies on } \Gamma_0 \text{ ,} \end{cases}$$

$$\begin{aligned} G_{ij}(\mathbf{x},\mathbf{x_0}) &= -\delta_{ij}\ln r + \frac{\hat{x}_i\hat{x}_j}{r^2} \ , \\ T_{ijk}(\mathbf{x},\mathbf{x_0}) &= -4\frac{\hat{x}_i\hat{x}_j\hat{x}_k}{r^4} \ , \end{aligned}$$

where $\hat{\mathbf{x}} \equiv \mathbf{x} - \mathbf{x_0}$, $r = |\hat{\mathbf{x}}|$.

Equation (4.11) alone does not ensure a unique solution [80], since superposition of any arbitrary rigid body motion will not alter stress field at the boundary Γ_o. Thus we need to specify extra conditions to constrain those rigid body motions. To ensure rotation free solution we assume that there is no internal rotation in the fluid and using Stokes theorem we arrive at an extra condition given as

$$\oint_{\Gamma_0} \mathbf{u}\cdot\mathbf{t}dl(\mathbf{x}) = 0 \ , \tag{4.12}$$

where $\mathbf{t}$ is unit tangent vector. Since the shape evolution of particles during coalescence is not influenced by any superimposed rigid body motion, the translational motion is constrained by ensuring that velocity of center of mass of the domain is zero.

The system of algebraic equations obtained after discretization of integral equation (4.11) along with boundary condition (4.7) and extra condition (4.12) will result in over-constrained system. This system of algebraic equations is solved using the least squares method to get the required undisturbed velocity component.

Now an integral equation is formulated combining the boundary integral formulations for motion of solid particles suspended in viscous fluid and Stokes flow of a fluid due to free surface [84].

The standard boundary integral equation for disturbance velocity at any point $\mathbf{x_0}$ in Stokes flow is given by

$$u_j^D(\mathbf{x_0}) = -\frac{1}{4\pi\mu}\sum_{a=0}^{2}\int_{\Gamma_a} f_i^D(\mathbf{x})G_{ij}(\mathbf{x},\mathbf{x_0})dl(\mathbf{x}) + \frac{1}{4\pi}\sum_{a=0}^{2}\int_{\Gamma_a} u_i^D(\mathbf{x})T_{ijk}(\mathbf{x},\mathbf{x_0})n_k dl(\mathbf{x}), \tag{4.13}$$

where superscript D denotes the disturbance component. Knowing that double layer integral over the surface of rigid body is equal to zero, i.e.

$$\int_{\Gamma_a} u_i^{RBM}(\mathbf{x})T_{ijk}(\mathbf{x},\mathbf{x_0})n_k dl(\mathbf{x}) = 0, \tag{4.14}$$

where $a = 1, 2$ for solid-liquid interface and using equations (4.10), (4.13), and (4.14), we get

$$\begin{aligned} u_j^D(\mathbf{x_0}) = &-\frac{1}{4\pi\mu}\sum_{a=0}^{2}\int_{\Gamma_a} f_i^D(\mathbf{x})G_{ij}(\mathbf{x},\mathbf{x_0})dl(\mathbf{x}) + \frac{1}{4\pi}\int_{\Gamma_0} u_i^D(\mathbf{x})T_{ijk}(\mathbf{x},\mathbf{x_0})n_k(\mathbf{x})dl(\mathbf{x}) \\ &-\frac{1}{4\pi}\sum_{a=1}^{2}\int_{\Gamma_a} u_i^{\infty}(\mathbf{x})T_{ijk}(\mathbf{x},\mathbf{x_0})n_k(\mathbf{x})dl(\mathbf{x}) \ . \end{aligned} \tag{4.15}$$

Again by using reciprocal theorem [99], the double-layer integrals over the solid-liquid interfaces in equation (4.15) are are replaced by single layer integrals as

$$\int_{\Gamma_a} u_i^{\infty}(\mathbf{x})T_{ijk}(\mathbf{x},\mathbf{x_0})n_k(\mathbf{x})dl(\mathbf{x}) = \frac{1}{\mu}\int_{\Gamma_a} f_i^{\infty}(\mathbf{x})G_{ij}(\mathbf{x},\mathbf{x_0})dl(\mathbf{x}) \ , \tag{4.16}$$

to obtain the combined integral representation for any point $\mathbf{x_0}$ located in fluid regoin excluding the boundaries as

$$\begin{aligned} u_j^D(\mathbf{x_0}) = &-\frac{1}{4\pi\mu}\int_{\Gamma_0} f_i^D(\mathbf{x})G_{ij}(\mathbf{x},\mathbf{x_0})dl(\mathbf{x}) + \frac{1}{4\pi}\int_{\Gamma_0} u_i^D(\mathbf{x})T_{ijk}(\mathbf{x},\mathbf{x_0})n_k(\mathbf{x})dl(\mathbf{x}) \\ &-\frac{1}{4\pi\mu}\sum_{a=1}^{2}\int_{\Gamma_a} f_i(\mathbf{x})G_{ij}(\mathbf{x},\mathbf{x_0})dl(\mathbf{x}) \ . \end{aligned} \tag{4.17}$$

For $\mathbf{x_0}$ located on boundaries we take limit as the point $\mathbf{x_0}$ approaches the free surface or the rigid core surface and rewrite equation (4.17) as

$$\begin{aligned} cu_j^D(\mathbf{x_0}) = &-\frac{1}{4\pi\mu}\int_{\Gamma_0} f_i^D(\mathbf{x})G_{ij}(\mathbf{x},\mathbf{x_0})dl(\mathbf{x}) + \frac{1}{4\pi}\int_{\Gamma_0} u_i^D(\mathbf{x})T_{ijk}(\mathbf{x},\mathbf{x_0})n_k(\mathbf{x})dl(\mathbf{x}) \\ &-\frac{1}{4\pi\mu}\sum_{a=1}^{2}\int_{\Gamma_a} f_i(\mathbf{x})G_{ij}(\mathbf{x},\mathbf{x_0})dl(\mathbf{x}), \end{aligned} \tag{4.18}$$

where

$$c = \begin{cases} \frac{1}{2} & \text{if } \mathbf{x_0} \in \Gamma_0 \ , \\ 1 & \text{if } \mathbf{x_0} \in (\Gamma_1 \cup \Gamma_2) \ . \end{cases}$$

When $\mathbf{x_0}$ lies on solid-liquid interface then $u_j^D(\mathbf{x_0}) = u_j^{RBM}(\mathbf{x_0}) - u_j^{\infty}(\mathbf{x_0})$. The integral equation (4.18) along with hydrodynamic force and torque constraints (4.6) for solid cores provides a complete set of algebraic equations for determining the motion of solid cores and free surface. The integral equation (4.18) can not be solved uniquely when $\mathbf{x_0}$ is located on any of the solid-liquid interfaces. To render the solution of equation unique, we employ a purely mathematical approach [68, 99] to remove multiple eigenfunction of the single-layer operator at the solid-liquid interface by adding a deflating term. After deflating following integral equation is obtained.

$$\begin{aligned} cu_j^D(\mathbf{x_0}) = &-\frac{1}{4\pi\mu}\int_{\Gamma_0} f_i^D(\mathbf{x})G_{ij}(\mathbf{x},\mathbf{x_0})dl(\mathbf{x}) + \frac{1}{4\pi}\int_{\Gamma_0} u_i^D(\mathbf{x})T_{ijk}(\mathbf{x},\mathbf{x_0})n_k(\mathbf{x})dl(\mathbf{x}) \\ &-\frac{1}{4\pi\mu}\sum_{a=1}^{2}\int_{\Gamma_a} f_i(\mathbf{x})G_{ij}(\mathbf{x},\mathbf{x_0})dl(\mathbf{x}) - 2\left(c-\frac{1}{2}\right)n_j(\mathbf{x_0})\left[\int_{\Gamma_m} f_i(\mathbf{x})n_i(\mathbf{x})dl(\mathbf{x}) - b_m\right], \end{aligned} \tag{4.19}$$

where

$$\Gamma_m = \begin{cases} \Gamma_1 & \text{if } \mathbf{x_0} \in \Gamma_1 \\ \Gamma_2 & \text{if } \mathbf{x_0} \in \Gamma_2 \ , \end{cases}$$

b_m is an arbitrary constant and the term $2(c-\frac{1}{2})$ is multiplied to deflation term to ensure that it vanishes when $\mathbf{x_0}$ lies on free surface.

4.2.3 Numerical implementation

Implementing boundary element method involves setting up a system of linear algebraic equations. This is achieved by discretizing the boundary of the computational domain with a collection of boundary elements and subsequently approximating the integrals over the domain boundary with the sum of integrals over the boundary elements. A system of linear equations is obtained by ensuring that the boundary integral equation (4.19) is satisfied at the mid-point of each element along with the integral constraints given by equation (4.6). The set of linear equations can be solved by using matrix inversion.

Once the velocities of solid particles and that of free surface are obtained, the new positions of cores and free surface for next time step is updated using a simple Euler discretization scheme for Eq. (4.8).

$$\mathbf{x}(t + \Delta t) = \mathbf{x}(t) + \Delta t \mathbf{u} \cdot \tag{4.20}$$

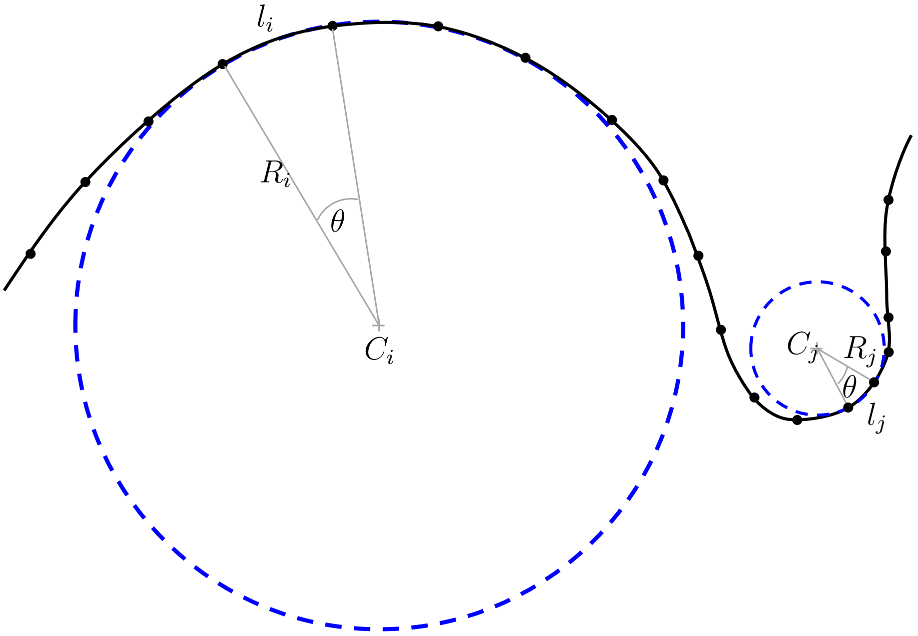

Figure 4.2 Node distribution depending on boundary curvature

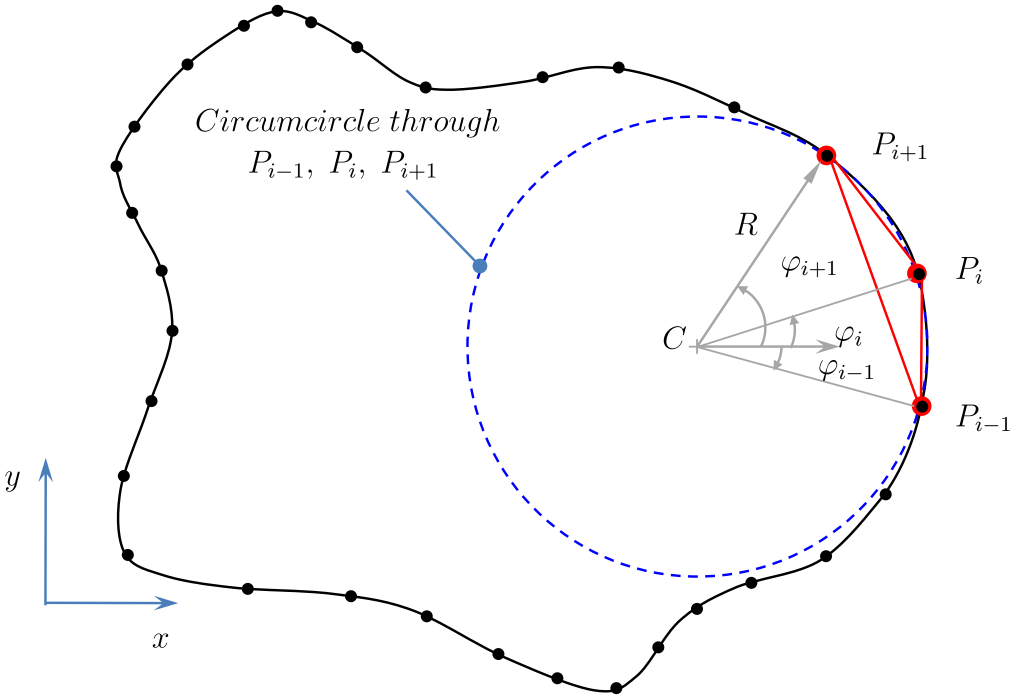

Figure 4.3 Approximation of domain boundary using circular arcs

4.2.3.1 Mesh optimization and node redistribution

The new location of boundary nodes obtained after boundary displacement requires frequent redistribution especially in the neck region, since a optimal distribution of boundary nodes is needed to ensure accurate evaluation of curvature. Mesh redistribution algorithm used in [123], which is based on equidistribution of curvature, is fairly complicated and requires many input constrains. It is found that by properly devising the mesh redistribution scheme and redistribution criterion, considerable simplification can be obtained with improved accuracy in calculation of surface normal vectors and curvature [54]. For optimum distribution of node points on the boundary the nodes have to be closely spaced in the regions of high curvature and have to be spaced relatively far apart when curvature of the boundary is low. The arc length is denoted by l and local radius of curvature of the boundary arc by R_K. Assuming the boundary arc to be circular, the arc length l can be computed as (see Fig. 4.2)

$$l = \theta R_K \ , \tag{4.21}$$

where θ is the angle subtended by the arc at center of circle. If the circular arcs are used to represent domain boundary, then the value of θ can serve as an ideal criterion for determining node spacing along the boundary curve. If θ is kept within a predefined limits, the arc length l will vary depending on R_K (see Eq. (4.21)). The idea is to represent each triplet of nodes with a circular arc [54, 99] and then to use θ to redistribute nodes along that circular arc. For three successive non-collinear nodes P_{i-1}, P_i, P_{i+1} on the boundary, we can identify a circular curve passing through them using simple geometrical concept of circumcircle of a triangle formed by three points (see Fig. 4.3). Using a local polar coordinate system with origin at the center of identified circumcircle, the nodal points are redistributed by adding a new point or removing an existing point on the circular curve so as to ensure that angle θ subtended by adjacent node pair is always within the predetermined limits, i.e.

$$\begin{aligned} \theta_{min} &\leqslant \theta_i \leqslant \theta_{max} \ , \\ \theta_i &= \varphi_{i+1} - \varphi_i \quad \text{for } i = 1 \text{ to } N \ , \end{aligned}$$

where φ is the polar angle subtended by the boundary point in the local coordinate system and N is total number of nodes on the closed boundary. The curvature and unit normal vector at any point on that curve are obtained directly as

$$\begin{aligned} K_i &= \frac{1}{R_{Ki}} \ , \\ \hat{\mathbf{n}}_i &= (\cos\varphi_i, \sin\varphi_i) \ . \end{aligned}$$

If $\theta_i > \theta_{max}$, then a new point is added at the center of circular arc between the nodes P_{i+1} and P_i, on the other hand if $\theta_i < \theta_{min}$ then the point P_i is removed from the circular arc.

4.2.3.2 Calculating the nodal velocity

The resultant interface velocity and direction of normal vector at the common end point shared by two adjacent boundary elements is obtained by vector addition of normal velocities at each element as shown in Fig. 4.4. Unlike weighted averaging approach commonly employed to determine the normal vector and the velocity at the element end points, this novel method is physically realistic and accurate. The resulting velocity vector at each of the element end points is given by

$$
\begin{aligned}
\vec{\mathbf{v}}_{res} &= \vec{\mathbf{a}} + \vec{\mathbf{b}}, \\
|\vec{\mathbf{a}}| &= \frac{|\vec{\mathbf{v}}_n^{(i)}|}{\cos\theta}, \\
|\vec{\mathbf{b}}| &= \frac{|\vec{\mathbf{v}}_n^{(i-1)}|}{\cos\theta}, \\
\theta &= (\angle(AOB) - 90^o)\cdot
\end{aligned}
$$

In physical sense this resulting velocity vector (see Fig. 4.4.) exactly corresponds to the new position of the common end point of the adjacent boundary elements when they move with their respective normal velocities. The predicted locations of a corner node by two methods are compared in Fig. 4.5. The averaging method lead to significant deviation from the correct position, especially when elements represent sharp corners or when the normal velocities of adjacent elements differ significantly. The vector addition method is applicable for all cases except when the $\angle(AOB) = 180^o$, when the direction of the normal vector at common end point is same as that of elements and magnitude can be obtained by averaging.

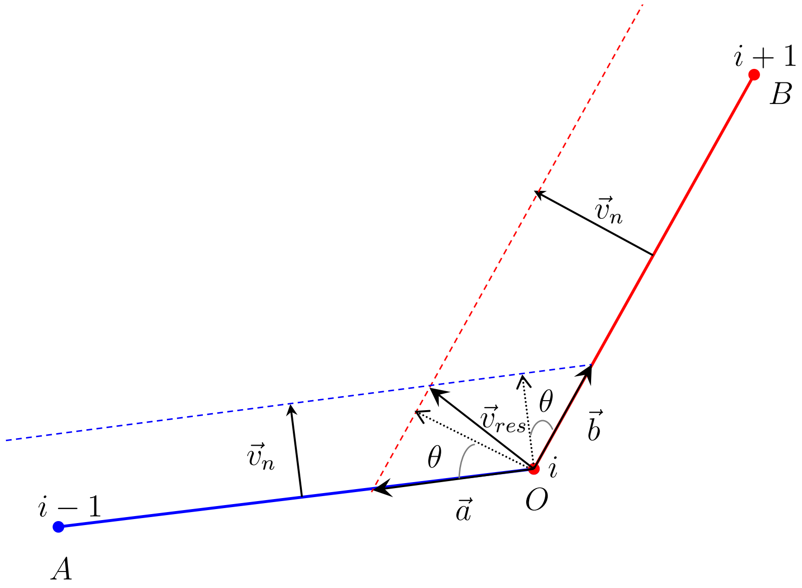

Figure 4.4 Resultant velocity vector at the end points of a boundary element

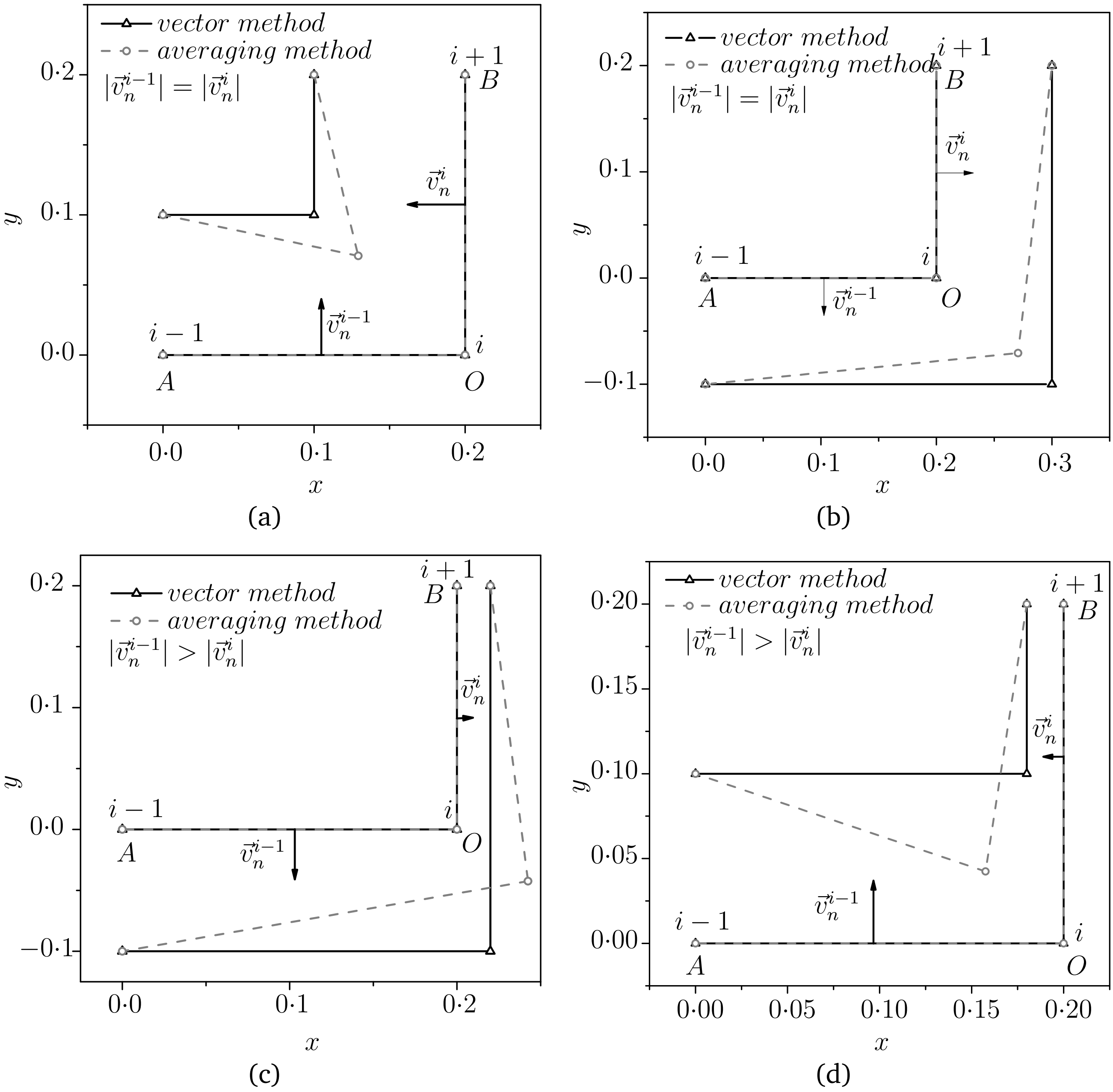

Figure 4.5 Comparison of vector addition method and averaging method for different configurations

4.2.4 Validation

The accuracy of the numerical method employed is checked by comparing numerical results with analytical solutions available in literature. Comparison of neck radius evolution for viscous sintering of two equal completely viscous cylinders is shown in Fig 4.6. The results of boundary element solution agree well with the analytical solution of [55] for the neck radius. A validation case for a domain having multiple boundary is illustrated in Fig. 4.7. It shows the shrinkage of circular disk with a circular hole at the center. Numerically computed evolution of inner and outer radius agrees well with the analytical solution [122].

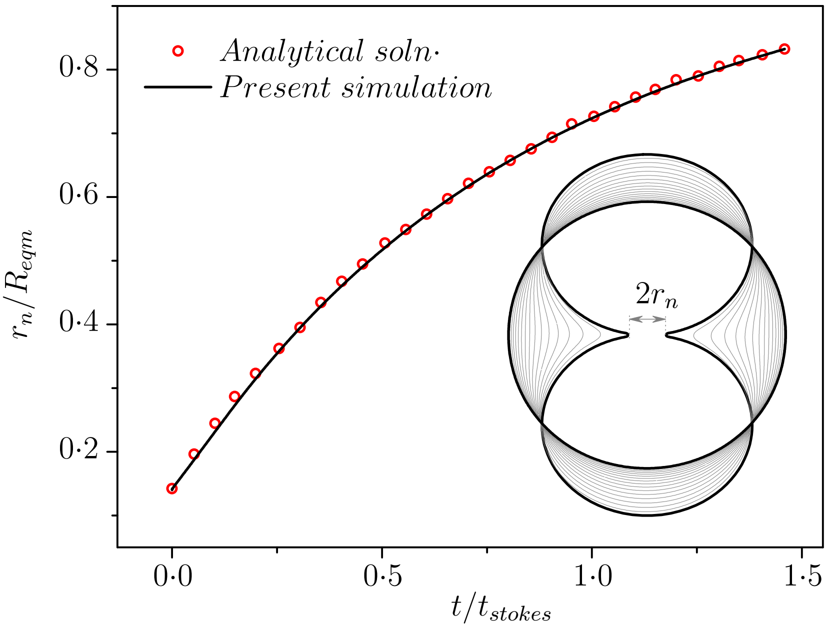

Figure 4.6 Comparison of boundary element solution with the analytical solution of Hopper [55].

Numerical experiments have been performed to check the grid dependency of the solution. Grid refinement was carried out for the representative case of sintering of two equal cylinders. Figure 4.8 shows neck radius evolution for numerical solutions obtained using four different total numbers of boundary elements along the domain boundary. It is clearly visible that numerical solution is converging to analytical solution with grid refinement.

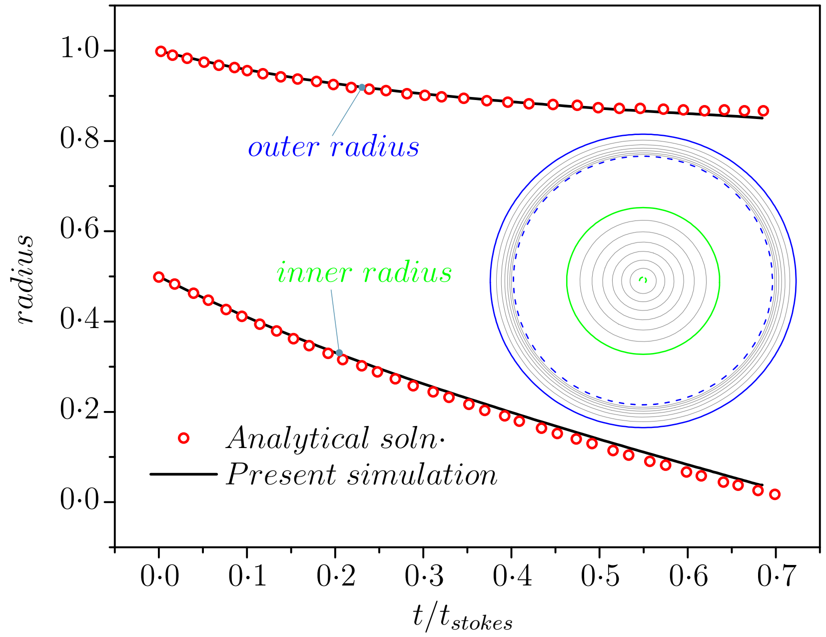

Figure 4.7 Variation of inner and outer radius with time during shrinkage of circular disc having hole at the center.

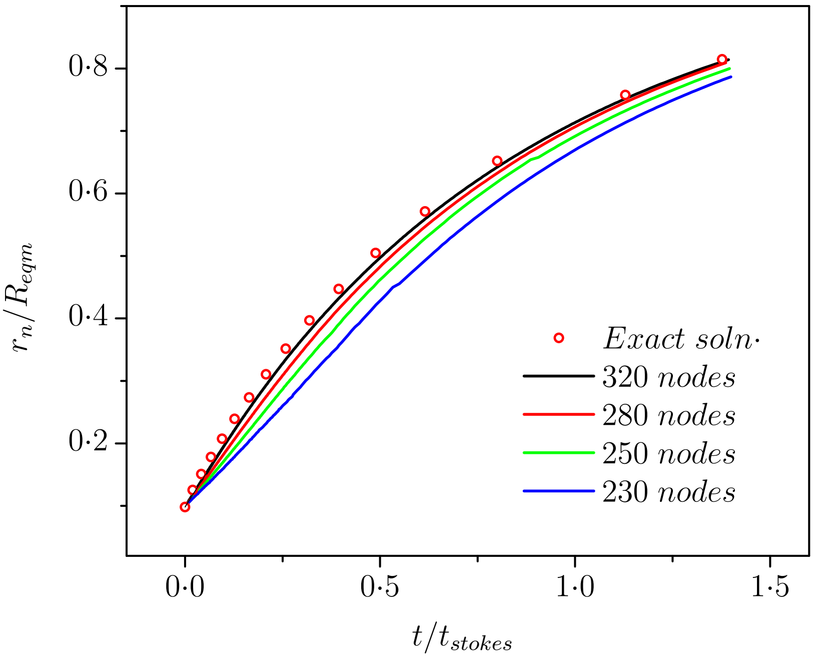

Figure 4.8 Convergence of numerical solution to exact solution with increasing number of nodes.

4.3 Simultaneous heat transfer, phase change and coalescence

The isothermal coalescence model is further extended in this section to include the variation of core size depending on heat transfer and phase change. Therefore, the problem now involves a free surface Γ_o evolving under the action of surface tension forces and solid-liquid interfaces $\Gamma_{1,2}$ moving due to phase change (see Fig. 4.1).

The energy balance for solid and liquid phases are solved separately with interface temperature being at the melting point. The interfacial velocity during phase change is obtained using Stefan condition at the interface. Based on the derivation of laser source term for our earlier model for heat transfer in single model in Section 3.4.4, thermal boundary condition at the particle-gas interface is specified as heat flux boundary. Since it is found that - owing to small optical penetration - the volumetric heat source due to laser is negligible in the whole particle except for a very thin later near the particle surface. Consequently the laser source can also be modelled as heat flux on the particle surface while maintaining the same accuracy.

4.3.1 Mathematical model

The governing differential equation for heat transfer in a material with constant properties in the absence of heat generation has the following form:

$$\nabla^2 T_s(\mathbf{x},t) = \frac{1}{\kappa_s}\frac{\partial T_s(\mathbf{x},t)}{\partial t}\ , \qquad \mathbf{x} \in \Omega_s(t)\ , \tag{4.22}$$

$$\nabla^2 T_l(\mathbf{x},t) = \frac{1}{\kappa_l}\frac{\partial T_l(\mathbf{x},t)}{\partial t}\ , \qquad \mathbf{x} \in \Omega_l(t)\ , \tag{4.23}$$

where the subscripts s and l refer to the solid and liquid phases respectively and κ denotes the thermal diffusivity. It should be noted that the heat transfer in a liquid phase is described by a heat conduction equation. The heat convection is negligible, since the creeping flow in a viscous metal melt is characterized by a low Reynolds number. Moreover, the Prandtl number of molten metals is usually very low. As a result, the Peclet number, which is a product of the Reynolds number and the Prandtl number, is very low. The Peclet number characterizes the ratio between the heat transport by convection and the heat transport by conduction. If this ratio is small, the convective terms of the energy equation can be neglected.

Other conditions required to define the thermal problem completely are given by the following equations:

$$T(\mathbf{x}, 0) = T_0 \ , \tag{4.24}$$

$$\lambda \frac{\partial T(\mathbf{x}, t)}{\partial n} = q(\mathbf{x}, t) \ , \qquad \mathbf{x} \in \Gamma_o \ , \tag{4.25}$$

$$T(\mathbf{x}, t) = T_{mp} \ , \qquad \mathbf{x} \in \Gamma_{1,2} \ , \tag{4.26}$$

where T_0 and T_{mp} are initial temperature and melting point temperature of the particles, respectively, and q is the prescribed time-dependent heat flux at the particle surface. The Stefan condition at the solid-liquid interface leads to the following relation between heat flux and normal velocity of the interface:

$$\lambda_l \frac{\partial T_l(\mathbf{x}, t)}{\partial n_l} - \lambda_s \frac{\partial T_s(\mathbf{x}, t)}{\partial n_l} = \rho_s H_f v_n \ , \qquad \mathbf{x} \in \Gamma_{1,2} \ , \tag{4.27}$$

for melting or

$$\lambda_s \frac{\partial T_s(\mathbf{x}, t)}{\partial n_s} - \lambda_l \frac{\partial T_l(\mathbf{x}, t)}{\partial n_s} = \rho_l H_f v_n \ , \qquad \mathbf{x} \in \Gamma_{1,2} \ , \tag{4.28}$$

for resolidification, where λ_s, λ_l denote thermal conductivities of solid and liquid phase, respectively, and ρ_s, ρ_l are the densities of respective phases, H_f is the enthalpy of fusion, and v_n is the normal velocity of the interface. The time evolution of the interface is obtained from the velocity v_n as

$$\frac{d\mathbf{x}(t)}{dt} \cdot \hat{\mathbf{n}} = v_n \ , \qquad \mathbf{x} \in \Gamma_{1,2} \ , \tag{4.29}$$

where $\hat{\mathbf{n}}$ is unit normal vector at the solid-liquid interface pointing outward from the solid region. The first part of problem involving heat transfer and phase change is complete by solving equations (4.22-4.29) for interface velocity and temperature field.

4.3.2 Boundary element formulation

This section represents the brief outline of the method employed to derive the final integral equations for transient heat transfer problem. The basic equations governing heat transfer for both phases are linear. However, the problem is inherently nonlinear due to the presence of the moving interface. Using the fundamental solution of Laplace equation and reciprocal identity, the transient heat transfer equation is formulated in the integral form as:

$$cT(\mathbf{x_0},t) = \iint_{\Omega} \frac{1}{\kappa} G(\mathbf{x},\mathbf{x_0}) \frac{\partial T(\mathbf{x},t)}{\partial t} dxdy + \int_{\Gamma} T(\mathbf{x},t) \frac{\partial G(\mathbf{x},\mathbf{x_0})}{\partial n} dl(\mathbf{x}) - \int_{\Gamma} G(\mathbf{x},\mathbf{x_0}) \frac{\partial T(\mathbf{x},t)}{\partial n} dl(\mathbf{x}) \ , \tag{4.30}$$

where $\mathbf{x_0} \in (\Omega \cup \Gamma)$, $G(\mathbf{x},\mathbf{x_0})$ is fundamental solution of Laplace equation [4] and

$$c = \begin{cases} 1 & \text{if } \mathbf{x_0} \in \Omega \ , \\ \frac{1}{2} & \text{if } \mathbf{x_0} \in \Gamma \ , \\ 0 & \text{otherwise} \ \cdot \end{cases}$$

Equation (4.30) contains line integral terms and domain integral term. In order to avoid discretizing the whole domain into small elements, dual-reciprocity method (DRBEM) [4, 12] is used. The main idea of the dual reciprocity method is to approximate the domain integral term by using a radial basis function $f_r = 1 + r$. It is a function of radial distance between the source point $\mathbf{x_0}$ and the field point $\mathbf{x}$. The transient term appearing under the domain integral can be approximated as

$$\frac{1}{\kappa} \frac{\partial T(\mathbf{x_i},t)}{\partial t} \approx \sum_{m=1}^{N+N_L} \beta_m f_r(\mathbf{x_i},\mathbf{x_m}) \ , \tag{4.31}$$

where N is number of collocation points on the domain boundary and N_L is the number of internal nodes points in the domain. The coefficients β_m have to be determined by generating a system of equations from Eq. (4.31) for $i = 1$ to $N + N_L$. Therefore,

$$\begin{bmatrix} \beta_1 \\ \cdot \\ \beta_m \\ \cdot \\ \beta_{N+N_L} \end{bmatrix} = \begin{bmatrix} \\ \\ f_r(\mathbf{x_i},\mathbf{x_m}) \\ \\ \\ \end{bmatrix}^{-1} \begin{bmatrix} \\ \\ \frac{1}{\alpha}\frac{\partial T(\mathbf{x_i},t)}{\partial t} \\ \\ \\ \end{bmatrix} \cdot$$

A new function $\chi(\mathbf{x},\mathbf{x_0})$ satisfying the equation is now introduced

$$\nabla^2 \chi(\mathbf{x},\mathbf{x_0}) = f_r(\mathbf{x},\mathbf{x_0}) \ \cdot \tag{4.32}$$

Using the reciprocal identity and Eqs. (4.30-4.32), the final integral equation is obtained as:

$$\begin{aligned} cT(\mathbf{x_0},t) = \sum_{m=1}^{N+N_L} \beta_m \Bigg[& c\chi(\mathbf{x_0},\mathbf{x_m}) + \\ & \int_\Gamma \left\{ G(\mathbf{x},\mathbf{x_0}) \frac{\partial \chi(\mathbf{x},\mathbf{x_m})}{\partial n} - \right. \\ & \left. \chi(\mathbf{x},\mathbf{x_m}) \frac{\partial G(\mathbf{x},\mathbf{x_0})}{\partial n} \right\} dl(\mathbf{x}) \Bigg] + \\ & \int_\Gamma T(\mathbf{x},t) \frac{\partial G(\mathbf{x},\mathbf{x_0})}{\partial n} dl(\mathbf{x}) - \\ & \int_\Gamma G(\mathbf{x},\mathbf{x_0}) \frac{\partial T(\mathbf{x},t)}{\partial n} dl(\mathbf{x}) \end{aligned} \tag{4.33}$$

for $\mathbf{x_0} \in (\Omega \cup \Gamma)$. The final integral equation does not contain any domain integral term. Instead there are some collocation points in the domain in addition to boundary collocation points.

4.3.3 Numerical implementation

As explained before, integral equations for the domain boundary are transformed to a system of linear algebraic equations for solving them numerically. This is achieved by discretizing the boundary of the computational domain with a collection of boundary elements and subsequently approximating the integrals over the domain boundary with the sum of integrals over the boundary elements. Ensuring that the boundary integral equation (4.33) is satisfied at the mid-point of each element along with the boundary conditions. A system of linear equations is obtained which can be solved by using matrix inversion. The discretized form of final integral equation (4.33) for transient heat transfer in the solid and liquid phases is given by

$$\begin{aligned} cT(\mathbf{x_0},t) = \sum_{m=1}^{N+N_L} \beta_m \Bigg[& c\chi(\mathbf{x_0},\mathbf{x_m}) + \\ & \sum_{a=1}^{N} \int_{E_a} \left\{ G(\mathbf{x},\mathbf{x_0}) \frac{\partial \chi(\mathbf{x},\mathbf{x_m})}{\partial n} - \right. \\ & \left. \chi(\mathbf{x},\mathbf{x_m}) \frac{\partial G(\mathbf{x},\mathbf{x_0})}{\partial n} \right\} dl(\mathbf{x}) \Bigg] + \\ & \sum_{a=1}^{N} \int_{E_a} T(\mathbf{x},t) \frac{\partial G(\mathbf{x},\mathbf{x_0})}{\partial n} dl(\mathbf{x}) - \\ & \sum_{a=1}^{N} \int_{E_a} G(\mathbf{x},\mathbf{x_0}) \frac{\partial T(\mathbf{x},t)}{\partial n} dl(\mathbf{x}), \end{aligned} \tag{4.34}$$

where E_a denotes a boundary element and the coefficients β_m is expressed as a function of time derivative term of the governing equation as shown in Section 4.3.2. Approximating the temperature time derivative during a time step by central difference scheme and approximating the temperature as an average value between the temperature at the time instant $t - \Delta t/2$ and $t + \Delta t/2$ as

$$T(\mathbf{x}, t) \approx \frac{T(\mathbf{x}, t + \frac{\Delta t}{2}) + T(\mathbf{x}, t - \frac{\Delta t}{2})}{2} \tag{4.35}$$

and

$$\frac{T(\mathbf{x}, t)}{dt} \approx \frac{T(\mathbf{x}, t + \frac{\Delta t}{2}) - T(\mathbf{x}, t - \frac{\Delta t}{2})}{\Delta t}, \tag{4.36}$$

where Δt is the time step size, one can solve the final set of linear equations containing $N + N_L$ unknowns for consecutive time levels are solved starting from the initial conditions.

The solution of heat transfer equations at every time step along with Eqs. (4.27, 4.28) determines the interface velocity due to phase change, which in turn governs the solid core size of the melting or solidifying particles. Having known the size of solid cores, the solution of hydrodynamic problem is used to update new positions of cores and the free surface for next time step.

4.3.4 Solution algorithm

The following solution algorithm has been adopted to solve the coalescence problem:

1. Solve the transient energy equation subject to initial and boundary conditions till the surface temperature equals the melting temperature.
2. As the surface temperature reaches the melting temperature, the following actions have to be performed at each time step:
    (a) Based on the solution of energy equation, determine the solid-liquid interface velocity using a predictor-corrector iterative algorithm as employed by [128].
    (b) Update the position of solid-liquid interface and redefine the solid and liquid domains separated by an interface
    (c) Solve the hydrodynamic part of the problem to determine the final positions of solid cores and free surface
    (d) Redistribute the boundary nodes to achieve the optimal density of the nodes corresponding to local interface curvature
    (e) Solve the energy equation for the new node distribution

The computer implementation of boundary element models and solution algorithm are done using Fortran 90 for Windows/Linux platforms using Intel Fortran compiler.

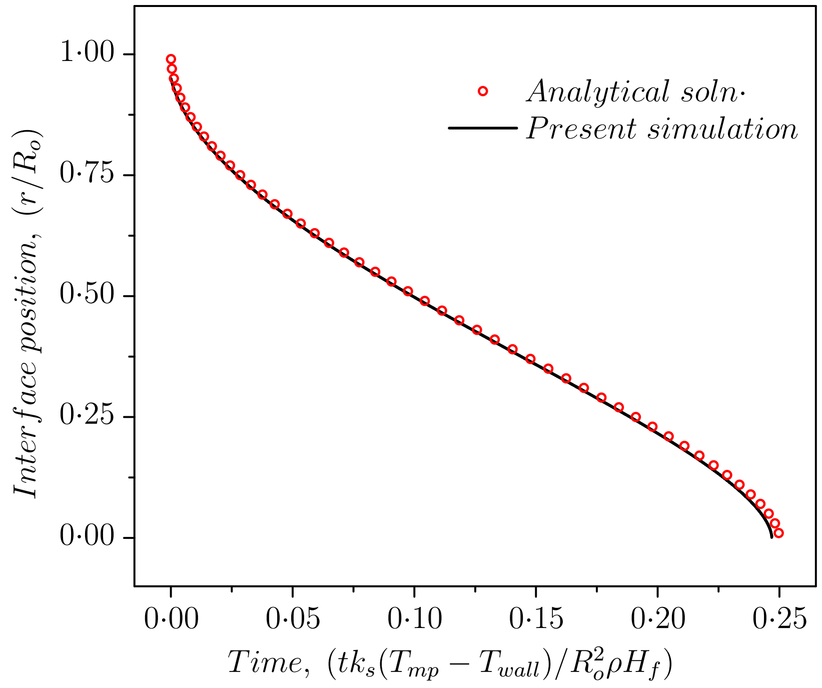

Figure 4.9 Comparison of interface position during solidification of a molten cylinder of outer radius R_o

4.3.5 Validation

The validation of numerical scheme for solution of heat transfer and phase change is illustrated in Fig. 4.9. This figure shows the DRBEM solution compared against the analytical solution [113] for position of solid-liquid interface during solidification of molten cylinder initially maintained at melting temperature (T_{mp}). The cylinder boundary is subjected to constant wall temperature and the heat capacity of the material is assumed to be very small with respect to the enthalpy of fusion. It is assumed that the thermal diffusivity of the liquid and solid phases are equal to each other: $\kappa_s = \kappa_l = \kappa$. It is clearly seen from Fig. 4.9 that the agreement between the simulated results and the analytical solution [113] is very good.

5

Results and discussion

5.1 Introduction

In this chapter, the developed heat transfer and coalescence models in the previous chapters are used to simulate the physical phenomena during laser sintering. The whole chapter is structured into three parts. The first part includes generating the geometric model of a powder bed of required packing parameters, followed by investigating energy absorption characteristics and heat transfer in the powder bed subjected to moving laser source. The predicted results are compared with measurements from experiments. In part two thermal behaviour of single particle in the powder bed is described. Finally the coupled heat transfer and coalescence of two representative particles is described in last part.

5.2 Packing characteristics

Granular powder is raw material for laser sintering. Isothermal powder bed represents the initial condition of powder during sintering. Final sintered product is invariably affected by the packing characteristics. The properties of granular material are significantly different from that of the corresponding bulk material. Making an assessment of its properties is difficult and generally approximate, mostly focussed on mean behaviour of bed with very little or no consideration to local variation. The complexity introduced by multitude of factors influencing bed characteristics is such that, there is no formal mathematical model (analytical approach) to define a physical packing itself [94]. Nevertheless, computer simulations can be used as

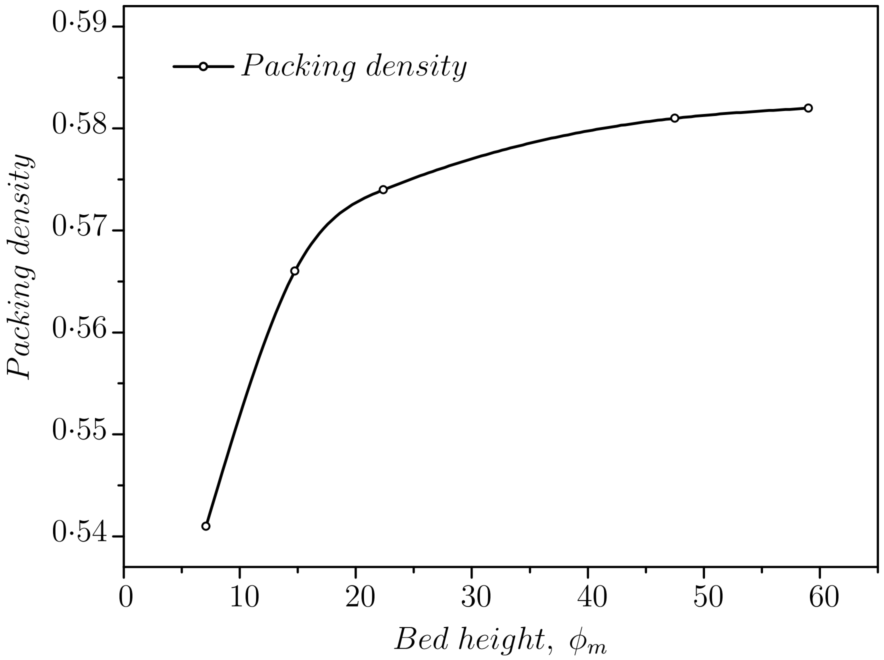

Figure 5.1 Variation of packing density with bed height

statistical means to predict properties of granular material. A detailed overview of required powder characteristics with respect to laser sintering is given in [66].

In the following sections we report the results of simulations of the bed geometry using the method described in Section 3.2. The mean packing characteristics and effective bed properties for simulated powder beds are presented.

5.2.1 Mean packing parameters

The influence of bounding walls on the packing structure of granular bed is widely known [44, 46, 112]. For small packing structures having bed dimensions of few mean diameters, the confining boundaries have strong influence on the simulated packing. In order to minimize this effect as well as to prevent variation due to inconsistent geometric ratios and bed dimensions across simulated configurations, random packing of mono-dispersed powder is initially used to fix the bed dimensions. These dimensions are measured in terms of mean diameter (ϕ_m) of the powder grains in the bed.

A number of packings with increasing bed height are generated and corresponding bed parameters are plotted as shown in Fig. 5.1. It is seen that packing parameters hardly vary for bed depth above 35 particle diameters. The convergence of packing parameters with increasing bed depth may be attributed to decreasing influence of bottom wall on overall packing as the bed depth increases. Variation of local bed density with height is shown in Fig. 5.2. The local packing density at a given bed height is obtained by calculating the number of particles confined between two imaginary horizontal planes separated by a distance of one mean diameter. The large fluctuations observed near the bottom wall are due to the wall effect. Furthermore the

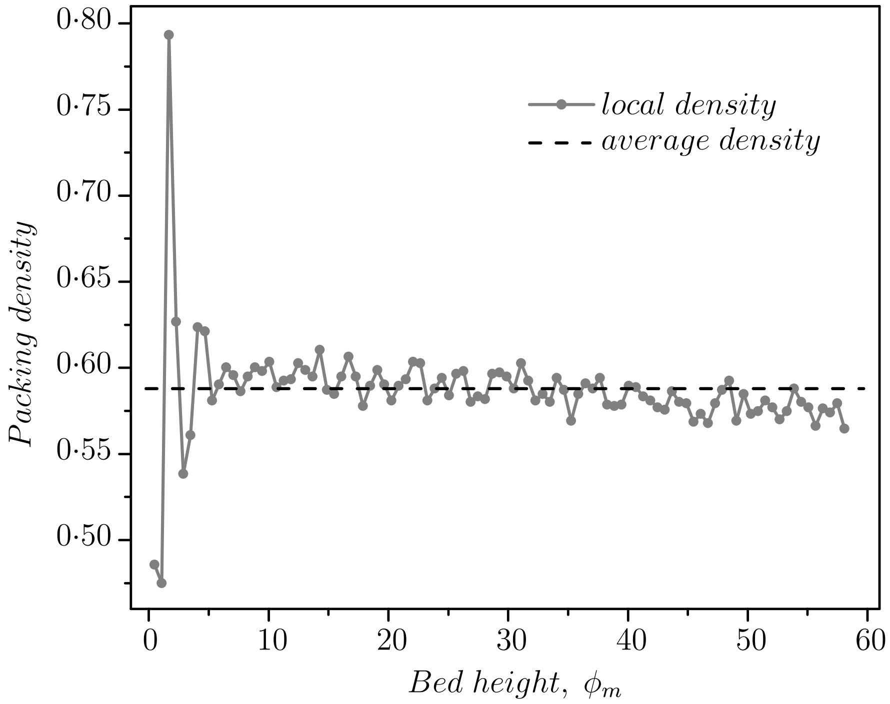

Figure 5.2 Local packing density variation along bed height

influence of vertical walls on the packed structure is minimised by imposing periodic conditions at vertical boundaries of the bed. After fixing bed dimensions same ratios of bed dimensions are then used to generate all other powder bed configurations. Even for obtaining shallow beds, the deep bed configuration is generated first and then levelling is used to achieve desired bed height.

Due to statistical nature of packing simulation, packing characteristics are expected to vary for every packed state. In order to check and quantify the repeatability of randomly generated bed, we have simulated a number of packings under similar set of input conditions while slightly varying the lateral dimensions (ideally variation of lateral dimensions should not alter packing structure due to periodic conditions) of bed. Table 5.1 shows packing parameters for five beds each having slightly different lateral dimensions of powder bed while other input parameters are kept the same. It is evident that variation of mean bed parameters for each configuration is within allowable statistical limits, the standard deviation in packing density for five samples of powder bed is $9{\cdot}22 \times 10^{-4}$ and for Coordination number the standard deviation is $0{\cdot}0244$. A typical sample statistics plots for a powder bed is also shown in Fig. 5.3. The results ensure the repeatability of simulated data.

In Table 5.2 the averaged value of packing density and coordination number obtained from these five simulations are further compared against the experimental and numerical results in literature for random loose packing of mono-dispersed powders. The average packing density of simulated assemblies is very close to values reported in literature. The average value of coordination number is close to the prediction method of Jodrey and Tory [63], and is interme-

Table 5.1 Mean packing parameters for randomly packed mono-dispersed beds

Bed dimensions $(L \times B)$, ϕ_m	Packing density	Coordination number
24×25	0.5767	5.9043
25×24	0.5769	5.9215
25×25	0.5766	5.9621
25×26	0.5783	5.9159
26×25	0.5785	5.9012

diate between the reported simulation values by Visscher and Bolsterli [125] and experiments of Bernal and Mason [9]. The observed variation in the cited values of coordination number can be attributed to lack of standard criterion for defining two particles in contact as well as lack of standard size of the packing assembly. When considering true contact between the particles, the computed value of mean coordination number for a packing assembly is 6.02. This value jumps to 6.62 on relaxing the contact criterion by considering particles within $1{\cdot}01 \times \left(\frac{\phi_1 + \phi_2}{2}\right)$ to be in contact. Figure 5.4 shows the histograms for number contacts between the particles depending upon the selected contact criterion. The distribution is found to shift towards higher coordination numbers with relaxed condition to qualify for contact. In this study we have considered only the true contact between the particles for computing coordination number. Finally a good agreement between simulation results and results from literature establish the validity of adopted method. In actual manufacturing the grain size distribution for a powder is non-uniform and generally granular systems are poly-dispersed having a Gaussian, log-normal

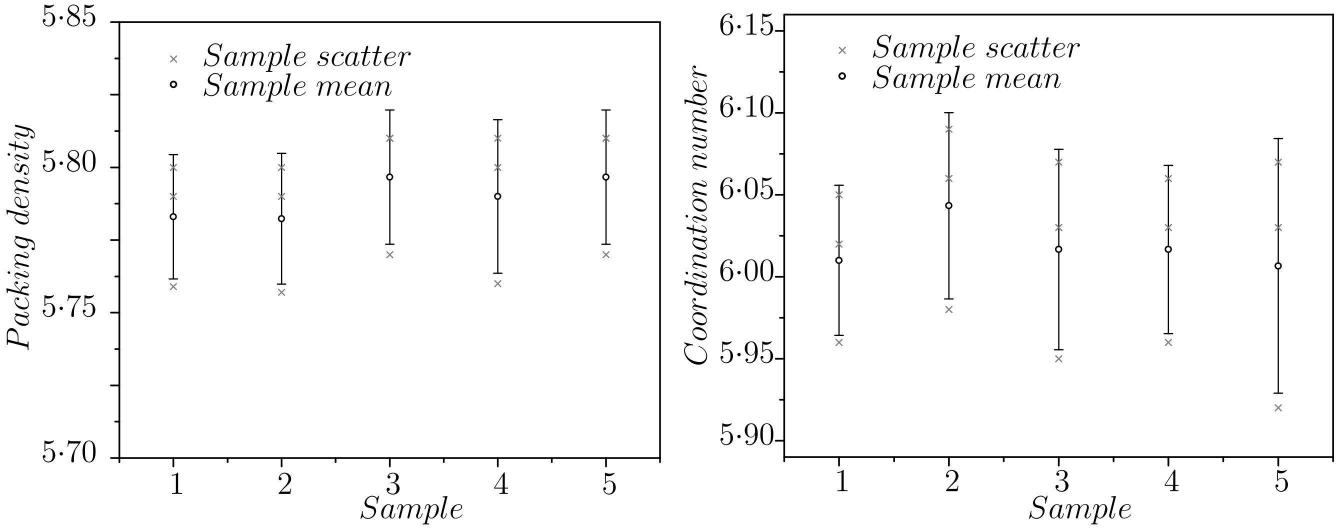

(a) (b)

Figure 5.3 Sample statistics for set of powder beds generated under similar conditions: (a) packing density; (b) coordination number

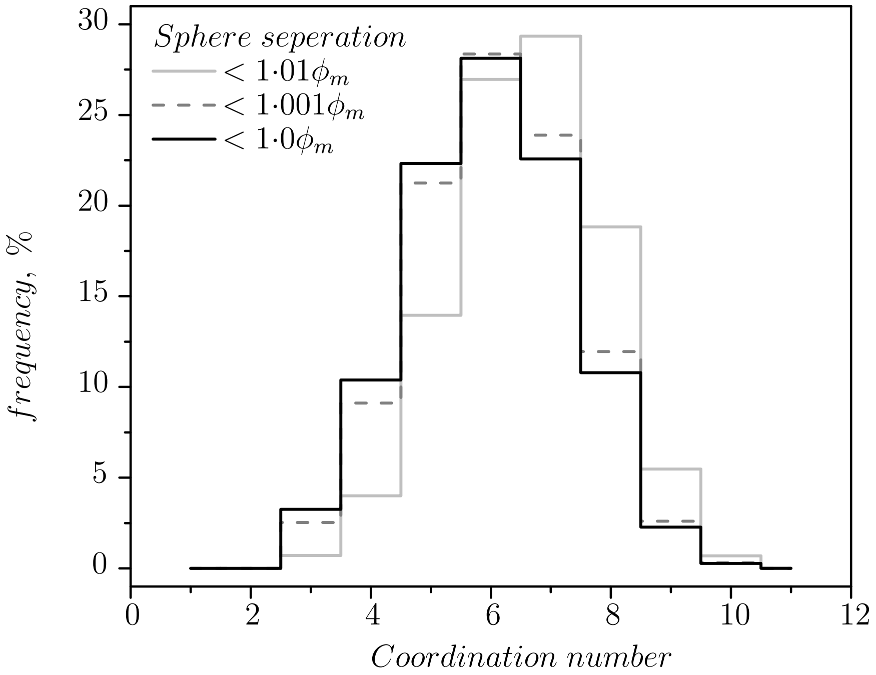

Figure 5.4 Variation in contact distribution based on selected contact criterion (frequency here represents percentage of particles of respective coordination number in the simulated bed)

Table 5.2 Comparison of simulated data with literature

	Packing density	Coordination number
Present simulation	0.5774±0.001	5.921±0.024
Jodrey and Tory [63]	0.59	6.001
Visscher and Bolsterli [125]	0.582	6.4
Bernal and Mason [9]	0.6	5.5

Table 5.3 Statistical details of a simulated bed

	Type	Size ratio (ϕ_{max}/ϕ_{min})	cov (SD/ϕ_m)	mean (μm)	mode (μm)
Desired distribution	Normal	2.0	0.1	30	30
Resulting distribution	Normal	1.99	0.095	29.6	29.4

or bimodal distribution. A poly-dispersed powder bed having Normal distribution of particles in the bed of are shown in Fig. 5.5 along with their size distribution plots. For the packing model being stochastic in nature, a quantitative comparison of descriptive statistics between the desired input distribution and resulting simulated distribution is presented in Table 5.3. The resulting size distribution of simulated bed is very close to the required input distribution.

The three commonly encountered powder bed configurations (see Table 5.4) are considered to investigate the influence of size distribution on random loose packing. The geometrical similarity is maintained across all the simulated configurations.

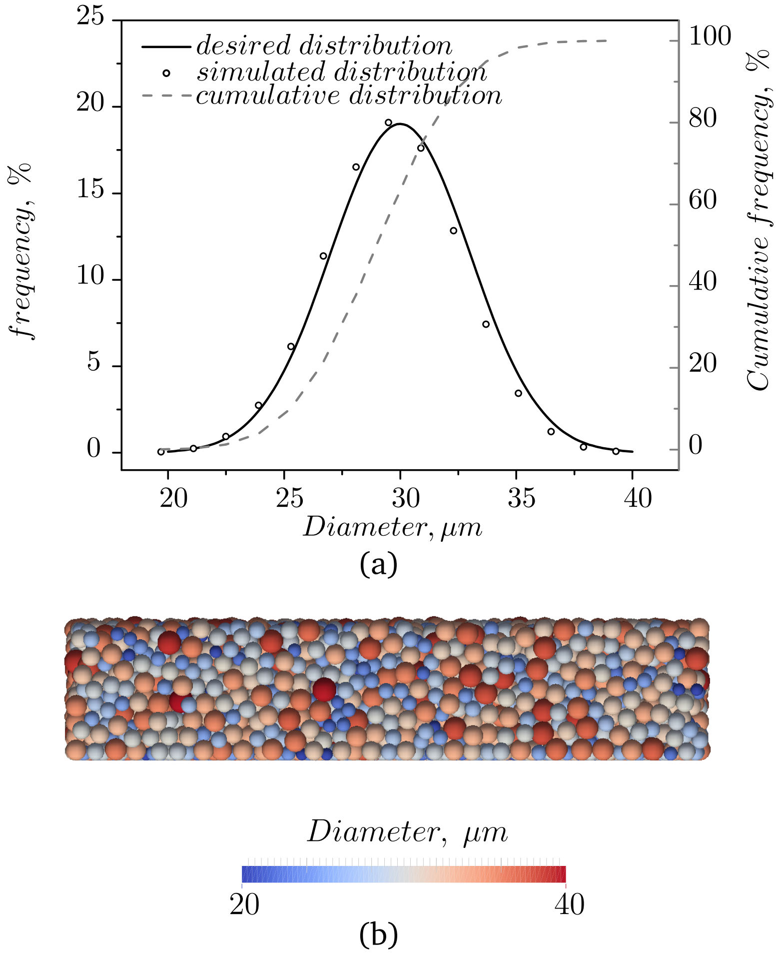

Figure 5.5 A poly-dispersed powder bed with Normal distribution of particles in the bed: (a) statistical size distribution of particles in the bed; (b) the levelled packed bed of corresponding size distribution

Table 5.4 Powder bed configurations

Type	Distribution	Mean grain size (μm)	Size ratio (ϕ_{max}/ϕ_{min})
Monodispersed	Uniform	15-45	1.0
Bidispersed	Uniform	30	1.5-3
Polydispersed	Normal	30	1.5-3

Monodispersed packing A mono-dispersed bed is the most simple packing assembly with randomly packed particles of uniform size. The only variable that can influence packing structure of a mono-dispersed bed is powder grain size. Figure 5.6(a) shows the variation of mean packing parameters with grain size. Any influence of powder grain size on packing structure is hardly evident due to lack of distinctly observable trend. This behaviour is common to other size distributions as well (see Fig. 5.6(b) and 5.6(c)), which is verified by simulating a number of poly-dispersed (Normal distribution) and bi-dispersed beds with varying mean grain size while maintaining their respective size distribution as well as size ratio fixed. The observed variation in mean packing parameters is less than 1% in response to a three times increase in grain size.

Thus a randomly packed loose structure is nearly independent of mean grain size for a given size distribution.

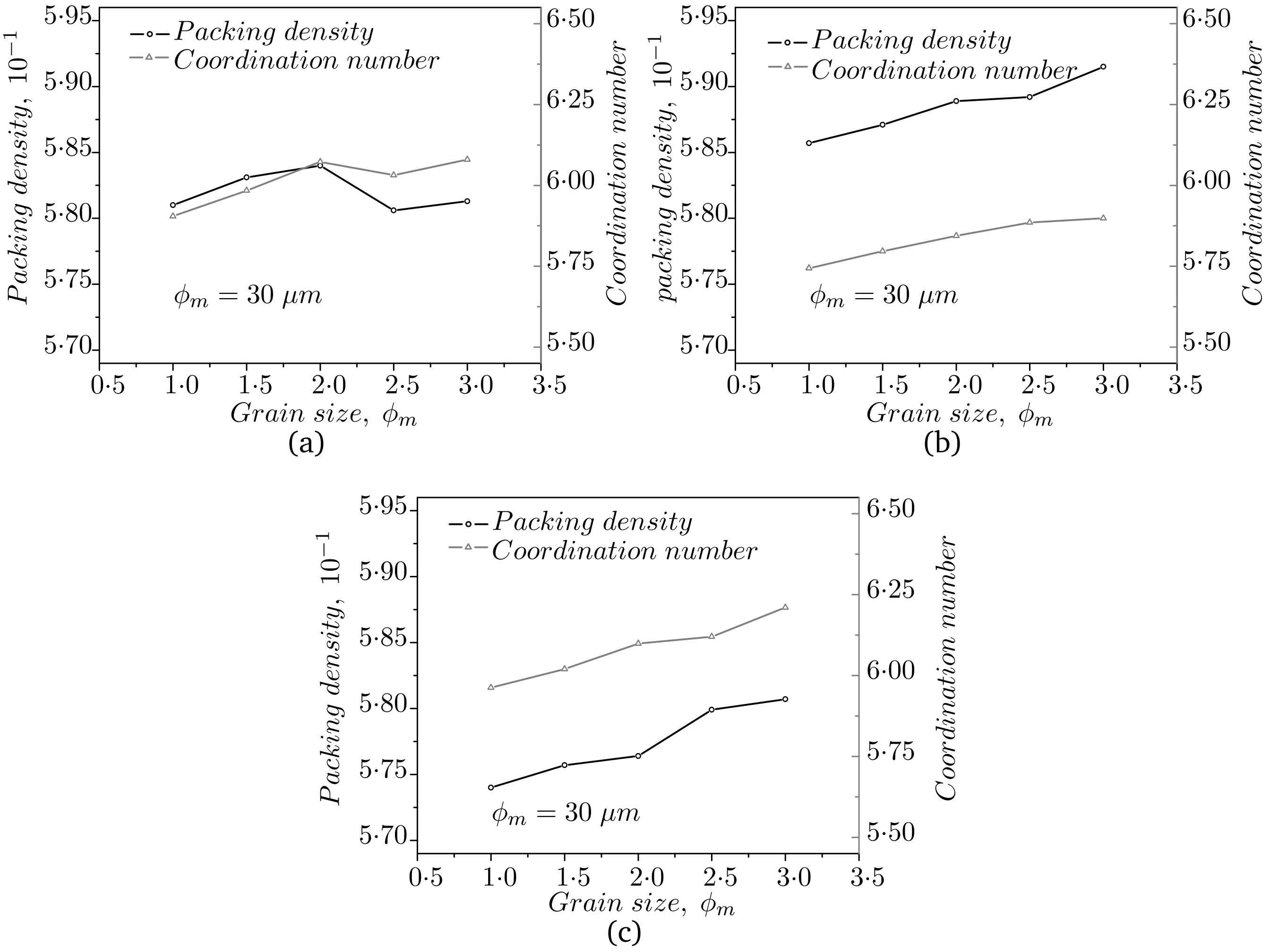

Figure 5.6 Influence of grain size on packing structure: (a) mono-dispersed bed; (b) bi-dispersed bed; (c) poly-dispersed bed;

Bidispersed packing A bi-dispersed granular system can be regarded as mixture of two different mono-dispersed configurations. The packing structure of thus generated configuration is governed by particle size ratio and the quantity of each size in the mixture. Thus a variety of resulting configurations can be obtained by varying either or both of size ratio and quantity of grains. Bi-dispersed packings are commonly recommended granular systems for powder based layer manufacturing [73]. Particularly for selective laser sintering, use of bi-dispersed powder limits occurrence of balling phenomenon to great extent [71]. Even for single component powder systems bi-dispersed configuration enables preferential melting of smaller sized powder grains. Table 5.5 lists the range of volume fraction and size ratio considered to investigate their influence on resulting packing structure. The packing density and coordination number for all

Table 5.5 Range of governing parameters for bi-dispersed powder bed

Volume fraction of small sized grains								
0.1	0.2	0.3	0.4	0.5	0.6	0.7	0.8	0.9

Size ratio (r_{max}/r_{min})			
1.5	2.0	2.5	3.0

the 36 combinations are plotted as shown in Fig. 5.7 and 5.8 respectively. Packing for a bidispersed bed is generally expected to be denser than monodispersed bed, because in an assembly of unequal particles, smaller particles tend to occupy the space between bigger particles. The simulated packing density is as per expectation for majority of size ratios and volume fractions. On the other hand predicted variation of coordination number is surprisingly different form established fact (for mono-dispersed beds) that coordination number of a packed bed relates directly to its packing density (dense packings produce higher coordination number). In fact, the simulated data are indicating an inverse relation between mean coordination number and packing density, contradicting the common intuition. The details of the dependencies shown are important for design of new systems and need to be discussed.

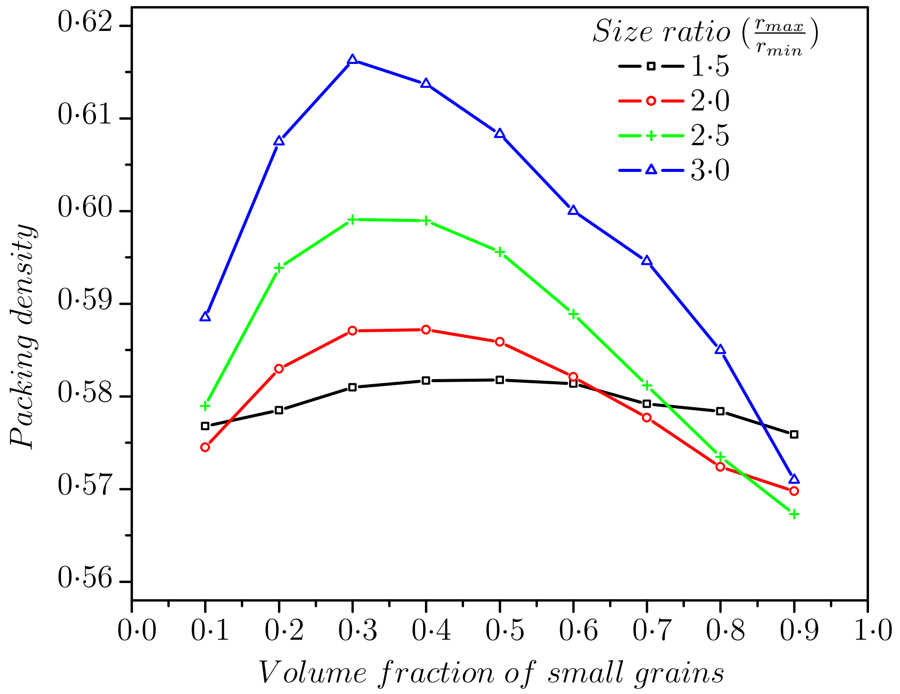

Figure 5.7 Dependence of packing density on volume fraction of smaller particles in a bi-dispersed bed

The observed variation of packing density with volume fraction follows an exclusive trend for all size ratios considered. With increasing concentration of small particles the packing density

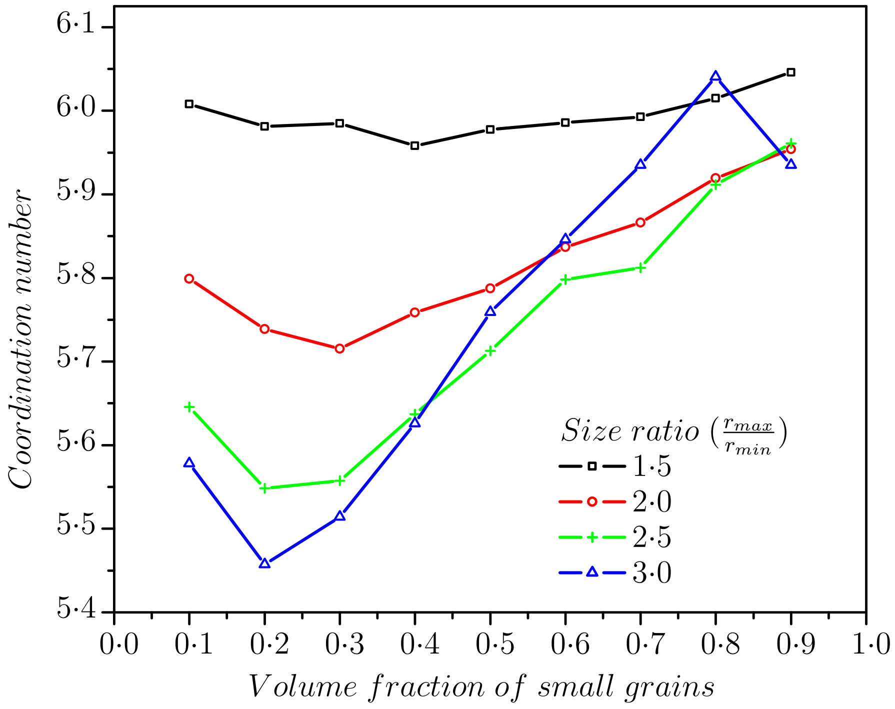

Figure 5.8 Dependence of coordination number in volume fraction of smaller particles in a bi-dispersed bed

first increases to maximum at volume fraction between 0.3 to 0.4, before decreasing to minimum for very high concentrations. Figure 5.9 provides an idea of changing spatial distribution of small and big particles with increasing concentration of small particles. The initial rise in packing density with concentration of small particles is due to growing instances of pore filling as well as clustering of small particles around bigger grains. For higher concentrations of small particles the relative influence of small particles alone increases since the pore filling is no more possible, and the instances of small particles clustering around big ones are relatively few in the a assembly. Besides this, bigger size ratios are found to yield higher packing density. For a poly-dispersed powder bed, it is important to recognise that multiple types of contacts (with

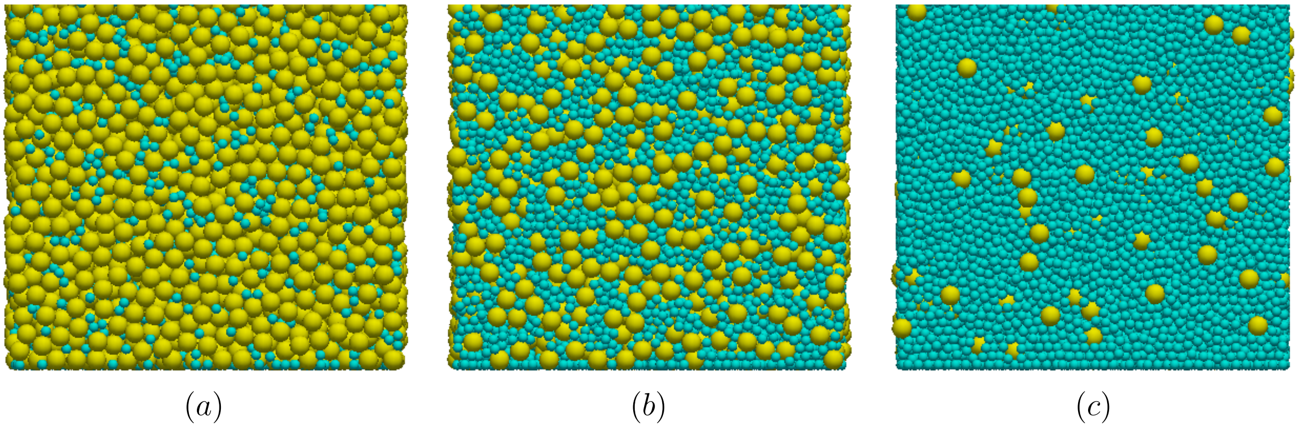

Figure 5.9 Spatial distribution of particles in a bidispersed bed of size ratio = 2.0 for increasing fraction of small sized component ((*a*) $volume\ farction = 0{\cdot}1$, (*b*) $volume\ farction = 0{\cdot}4$, (*c*) $volume\ farction = 0{\cdot}9$).

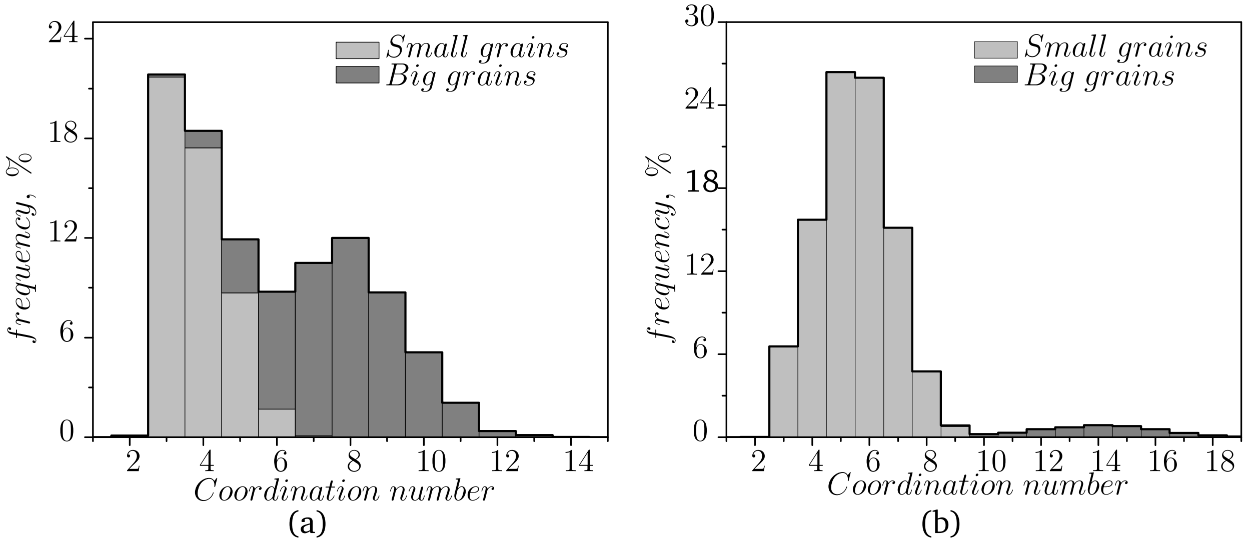

(a)

(b)

Figure 5.10 Contribution of each grain type towards contact distribution in a bi-dispersed bed: (a) volume fraction of small sized grains = 0.1, size ratio = 2.0, mean coordination number = 5.8; (b) volume fraction of small sized grains = 0.7, size ratio = 2.0, mean coordination number = 5.87

respect to size of particles in contact) exists in the assembly [95] and each of them contributes differently to packing depending on the size ratio of a contact pair as well as number of such pairs in the system. However, the existing method for calculating coordination number only account for total number of contacts per particle regardless of contact types, which renders it grossly misleading for poly-dispersed beds. (e.g. in case of bi-dispersed bed, when the packing is growing denser the calculated coordination number is found to decrease with increasing volume fraction of small particles (see Fig. 5.8)). This is further supported by histograms (see Fig. 5.10) indicating the distribution of contacts and relative contribution by each size. As compared to mono-dispersed bed the observed range for number of contacts per particle is significantly wider. This indicates the existence of two distinct modes dominated by coordination number for small particle and for big particle each. In a binary mixture of unequal particles, small particles will have fewer contacting particles as compared to that of big particles. This difference is clearly seen in the histograms. Furthermore, the influence of small particles on the overall coordination number tend to dominate with their growing number (see Fig. 5.10(b) and 5.11, where distribution of coordination number for different volume fractions of small particles is compared). Now returning back to coordination number it is desired to adopt a suitable weighing approach to properly account for different contact types depending on size of particles in contact [85]. This will ensure a meaningful relation between coordination number and packing density for bidispersed beds. A detailed study of various packing states is useful in designing material systems for selective laser sintering. The packing model and associated algorithms developed serve as necessary tool for design and analysis of new material systems for selective laser sintering.

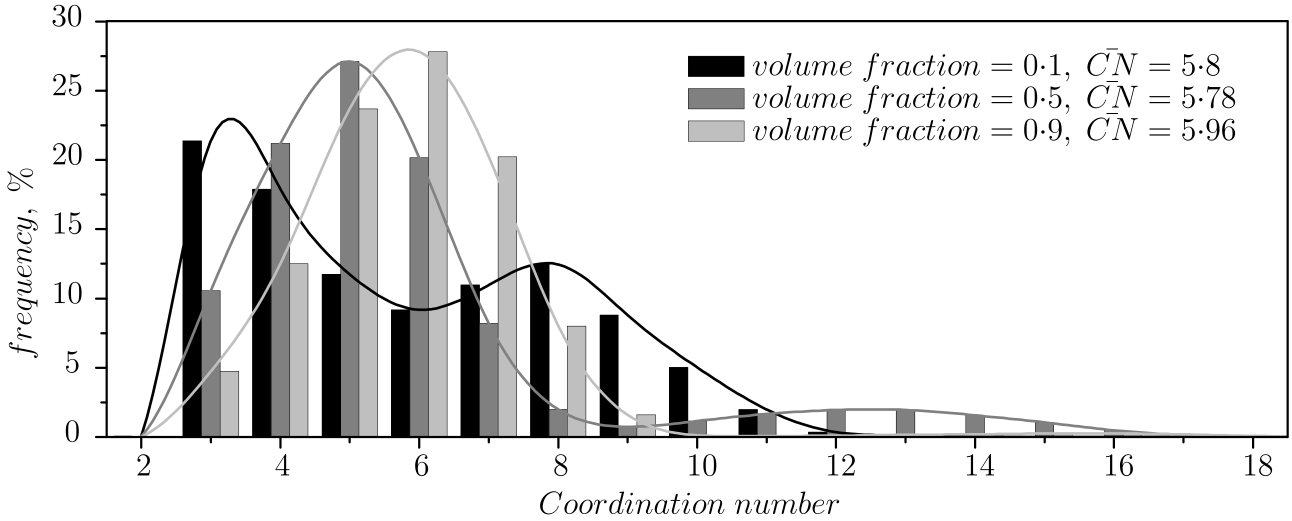

Figure 5.11 Variation of contact distribution with volume fraction of smaller particles for a bi-dispersed powder bed having size ratio = 2.0

5.3 Energy absorption and radiative properties of a granular bed

Here we have used ray-tracing to model radiative heat absorption in the powder bed and to compute radiative properties of the bed. In order to highlight the spatial distribution of absorbed laser energy, the influence of inter-particle radiation and conduction is not considered.The details of laser energy absorption in the bed are sufficient to predict effective radiative properties of powder bed.

5.3.1 Laser radiation absorption in granular bed

To predict laser energy absorption, ray-tracing provides us with key ray-particle interaction details (e.g. point of interaction, energy absorbed at each interaction and number of interactions) since each ray-surface interaction is explicitly recorded. Scatter plot of all the recorded interactions in three dimensional space for case of Gaussian energy profile and uniform energy profile of laser beam is shown in Fig. 5.12 as a measure of laser penetration and absorbed energy distribution in the powder bed. The ray energy is normalized with respect to average energy per ray (beam power/total number of rays). The contrast between spatial energy distribution due to absorption in powder beds comprised of low and high emissivity material is clearly observable. The plots represent the relative distribution of laser energy in the powder bed, while the absolute values of energy absorbed depend on source power and scan speed. The quantitative representation of spatial distribution of absorbed laser energy in the powder bed is represented by plotting its variation in axial and radial directions with respect to laser beam center. The idea is to divide the powder bed into number of successive imaginary parallel planes and then evaluate energy absorbed by particles at each ray-particle interaction between the adjacent planes. The amount of laser energy absorbed between two consecutive planes depends on separation

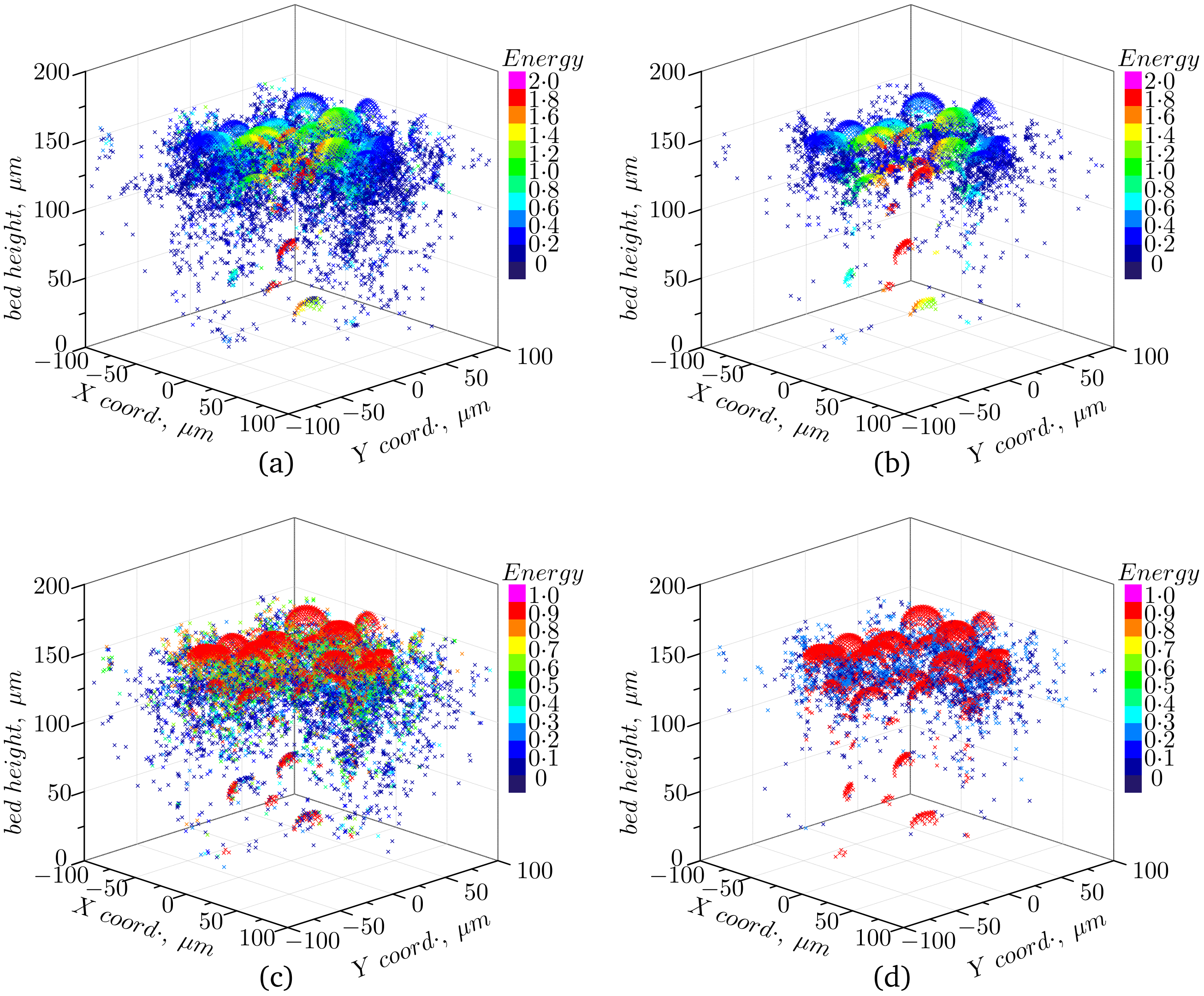
(a) (b) (c) (d)

Figure 5.12 An instance of partitioned rays interacting with powder bed in 3D space(energy levels indicate normalized ray energy prior to interaction and this normalization is done with respect to average energy per ray). (a) Emissivity = 0.2, Beam energy profile is Gaussian; (b) Emissivity = 0.8, Beam energy profile is Gaussian;(c) Emissivity = 0.2, Beam energy profile is uniform;; (d) Emissivity = 0.8, Beam energy profile is uniform.

between them. Therefore, local energy density values are used in the plots to make the distribution independent of gap between the planes and these values are normalized with respect to average energy density in the bed depth of three mean diameters.

Figure 5.13(a) shows variation of energy density along the bed depth. A marked difference in energy absorption profile is observed when compared to fully dense material since the peak energy density is not at the bed top surface. This is predominately due to porous structure of the medium allowing for significant number of high energy ray-particle interactions (see Fig. 5.15(a)) in the powder bed beyond the top surface and also enabling multiple reflections. It is found that the depth to which laser energy penetrates depends strongly on the powder grain size. This results from the fact that the energy of absorbance-free path in the powder bed is proportional to the powder grain size. Consequently, on selecting the mean size of powder

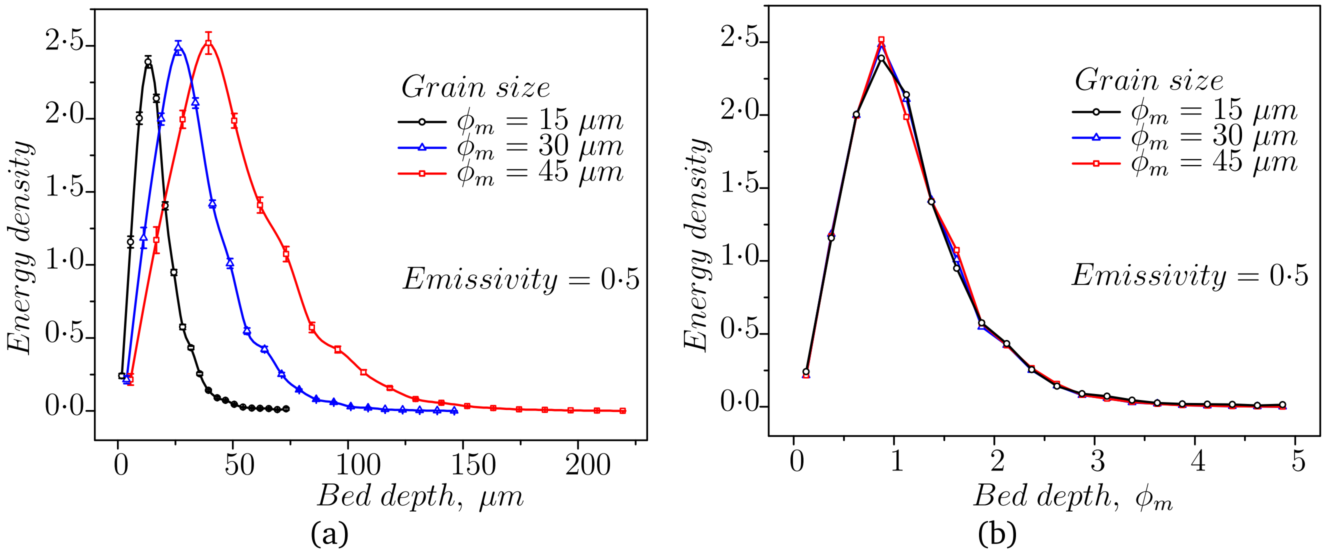

(a) (b)

Figure 5.13 Laser energy deposition along bed depth; energy density is normalized with average energy density in the bed depth of three mean diameters. (a) Bed depth measured in absolute units; (b) Bed depth scaled by powder grain size.

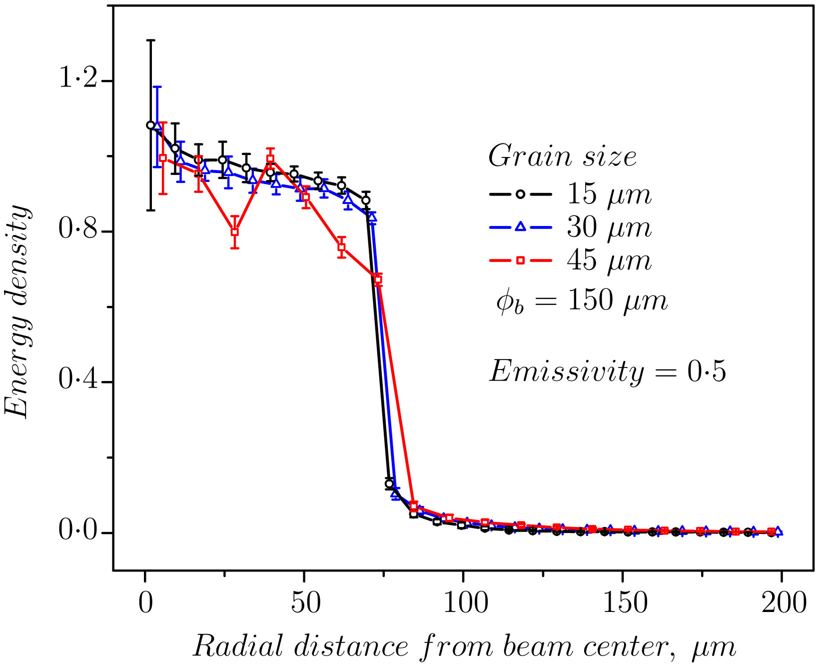

Figure 5.14 Laser energy distribution in radial direction with respect to laser beam centre.

particles as scaling parameter, it is found that most of the beam energy is deposited within two to three mean diameters from bed top surface(see Fig. 5.13(b)). The maximum energy density is observed at the depth of about one mean diameter from the top surface of powder bed.

The emissivity of the powder particles also influence energy distribution in the bed. Increasing the material emissivity leads to increasing energy absorption by each particle and to decreasing the depth of energy penetration in the bed (see Fig. 5.12 and 5.16). Unlike energy distribution in axial direction, the variation of energy density in radial direction is almost independent from the powder particle size (see Fig. 5.14). In case of uniform beam energy profile the energy density is found to be nearly uniform in radial direction having peak density at the beam center and steep drop in energy absorption in particles beyond laser beam radius. The corresponding three-dimensional scatter plots along axial and radial directions indicating number of ray-particle interaction with associated ray energy are shown in Fig. 5.15. The energy level in the plot refers to fraction of initial ray energy left with the ray. (e.g. after n number of reflections energy level of ray becomes $E_n = (1-\epsilon)^n$). Across all energy levels maximum number of interactions are found to occur between the depth of one to two mean diameters. The number of interactions in radial direction with increasing distance from beam centre till one beam radius and then decreases beyond that. The increase in number of interactions should not be interpreted as increasing energy density with distance from beam center because of simultaneous increase in volume in which these interactions occur.There is significant drop in number of interactions just after first reflection clearly indicating that a large fraction of rays leave the bed. In contrast to this, number of interactions after subsequent reflections decrease very gradually, indicating that a few rays escape out of bed after the second reflection.

Understanding the influence of material emissivity and particle size on spatial energy distribution in the powder bed is also helpful for achieving preferential heating in the powder bed. Figure 5.17 shows a bi-dispersed powder bed irradiated by moving laser beam (colours mapped to particle temperature corresponding to absorbed laser radiation energy without considering interparticle conduction). Relatively higher temperature of all the small particles in laser scan path clearly indicates selective heating. This is due to increasing surface area to volume ratio with decreasing particle size. Similarly, adding a high absorptivity mixing component to powder

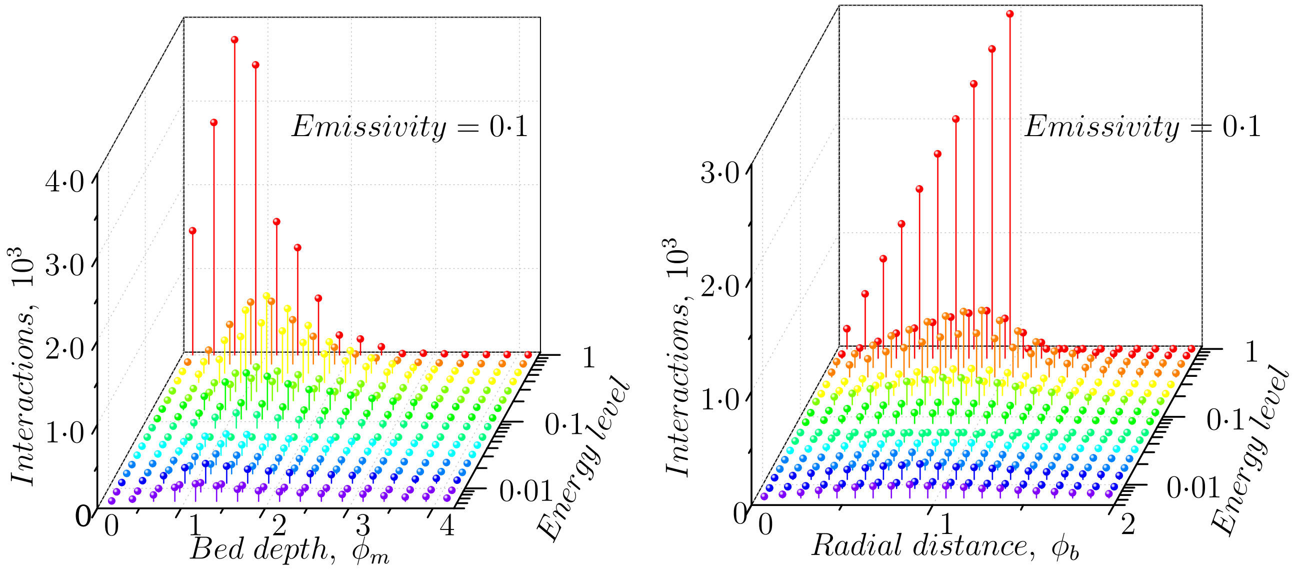

(a) Along bed depth (b) Along radial direction

Figure 5.15 Number of ray particles interactions corresponding to each energy level along axial and radial directions.

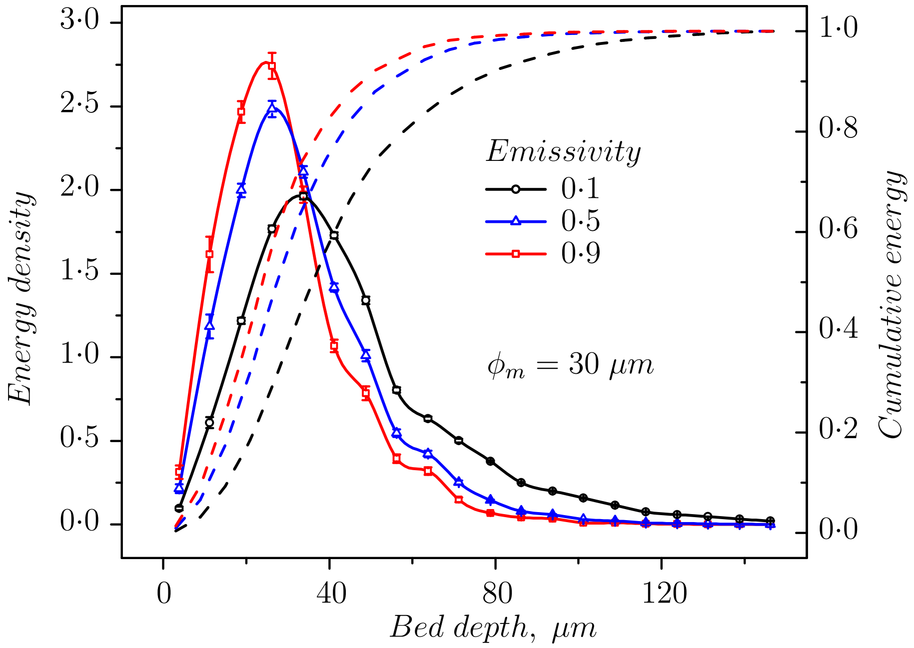

Figure 5.16 Influence of material emissivity on energy deposition along bed depth.(dashed lines represents cumulative energy deposited)

bed is also effective in obtaining preferential heating as shown in Fig. 5.18. The figure shows a monodispersed powder mixture in cold isothermal state (colours mapped to particle emissivity) and state after laser heating (colours mapped to temperature).

5.3.2 Effective bed emissivity

From the definition effective hemispherical emissivity for monochromatic laser source can be estimated as fraction of incident energy that is absorbed in the powder bed. Thus, estimating

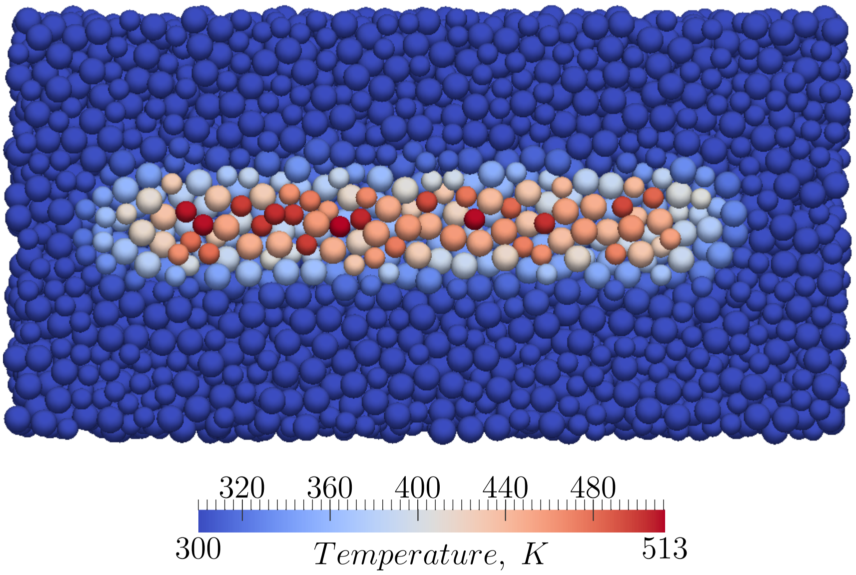

Figure 5.17 Temperature distribution in a laser irradiated bidispersed powder bed ($\epsilon = 0{\cdot}1,\ \phi_1 = 32\ \mu m,\ \phi_2 = 40\ \mu m,\ P_0 = 10\ W,\ V_s = 1\ ms^{-1},\ \phi_b = 150\ \mu m$).

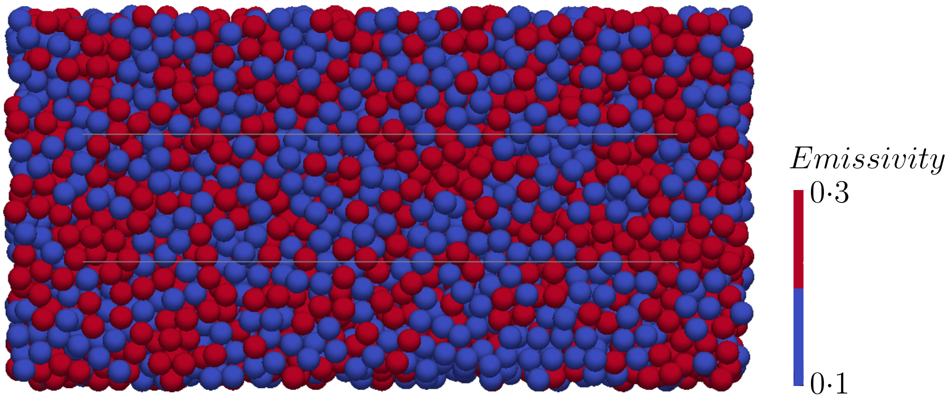

(a) Cold state

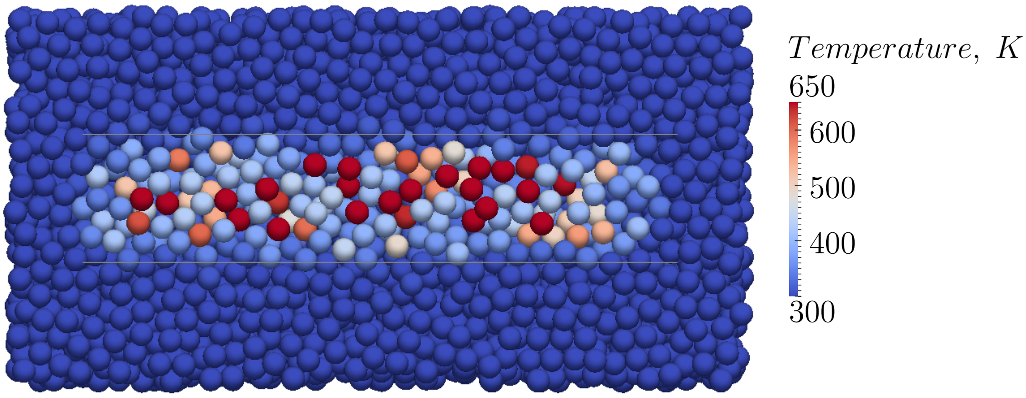

(b) After irradiation

Figure 5.18 Preferential energy absorption by higher emissivity particles in the mixture ($\epsilon_1 = 0{\cdot}1,\ \epsilon_2 = 0{\cdot}3,\ \phi_m = 35\ \mu m,\ P_0 = 10\ W,\ V_s = 1\ ms^{-1},\ \phi_b = 150\ \mu m$).

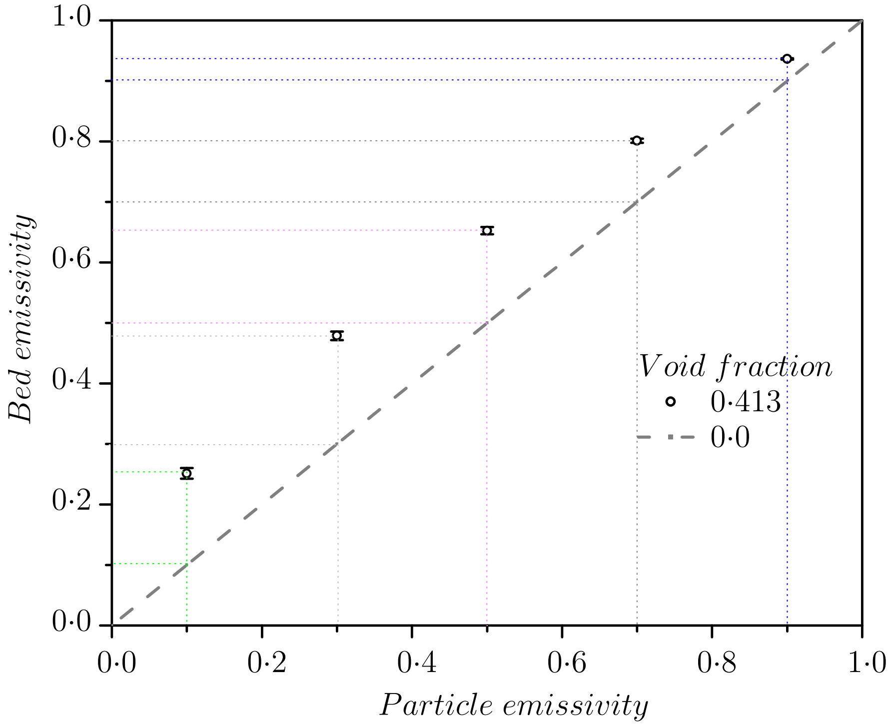

Figure 5.19 Predicted powder bed emissivity corresponding to material emissivity.

total energy absorbed in the bed using ray-tracing enables us to predict effective emissivity of powder bed.

Figure 5.19 shows variation of bed emissivity for known emissivity(s) of the powder material(s). The predicted bed emissivity is higher than corresponding powder material. This is due to open pore structure of powder allowing radiation to penetrate several particle diameters deep (due to multiple reflections) into the bed as compared to dense material. In other words, the voids on the bed surface acts as black surface, thus increasing emissivity in powder form. Bed emissivity tends to approach the material emissivity for highly absorbing material because the particles absorb the major part of the incident energy. In other words relative influence of voids (apparent black surfaces) diminishes with increasing emissivity of material.

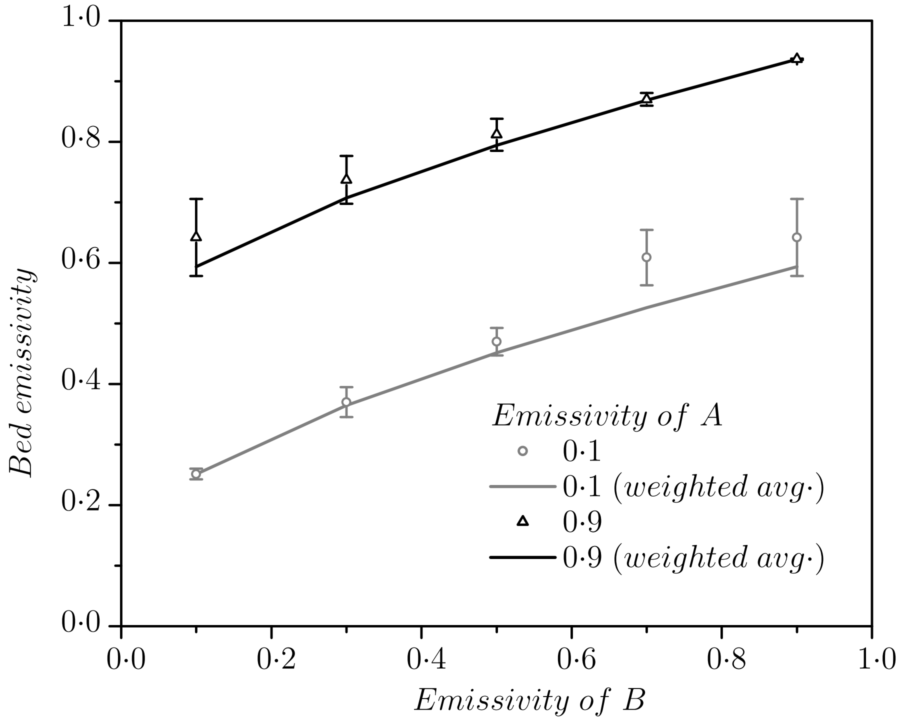

Figure 5.20 Emissivity predictions for a powder mixture having two components A and B of given emissivities.

The predicted emissivity values for a powder mixture are plotted in Fig. 5.20. Only the emissivity values of mixing components are different while the grain size and volume fraction are same for both the components of the mixture. We observe that mixture emissivity can be predicted using weighted average volume fractions of individual segregated powder bed. However, the mismatch between simulated values and weighted average increases with growing difference between the component emissivities. The influence of varying particle size is hardly evident on the bed emissivity as seen in the Fig. 5.21.

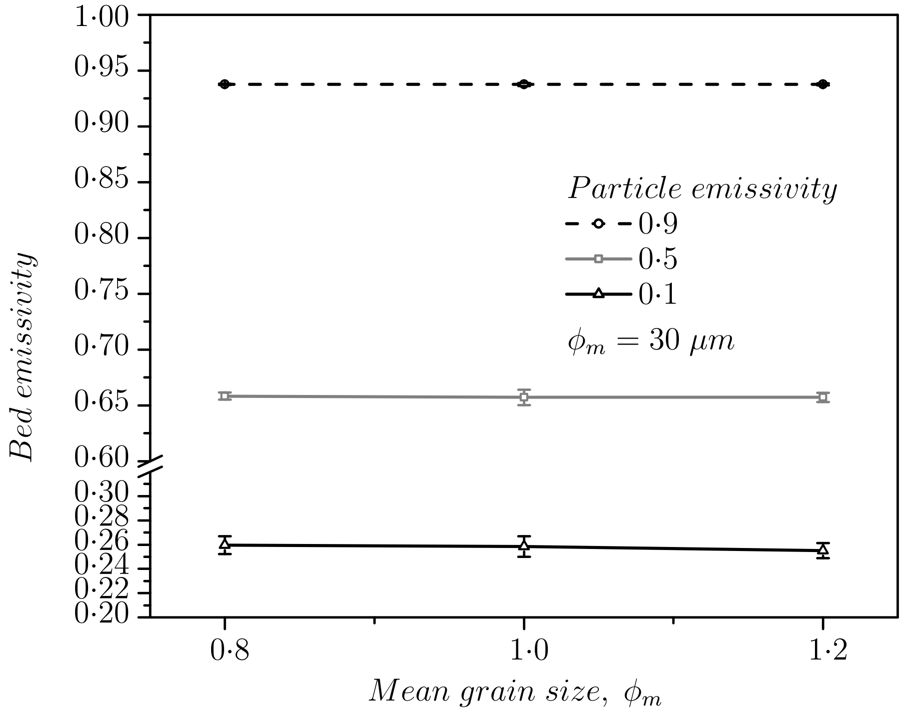

Figure 5.21 Influence of grain size on bed emissivity.

5.3.3 Optical penetration depth

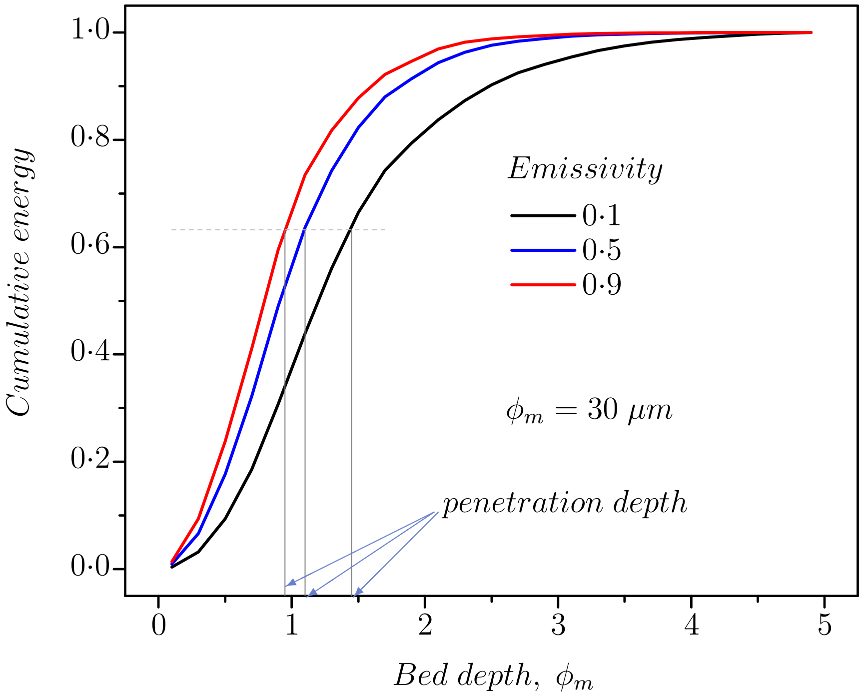

Figure 5.22 Optical penetration depth from cumulative energy distribution in the powder bed.

Penetration depth is a measure of how deep light or any electromagnetic radiation can penetrate into a material. It is defined as the depth at which the intensity of the radiation inside the material falls to 1/e (about 37%) of its original value at the surface [38]. It is function of both the incident radiation and the material properties. For a granular medium optical penetration will further depend on packing structure and is expected to be higher due to absorbance free path in the voids. In the limits of geometrical optics, ray-tracing can be used to predict penetration depth in the powder bed, by estimating the axial (along the bed depth) distribution of absorbed energy from radiation source. It is the depth at which at which cumulative energy absorbed in the bed is equal to $(1 - \frac{1}{e})$ times total energy absorbed in the bed. The cumulative energy distribution plots, for monodispersed and polydispersed beds having a range of material emissivity as shown in Fig. 5.22, are used to determine optical penetration depth in terms of mean grain size. Penetration depth (δ_p) is function of mean particle size for a given material emissivity. It is an important parameter needed to model heat transfer in discrete medium using homogeneous approach.

5.4 Heat transfer in granular bed

Heating of powder grains beyond the melting point for liquid phase sintering is mainly due to direct absorption of laser radiation by particles, while inter-particle radiation and conduction tend to distribute absorbed energy in the bed. They are included in the modelling to simulate temporal and spatial evolution of temperature due to moving laser source. This is necessary to investigate the influence of process parameters (e.g. laser power, scan velocity, beam size etc.) on quality and stability of sintered tracks. In this section we focus on predicting sintered track shape and optimal process window for given set of input parameters. We have used lumped approach to model heat transfer between the particles. The phase change is not included explicitly. It is implied that any particle heated to temperature above its melting point is melted. The properties of the powder material (Stainless Steel 1.4542) and relevant parameters used in this simulation are given in Table 5.6. In fact the thermal conductivity of the particle will not have any influence on the temperature evolution of particles (as we have adopted lumped approach), however, it will have direct implication on contact thermal resistance as per Eqn. (3.23).

Table 5.6 Thermo-physical properties and other parameters used in simulation

Property	Value
Melting point (T_{mp})	$1673{\cdot}0\ K$
Enthalpy of fusion (H_f)	$285{\cdot}0\ kJ \cdot kg^{-1}$
Specific heat (C_p)	$500{\cdot}0\ J \cdot kg^{-1} \cdot K^{-1}$
Density (ρ)	$7800{\cdot}0\ kg \cdot m^{-3}$
Thermal conductivity (λ)	$40{\cdot}0\ W \cdot m^{-1} \cdot K^{-1}$
Emissivity (ϵ)	$0{\cdot}2$
Size distribution	mono-dispersed
Grain size	$30\ \mu m$
Laser beam size	$140\ \mu m$

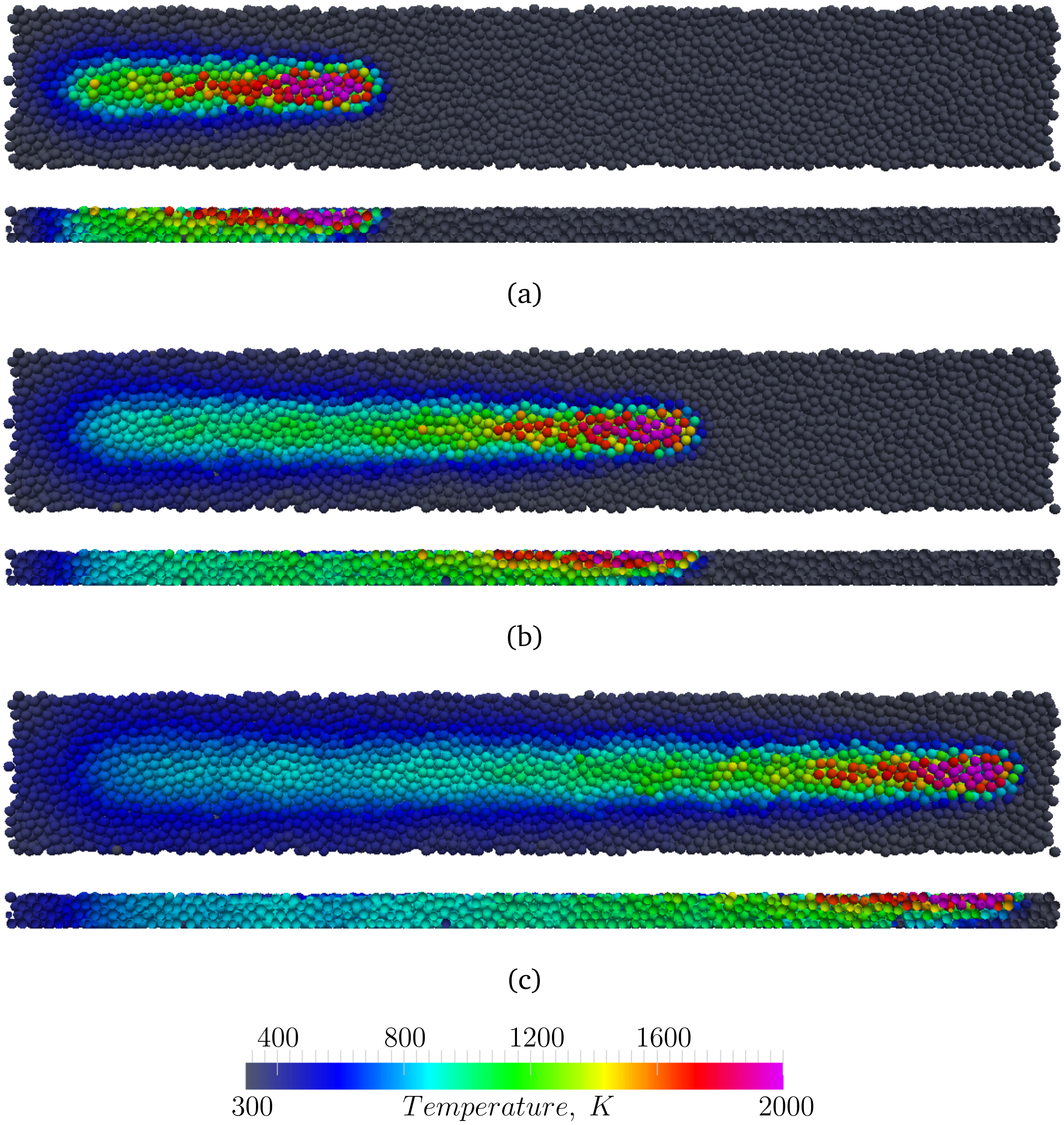

Figure 5.23 Temperature evolution in powder bed at three time instants during scanning laser beam of $P_o = 110\ W,\ V_s = 0{\cdot}8\ m/s$: (a) $t = 0{\cdot}875\ ms$; (b) $t = 1{\cdot}787\ ms$; (c) $t = 2{\cdot}707\ ms$.

Transient temperature evolution in the powder bed during laser scan along a straight path is shown in Fig. 5.23. The moving beam imparts most of energy to the particles directly under it while the surrounding particles heat up due to conduction and radiation exchange. The observed temperature distribution around the beam is almost identical for all the three instants. The selected combination of laser power and scan speed is sufficient to melt the particles exposed to laser beam during interaction for a continuously melted track. Corresponding plots along vertical section through centre of the track are also shown, indicating extent of melting along powder depth. The peak temperature in the bed is significantly above the melting point. This is indeed needed to achieve high density sintered parts as in case of experiments performed under same input parameters. Figure 5.24 shows an instance of temperature field in the powder bed, which is heated by laser source moving at three different scan speeds. Corresponding plot along vertical section through centre of the beam is also shown. The combination of laser power ($50\ W$) and scan speed ($0{\cdot}2\ m/s$) is sufficient to melt the particles exposed to laser beam during interaction to form a continuous melted track. The peak temperature in the powder bed is significantly above the melting point, which is necessary to achieve continuous melted track. On further increasing the scan speed up to $1{\cdot}0\ m/s$ while keeping the laser power constant, interaction time decreases, and only a few particles under the beam seem to undergo melting.

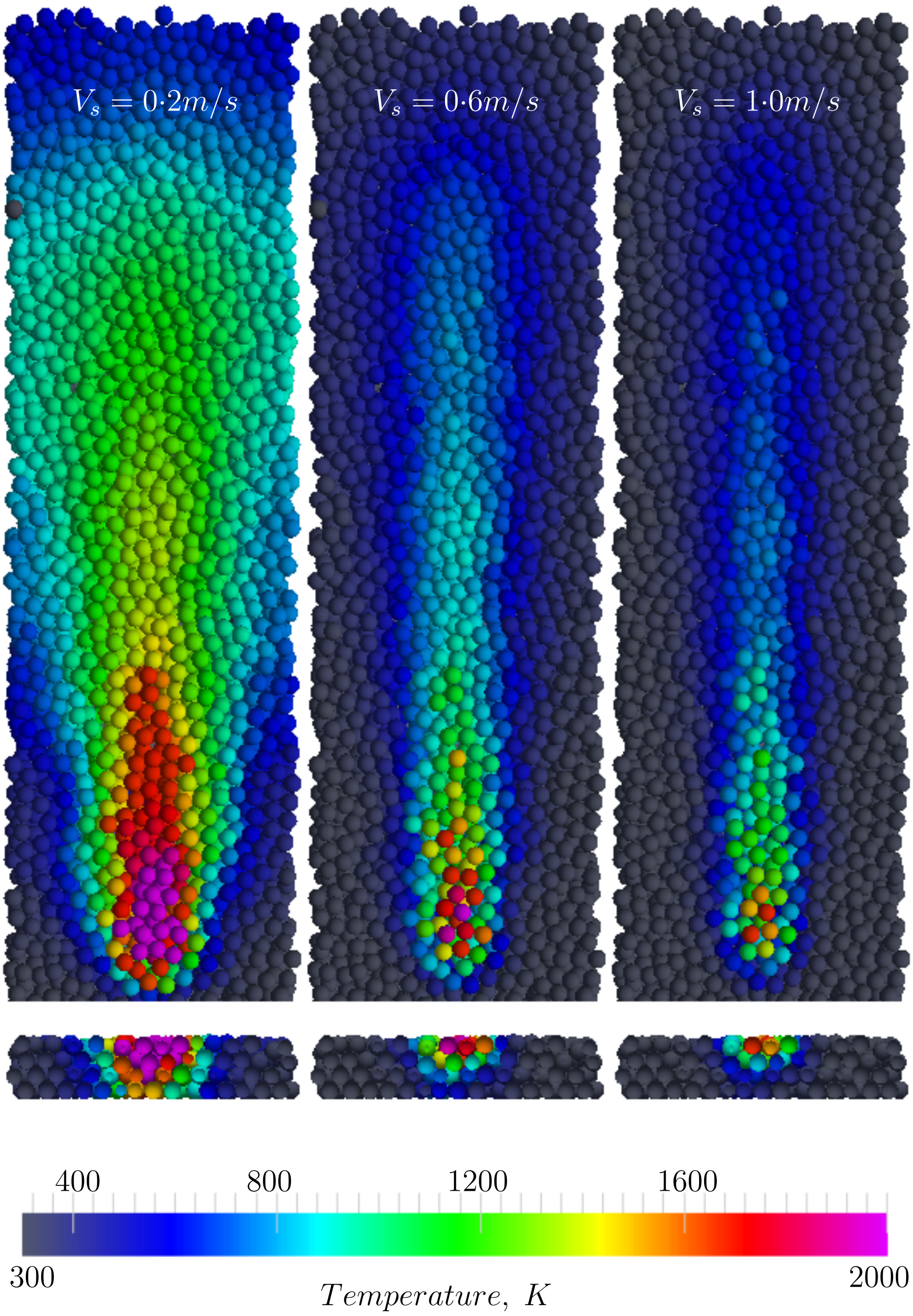

Figure 5.24 Temperature distribution in powder bed for increasing scan speed at $P_o = 50\ W$

The peak temperature hardly exceed melting point for this case, indicating that energy absorbed is not enough to yield a continuously melted track. (see Fig. 5.35 for actual sintered tracks for corresponding laser power and scan speeds).

Due to Gaussian energy profile of laser beam, particles in the powder bed are subjected to position dependent time varying heat flux during exposure. Figure 5.25 shows the variation of laser irradiation flux at the surface of powder particles. It is obtained by evaluating total energy from the laser source that is absorbed by the particles at every simulation time step. The net heat flux variation and corresponding temperature evolution of a particle positioned at the centre of scanning laser beam is shown in Fig. 5.26. In this figure, individual contributions to net heat flux are also plotted. During exposure, incident laser radiation from source to particles is dominant and the particles are completely melted. After that the temperature of the particle increases beyond the melting point. Heated particles after exposure cool due to interparticle conduction and thermal radiation. The heat transfer due to conduction mode is dominant during cooling.

The temperature history of individual particles in the scan path under different combinations of power and scan speed is shown in Fig. 5.27. The observed trends with increasing power and scan velocity are mutually opposite. This suggests that the ratio between the power and scan speed can serve as important derived parameter to characterize thermal behaviour of heated particles in the bed. Physically it represents amount of source energy per unit length of track. Also the nature of sintered track depends strongly on source energy, thus making it possible to analyse nature of track for range of beam power and scan speed while keeping energy per unit

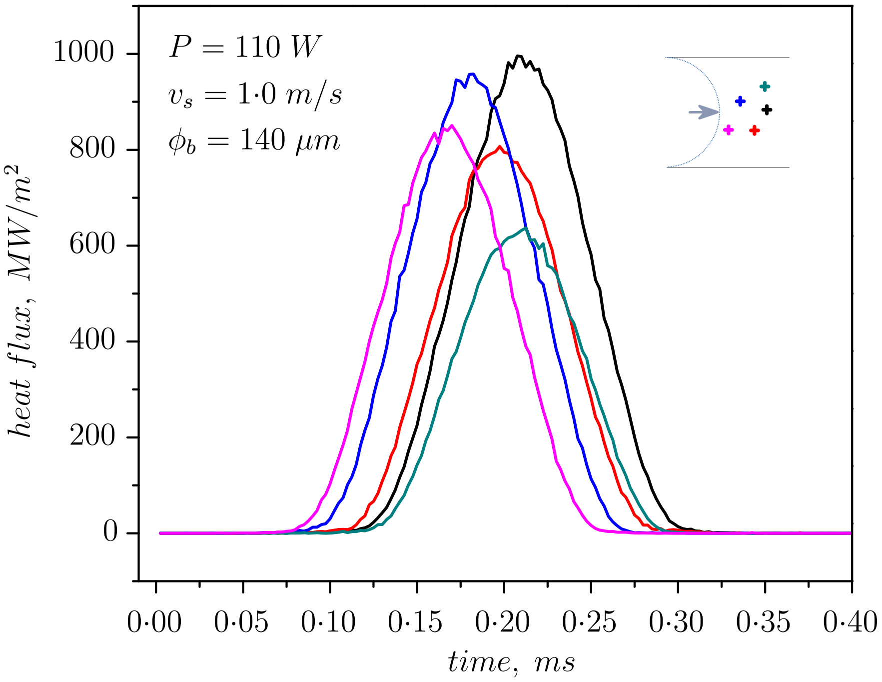

Figure 5.25 Laser irradiation flux at the particle surface; the relative positions of the particles in the scan path are shown in inset

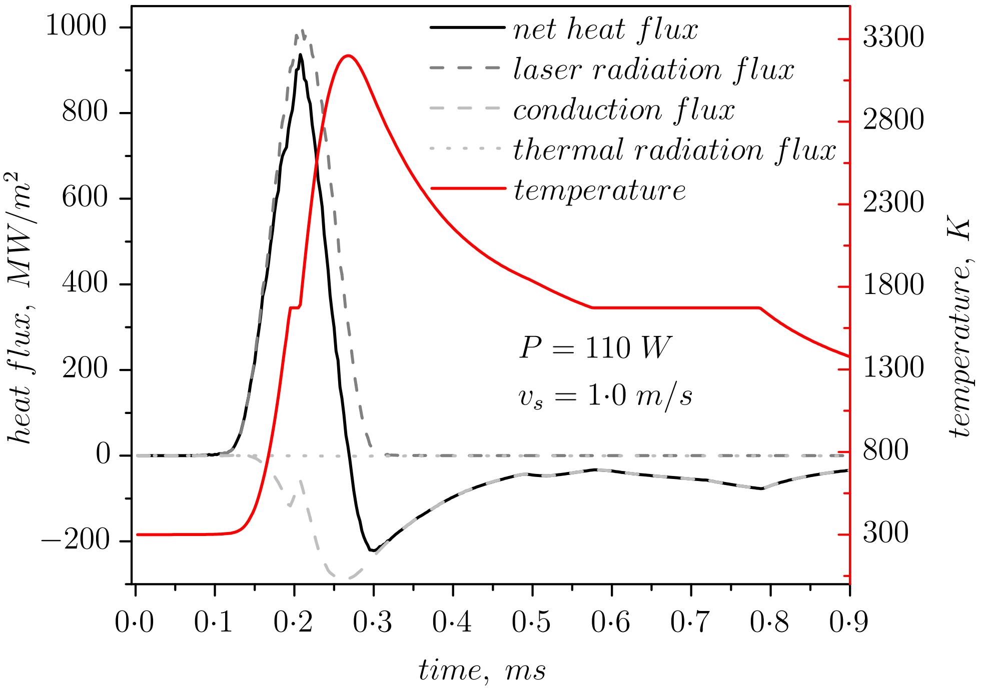

Figure 5.26 Net flux variation as the laser beam scans over the particle surface

length of track fixed and help fixing process map boundaries. Figure 5.28 indicates that any combination of laser power and scan speed resulting in source energy per unit length (P/v_s) less than $80\ J/m$ is not sufficient to melt the exposed particles under the beam in the powder bed. This is also supported by experiments where only fragmented tracks are obtained beyond a boundary that can be approximated by a straight line representing $P/v_s \approx 100\ J/m$ as shown in process chart (see Fig. 5.38).

In order to melt the exposed particles under the laser beam, the source energy can be increased, However, there are many other factors (wetting, substrate remelting, contact angle,

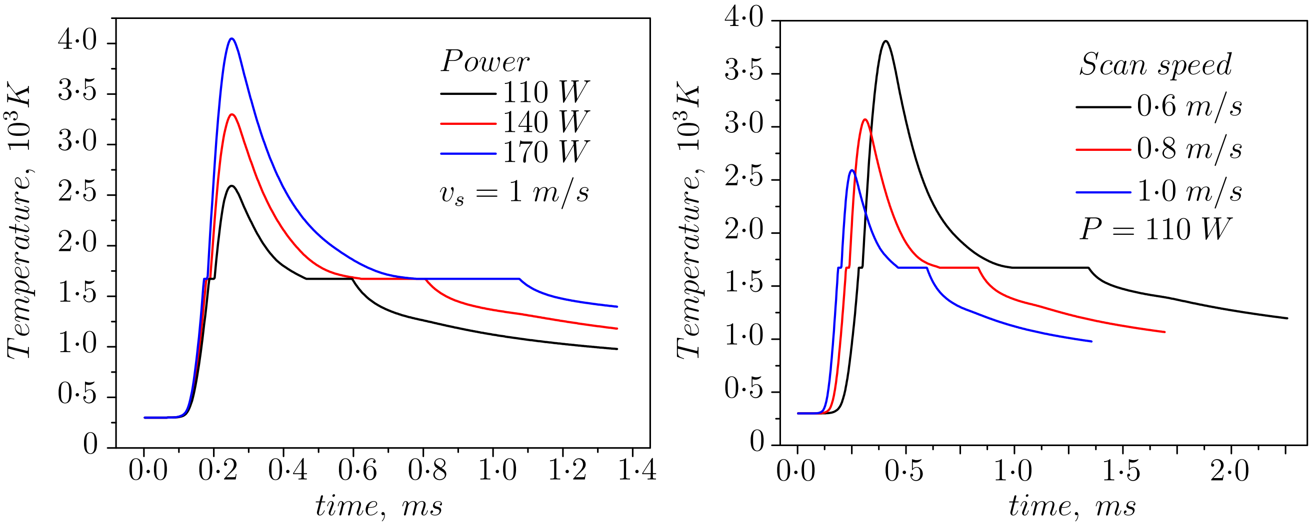

(a)
(b)

Figure 5.27 Temperature history of a particle in the laser scan path.

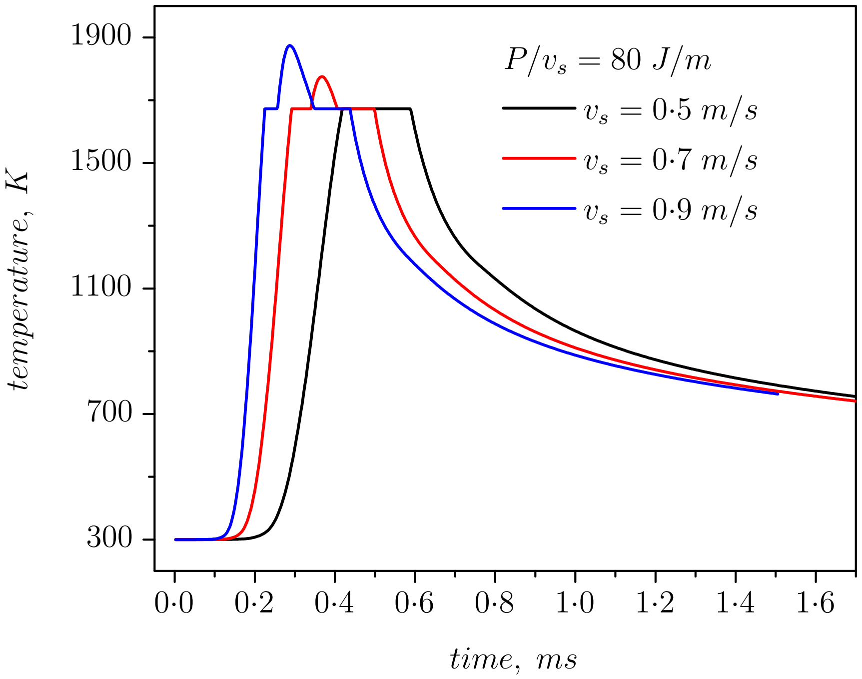

Figure 5.28 Temperature evolution of a particle for constant P/v_s ratio.

pool length, homologous melting solidification etc.) influencing the stability of molten track. In the following we use the numerically obtained data to estimate the molten pool length and width and to predict nature of sintered tracks for given combination of process parameters. We assume that the Rayleigh-Plateau capillary instability [22] plays an important role in evolution of molten tracks. In the case of cylindrical liquid column the stability criterion is:

$$\frac{\pi D}{L_p} < 1 \,, \tag{5.1}$$

where πD, L_p are circumference and length of molten cylinder respectively. If this criterion is fulfilled, the varicose deformation of the cylinder surface takes place with the dominant wavelength exceeding the circumference of the cylinder. In our analysis we assume that molten pool has a cylindrical shape and determine characteristic length and diameter in order to apply the stability criterion (5.1)

At first the instantaneous length of molten track (liquid cylinder) is obtained by calculating distance between farthest molten particles in the bed at each time step during simulation. Figure 5.29 shows time evolution of instantaneous molten track length. At the beginning of scan cycle the rate of laser energy absorption by the powder grains exceeds the heat loss by molten portion of the track, leading to increasing length of molten track. However, heat loss to ambient and surrounding particles also increases with growing length of molten track and eventually balance the energy absorption. Beyond that point in time the length of molten track ceases to grow further and fluctuates in a very narrow range. The mean value of molten length is thus obtained by neglecting the initial growth period and averaging for remaining portion.

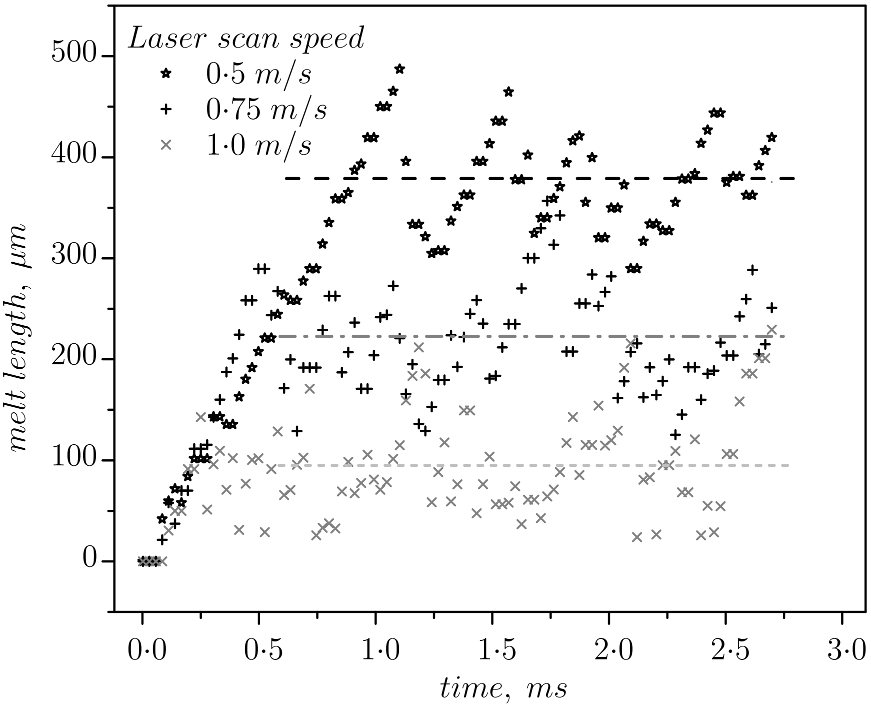

Figure 5.29 Instantaneous length of the molten track; dashed lines show the respective average over the time duration

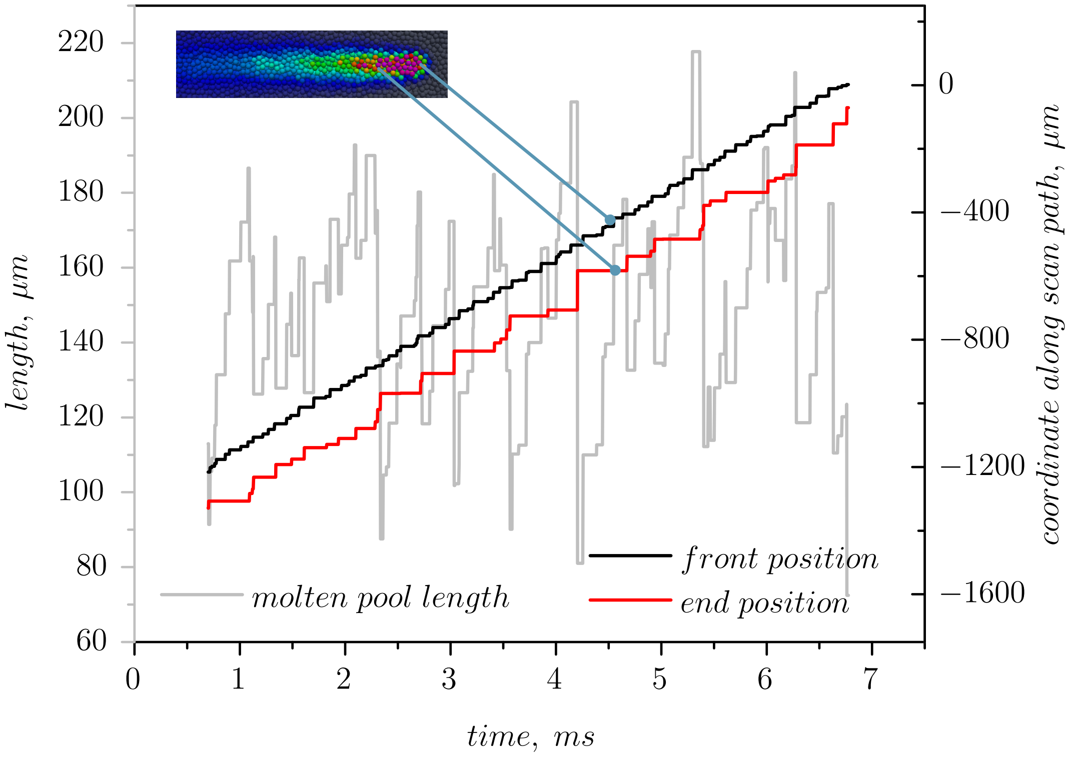

Figure 5.30 Evolution of molten pool length during laser scan

However, this approach for estimating instantaneous length of molten pool is grossly an over prediction. Since the width of measured molten track near the tail end (as observed in Fig. 5.23) is hardly more than a particle size, thus a major portion of track is almost solidified while being considered as molten in Fig. 5.29. To estimate instantaneous length of molten pool only the unmelted portion of the track must be considered. This is done by calculating the distance between the particles satisfying two separate set of conditions to fix front and end position of molten pool. Front position is specified by a particle which is molten and positioned ahead (in scan direction) of all other molten particles in the pool. Likewise, molten pool end is specified by a particle which is just solidified from molten state and positioned ahead of all such particles. In addition, a new position of molten pool end can only move forward in direction of laser scan vector or remain unchanged, but backward movement is restricted as it is not physical. Figure 5.30 shows evolution of front and end position of molten pool along with corresponding length. The circumference of the molten pool is approximated by calculating the total volume of molten particles in molten the molten pool.

The plots computed in Fig. 5.31 show variation of molten pool length and circumference with scan speed for fixed power. The point at which two curves intersect represents threshold velocity beyond which track becomes unstable and splits into fragments based on stability criterion (5.1). Coincidently, the ratios of beam power to corresponding threshold velocities (v_s^p) for three cases are approximately same. This again points to a fixed value of energy per unit length. The importance of this result in fixing the processing window will be discussed next.

The locus of the points that satisfy the condition given by

$$\frac{P}{v_s^p} = C1 \,, \tag{5.2}$$

on the process chart is a straight line that is uniquely defined (see Fig. 5.33). The value of constant $C1$ in Eqn. (5.2) is unique for a material. This line marks the boundary between the region of fragmented tracks and continuous tracks. Furthermore, from the temperature history plots we find that, the time duration for which a particle remains in molten state is almost unchanged

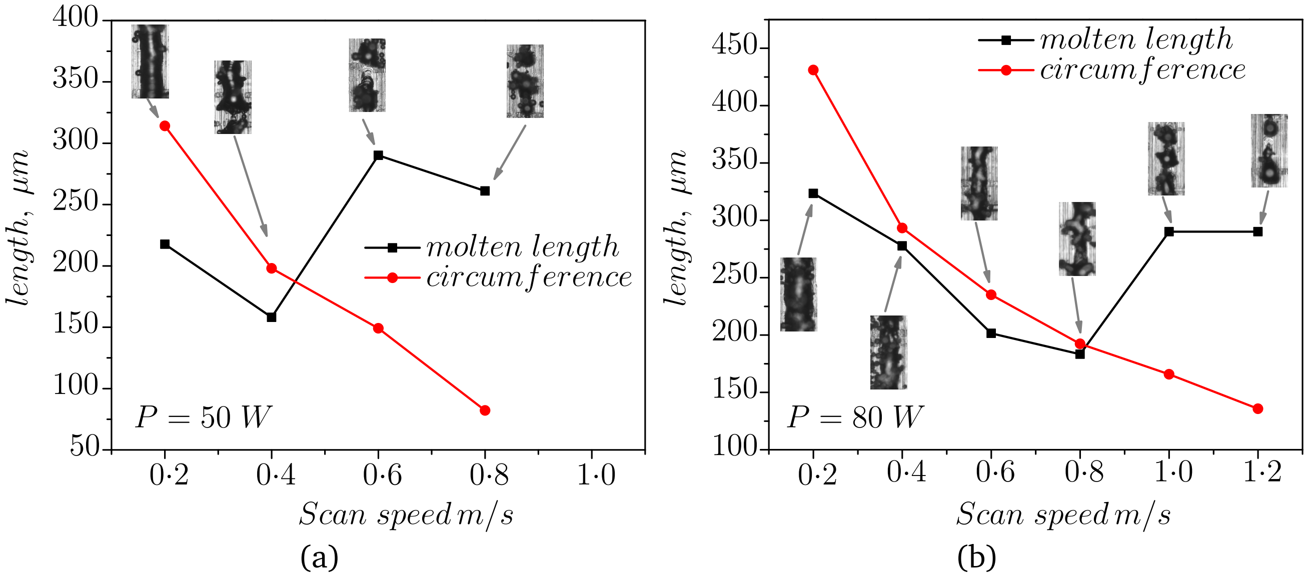

Figure 5.31 Variation of molten pool length and its circumference with laser scan speed.

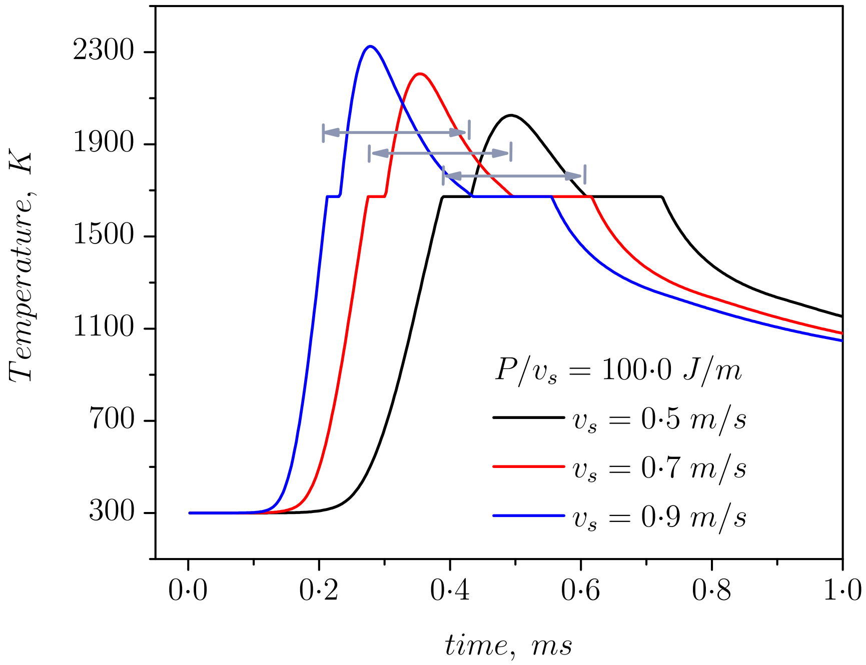

Figure 5.32 Temperature history of a particle for constant P/v_s ratio; the duration for which particle remains molten is indicated.

for a constant P/v_s ratio (see Fig.5.32). This directly translates into increasing length of molten pool with increasing scan speed because the distance travelled by beam increases hence exposing more particles in fixed time duration. Therefore, in case of a fixed power to scan velocity ratio ($P/v_s \geqslant C1$), increasing scan velocity will lead to increase in molten pool length as long as stability criterion (5.1) is satisfied. Beyond a limiting scan velocity v_s^c for constant P/v_s ratio, the sintered track becomes unstable. This limiting velocity (v_s^c) is again unique to a given P/v_s ratio. Moreover, the limiting speed must decrease with increasing P/V_s ratio as higher ratio aids longer molten state. This effect is also observed in process map (see Fig. 5.38) obtained experimentally. Based on these observations from numerical as well as experimental studies a schematic of process chart is shown in Fig. 5.33, to illustrate the criteria to approximately fix boundaries defining region of stable continuous tracks on the process chart for a given material system.

5.5 Experimental validation

Validation experiments were conducted on a Laser sintering system Eosint M270 using commercially available 1.4542 (US: 17-4 PH) stainless steel powder ($d50 \approx 28\ m;\ d90 \approx 41\ \mu m$). The system is equipped with a continuous wave Yb-fibre laser ($\lambda = 1064\ nm$) and beam expander with an incremental adjustment possibility of the laser spot diameter ϕ_b between $100\ \mu m$ and $500\ \mu m$. The laser has a Gaussian beam profile. PRIMES Focus/Beam Monitor is used to verify the laser power output and laser spot diameter. Theoretically, a Gaussian beam does not have characteristic size and for most practical purposes size of beam is defined as the radius at which

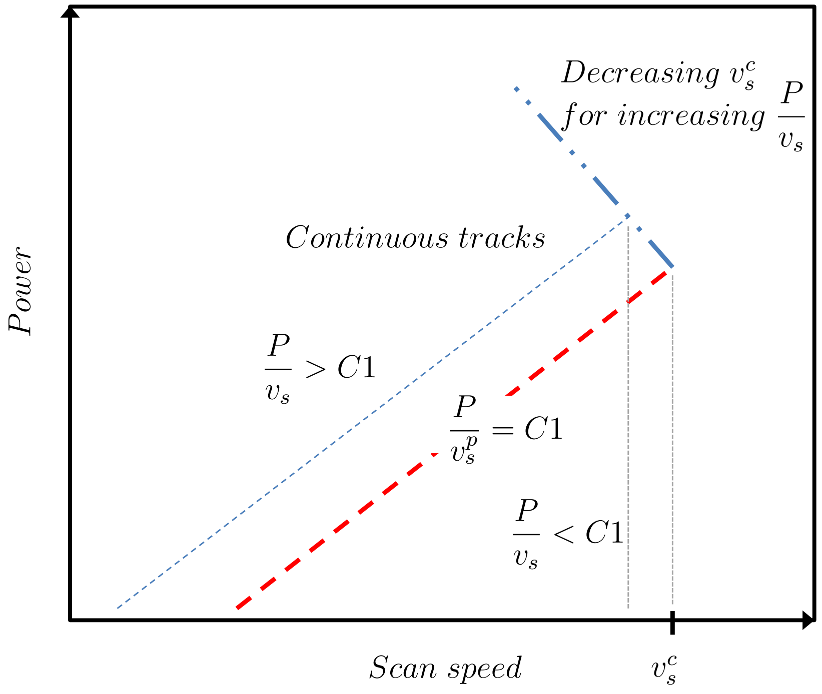

Figure 5.33 Schematic of process map for laser sintering

the amplitude of laser intensity becomes $1/e$ times its axial value. Accordingly, the laser spot diameter accounts for the area covering $86{\cdot}5\%$ of total laser power. In order to minimize undesirable heating effects in optical path of the laser beam, laser spot size needs to be adjusted depending on desired power output. Therefore, the laser spot diameter was analysed for maximum ($P = 195\ W$) and minimum ($P = 20\ W$) laser power outputs. Linearity between these two values is assumed to calculate the laser spot diameter of any given laser power output. The beam expander was adjusted to allow a laser spot diameter of $140\ \mu m$ (at a laser power of $100\ W$), which is recommended for the material used and corresponding standard parameters. This setting was kept constant for all conducted experiments. The unconsolidated powder layers were exposed to scanning laser beam, and resulting consolidated tracks were analysed. A schematic of track experiments conducted is shown in Fig. 5.34. A full factorial design with three parameters was used: 1) scan speed, 2) laser power, 3) layer thickness. Table 5.7 summarizes the three different parameters and corresponding design points. In total 216 different

Table 5.7 Parameter range for the experiment

Parameter	Minimum	Maximum	Step size
Laser power (W)	50	200	30
Scan speed (m/s)	0·2	1·2	0·2
Layer thickness (μm)	0	100	20

parameter combinations have been tested. Each track was analysed with a Leica DM6000 fluorescence microscope (magnification: 100x). For each design point three images were taken to avoid random scattering. The width of each melt track was measured at multiple positions along track for statistical purposes.

Figure 5.35 shows the sintered tracks generated for powder layer thickness of $80\ \mu m$ and laser power $50\ W$ at different scan speeds. Depending on various input conditions, sintered track can be continuous, fragmented or even exhibit balling phenomenon. The predictions of developed thermal model are compared with measurements of sintered track width in Fig. 5.36(a). The trend observed in the simulation is consistent with experimental results. However, calculations are found to overpredict experimental values of track width. Overprediction is expected as melt flow (not modelled) driven by surface tension forces tend to minimize surface area of melt pool forming dense consolidated track on solidification. Indeed, an excellent agreement is obtained (see Fig. 5.36(b)) on accounting the shrinkage by multiplying the predicted values with a shrinkage factor F_{sh} given as

$$F_{sh} = \rho_{pack}^{1/3}, \tag{5.3}$$

where ρ_{pack} is packing density of powder bed.

A quantitative estimation of melt depth for a range of power and scan speed is given in Fig. 5.37. This is obtained by measuring the extent of melt depth at every time step during simulation and then averaging. As expected melt depth in the bed decreases with decreasing laser power or increasing scan speed.

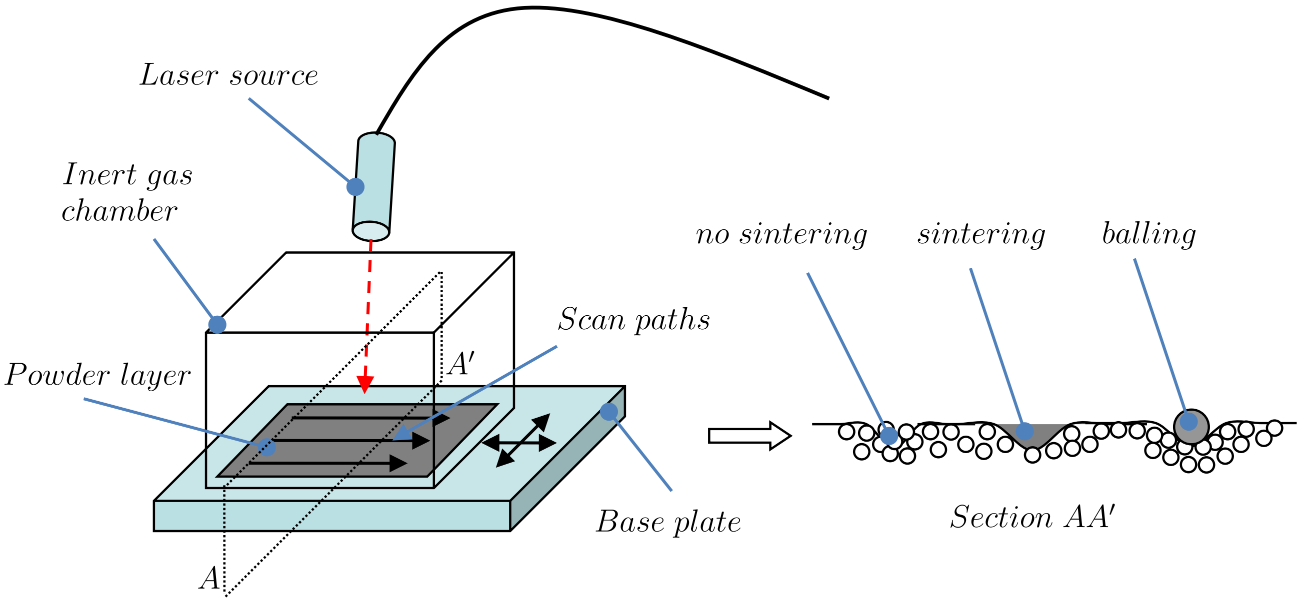

Figure 5.34 Schematic of track experiment

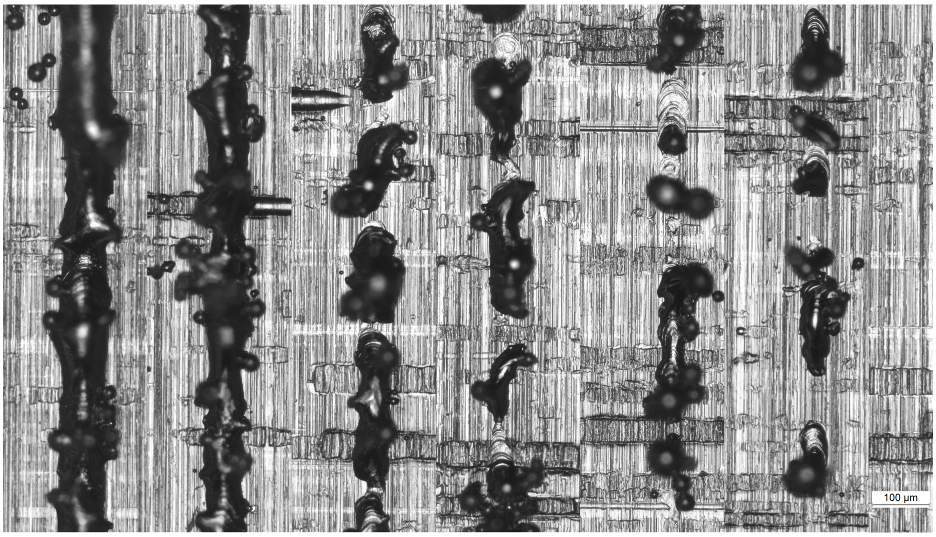

Figure 5.35 Actual sintered tracks corresponding to laser power $P_o = 50W$ and $v_s = 0{\cdot}2(0{\cdot}2)1{\cdot}2\ m/s$

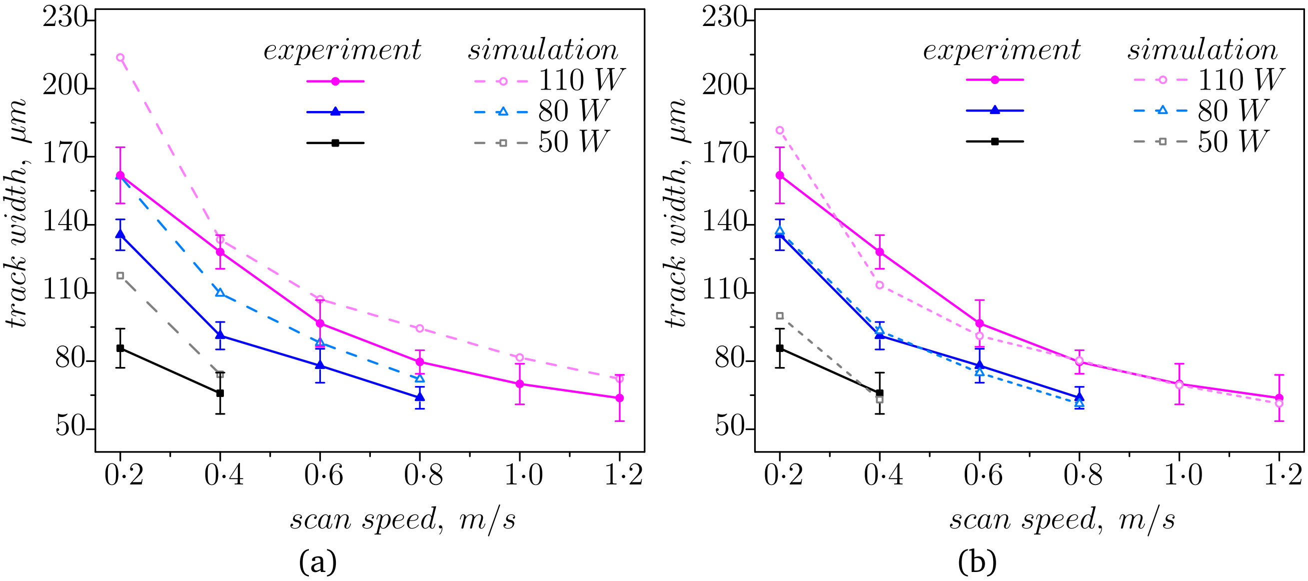

Figure 5.36 Estimated track width compared with experimental measurements (a) without considering shrinkage; (b) after accounting shrinkage

A typical process map obtained by visual analysis of sintered tracks for the range of parameters considered in experiment is shown in Fig. 5.38(a). Sintered tracks are found to be continuous (cylindrical or flat), fragmented and even exhibit balling phenomenon. The predicted stability matrix based on numerical calculation is also shown (see Fig. 5.38(b)) for comparison with experimentally obtained process map. We are able to predict track breakup based on presented thermal model for laser power up to $110\ W$, coincidently The predictions are surprisingly good, since the fluid flow is not modelled. We don't expect a perfect agreement between numerical predictions and experimental measurements, since that instability of a molten liquid pool is an extremely complex phenomenon depending on multitude of factors not accounted for in the

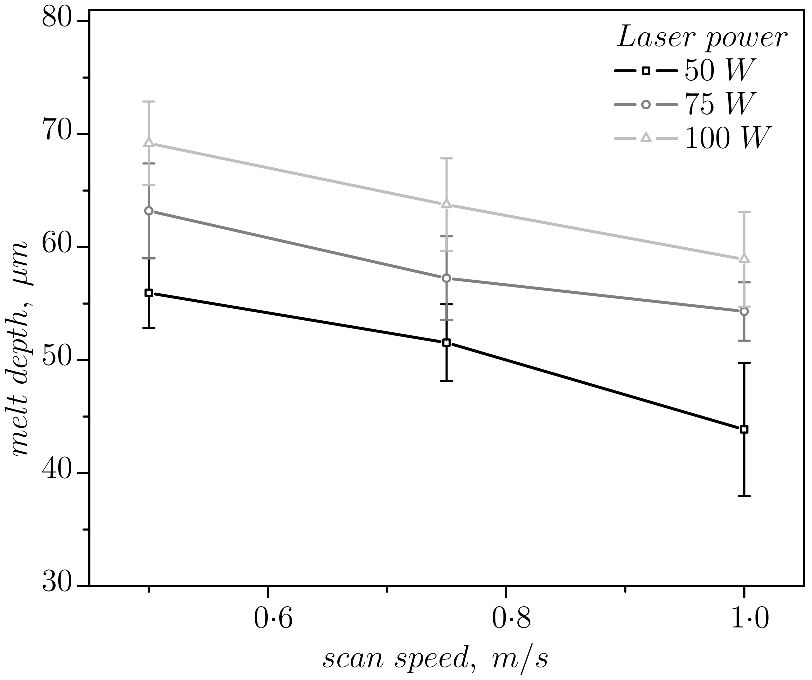

Figure 5.37 Variation of melt depth with laser scan speed

present model. We have only attempted to correlate the heat transfer data from the model to predict stability thresholds in terms of laser power and scan speed.

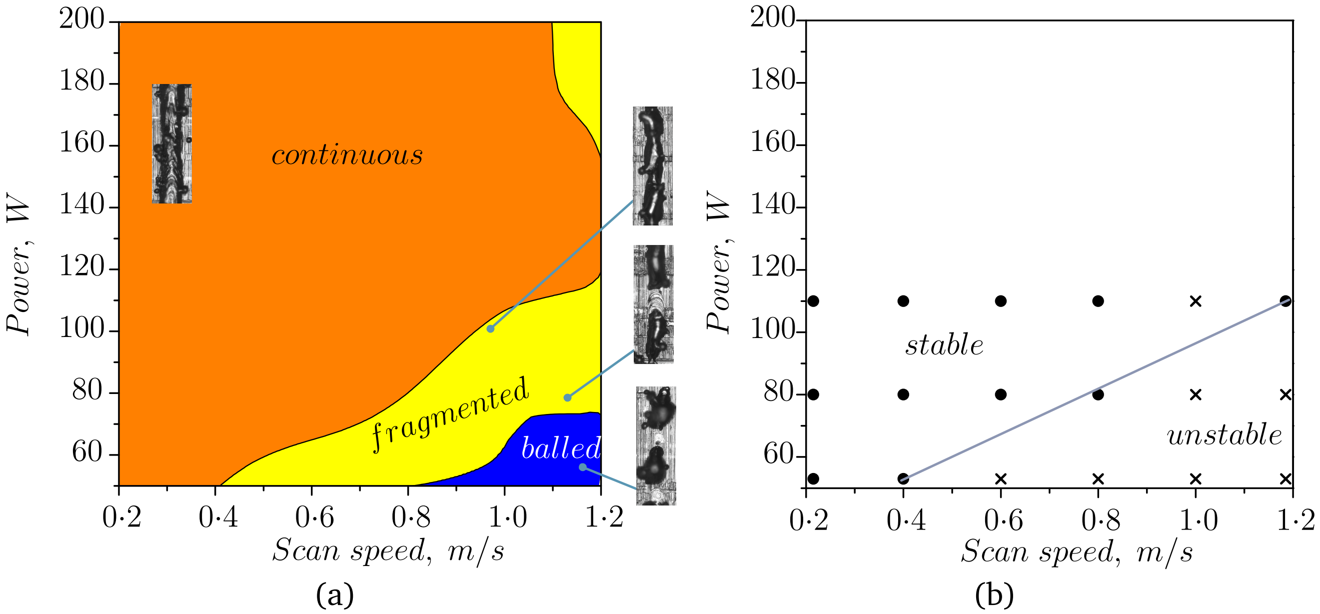

Figure 5.38 Process map showing nature of sintered tracks for a range of laser power and scan speed; (a) process map obtained experimentally, (b) process map obtained numerically, Cross = unstable tracks, Dots = stable tracks.

5.6 Thermal behaviour of a particle in granular bed

In the previous section we have focussed primarily on laser heating of powder bed and investigated overall behaviour of bed while considering it as a discrete medium. Furthermore, the smallest resolved length scale for heat transfer in the bed is limited to grain size of the medium, considering the large number of randomly distributed particle grains in the medium. Thus detailed thermal behaviour of an individual is still unknown. This section is dedicated to bridge that gap by using the information available from the higher scale model as appropriate input condition for particle scale heat transfer model.

Thermal response of a particle is characteristically different depending upon the nature of laser source (continuous wave or pulsed). The characteristic features associated with both the heating modes are discussed here while the modelling details are provided in chapter 3.

The effective physical properties of the powder and that of the bulk material considered in the simulation are summarized in the Table 5.8. The effective specific heat of powder is obtained by mass weighted average of constituents. These properties correspond to commercially pure Titanium, which is selected since it is widely subjected to laser treatment including laser sintering, cutting and welding.

Table 5.8 Material properties for laser particle interaction model

Propertiy	Bulk material	Powder
Thermal conductivity (λ)	$22{\cdot}1$	$1{\cdot}45$
Density	$4540{\cdot}0$	$2931{\cdot}5$
packing density	$1{\cdot}0$	$0{\cdot}646$
Specific heat	$523{\cdot}5$	$523{\cdot}6$
Enthalpy of fusion	$288{\cdot}0 \times 10^3$	$288{\cdot}0 \times 10^3$
Optical penetration depth	$6{\cdot}0 \times 10^{-9}$	$63{\cdot}0 \times 10^{-6}$
emissivity	$0{\cdot}3$	$0{\cdot}48$
Absorption coefficient	$1{\cdot}67 \times 10^8$	$1{\cdot}59 \times 10^4$

A schematic of comparison between a pulsed laser source and continuous wave laser source is shown in Fig. 5.39. During continuous wave heating, the powder particles subjected to laser irradiation are continuously heated. The source is specified by its average power, beam diameter and scan velocity. whereas, to define a pulsed laser source, frequency and duration of heating pulse is also needed in addition to average power, beam diameter and scan velocity. During the pulsed heating the powder bed is subjected to short bursts of high energy pulses.

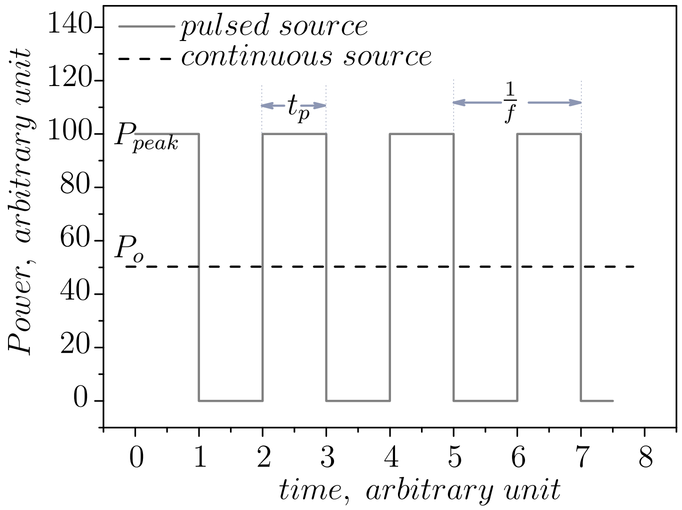

Figure 5.39 Schematic of a pulsed laser source and corresponding continuous source

5.6.1 Pulsed heating

A particle is subjected to repeated heating cycles during its interaction with a puled laser beam. A typical pulsed heating cycle [41] consists of three distinct stages identified by heating during the laser pulse followed by thermalization and then cooling.

5.6.1.1 Pre-melting stage

Here we will discuss the influence of various governing parameters on heat transfer in the particle while the particle temperature is below the melting point of the material at any moment between the consequent pulses. As shown in Fig. 5.40, each laser pulse leads to a sharp rise in particle surface temperature to a temporary peak. Immediately after the pulse, the surface temperature drops while core temperature is still rising, and almost a uniform temperature is established in the particle. The increase in mean temperature of a particle during the first few

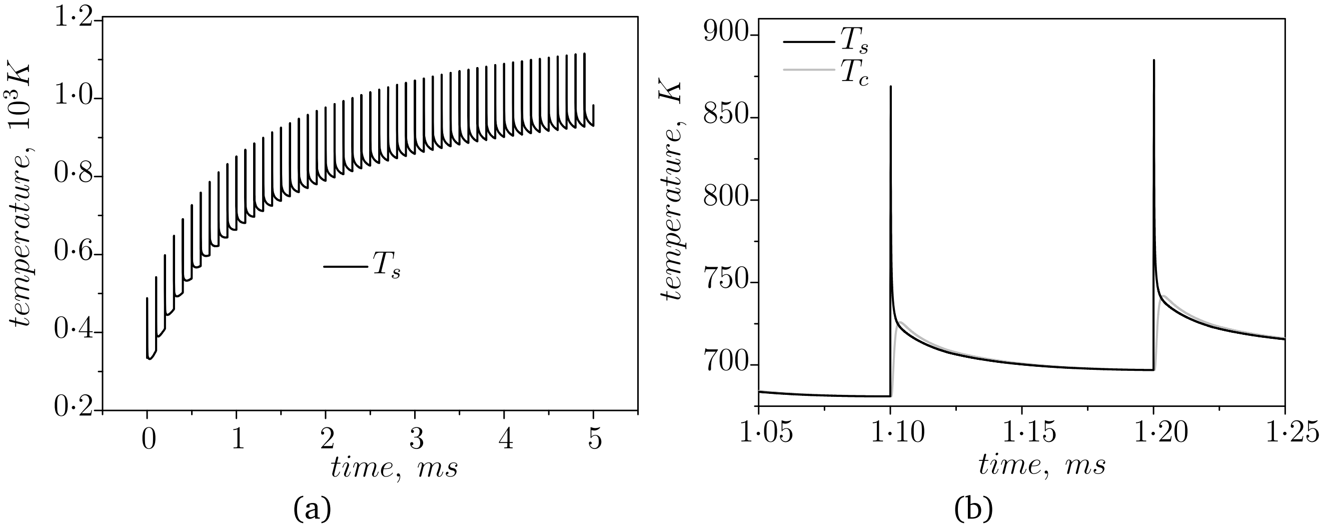

(a) (b)

Figure 5.40 Particle surface temperature evolution due to successive laser pulses; $P_o = 1\ W,\ f = 10\ kHz,\ t_p = 200\ ns,\ r_p = 12\ \mu m$

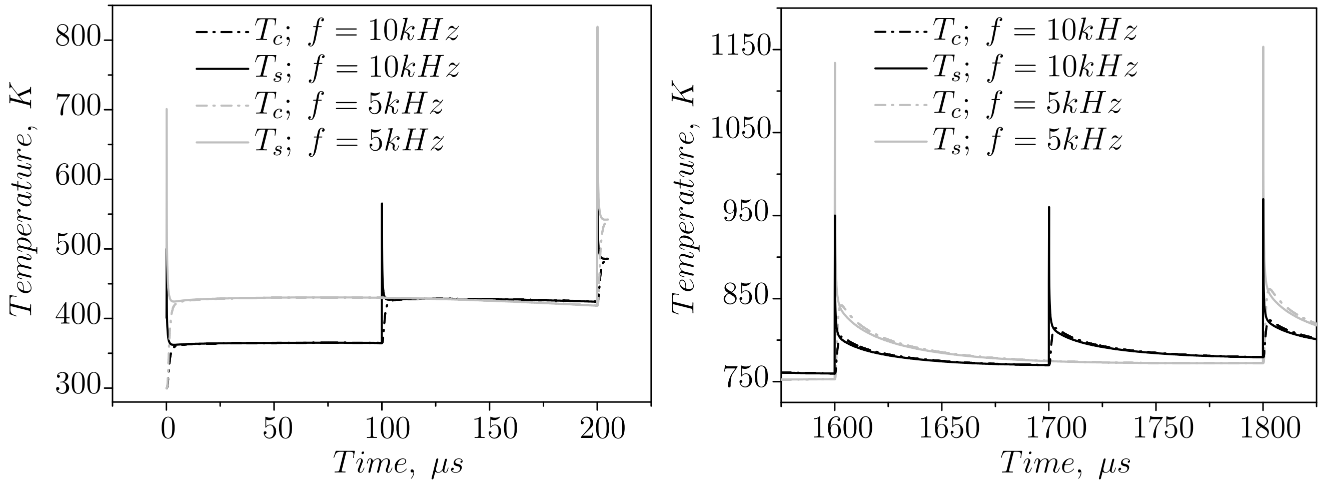

(a) (b)

Figure 5.41 Temperature evolution at the particle surface and core; $P_o = 1\ W,\ t_p = 150\ ns,\ r_p = 11\ \mu m$; (a) for initial few pulses; (b) after initial transition.

laser pulses is much higher than during the following pulses. This is due to low heat transfer rate from heated particles to the unheated powder owing to small temperature difference between the heated and unheated particles at the beginning of the laser scan cycle. As the average temperature of the heated particles increases, the heat loss to the unheated surroundings influences the particle temperature evolution.

It is observed that both the peak surface temperature and the mean temperature of the particle approach their respective maximal temperatures asymptotically. This maximal temperature corresponds to a steady state temperature reached in the center of a spherical domain $0 < r < r_*$ heated with constant and uniform heat source and surrounded by a an infinite unheated space. Contrary to this, earlier models [40, 71] predict a linear rise in particle temperature. This disagreement can be attributed to the fact that the computations were either performed for the initial stage of laser scan cycle, when the particle peak temperature and average temperature are far from their maximal values [40], or to the fact that the models take into account interaction between laser beam and a powder particle alone in isolation from its surroundings [71] and thus does not reflect the influence of heat transfer between the particle and surrounding medium on temperature evolution of single particle.

The difference in temperature evolution during the beginning of the laser scan cycle and later stages is shown in Fig. 5.41. At the beginning of the laser scan cycle the particle average temperature hardly drops below the thermalization temperature (corresponding to the temperature at which the core and the surface temperature curves intersect) and remains almost constant during the pulse gap (time interval between the pulses), whereas for later stage the particle average temperature continuously decreases during the pulse gap. Furthermore, the peak surface temperature achieved during a pulse decreases with increasing pulse frequency as seen in Fig. 5.41. This can be explained by the fact that the power is distributed equally among the pulses and therefore the energy per pulse varies inversely with the frequency.

Figure 5.42 represents the evolution of temperature field in the particle and its surroundings after the first pulse. The thin heated layer at the particle surface is at higher temperature than its interior during the pulse and immediately afterwards. This is because the optical penetration depth of laser radiation in the bulk material is much smaller than the particle radius, therefore the heat generated during the laser-particle interaction is limited to a very thin layer on the particle surface. In addition to that, the pulse duration is much short than the characteristic time of the thermal conductivity in the particle.

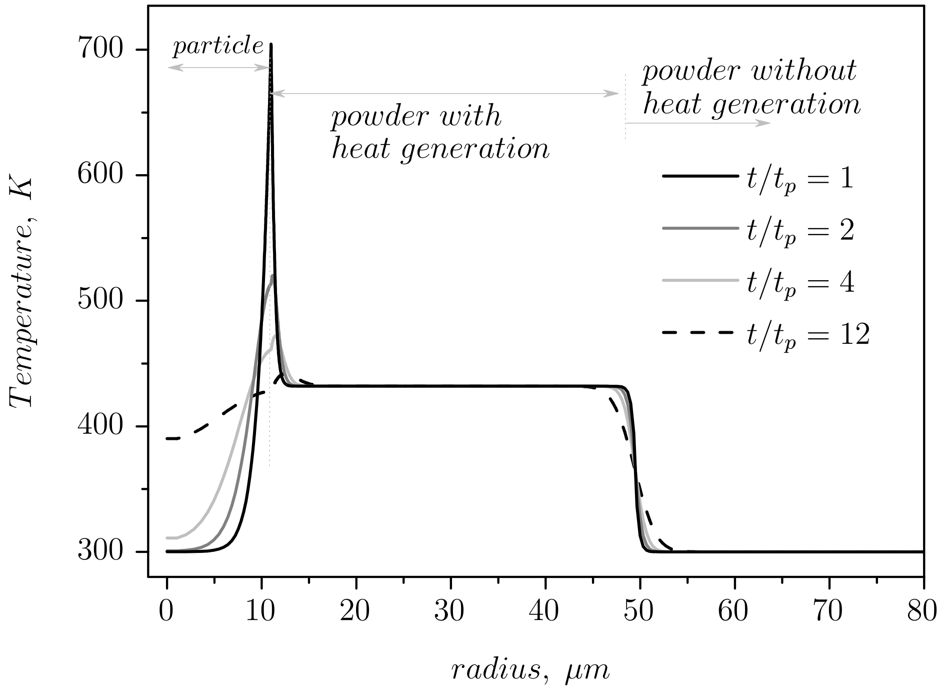

Figure 5.42 Temperature evolution within the particle ($r_p = 11\ \mu m$) and its surrounding at $P_o = 1\ W,\ t_p = 150\ ns,\ f = 5\ kHz\cdot$

Knowing the thermal response of a particle for a given pulse frequency enables us to adjust frequency for initiating sintering at lower laser power, as seen in Fig. 5.43. The plot shows the particle surface temperature evolution for the laser sources with the same average power but different pulse frequencies at different degrees of preheating to initiate melting at same instant. The lower preheating required for low frequency source clearly indicates lower power required. Therefore, when comparing two sources with different frequencies, the low frequency source enables either low power consumption (as well as sintering at lower mean temperature) or faster sintering for the case when average power of the sources is the same.

The influence of pulse duration on the temperature evolution in the particle is represented in Fig. 5.44. It can be observed that the peak surface temperature of the particle increases with decreasing pulse duration, while the thermalization temperature as well as average temperature

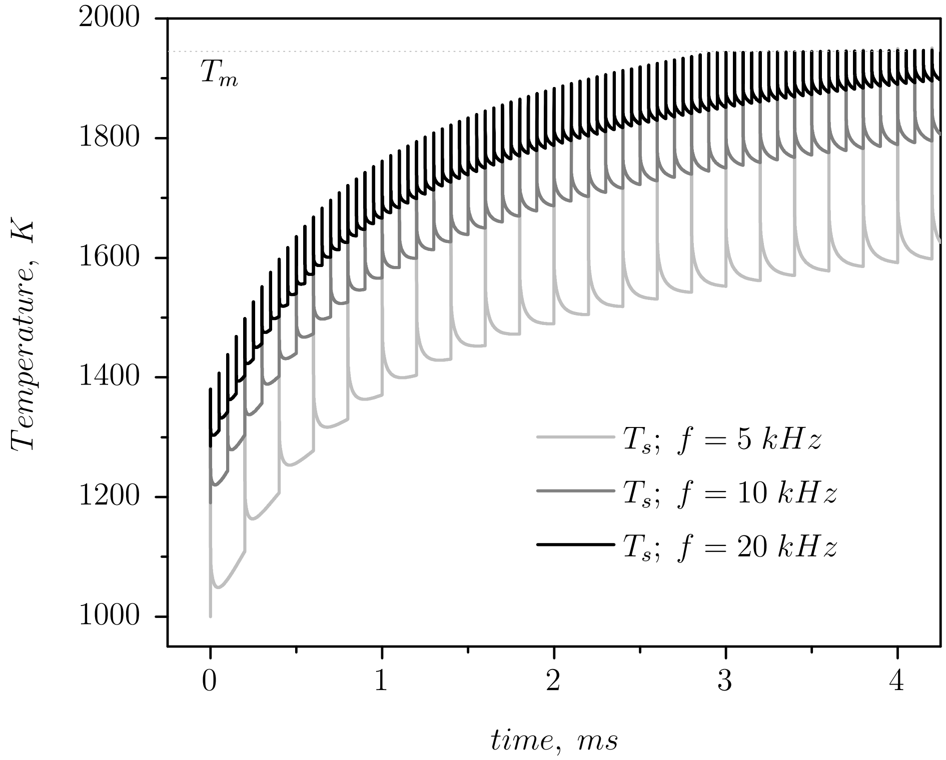

Figure 5.43 Particle surface temperature for different degrees of preheating corresponding to different frequencies to initiate melting in the particle ($r_p = 11\ \mu m$) for $P_o = 1\ W,\ t_p = 150\ ns$

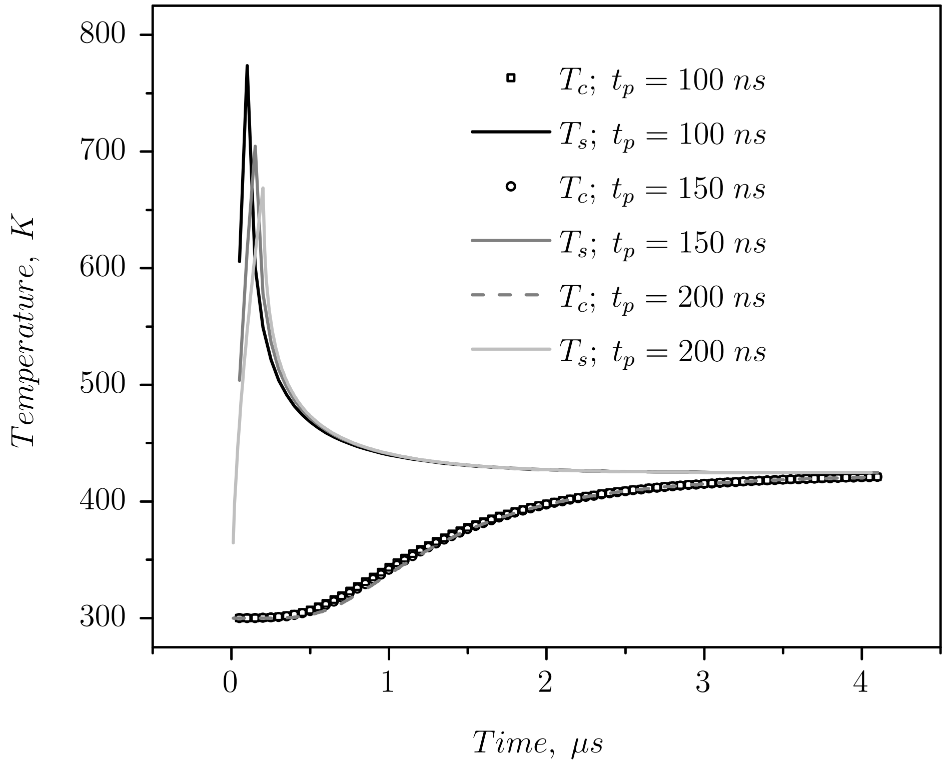

Figure 5.44 Influence of pulse duration on particle surface temperature ($r_p = 11\ \mu m,\ P_o = 1\ W,\ f = 5\ kHz$.

of the particle remains almost unchanged. This behavior is due to the fact that the same amount

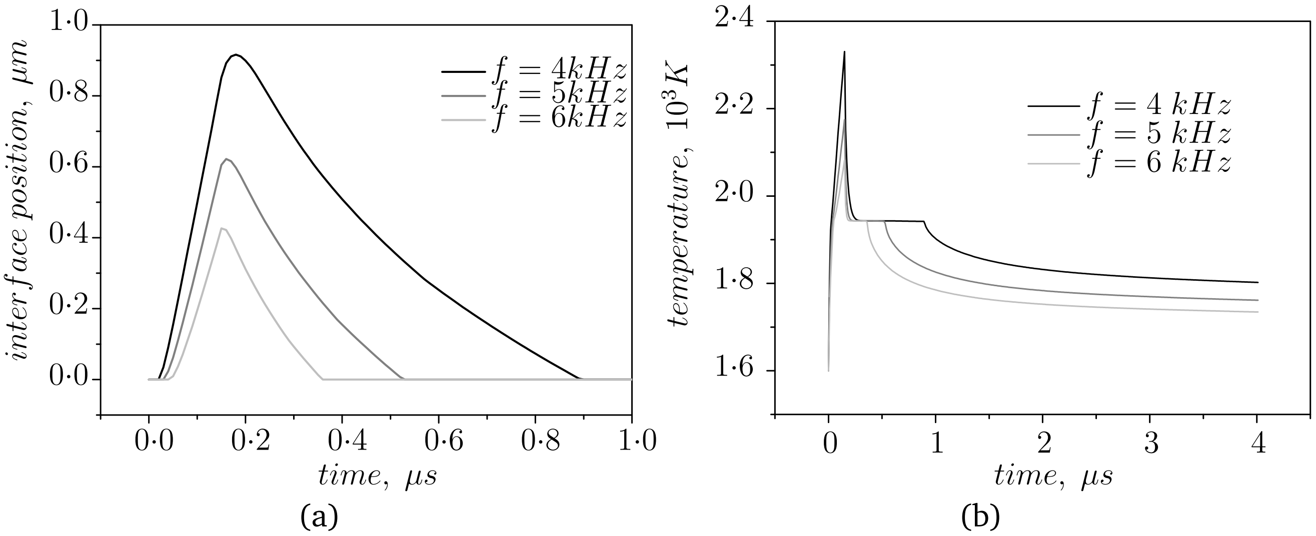

Figure 5.45 Influence of pulse frequency on ; (a) solid-liquid interface position; (b) surface temperature ($P_o = 2\ W,\ t_p = 150\ ns,\ r_p = 11\ \mu m$).

of energy is transferred in shorter time for short duration pulse, thus increasing the peak power per pulse which can be calculated as $P_{peak} = P_o/t_p f$.

Since the actual interaction between the laser beam and the particle during a single pulse is on a nanosecond scale and most of the pulse energy is delivered over a very narrow near-surface layer of thickness equal to the optical penetration depth, the temperature gradients in the vicinity of the particle surface achieve very high values. The particle surface is at higher temperature than its interior and the surroundings (see Fig. 5.42).

5.6.1.2 Melting and resolidification

In this section we discuss heat transfer in the powder particle and its surroundings in the presence of phase change (melting and solidification). The average power has been chosen in such a way that the melting temperature is achieved at the particle surface in a single pulse starting from initial temperature of particle at $1600\ K$.

Figures 5.45(a) and 5.45(b) show phase interface location (distance from the particle surface to the interface) and the evolution of surface temperature, respectively, for different pulse frequencies. It can be seen that for low frequency source melting begins earlier, a larger fraction of particle undergoes melting, and solidification is completed later. It can be observed from Fig. 5.45(b) that very high peak surface temperatures can be achieved during laser-particle interaction; especially at relatively low pulse frequencies. Further lowering of frequency may lead to evaporation of the particle material and plasma formation [3].

The curves plotted in Fig. 5.46(a) show the solid-liquid interface position for a constant average laser source power and various pulse durations. It is seen that the fraction of particle melted during a single pulse increases with decreasing pulse duration. This is because with reducing

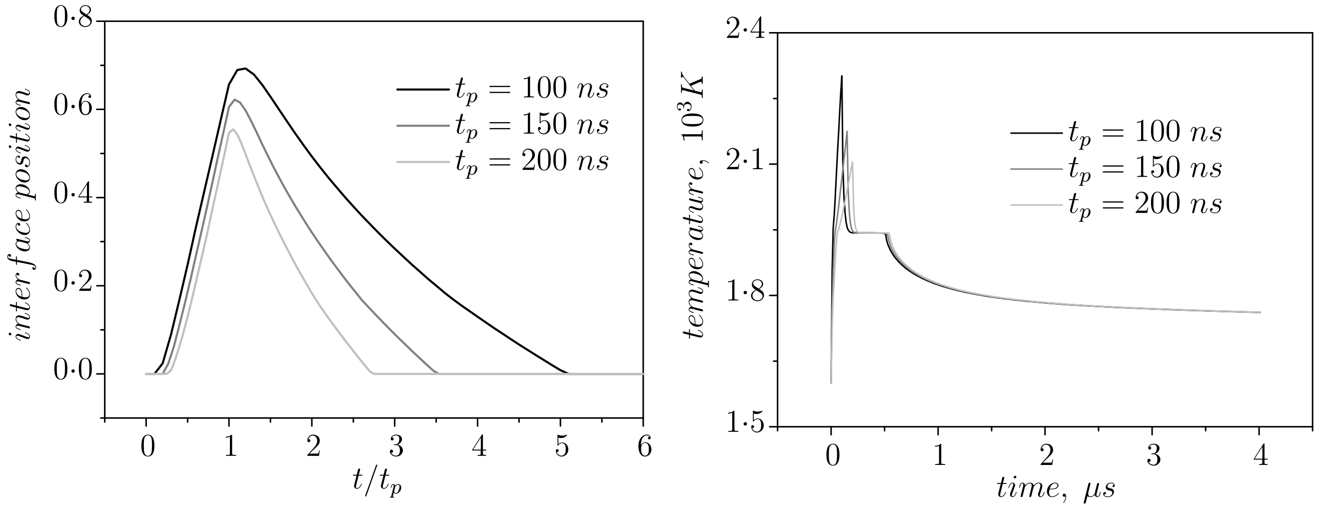

(a) (b)

Figure 5.46 Influence of pulse duration on ; (a) solid-liquid interface position; (b) surface temperature ($P_o = 2\ W,\ f = 5\ kHz,\ r_p = 11\ \mu m$).

the pulse duration, large fraction of heat generated is utilized for phase change, rather than being conducted to the particle center and to surroundings. The major advantage of varying pulse duration is that the peak skin temperature as well as melting rate can be controlled without affecting other parameters like thermalization temperature, time taken to achieve thermalization and average temperature of the particle (see Fig. 5.46(b)).

5.6.2 Continuous wave heating

Figure 5.47(a) shows the temperature evolution of particle at its surface and core. In this case the laser beam energy is continuous as opposed to the pulsed source. The temperature peaks at the surface - as observed in pulsed heating - are not found for continuous wave heating. There is hardly any difference observed between temperature evolution at the particle surface and the core. This indicates that thermal response of the particle in this case is faster than the heating rate by the source and particle is thermalized during heating. Moreover, by comparing the temperature evolution with a pulsed source of same average power (see Fig. 5.47(b)), it is found that particle temperature during continuous heating closely follow the averaged temperature (temporal and spatial) of pulsed heated case. Thermal transients of a particle subjected to continuous wave heating have been discussed during investigation of heat transfer in the granular bed and the phase change characteristics will be treated during combined heat transfer and coalescence modelling in the next sections.

5.7 Particles coalescence

This section is devoted to the hydrodynamics of coalescing particles in the powder bed. Building upon the results of pure thermal studies in the previous sections, where it is found that particles

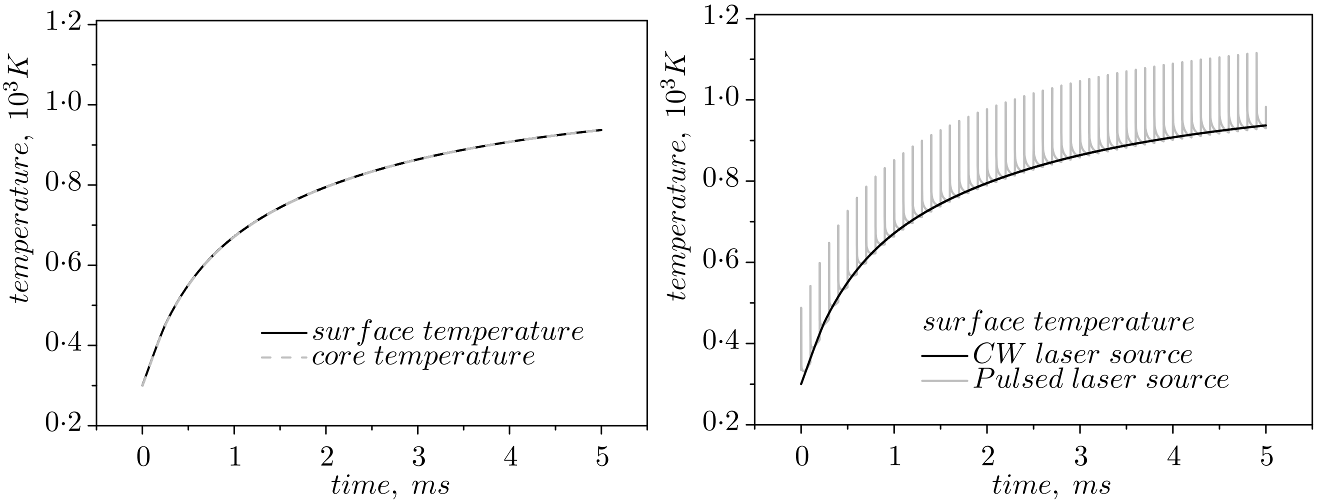

(a) (b)

Figure 5.47 Particle surface temperature evolution during continuous wave heating; $P_o = 1\ W,\ f = 10\ kHz,\ t_p = 200\ ns,\ r_p = 12\ \mu m$

are subjected to repeated cycles of partial melting and resolidification at the outer surface while the core remains solid during exposure to pulsed laser source. A good idealization would be to consider a representative case of two particles with solid cores and viscous shell, having a finite contact as shown in Fig. 4.1. The size of solid cores is fixed during isothermal coalescence. We first describe the pure hydrodynamics of isothermal coalescence of particles while simultaneous heat transfer, phase change and coalescence will follow next, where the variation in the core size is considered.

5.7.1 Isothermal coalescence

The results presented here describe the coalescence of two particles. We have considered two different configurations relevant to the sintering of single component powder and two component powder. For single component powder, both the coalescing particles are assumed to have equal core size. It can be due to partial melting of metallic particles or specially prepared coated particles with the coating acting as viscous fluid. In case of two component powders, coalescence between a fully melted particle and a partially melted particle is investigated.

5.7.1.1 Single component powder

For single component metallic powders all particles are of same material. The two representative particles of radius r_p are assumed to be partially melted. The solid core of radius r_c are assumed to be at the centre of each particle initially. Multiple cases of different core to particle ratio (r_c/r_p) are considered to study the influence of core size on the densification behaviour. Figure 5.48 shows the shape evolution of two coalescing particles. The initial stage of sintering is characterized by fast densification rate due to high curvature gradients along the free surface in the neck region, causing large surface tension force driving the flow. With increasing of the

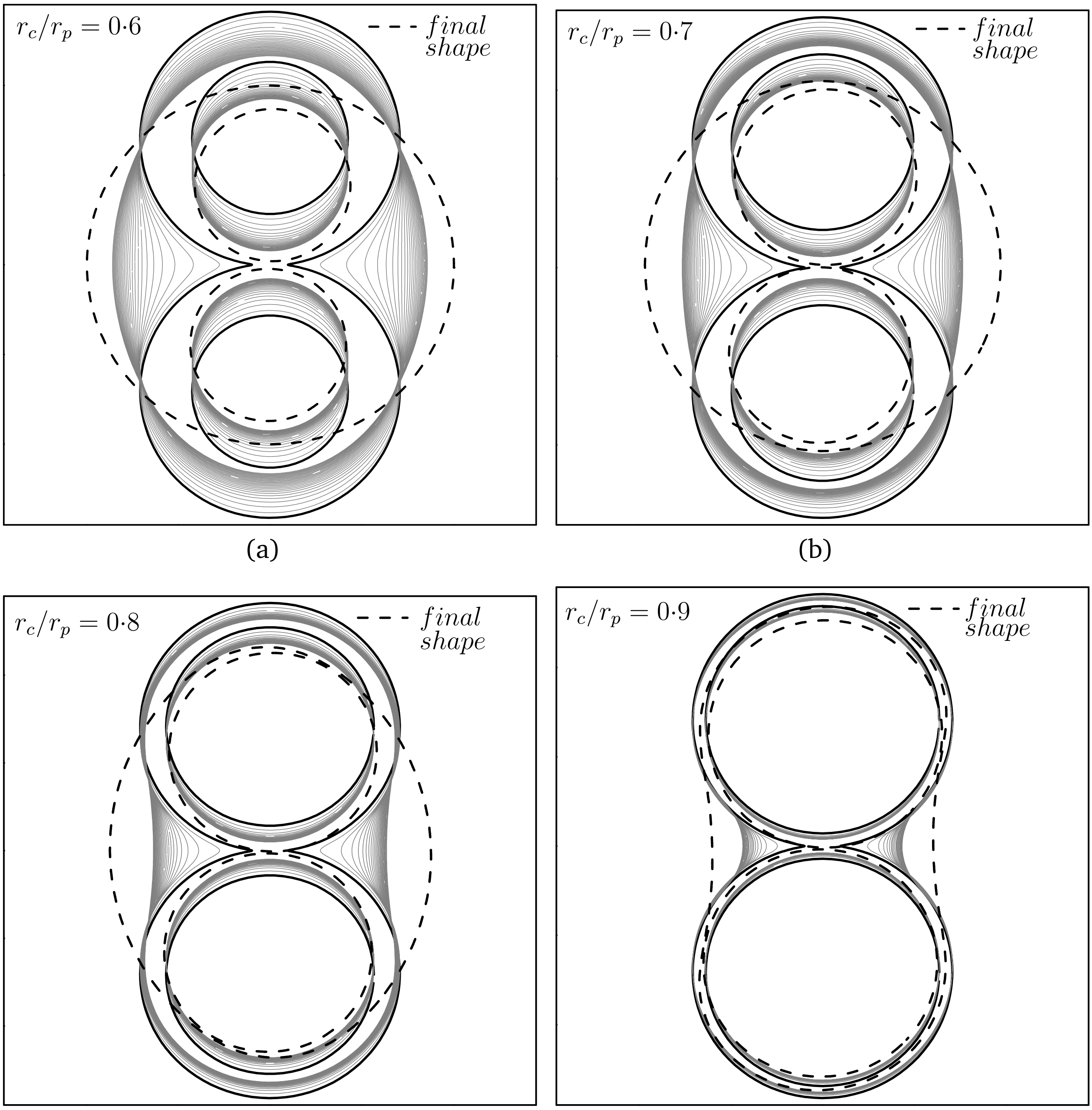

(a) (b) (c) (d)

Figure 5.48 Shape evolution of coalescing particles for single component material system.

neck radius and decreasing curvature gradients along the boundary, densification significantly slows down with progressing time.

The coalescing particles tend to attain the equilibrium shape of a cylinder of radius equal to $r_p\sqrt{2}$ as long as core to particle ratio $r_c/r_p < 1/\sqrt{2}$. If $r_c/r_p \geqslant 1/\sqrt{2}$ the volume of the minimal circle encompassing both solid cores exceeds the combined volume of the solid and liquid phases in the particles. In this case the equilibrium shape is not circular, and the liquid layer will dewet a part of the solid core. The simulations up to dewetting point are beyond the scope of the present study.

The dashed lines in Fig. 5.48(a)-5.48(b) show the equilibrium circular shape of the coalesced particles and the final position of the solid cores. The dashed lines in Fig. 5.48(c)-5.48(d) show the shape of particles just before the rupture of the viscous layer and the position of solid cores at the same instant. For $r_c/r_p = 0{\cdot}8$ the rupture is likely to occur at the apex of the solid core. As the ratio r_c/r_p approaches unity, the position of the rupture point shifts to side and it can be suggested that the equilibrium shape of the coalesced particles consists of a liquid bridge between two solid cores and an additional liquid "cap" in the vicinity of the apex of each particle.

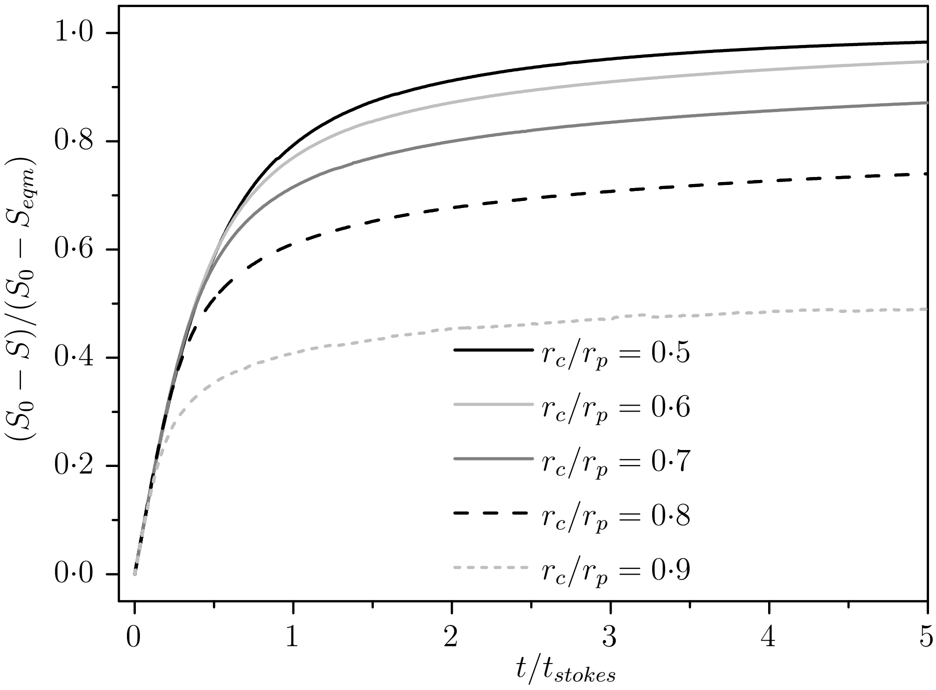

Figure 5.49 Influence of core size on densification rate

Figure 5.49 shows the densification rates for various core to particle ratios. The influence of solid core size on initial stages of sintering is not significant for small core to particle ratios, but its effect is visible during the later stages, when two cores come close to each other obstructing the bulk flow. It can be seen that all curves overlap at initial stage indicating no influence of core at this stage. The rapid decrease in densification rate at the later stages is due to the presence of core. The maximum attainable density for a given time is limited by the core size.

To study the influence of core eccentricity on densification rates and final shape, the initial position of each core has been shifted (along the line joining the centers of particles) either towards the contact point or away from the contact point. Figure 5.50 compares the densification rates for eccentric cores. The cores are shifted by 15% of particle radius. It is found that, if the cores are shifted away from the contact point, faster densification is achieved, since the cores do not obstruct the flow near the neck region during the initial stages of sintering, when the sintering

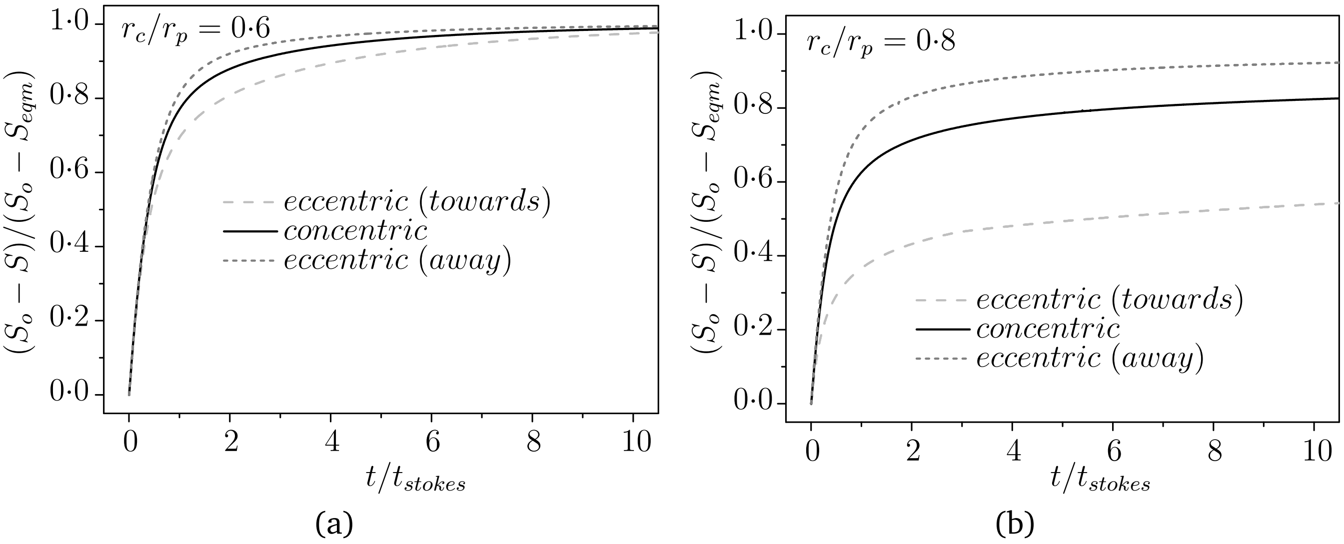

Figure 5.50 Influence of core eccentricity on densification

rates are fastest. On the other hand it is also evident that influence of eccentricity is significant only for high core to particle size ratios.

5.7.1.2 Two component powder

It is assumed that both the particles have equal viscosity of the liquid phase and the interfacial tension between two liquids is negligible. Shape evolution for this case is shown in Fig. 5.51. It can be concluded that the influence of core size is very limited for the case of coalescence between a particle with solid core and a fully viscous particle since the final shapes are almost identical and are close to equilibrium shape of a circle. It is further evident from densification curves (see Fig. 5.52) that for the systems having only one solid core, densification rates are only marginally affected by the presence of core and only for high core to particle ratio. Most of the densification occurs up to time $t/t_{stokes} = 1{\cdot}0$ and the densification rates are almost similar during this time for core to particle ratio less than 0.9.

5.7.2 Coupled heat transfer, phase change and coalescence

Here we consider the basic case of heat transfer, melting and coalescence of two representative particles in contact. The final state of fused particles is governed by rates of melting and coalescence. The variation of core size is not known a priori and depends on heat transfer and free surface geometry. At the same time evolution of free surface depends upon the core size and molten thickness.

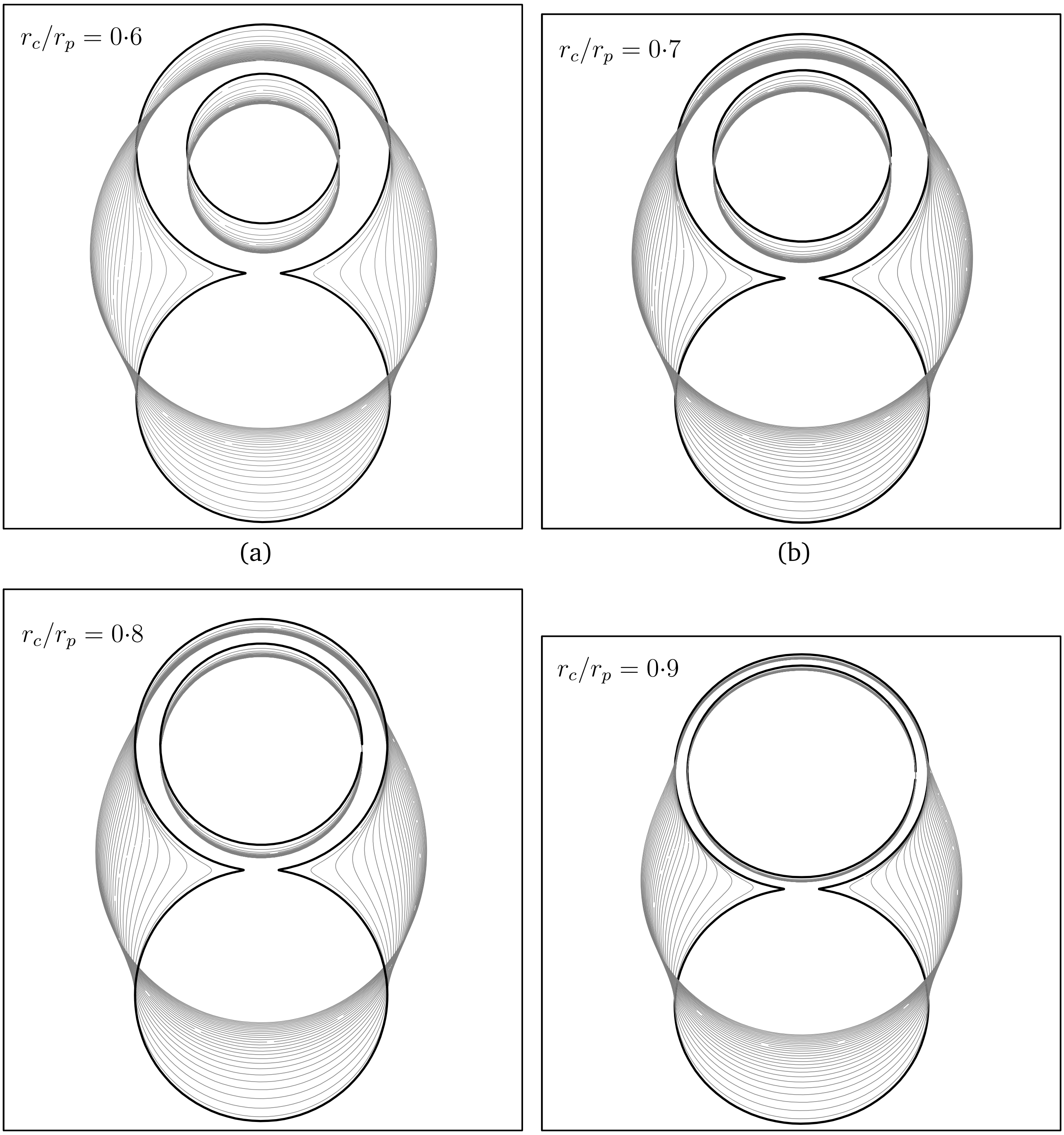

(a) (b)

(c) (d)

Figure 5.51 Shape evolution of coalescing particles for two component material system.

The laser heating is modelled as heat flux on the particle surface. The expression for applied heat flux at the free surface of coalescing particles is given as

$$q = \frac{(1-\epsilon_e)\left(1-\frac{1}{e}\right)P_o}{N_p 4\pi r_p^2}\,. \tag{5.4}$$

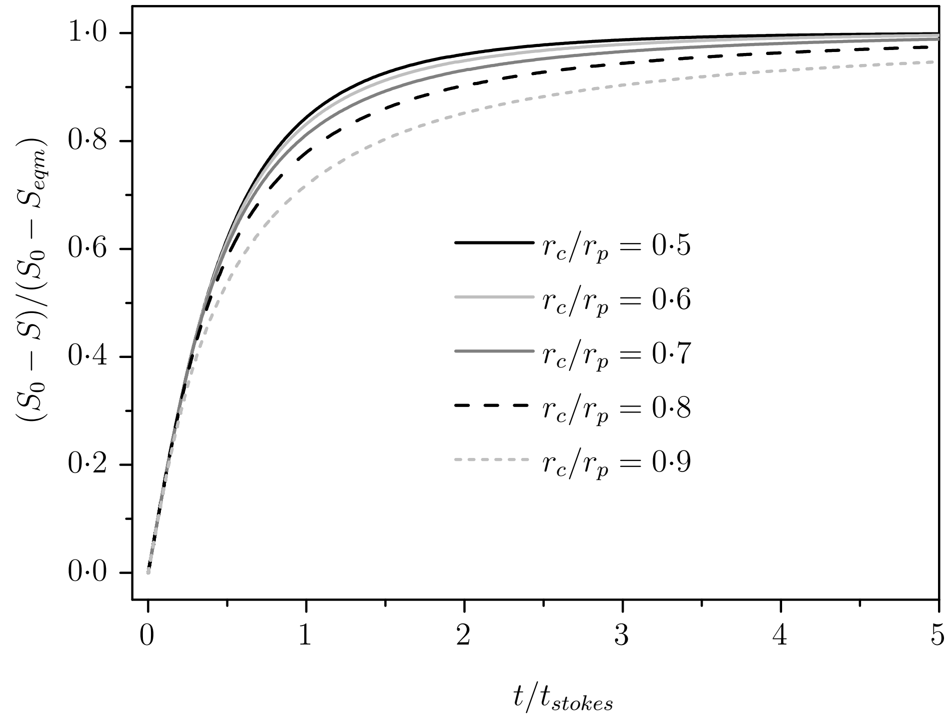

Figure 5.52 Influence of core size on densification rate for two component powder

Table 5.9 Thermo-physical properties of material used in simulation

Property	Value
Melting point (T_{mp})	$1943{\cdot}0\ K$
Enthalpy of fusion (H_f)	$288{\cdot}0\ kJ \cdot kg^{-1}$
Specific heat (C_p)	$523{\cdot}3\ J \cdot kg^{-1} \cdot K^{-1}$
Density (ρ)	$4540{\cdot}0\ kg \cdot m^{-3}$
Thermal conductivity (λ)	$22{\cdot}1\ W \cdot m^{-1} \cdot K^{-1}$
Emissivity (ϵ)	0.2
Powder emissivity (ϵ_e)	0.4

The complete derivation for heat flux at the particle surface is given in modelling section 3.4.4. The properties of reference material used in the simulation are given in Table 5.9. The interdependence of melting and coalescence govern the final shape of fused particles. These phenomena have their respective characteristic times. Apart from material properties, melting time strongly depends on applied heat flux. Accordingly, we have defined characteristic time for melting as time required to melt a particle (which is at melting point) completely and its expression is given by

$$t_{melt} = \frac{\frac{4}{3}\pi r_p^3 \rho H_f}{P}, \tag{5.5}$$

where P is heat flow rate to the particle. While the characteristic time of coalescence is defined as

$$t_{stokes} = \frac{R_{eqm}\mu}{\gamma}, \tag{5.6}$$

where R_{eqm} is the radius of completely molten coalescing particles at equilibrium state, that corresponds to a circular shape having combined area of coalescing particles. The ratio of two characteristic times is an important non-dimensional parameter influencing coalescence during phase change. The following dimensionless parameters have been used in this study.

$$\begin{aligned}
\mathbf{X} &= x/R_{eqm}, \\
\mathbf{Y} &= y/R_{eqm}, \\
\theta &= (T - T_{mp})/(T_{mp} - T_0), \\
St &= C_p(T_{mp} - T_0)/H_f, \\
Q &= qR_{eqm}/H_f\rho\kappa, \\
F_{stokes} &= t_{stokes}/t_{ht}, \\
F_{melt} &= t_{melt}/t_{ht}, \\
t^* &= t/t_{ht}
\end{aligned}$$

where St is the Stefan number, Q is the dimensionless parameter characterizing the applied heat flux, and $t_{ht} = R_{eqm}^2/\kappa$ is the characteristic time of heat conduction. We assume that material properties are invariable during the phase change.

The diameter of powder particles commonly encountered in laser sintering may vary from $10\ \mu m$ to $50\ \mu m$ in diameter. The size of the particles considered in this study is $30\ \mu m$. Heat transfer and phase change evolution of single particles for two different heat fluxes have been simulated as reference cases. The heat flux values of $10^8\ Wm^{-2},\ 5{\cdot}0 \times 10^8$ and $10^9\ Wm^{-2}$ have been selected corresponding to laser power of $50\ W,\ 250\ W$ and $500\ W$ respectively. The same laser parameters have been used for simulating melting and coalescence of two representative particles in the powder bed.

The time during which particle is exposed to applied heat flux depends on the scanning speed of laser beam and its spot size as $t_{exp} = v_s/\phi_b$. The predictions about melting initiation and subsequent growth of molten film on single particle can be used to fix laser parameters. Time needed to initiate melting on a particle surface from initial state (room temperature) is determined by sensible heating, which depends on heat capacity of material and heat source strength, whereas time to melt completely depends on enthalpy of melting.

The evolution of molten film thickness on the particle surface due to phase change is shown in Fig. 5.53. The zero on independent time axis indicates melting initiation for respective case. As expected the melting initiation and its progress is much faster for high heat flux case. Progressively increasing slope of both the curves indicate rising interface velocity. This is due to decreasing size of solid cores as melting progress. For $Q = 0{\cdot}2$ the melting initiates at around $t^* \approx 6$ whereas exposure time (during which particles are subjected to heating) corresponding to beam diameter of $140\ \mu m$ and laser scan speed of $1{\cdot}0\ ms^{-1}$ is $t^* \approx 3$. Therefore sintering is

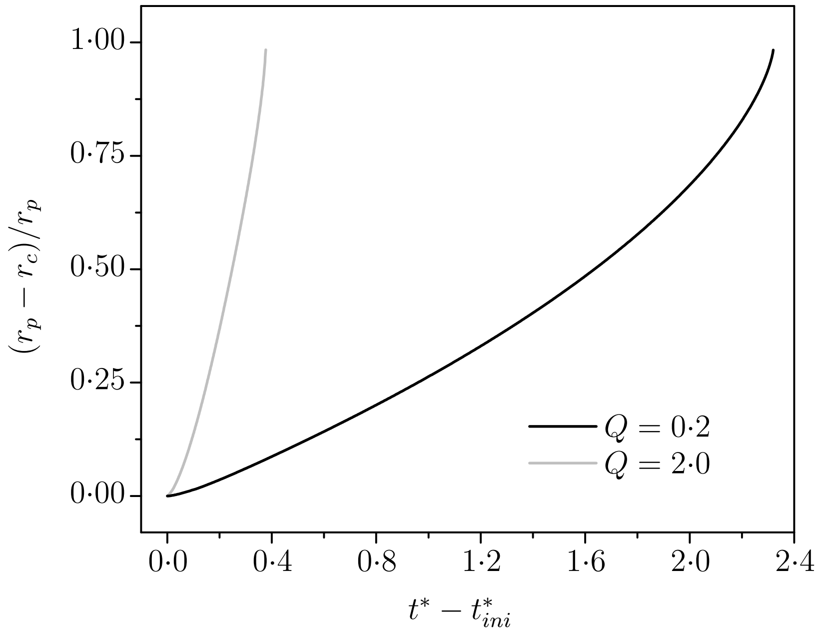

Figure 5.53 Molten film thickness growth for particles subjected to constant heat flux condition (values are normalized with respect to particle radius)

unlikely in this case. However, to achieve sintering for the same laser power, scan speed must be reduced in proportion to the desired increase in interaction time. On the other hand, for the laser scan speed of $1{\cdot}0\ ms^{-1}$ exposure time is sufficiently long to completely melt the particle for $Q = 2{\cdot}0$.

5.7.2.1 Phase change and coalescence

To understand the role of governing variables in actual sintering process, simultaneous melting and coalescence of two particles in contact is simulated. The maximal coalescence rate for given particle size and material properties can be obtained under assumption that the particles in contact completely viscous, while the presence of solid cores is expected to retard the densification rate. Therefore, the liquid film thickness growth rate is major parameter governing densification of particles during laser sintering. Simulations have been carried out for different combinations of F_{stokes} and F_{melt} by varying each of them independently.

Figure 5.54 shows the evolution of the melting front for $F_{stokes} = 1{\cdot}34$. The observed melting front is not circular. This is due to reducing heat flow from the region near the contact area as melting proceeds. Besides growing contact between the particles, the coalescence process is accompanied by decreasing surface area exposed to heat source. It appears that hardly any coalescence occurs for high heat flux ($Q = 2{\cdot}0$) case. However, it is important to consider the respective time scales during which melting takes place for both the heat flux conditions. The melting time for the case $Q = 2{\cdot}0$ is about an order of magnitude smaller than for the case $Q = 0{\cdot}2$, whereas time scale for coalescence is the same for both the cases. Thus, for higher heat flux the particles are completely melted before any appreciable change in the shape of

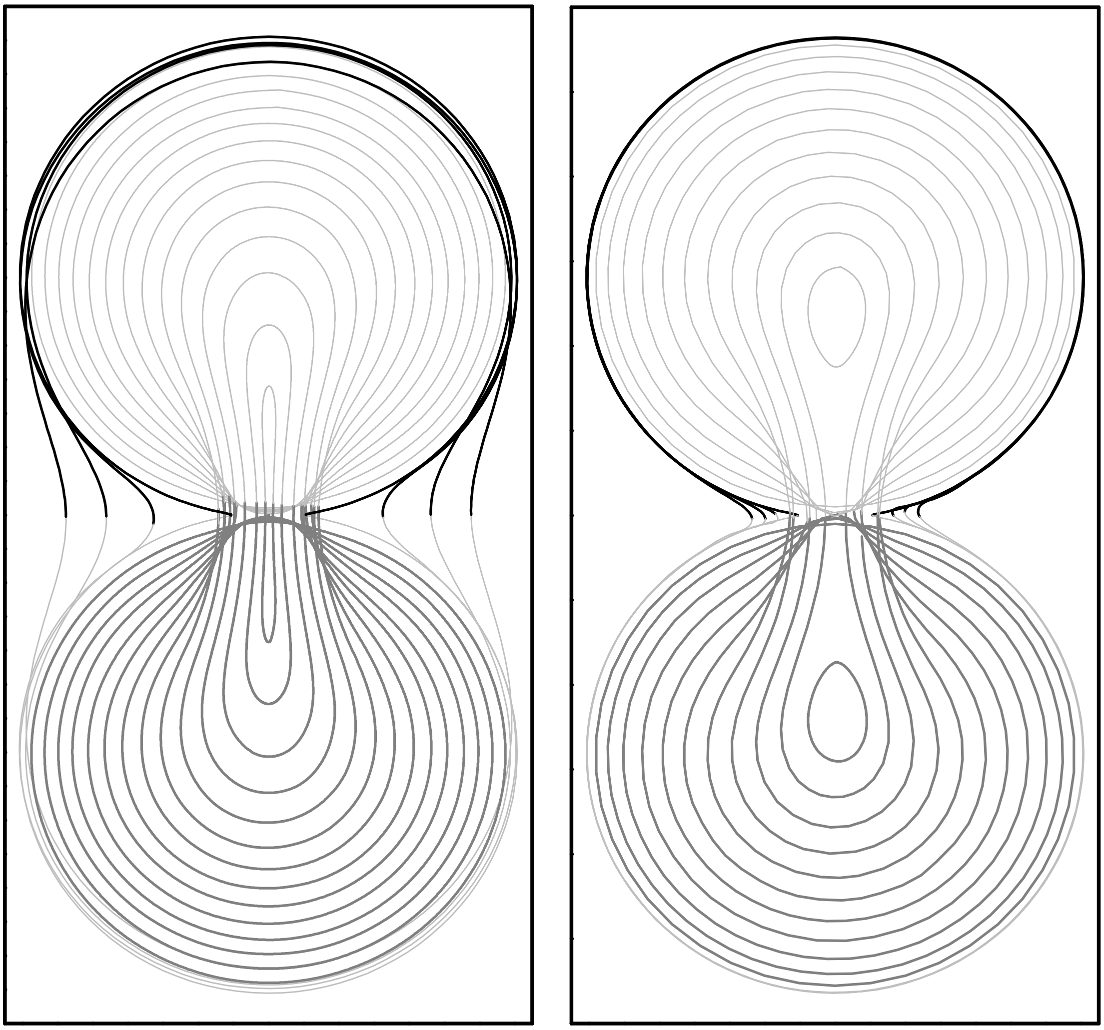
(a) (b)

Figure 5.54 Evolution of melting front for two coalescing particle for $F_{stokes} = 1{\cdot}34$ and subjected to constant heat flux at the surface: (a) $Q = 0{\cdot}2,\ t^* = 6{\cdot}0(0{\cdot}2)8{\cdot}7$; (b) $Q = 2{\cdot}0,\ t^* = 0{\cdot}58(0{\cdot}034)0{\cdot}92$

outer free surface of particles is evident. The densification in this case closely follows the case of completely viscous particles. Figure 5.55 illustrates the evolution of neck radius (measure of contact growth) during coalescence of two particles. The evolution of neck radius in case of purely viscous particles is shown in the same figure for comparison. It is seen in Fig. 5.55(b) that the growth of neck radius (measure of contact growth) is nearly identical to viscous coalescence. For low heat flux condition ($Q = 0{\cdot}2$), since melting time scale is comparable with coalescence time scale, these two phenomena are strongly coupled. This is evident from figures 5.54(a) and 5.55(a). It is found that solid cores are being pulled towards each other due to surface tension forces acting at free surface of the melting particles. Two cores appear to touch and continue to melt as single domain after that. The touching of solid cores as well as eccentricity towards contact can influence densification significantly [31]. Nevertheless, cores are found to melt considerably ($r_c/r_p \leq 0{\cdot}6$) to have any significant influence on contact growth in this case. The neck growth is considerably slow than in the limiting case of completely melted particles.

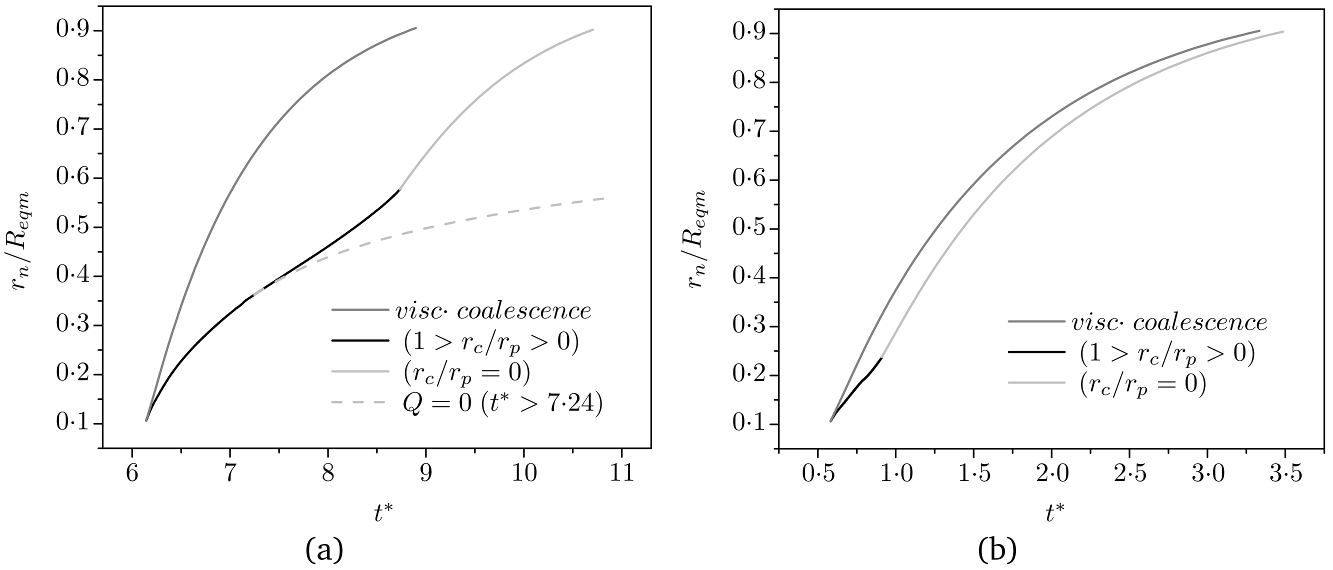

(a) (b)

Figure 5.55 Neck radius growth for coalescing particles for $F_{stokes} = 1{\cdot}34$: (a) Q = 0.2; (b) Q = 2.0

For completely molten particles coalescence the slope of curve showing neck radius growth is maximal at the beginning of coalescence and it continuously decreases there after. For coalescence with melting cores, the contact growth is obviously slow due to dominant influence of cores. However, the effect of cores decreases with decreasing of their size during melting. This is evident by observed increase in slope of neck radius curve during coalescence in Fig. 5.55(a). Consequently we can classify densification into three phases based on influence of melting cores.

- When melting has just began and cores are relatively big ($1 > r_c/r_p > 0{\cdot}7$) to influence the contact growth significantly. This phase is characterized by continuous decrease in rate of neck radius growth.
- This is characterized by decreasing influence of melting cores ($0{\cdot}7 > r_c/r_p > 0$) as the slope of neck growth curve begin to increase.
- After the cores are completely melted, the molten particles continue to coalesce till free surface begins to freeze due to cooling.

In addition to subjecting particles to heat flux till complete melting take place, another case is considered where heat flux at the boundary is reduced to zero after certain amount of melting. This represents increased scan speed for which laser beam passes over the coalescing particles before they are completely melted. Among many likely scenarios, we have assumed domain boundary to be adiabatic owing to presence of other adjacent particles which are also heated by same source. Other obvious reason for investigating adiabatic boundary condition, while heat loss to surrounding is also likely, is that as long as there is no solidification initiating at free surface, melting process of solid cores govern the coalescence. The solidification initiating

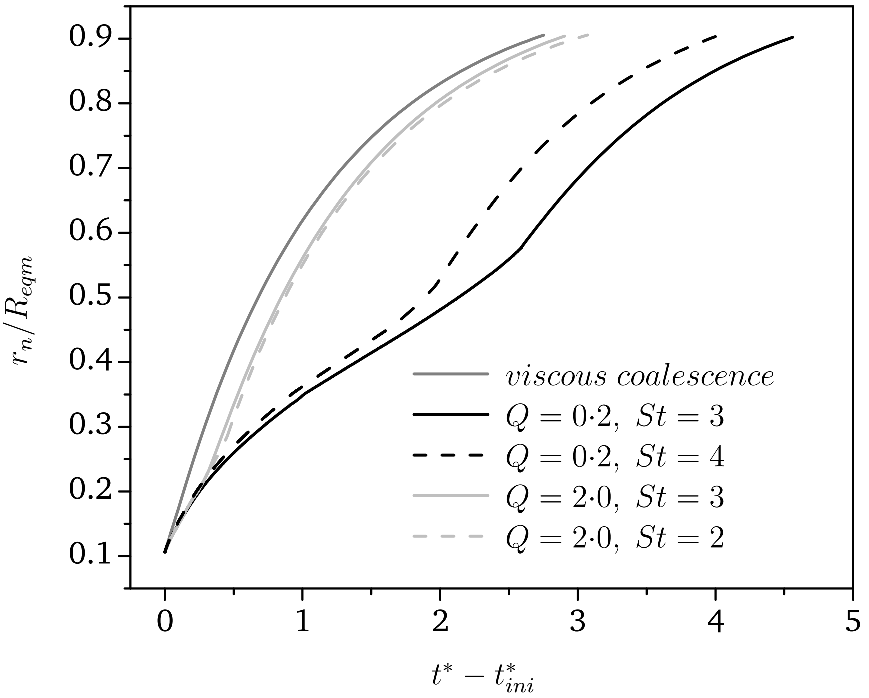

Figure 5.56 Influence of melting rate on coalescence

from free surface driven by the heat loss to surroundings would freeze it irrespective of the subsequent thermal state of the particles.

It is found that, despite stopping energy supply, melting of solid cores continue, however slowly, due to heat conduction from superheated liquid melt to subcooled solid core. The equilibrium state of particles will depend on the laser power, exposure time, particle size and material properties. The densification rate for such case will depend upon relative size of cores with respect to particle size in other words liquid melt thickness. Dashed line in Fig. 5.55(a) indicate neck radius growth when subjected to adiabatic boundary condition starting from $t^* = 7{\cdot}24$ corresponding to laser scan speed of $0{\cdot}4\ ms^{-1}$. Contact growth rate is significantly reduced compared to the case with constant heat supply.

Further simulation cases are considered for variation of melting rates by changing latent heat of fusion from reference value, for the both selected heat flux conditions. For high heat flux ($Q = 2{\cdot}0$) melting rate is reduced by increasing enthalpy of melting ($St = 2$), whereas for low heat flux ($Q = 2{\cdot}0$) melting rate is increased by decreasing enthalpy of fusion ($St = 4$) as expected. Figure 5.56 shows evolution of contact growth in comparison to the respective reference case ($St = 3$). Though it is evident that higher melting rate will enable faster densification, however, the influence is not as significant for high heat flux case as predicted in the low heat flux case. This is because when melting time scale is smaller than coalescence time scale, the influence of core size that is more significant at later stages of sintering [31] is almost negligible as particles are completely melted during early stages itself and coalesce as purely viscous particles till solidification. On the other hand when melting time scale is comparable to coalescence time scale, melting rate strongly affects coalescence and the increase in the melting rate results in a comparable increase in coalescence rate. Therefore, influence of melting rate is dominant when melting time scale is equal or more than coalescence time scale. Based on above discussion,

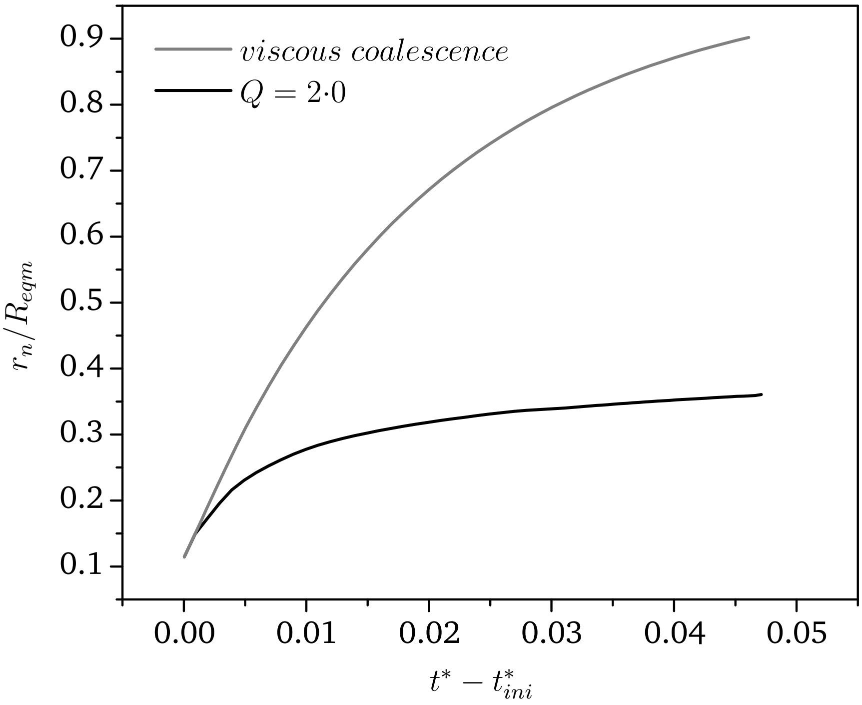

Figure 5.57 Neck radius growth for coalescing particles for $F_{stokes} = 0{\cdot}023$

it is apparent that contact growth between the particles can be uniquely specified by the ratio of melting and coalescence time scales. This is found to be true as long as solid cores do not touch each other during coalescence. However, slight deviation from expected variation in contact growth has been found due to large solid cores touching each other during early stages of sintering. Figures 5.57 and 5.58 show the neck radius and shape evolution of coalescing particles for $Q = 2{\cdot}0$ and $t_{stoke}/t_{melt} = 0{\cdot}17$ respectively. We observe that during initial stages, cores, that are still large ($r_c/r_p \approx 0{\cdot}9$), are pulled close to each other and thus obstruct the flow near the neck region and retard the contact growth. In our earlier study on coalescence of particles with solid cores of fixed size [31] it was found that for high core to particle ratios even a small amount of eccentricity of cores towards neck region significantly affects densification.

Figure 5.60 shows temperature contour plots at different time steps during heating. The solid-liquid interface position at the corresponding time steps is indicated by dashed lines. Unlike single particle case, the non-uniformity in temperature distribution along the surface of the particles near the contact area (neck region) is clearly evident and is found to increase with time. Moreover, the lowest temperature on the free surface of coalescing particles is found to occur at contact points where the curvature is highest. This can be justified as free surface comprising neck region is relatively close to interface (see Fig. 5.54), which always remains at melting point, hence low surface temperatures near neck region for fixed heat flux conditions applied at the free surface. Figure 5.59 shows particle surface temperature at three different time steps. A large temperature gradient along the particle surface in the contact region develops from the beginning of coalescence. Therefore in addition to flow due to curvature gradients, Marangoni flow due to surface tension gradients is also expected to influence sintering. This effect should be taken into account in the future works.

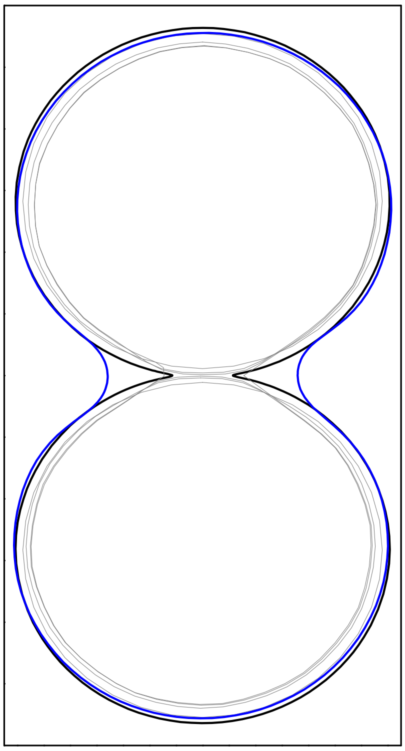

Figure 5.58 Shape evolution of coalescing particles for $F_{stokes} = 0{\cdot}023,\ Q = 2{\cdot}0,\ t^{*} = 0{\cdot}58 - 0{\cdot}6 - 0{\cdot}613 - 0{\cdot}625$

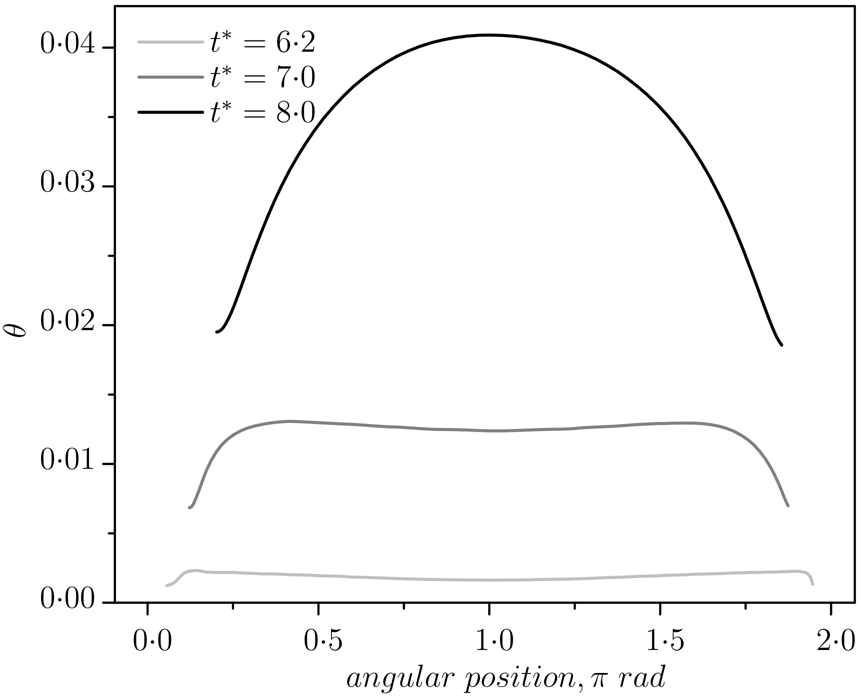

Figure 5.59 Temperature variation along the particle surface between the contact points.

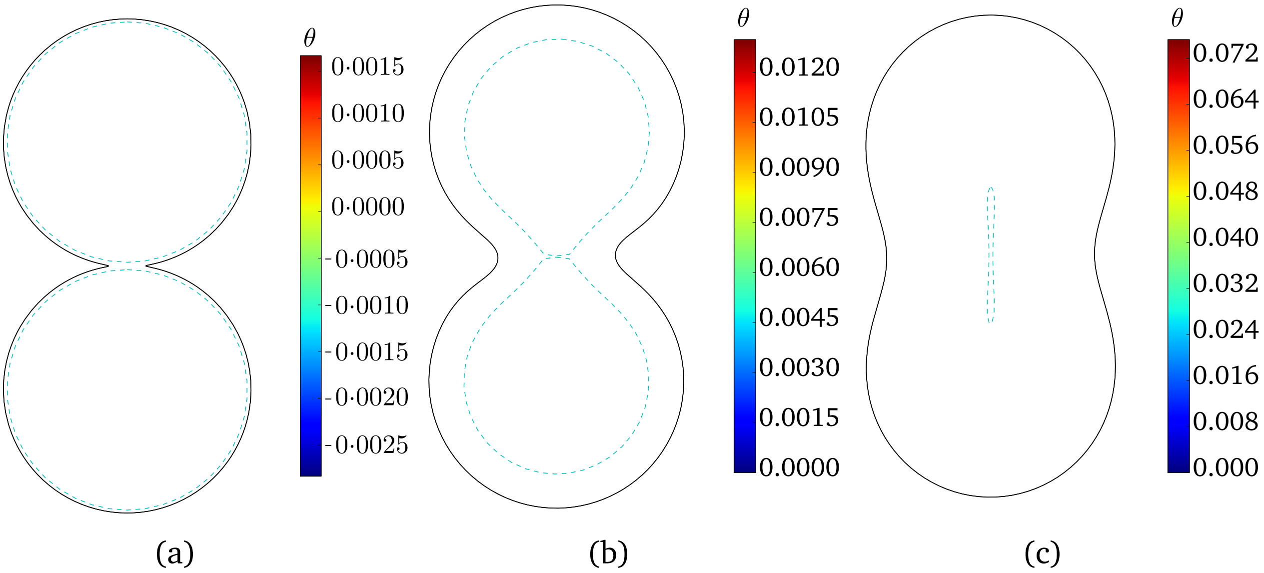

(a) (b) (c)

Figure 5.60 Temperature contour for coalescing particles subjected to constant heat flux corresponding to $Q = 0{\cdot}2$: (a) $t^* = 6{\cdot}14$; (b) $t^* = 7{\cdot}0$; (c) $t^* = 8{\cdot}7{\cdot}$

6

Summary and Outlook

To conclude, the work done in the scope of present thesis is subdivided into two stages. The first stage consists of model development, computer implementation, and validation of developed models. The second stage consists of simulation of selective laser sintering process using developed models.

6.1 Model development, numerical implementation and validation

In order to investigate the dominant phenomena during laser sintering process, multi scale heat transfer models and hydrodynamic models have been developed in this work. All the developed models are implemented as stand-alone computer codes using scientific programming language Fortran 90 for Windows as well as Linux platforms. The validation of the developed codes is done by comparing the results with standard benchmark problems in literature. The chronological summary of the modelling work is listed as follows:

1. We began with modelling the power bed geometry of desired size distribution of particles. This randomly distributed packed bed geometry is obtained using open source granular package in LAMMPS molecular dynamic code, while the auxiliary codes were developed in Fortran 90 to define its mean packing characteristics and to evaluate effective radiative emissivity.
2. A discrete thermal model is developed to investigate the spatial and temporal behaviour of powder bed when subjected to localized heating due to moving laser beam. Ray-tracing

approach is used to model laser radiation absorption and transport in the powder bed. Interparticle thermal radiation and conduction is also considered the modelling. A novel method for solving radiation heat exchange between surfaces is developed.

3. A particle scale thermal model is developed to investigate the details of thermal transients during very short time frame of laser particle interaction. This model accounts for phase change in the particle and the particle surroundings are considered as homogeneous medium in this case.
4. A Boundary Element model is developed for description of isothermal coalescence of two representative particles with viscous shell and solid core at the centre of each particle. The solid core size is assumed to be fixed in this model.
5. The isothermal coalescence model is further extended to include the variation of core size induced by heat transfer and phase change. Dual reciprocity boundary element approach is used to include transient heat transfer and phase change. A simple and novel vector addition approach is developed to derive nodal velocity from the normal velocities of adjacent elements.

6.2 Numerical simulation and analysis of SLS

The developed computer codes were used to simulate the heat transfer and coalescence phenomena during selective laser sintering of metallic powders. The influence of important process parameters, namely laser power, scan speed, laser pulse frequency, pulse duration, powder grain size has been investigated. In addition, validation experiments were performed and the measurements were compared with simulation results. Based on simulation results an attempt is made to predict the process window of operation for obtaining continuous sintered tracks. The major findings of the study are:

1. The spatial and temporal variation of dominant heat transfer phenomena in the powder bed due to moving laser source is investigated and the model predictions for track parameters are compared with experimental measurements to validate our model.
2. Besides regular powder materials, the developed discrete thermal model is especially suitable to predict thermal behaviour of new material systems involving large discontinuity in terms of physical properties, particle grain size etc.
3. Thermal response of an individual particle in laser beam path is analysed for a range of laser power and scan speed combinations. During exposure the incident laser radiation from source to particle is dominant while heat transfer due to interparticle conduction is dominant during cooling. The relative influence of interparticle thermal radiation is negligible.

4. The source energy per unit length of the scanned track (P/v_s) is important parameter to determine the operating window for process parameters.

5. The thermal response of a particle in the powder bed is strongly influenced by nature of laser source. In case of pulsed laser source the particle surface experiences repeated peaks during short bursts of heat generated at the periphery of the particle. The laser pulse frequency and duration can be selected to achieve a series of phase change cycles (partial melting and resolidification) along the periphery of the particle.

6. The influence of solid cores on the densification rates of coalescing particles under isothermal conditions is studied. In case of single component powder solid cores for $r_c/r_p > 0{\cdot}7$ significantly influence densification rate as well as maximum achievable density. On the other hand, for two component powder mixture the influence of solid core is very limited even for $r_c/r_p \geqslant 0{\cdot}9$.

7. The relative influence of melting and coalescence time scales is highlighted and discussed. For small ratios between the melting time scale and coalescence time scale, contact growth is fast and determined by liquid melt properties. On the other hand, when melting time scale is large as compared to coalescence time scale, contact growth is determined by the rate of melting. Contact growth between the coalescing particles is classified into three zones based on influence of melting cores.

8. Despite large r_c/r_p contact growth is fastest at the beginning, driven by surface tension forces due to large curvature gradients in the contact region.

6.3 Outlook

In present thesis, multiple numerical models are developed, implemented, validated and used to investigate dominant phenomena during Selective laser sintering. Each model can be used as an individual code to carry out detailed parametric study of relevant phenomena or can act as auxiliary code to provide supporting/input data needed to account for its effect on other phenomena. The study provided details of heat transfer, phase change phenomena occurring at both the particle scale as well as powder bed scale and densification due to coalescence. The submodels developed in the scope of this work can be combined into one integrated process model for SLS and applied to carry out pre-production simulation and planning.

A method is proposed in the thesis to determine process window for a given material, however, further detailed parametric study is required to investigate the influence of parameters like beam size, powder grain size distribution etc. In the future, increased confidence can be achieved by performing simulations for much broader range of materials and parameters.

The actual operating conditions during laser sintering are far more complex then the modelled conditions. The developed models can be extended with an aim to incorporate some of the complexities for example, including the influence of geometrical changes in the granular bed due to coalescence of particles in contact. Such development would greatly enhance the accuracy and ensure wide applicability of the model.

Further studies can be carried out to develop relation between the input process parameters (laser power, frequency, scan speed, powder material, powder particles size) and the parameters of the resulting sintered parts. However, experimental study is also needed in parallel to numerical study in order to generate reliable data for validation and provide a basis for the process optimization.

Bibliography

[1] Disruptive technology search for space applications. *Deutsches Zentrum fur Luft - und Raumfahrt (DLR)*, DST-TN-05(2), 2012.

[2] F. Abe, K. Osakada, M. Shiomi, K. Uematsu, and M. Matsumoto. The manufacturing of hard tools from metallic powders by selective laser melting. *Journal of materials processing technology*, 111(1):210–213, 2001.

[3] M. V. Allmen and A. Blatter. *Laser-Beam interaction with materials*. Springer-Verlag, Berlin, second edition, 1987.

[4] W. T. Ang. *A Beginner's Course in Boundary Element Methods*. Universal Publishers, Boca Raton, USA, 2007.

[5] C. Argento and D. Bouvard. A ray tracing method for evaluating the radiative heat transfer in porous media. *International journal of heat and mass transfer*, 39(15):3175–3180, 1996.

[6] M. Badrossamay and T. Childs. Further studies in selective laser melting of stainless and tool steel powders. *International Journal of Machine Tools and Manufacture*, 47(5):779–784, 2007.

[7] G. Beer, I. Smith, and C. Duenser. *The boundary element method with programming: for engineers and scientists*. Springer, 2008.

[8] C. H. Bennett. Serially deposited amorphous aggregates of hard spheres. *Journal of applied physics*, 43(6):2727–2734, 1972.

[9] J. D. Bernal and J. Mason. Packing of spheres: co-ordination of randomly packed spheres. *Nature*, 188:910–911, 1960.

[10] D. L. Bourell, M. C. Leu, and D. W. Rosen. Roadmap for additive manufacturing - identifying the future of freeform processing, 2009.

[11] D. L. Bourell, H. L. Marcus, J. W. Barlow, and J. J. Beaman. Selective laser sintering of metals and ceramics. *International Journal of Powder Metallurgy*, 28(4):369–381, 1992.

[12] C. Brebbia and D. Nardini. Dynamic analysis in solid mechanics by an alternative boundary element procedure. *Engineering analysis with boundary elements*, 24(7):513–518, 2000.

[13] C. A. Brebbia. *Boundary element methods in engineering*. Springer New York, 1982.

[14] M. Brewster. Radiative heat transfer in fluidized-bed combustors. volume 83-WA/HT-82, 1983.

[15] H. Brooks and D. Aitchison. A review of state-of-the-art large-sized foam cutting rapid prototyping and manufacturing technologies. *Rapid Prototyping Journal*, 16(5):318–327, 2010.

[16] D. Bunnell, D. Bourell, and H. Marcus. Fundamentals of liquid phase sintering related to selective laser sintering. In *Proceeding of the Solid Freeform Fabrication Symposium*, pages 379–385, 1994.

[17] D. Bunnell, S. Das, D. Bourell, J. Beaman, and H. Marcus. Fundamentals of liquid phase sintering during selective laser sintering. In *Solid Freeform Fabrication Symposium Proceedings, Austin, USA*, pages 440–447, 1995.

[18] H. S. Carslaw and J. C. Jaeger. Conduction of heat in solids. *Oxford: Clarendon Press, 1959, 2nd ed.*, 1959.

[19] W. T. Carter and M. G. Jones. Direct laser sintering of metals. pages 51–59, 1993.

[20] J. Cartigny, Y. Yamada, and C. Tien. Radiative transfer with dependent scattering by particles: part 1 theoretical investigation. *Journal of heat transfer*, 108(3):608–613, 1986.

[21] C. K. Chan and C. L. Tien. Radiative transfer in packed spheres. *ASME J. Heat transfer*, 96:52–58, 1974.

[22] S. Chandrasekhar. *Hydrodynamic and hydromagnetic stability*. Courier Dover Publications, 1961.

[23] J. C. Chen and S. W. Churchill. Radiant heat transfer in packed beds. *AIChE Journal*, 9(1):35–41, 1963.

[24] G. Cheng, A. Yu, and P. Zulli. Evaluation of effective thermal conductivity from the structure of a packed bed. *Chemical Engineering Science*, 54(19):4199 – 4209, 1999.

[25] T. Childs, C. Hauser, and M. Badrossamay. Selective laser sintering (melting) of stainless and tool steel powders: experiments and modelling. *Proceedings of the Institution of Mechanical Engineers, Part B: Journal of Engineering Manufacture*, 219(4):339–357, 2005.

[26] H. Chung and S. Das. Numerical modeling of scanning laser-induced melting, vaporization and resolidification in metals subjected to step heat flux input. *International journal of heat and mass transfer*, 47(19):4153–4164, 2004.

[27] P. Ciraud. Verfahren und vorrichtung zur herstellung beliebiger gegenstande aus beliebigem schmelzbarem material. *German Patent Publication DE 2263777*, July 1973.

[28] A. Clarke and J. Wiley. Numerical simulation of the dense random packing of a binary mixture of hard spheres: Amorphous metals. *Physical Review B*, 35(14):7350, 1987.

[29] H. Cline and T. Anthony. Heat treating and melting material with a scanning laser or electron beam. *Journal of Applied Physics*, 48(9):3895–3900, 2008.

[30] P. A. Cundall and O. D. L. Strack. A discrete numerical model for granular assemblies. *Géotechnique*, 29(1):47–65, Jan. 1979.

[31] R. Dayal, E. Abele, and T. Gambaryan-Roisman. Numerical investigation of coalescence of viscous particles with solid cores. *Proceedings of the ASME 2013 11th International Conference on Nanochannels, Microchannels, and Minichannels*, 2013.

[32] R. Dayal, T. Gambaryan-Roisman, and E. Abele. Numerical study of heat transfer and phase change in a single metal particle of powder material in application to selective laser sintering. *Computational Thermal Sciences*, 3(3), 2011.

[33] C. R. Deckard. Method and apparatus for producing parts by selective sintering. *US Patent 4863538*, Sept. 1989.

[34] W. Di, Y. Yongqiang, S. Xubin, and C. Yonghua. Study on energy input and its influences on single-track, multi-track, and multi-layer in SLM. *The International Journal of Advanced Manufacturing Technology*, 58(9-12):1189–1199, 2012.

[35] G. DiGiuseppe. Surface-to-Surface Radiation Exchange Effects in a 3D SOFC Stack Unit Cell. *Journal of Fuel Cell Science and Technology*, 9(6):061007, 2012.

[36] L. Dong, A. Makradi, S. Ahzi, and Y. Remond. Three-dimensional transient finite element analysis of the selective laser sintering process. *Journal of materials processing technology*, 209(2):700–706, 2009.

[37] H. Exner, P. Regenfuss, L. Hartwig, S. Klötzer, and R. Ebert. Selective laser micro sintering with a novel process. In *Fourth International Symposium on Laser Precision Microfabrication*, pages 145–151. International Society for Optics and Photonics, 2003.

[38] R. P. Feynman, R. B. Leighton, and M. Sands. *The Feynman Lectures on Physics, Desktop Edition Volume I*, volume 1. Basic Books, 2013.

[39] M.-H. Fillion, J. Côté, and J.-M. Konrad. Thermal radiation and conduction properties of materials ranging from sand to rock-fill. *Canadian Geotechnical Journal*, 48(4):11, 2011.

[40] P. Fischer, N. Karapatis, V. Romano, R. Glardon, and H. Weber. A model for the interaction of near-infrared laser pulses with metal powders in selective laser sintering. *Applied Physics A: Materials Science & Processing*, 74 (4):467–474, April 2002.

[41] P. Fischer, N. Karapatis, V. Romano, R. Glardon, H. Weber, and E. Boillat. Sintering of commercially pure titanium powder with a Nd:YAG laser source. *Acta Materialia*, 51 (6):1651–1662, April 2003.

[42] M. Fukai, T. Horikawa, K. Nishiyama, and K. Okumura. Application of direct metal laser sintering for fabrication of production injection moulds. In *Proceedings of the Eighth International Conference on Rapid Prototyping*, pages 407–412, 2000.

[43] P. Furmanski. Effective macroscopic description for heat conduction in heterogeneous materials. *International Journal of Heat and Mass Transfer*, 35(11):3047–3058, Nov. 1992.

[44] K. Furukawa, K. Imai, and M. Kurashige. Simulated effect of box size and wall on porosity of random packings of spherical particles. *Acta mechanica*, 140(3-4):219–231, 2000.

[45] A. S. Glassner, editor. *An introduction to ray tracing*. Academic Press Ltd., London, UK, 1989.

[46] K. Gotoh, W. Jodrey, and E. Tory. Variation in the local packing density near the wall of a randomly packed bed of equal spheres. *Powder Technology*, 20(2):257–260, 1978.

[47] A. Gusarov and J.-P. Kruth. Modelling of radiation transfer in metallic powders at laser treatment. *International Journal of Heat and Mass Transfer*, 48(16):3423–3434, July 2005.

[48] A. Gusarov, I. Yadroitsev, P. Bertrand, and I. Smurov. Heat transfer modelling and stability analysis of selective laser melting. *Applied Surface Science*, 254(4):975–979, 2007.

[49] A. V. Gusarov, T. Laoui, L. Froyen, and V. Titov. Contact thermal conductivity of a powder bed in selective laser sintering. *International Journal of Heat and Mass Transfer*, 46(6):1103–1109, march 2003.

[50] A. V. Gusarov, I. Yadroitsev, P. Bertrand, and I. Smurov. Model of Radiation and Heat Transfer in Laser-Powder Interaction Zone at Selective Laser Melting. *Journal of Heat Transfer*, 131(7):072101, 2009.

[51] C. Hauser, T. Childs, and M. Badrossamay. Further developments in process mapping and modelling in direct metal selective laser melting. *15th Solid Free Form Fabrication Proceedings*, pages 2–4, 2004.

[52] C. Hauser, T. Childs, and K. Dalgarno. Selective laser sintering of stainless steel 314s hc processed using room temperature powder beds. In *Proceedings of the SFF Symposium*, pages 273–280, 1999.

[53] C. Hauser, T. Childs, K. Dalgarno, and R. Eane. Atmospheric control during direct selective laser sintering of stainless steel 314s powder. In *Proceedings of the Solid Free Form Fabrication*, pages 265–272, 1999.

[54] J. J. L. Higdon and C. Pozrikidis. The self-induced motion of vortex sheets. *J. Fluid Mech.*, 150:201–231, 1985.

[55] R. W. Hopper. Coalescence of two equal cylinders: exact results for creeping viscous plane flow driven by capillarity. *Journal of the American Ceramic Society*, 67:262–264, 1984.

[56] Z. Hou and R. Komanduri. General solutions for stationary/moving plane heat source problems in manufacturing and tribology. *International Journal of Heat and Mass Transfer*, 43(10):1679–1698, 2000.

[57] R. Housholder. Molding process. *US Patent 4247508*, Jan. 1981.

[58] J. R. Howell, R. Siegel, and M. P. Meng. *Thermal radiation heat transfer*. CRC press New York, NY, 2011.

[59] A. Jagota and P. R. Dawson. Simulation of the viscous sintering of two particles. *Journal of the American Ceramic Society*, 73(1):173–177, 1990.

[60] A. Jagota and C. Y. Hui. The Effective Thermal Conductivity of a Packing of Spheres. *Journal of Applied Mechanics*, 57(3):789, Sept. 1990.

[61] L. Jepson, J. J. Beaman, D. L. Bourell, and K. L. Wood. Sls processing of functionally gradient materials. *Proceedings of the Eighth Solid Freeform Fabrication Symposium*, Aug. 1997.

[62] W. Jodrey and E. Tory. Computer simulation of isotropic, homogeneous, dense random packing of equal spheres. *Powder Technology*, 30(2):111–118, 1981.

[63] W. S. Jodrey and E. M. Tory. Simulation of random packing of spheres. *Simulation*, 32(1):1–12, Jan. 1979.

[64] John R. Howell, Robert Siegel, Shaker Heights, and M. Pinar Menguc. *Thermal Radiation Heat Transfer*. CRC Press, 5th edition, 2010.

[65] K. L. Johnson and K. L. Johnson. *Contact mechanics*. Cambridge university press, 1987.

[66] P. Karapatis. Modelling and numerical simulation of viscous sintering. *PhD thesis, École polytechnique fédérale de Lausanne*, 2002.

[67] M. Kaviany. *Principles of Heat Transfer in Porous Media*. Mechanical Engineering Series. Springer New York, New York, NY, 1995.

[68] S. Kim and S. J. Karrila. *Microhydrodynamics: Principles and Selected Applications*. Dover publications, 2005.

[69] F. Klocke and C. Wagner. Coalescence behaviour of two metallic particles as base mechanism of selective laser sintering. *CIRP Annals-Manufacturing Technology*, 52(1):177–180, 2003.

[70] S. Kolossov, E. Boillat, R. Glardon, P. Fischer, and M. Locher. 3d fe simulation for temperature evolution in the selective laser sintering process. *International Journal of Machine Tools and Manufacture*, 44(2):117–123, 2004.

[71] C. Konrad, Y. Zhang, and Y. Shi. Melting and resolidification of a subcooled metal powder particle subjected to nanosecond laser heating. *International Journal of Heat and Mass Transfer*, 50(11):2236–2245, 2007.

[72] J. Kruth, M. Leu, and T. Nakagawa. Progress in additive manufacturing and rapid prototyping. *CIRP Annals-Manufacturing Technology*, 47(I):525–540, 1998.

[73] J. Kruth, G. Levy, F. Klocke, and T. Childs. Consolidation phenomena in laser and powder-bed based layered manufacturing. *CIRP Annals - Manufacturing Technology*, 56(2):730–759, Jan. 2007.

[74] J. Kruth, X. Wang, T. Laoui, and L. Froyen. Lasers and materials in selective laser sintering. *Assembly automation*, 23 (4)(4):357–371, 2003.

[75] J. Kruth, X. Wang, T. Laoui, and L. Froyen. Lasers and materials in selective laser sintering. *Assembly Automation*, 23(4):357–371, Jan. 2003.

[76] J.-P. Kruth, L. Froyen, J. Van Vaerenbergh, P. Mercelis, M. Rombouts, and B. Lauwers. Selective laser melting of iron-based powder. *Journal of Materials Processing Technology*, 149(1):616–622, 2004.

[77] J.-P. Kruth, P. Mercelis, J. Van Vaerenbergh, L. Froyen, and M. Rombouts. Binding mechanisms in selective laser sintering and selective laser melting. *Rapid Prototyping Journal*, 11(1):26–36, 2005.

[78] J.-P. Kruth, B. Vandenbroucke, v. J. Vaerenbergh, and P. Mercelis. Benchmarking of different SLS/SLM processes as rapid manufacturing techniques. 2005.

[79] K. Kudo, W. J. Yang, H. Taniguchi, and A. H. Hayasaka. Radiative heat transfer in packed spheres by monte carlo method. In *Heat Transfer in High Technology and Power Engineering Conference*, pages 529–540, 1985.

[80] H. Kuiken. Viscous sintering: the surface-tension-driven flow of a liquid form under the influence of curvature gradients at its surface. *Journal of Fluid Mechanics*, 214:503–515, 1990.

[81] D. Kunii and J. M. Smith. Heat transfer characteristics of porous rocks. *AIChE Journal*, 6(1):71–78, 1960.

[82] G. N. Levy. The role and future of the laser technology in the additive manufacturing environment. *Physics Procedia*, 5:65–80, 2010.

[83] G. N. Levy, R. Schindel, and J.-P. Kruth. Rapid manufacturing and rapid tooling with layer manufacturing (LM) technologies, state of the art and future perspectives. *CIRP Annals-Manufacturing Technology*, 52(2):589–609, 2003.

[84] X. Li and C. Pozrikidis. Film flow of a suspension down an inclined plane. *Philosophical Transactions of the Royal Society of London. Series A: Mathematical, Physical and Engineering Sciences*, 361(1806):847–869, 2003.

[85] K. Lochmann, L. Oger, and D. Stoyan. Statistical analysis of random sphere packings with variable radius distribution. *Solid State Sciences*, 8(12):1397–1413, 2006.

[86] B. D. Lubachevsky. How to simulate billiards and similar systems. *Journal of Computational Physics*, 94(2):255–283, 1991.

[87] A. J. Matheson. Computation of a random packing of hard spheres. *Journal of Physics C: Solid State Physics*, 7(15):2569–2576, 1974.

[88] P. Mercelis and J.-P. Kruth. Residual stresses in selective laser sintering and selective laser melting. *Rapid Prototyping Journal*, 12(5):254–265, 2006.

[89] P. Mrafko and P. Duhaj. Analysis of an aggregate of hard spheres. *physica status solidi (a)*, 23(2):583–589, 1974.

[90] K. A. Mumtaz, P. Erasenthiran, and N. Hopkinson. High density selective laser melting of waspaloy. *Journal of materials processing technology*, 195(1):77–87, 2008.

[91] J. C. Nelson, S. Xue, J. W. Barlow, J. J. Beaman, H. L. Marcus, and D. L. Bourell. Model of the selective laser sintering of bisphenol-a polycarbonate. *Industrial & Engineering Chemistry Research*, 32(10):2305–2317, 1993.

[92] J. R. Nielsen, V. Thornton, and E. B. Dale. The absorption laws for gases in the infra-red. *Reviews of Modern Physics*, 16(3-4):307–324, 1944.

[93] J. Pak and O. Plumb. Melting in a two-component packed bed. *Journal of heat transfer*, 119(3):553–559, 1997.

[94] J. Picka. Statistical inference for disordered sphere packings. *Statistics Surveys*, pages 1–54, 2012.

[95] D. Pinson, R. Zou, A. Yu, P. Zulli, and M. McCarthy. Coordination number of binary mixtures of spheres. *Journal of Physics D: Applied Physics*, 31(4):457–462, 1998.

[96] L. Pittaway. The temperature distributions in thin foil and semi-infinite targets bombarded by an electron beam. *British Journal of Applied Physics*, 15(8):967–982, 1964.

[97] S. Plimpton. Fast parallel algorithms for short-range molecular dynamics. *Journal of Computational Physics*, 117(1):1–19, Mar. 1995.

[98] D. A. Porter and K. E. Easterling. *Phase Transformations in Metals and Alloys, (Revised Reprint)*. CRC press, 1992.

[99] C. Pozrikidis. *Boundary Integral and Singularity Methods for Linearized Viscous Flow*. Cambridge University Press, 1992.

[100] S. M. Rao and H. Toor. Heat transfer from a particle to a surrounding bed of particles. effect of size and conductivity ratios. *Industrial & Engineering Chemistry Research*, 26(3):469–474, 1987.

[101] S. M. Rao and H. L. Toor. Heat transfer between particles in packed beds. *Industrial & engineering chemistry fundamentals*, 23(3):294–298, 1984.

[102] J. Ross, W. Miller, and G. Weatherly. Dynamic computer simulation of viscous flow sintering kinetics. *Journal of Applied Physics*, 52(6):3884–3888, 1981.

[103] R. Rutgers. Packing of spheres. *Nature*, pages 465–466, 1962.

[104] G. Scott and D. Kilgour. The density of random close packing of spheres. *Journal of Physics D: Applied Physics*, 2(6):863–866, 1969.

[105] Y. Shen, D. Gu, and P. Wu. Development of porous 316l stainless steel with controllable microcellular features using selective laser melting. *Materials Science and Technology*, 24(12):1501–1505, 2008.

[106] Z. Shen, S. Zhang, J. Lu, and X. Ni. Mathematical modeling of laser induced heating and melting in solids. *Optics & Laser Technology*, 33(8):533–537, 2001.

[107] L. E. Silbert, D. Ertaş, G. S. Grest, T. C. Halsey, D. Levine, and S. J. Plimpton. Granular flow down an inclined plane: Bagnold scaling and rheology. *Physical Review E*, 64(5):051302, 2001.

[108] B. Singh and M. Kaviany. Independent theory versus direct simulation of radiation heat transfer in packed beds. *International Journal of Heat and Mass Transfer*, 34(11):2869–2882, Nov. 1991.

[109] B. Singh and M. Kaviany. Modelling radiative heat transfer in packed beds. *International Journal of Heat and Mass Transfer*, 35(6):1397–1405, June 1992.

[110] W. Siu and S.-K. Lee. Transient temperature computation of spheres in three-dimensional random packings. *International Journal of Heat and Mass Transfer*, 47(5):887–898, Feb. 2004.

[111] H. Stoffregen, J. Fischer, D. Flaschentrager, M. Rauschenbach, J. Nuffer, T. Melz, and E. Abele. Additive manufacturing of adaptive components by selective laser melting. *Adaptronic Congress*, Sept. 2011.

[112] I. Taguchi, M. Kurashige, and K. Imai. Effects of cubic container's wall or floor on random packing structures of spherical particles. *JSME Int. J. Series A*, (49):265–272, 2006.

[113] L. C. Tao. Generalized numerical solutions of freezing a saturated liquid in cylinders and spheres. *AIChE J.*, 13(1):165–169, 1967.

[114] C. L. Tien. Thermal radiation in packed and fluidized beds. *ASME J. Heat transfer*, 110:1230–1242, November 1988.

[115] N. Tolochko, V. Mikhailov, S. Mozzharov, N. Sobolenko, and I. Yadroitsev. Kinetics of formation of interparticle contacts in the laser sintering of single component metallic powders. *Powder Metallurgy and Metal Ceramics*, 36(1-2):50–55, 1997.

[116] N. Tolochko, V. Mikhailov, S. Mozzharov, N. Sobolenko, and L. Yadroitsev. Theory and technology of sintering, heat, and chemical heat-trearment process: Experimental investigation of the kinetics of regrouping and zonal isolation of particles in the laser sintering of a monolayer of one-component metallic powder powder. *Powder metallurgy and metal ceramics*, 38(3-4):157–161, 1999.

[117] N. Tolochko, S. Mozzharov, N. Sobolenko, I. Yadroitsev, V. Goryushkin, and V. Dubovets. Problems and prospects of selective layer-by-layer laser sintering of powders. *Powder Metallurgy and Metal Ceramics*, 34(3-4):142–145, 1996.

[118] N. K. Tolochko, M. K. Arshinov, A. V. Gusarov, V. I. Titov, T. Laoui, and L. Froyen. Mechanisms of selective laser sintering and heat transfer in Ti powder. *Rapid prototyping journal*, 9(5):314–326, 2003.

[119] N. K. Tolochko, Y. V. Khlopkov, S. E. Mozzharov, M. B. Ignatiev, T. Laoui, and V. I. Titov. Absorptance of powder materials suitable for laser sintering. *Rapid Prototyping Journal*, 6(3):155–161, 2000.

[120] N. K. Tolochko, S. E. Mozzharov, I. A. Yadroitsev, T. Laoui, L. Froyen, V. I. Titov, and M. B. Ignatiev. Balling processes during selective laser treatment of powders. *Rapid Prototyping Journal*, 10(2):78–87, 2004.

[121] G. Van de Vorst, R. Mattheij, and H. Kuiken. A boundary element solution for two-dimensional viscous sintering. *Journal of Computational Physics*, 100(1):50–63, 1992.

[122] G. A. L. van de Vorst. Integral method for a two-dimensional stokes flow with shrinking holes applied to viscous sintering. *J. Fluid Mech.*, 257:667–689, 1993.

[123] G. A. L. van de Vorst. Modelling and numerical simulation of viscous sintering. *PhD thesis, Eindhoven University of Technology*, 1994.

[124] W. L. Vargas and J. J. McCarthy. Heat conduction in granular materials. *AIChE Journal*, 47(5):1052–1059, May 2001.

[125] W. M. Visscher and M. Bolsterli. Random packing of equal and unequal spheres in two and three dimensions. *Nature*, 239:504–507, 1972.

[126] M. J. Vold. A numerical approach to the problem of sediment volume. *Journal of colloid science*, 14(2):168–174, 1959.

[127] V. Voller and M. Cross. Accurate solutions of moving boundary problems using the enthalpy method. *International journal of heat and mass transfer*, 24(3):545–556, 1981.

[128] J. W. DeLima-Silva and L. C. Wrobel. A front-tracking boundary element formulation for solidification/melting problems. *Transactions on Engineering Sciences*, 5:235–243, 1994.

[129] T. Walker, S. Xue, and G. Barton. Numerical determination of radiative view factors using ray tracing. *Journal of Heat Transfer*, 132(7):072702–6, 2010.

[130] X. Wang and J.-P. Kruth. A simulation model for direct selective laser sintering of metal powders. In *International conference on engineering computational technology*, pages 57–71, 2000.

[131] E. W. Weisstein. Sphere point picking – from wolfram mathworld.

[132] T. Whitted. An improved illumination model for shaded display. *Communications of the ACM*, 23(6):343–349, June 1980.

[133] J. D. Williams and C. R. Deckard. Advances in modeling the effects of selected parameters on the sls process. *Rapid Prototyping Journal*, 4(2):90–100, 1998.

[134] T. Wohlers. Additive manufacturing state of the industry. *Wohlers Report*, 2012.

[135] T. Wohlers. Additive manufacturing state of the industry. *Wohlers Report*, 2013.

[136] W. Woodside and J. H. Messmer. Thermal Conductivity of Porous Media. I. Unconsolidated Sands. *Journal of Applied Physics*, 32(9):1688–1699, 1961.

[137] I. Yadroitsev, A. Gusarov, I. Yadroitsava, and I. Smurov. Single track formation in selective laser melting of metal powders. *Journal of Materials Processing Technology*, 210(12):1624–1631, 2010.

[138] S. Yagi and D. Kunii. Studies on effective thermal conductivities in packed beds. *AIChE Journal*, 3(3):373–381, 1957.

[139] Y. S. Yang, J. R. Howell, and D. E. Klein. Radiative heat transfer through a randomly packed bed of spheres by the monte carlo method. *ASME J. Heat transfer*, 105(2):325–332, 1983.

[140] M. F. Zäh and S. Lutzmann. Modelling and simulation of electron beam melting. *Production Engineering*, 4(1):15–23, 2010.

[141] Y. Zhang and A. Faghri. Melting and resolidification of a subcooled mixed powder bed with moving gaussian heat source. *Journal of heat transfer*, 120(4):883–891, 1998.

[142] Y. Zhang and A. Faghri. Melting of a subcooled mixed powder bed with constant heat flux heating. *International Journal of Heat and Mass Transfer*, 42(5):775–788, 1999.

[143] Y. Zhang, A. Faghri, C. Buckley, and T. Bergman. Three-dimensional sintering of two-component metal powders with stationary and moving laser beams. *Journal of heat transfer*, 122(1):150–158, 2000.

[144] J. Zhou, Y. Zhang, and J. Chen. Numerical simulation of random packing of spherical particles for powder-based additive manufacturing. *Journal of manufacturing science and engineering*, 131(3):031004, 2009.

[145] H. Zhu, Z. Zhou, R. Yang, and A. Yu. Discrete particle simulation of particulate systems: theoretical developments. *Chemical Engineering Science*, 62(13):3378–3396, 2007.

[146] A. Z. Zinchenko. Effective conductivity of loaded granular materials by numerical simulation. *Philosophical Transactions of the Royal Society of London. Series A: Mathematical, Physical and Engineering Sciences*, 356(1749):2953–2998, 1998.

Publications

In Journals

R. Dayal, T. Gambaryan-Roisman, E. Abele. Numerical study of Heat Transfer and Phase change in a single metal particle of powder material in application to Selective Laser Sintering, *Computational Thermal Sciences*, Vol. 3, No. 3, pages 169-177, 2011.

R. Dayal, T. Gambaryan-Roisman, E. Abele. Heat transfer, Phase change, and Coalescence of particles during Selective Laser Sintering of metal powders, *Computational Thermal Sciences*, Vol. 4, No. 5, pages 411-423, 2012.

In Conferences

R. Dayal, Hanns A. Stoffregen, J. Fischer, T. Gambaryan-Roisman, E. Abele. Heat Transport Phenomena Governing Selective Laser Melting: Numerical Investigation and Experimental Validation, *Fraunhofer Direct Digital Manufacturing Conference*, March 12-13, 2014, Berlin, Germany.

R. Dayal, E. Abele, T. Gambaryan-Roisman. Numerical investigation of Coalescence of viscous particles with solid cores, *Proceedings of the ASME 2013, 11th International Conference on Nanochannels, Microchannels, and Minichannels-ICNMM2013*, June 16-19, 2013, Sapporo, Japan.

R. Dayal, T. Gambaryan-Roisman, E. Abele. Heat Transfer, Phase change and Coalescence of particles during Selective Laser Sintering of metal powders, *Proceedings of CHT-12, ICHMT International Symposium on Advances in Computational Heat Transfer*, July 1-6, 2012, Bath, England.

R. Dayal, T. Gambaryan-Roisman. Melting, Solidification and Coalescence of metallic particles invoked by Laser Heating, *Proceedings of the 15th International Heat Transfer Conference*, IHTC-15, August 10-15, 2014, Kyoto, Japan (Accepted).

Other publications with abstracts

R. Dayal, T. Gambaryan-Roisman, E. Abele. A simple Numerical method for Radiation Heat Transfer in Complex Irregular geometries, *Indo-German Conference on Modelling, Simulation and Optimization in Applications*, September 5-7, 2012, TU-Darmstadt, Germany.

R. Dayal, T. Gambaryan-Roisman, E. Abele. Coupled Heat Transfer, Phase change and Coalescence of particles during Selective Laser Sintering of metal powders, *Annual meeting of the section of Heat and Mass Transfer*, March 22-23, 2012, Weimar, Germany.

R. Dayal, T. Gambaryan-Roisman, E. Abele. Heat transfer and Hydrodynamics during Selective Laser Sintering of metal powders for Rapid Manufacturing of Porous Micro-structured materials, *International Conference on Cellular Materials CELLMAT-2010*, October 27-29, 2010, Dresden, Germany.

Résumé

Ram Dayal, M.Tech.

Personal

Date of birth	31.05.1979
Place of birth	Jodhpur, India
Family status	Married
Nationality	Indian

Education

1997 – 2001	Bachelor of Engineering (Mechanical Engineering), Jai Narain Vyas University, Jodhpur (India) Thesis: Development of enhanced performance solar air heater
2002 – 2004	Master of Technology (Thermal Engineering) Indian Institute of Technology, Roorkee (India) Thesis: Flow and Transient temperature field estimation in a pressure vessel with internals using CFD techniques

Professional Experience

7/2001 – 6/2002	Graduate Engineer at Larsen & Toubro Limited Vendor development for Earthmoving Equipments
9/2004 – 2/2009	Scientist at BARC, Mumbai (India) Research area: Mathematical modelling and CFD analysis of process heat transfer equipments
3/2009 – 8/2012	Research associate at Center of Smart Interfaces Technische Universität Darmstadt, Germany Research area: Numerical modelling of selective laser sintering
Since 9/2012	Research associate at Institute of Technical Thermodynamics Technische Universität Darmstadt, Germany Research area: Numerical and experimental investigation of selective laser sintering